



HAL
open science

Multi-scale characterization of deformation mechanisms of bulk polyamide 6 under tensile stretching below and above the glass transition

Coraline Millot

► **To cite this version:**

Coraline Millot. Multi-scale characterization of deformation mechanisms of bulk polyamide 6 under tensile stretching below and above the glass transition. Materials. INSA de Lyon, 2015. English. NNT: 2015ISAL0028 . tel-01207840

HAL Id: tel-01207840

<https://theses.hal.science/tel-01207840>

Submitted on 1 Oct 2015

HAL is a multi-disciplinary open access archive for the deposit and dissemination of scientific research documents, whether they are published or not. The documents may come from teaching and research institutions in France or abroad, or from public or private research centers.

L'archive ouverte pluridisciplinaire **HAL**, est destinée au dépôt et à la diffusion de documents scientifiques de niveau recherche, publiés ou non, émanant des établissements d'enseignement et de recherche français ou étrangers, des laboratoires publics ou privés.

Multi-scale characterization of deformation mechanisms of bulk polyamide 6 under tensile stretching below and above the glass transition

Thèse présentée devant
L'Institut National des Sciences Appliquées de Lyon

Pour obtenir
Le grade de docteur

Ecole doctorale
Ecole Doctorale Matériaux de Lyon

Par

Coraline MILLOT

Ingénieure de l'École Nationale Supérieure des Ingénieurs en Arts Chimiques Et Technologiques

Soutenue le 7 Avril 2015 devant la commission d'examen

Jury

F. Auriemma	Professeur (Università Federico II, Napoli)	Rapporteur
N. Billon	Professeur (CEMEF-MINES ParisTech)	Présidente du jury
L.-A. Fillot	Docteur (Solvay-R&I centre-Lyon)	Correspondante industrielle
O. Lame	Professeur (INSA de Lyon)	Directeur de thèse
V. Miri	Maître de conférences (UMET, Lille1)	Rapporteur
R. Séguéla	Directeur de recherche (CNRS) (INSA de Lyon)	Examineur
P. Sotta	Directeur de recherche (CNRS) (LPMA)	Directeur de thèse
C. Rochas	Directeur de recherche (CNRS) (CERMAV)	Examineur

Laboratoires de recherche : MATEIS – INSA de LYON / CNRS (UMR 5510)
LPMA – SOLVAY / CNRS (UMR 5268)

INSA Direction de la Recherche - Ecoles Doctorales – Quinquennal 2011-2015

SIGLE	ECOLE DOCTORALE	NOM ET COORDONNEES DU RESPONSABLE
CHIMIE	<p>CHIMIE DE LYON http://www.edchimie-lyon.fr</p> <p>Sec : Renée EL MELHEM Bat Blaise Pascal 3^e etage 04 72 43 80 46 Insa : R. GOURDON</p>	<p>M. Jean Marc LANCELIN Université de Lyon – Collège Doctoral Bât ESCPE 43 bd du 11 novembre 1918 69622 VILLEURBANNE Cedex Tél : 04.72.43 13 95 directeur@edchimie-lyon.fr</p>
E.E.A.	<p>ELECTRONIQUE, ELECTROTECHNIQUE, AUTOMATIQUE http://edeea.ec-lyon.fr</p> <p>Sec : M.C. HAVGOUDOUKIAN eea@ec-lyon.fr</p>	<p>M. Gérard SCORLETTI Ecole Centrale de Lyon 36 avenue Guy de Collongue 69134 ECULLY Tél : 04.72.18 60.97 Fax : 04 78 43 37 17 Gerard.scorletti@ec-lyon.fr</p>
E2M2	<p>EVOLUTION, ECOSYSTEME, MICROBIOLOGIE, MODELISATION http://e2m2.universite-lyon.fr</p> <p>Sec : Safia AIT CHALAL Bat Darwin - UCB Lyon 1 04.72.43.28.91 Insa : H. CHARLES Safia.ait-chalal@univ-lyon1.fr</p>	<p>Mme Gudrun BORNETTE CNRS UMR 5023 LEHNA Université Claude Bernard Lyon 1 Bât Forel 43 bd du 11 novembre 1918 69622 VILLEURBANNE Cédex Tél : 06.07.53.89.13 e2m2@univ-lyon1.fr</p>
EDISS	<p>INTERDISCIPLINAIRE SCIENCES- SANTE http://www.ediss-lyon.fr</p> <p>Sec : Safia AIT CHALAL Hôpital Louis Pradel - Bron 04 72 68 49 09 Insa : M. LAGARDE Safia.ait-chalal@univ-lyon1.fr</p>	<p>Mme Emmanuelle CANET-SOULAS INSERM U1060, CarMeN lab, Univ. Lyon 1 Bâtiment IMBL 11 avenue Jean Capelle INSA de Lyon 696621 Villeurbanne Tél : 04.72.68.49.09 Fax :04 72 68 49 16 Emmanuelle.canet@univ-lyon1.fr</p>
INFOMATHS	<p>INFORMATIQUE ET MATHEMATIQUES http://infomaths.univ-lyon1.fr</p> <p>Sec :Renée EL MELHEM Bat Blaise Pascal 3^e etage infomaths@univ-lyon1.fr</p>	<p>Mme Sylvie CALABRETTO LIRIS – INSA de Lyon Bat Blaise Pascal 7 avenue Jean Capelle 69622 VILLEURBANNE Cedex Tél : 04.72. 43. 80. 46 Fax 04 72 43 16 87 Sylvie.calabretto@insa-lyon.fr</p>
Matériaux	<p>MATERIAUX DE LYON http://ed34.universite-lyon.fr</p> <p>Sec : M. LABOUNE PM : 71.70 –Fax : 87.12 Bat. Saint Exupéry Ed.materiaux@insa-lyon.fr</p>	<p>M. Jean-Yves BUFFIERE INSA de Lyon MATEIS Bâtiment Saint Exupéry 7 avenue Jean Capelle 69621 VILLEURBANNE Cedex Tél : 04.72.43 71.70 Fax 04 72 43 85 28 Ed.materiaux@insa-lyon.fr</p>
MEGA	<p>MECANIQUE, ENERGETIQUE, GENIE CIVIL, ACOUSTIQUE http://mega.universite-lyon.fr</p> <p>Sec : M. LABOUNE PM : 71.70 –Fax : 87.12 Bat. Saint Exupéry mega@insa-lyon.fr</p>	<p>M. Philippe BOISSE INSA de Lyon Laboratoire LAMCOS Bâtiment Jacquard 25 bis avenue Jean Capelle 69621 VILLEURBANNE Cedex Tél : 04.72 .43.71.70 Fax : 04 72 43 72 37 Philippe.boisse@insa-lyon.fr</p>
ScSo	<p>ScSo* http://recherche.univ-lyon2.fr/scso/</p> <p>Sec : Viviane POLSINELLI Brigitte DUBOIS Insa : J.Y. TOUSSAINT viviane.polsinelli@univ-lyon2.fr</p>	<p>Mme Isabelle VON BUELTZINGLOEWEN Université Lyon 2 86 rue Pasteur 69365 LYON Cedex 07 Tél : 04.78.77.23.86 Fax : 04.37.28.04.48</p>

*ScSo : Histoire, Géographie, Aménagement, Urbanisme, Archéologie, Science politique, Sociologie, Anthropologie

Abstract

Mechanical properties of bulk polyamide 6 (PA6) have been studied in relation to microscopic deformation mechanisms. By applying various thermal treatments, sets of samples with different semi-crystalline microstructures, namely various crystalline allotropic forms (denoted α , γ and β) and different values of the crystallinity index (from 24 to 35%) and of the long period of the lamellar stacks (from 7 to 12 nm), have been obtained, for two different molecular masses. Mechanical properties have been measured in the linear (viscoelastic) and nonlinear (plastic) regimes below and above the glass transition of the amorphous phase (T_g). Differences of behavior have been observed depending on the microstructure. While the crystallinity index seems to be the predominant factor affecting the mechanical behavior above T_g , other structural parameters such as the crystalline form and the lamellar morphology (thickness and aspect ratio) have to be taken into account below T_g . Deformations at the scales of lamellar stacks and of the crystalline unit cell have been characterized by small and wide angle X-ray scattering (SAXS and WAXS) performed in-situ during tensile tests. In samples with predominantly β phase, lamellae tend to orient perpendicular to the tensile direction (TD). This orientation mechanism (which we denote as 'Chain Network model') is driven by the amorphous chains which transmit the stress between adjacent lamellae. The tensile strain in lamellar stacks perpendicular to TD is lower than the macroscopic tensile strain, which must be compensated by increased shear in inclined stacks. Also, at high extension ratios, the β phase transforms into α phase. In samples with predominantly α phase and above T_g , morphology changes are more complex. In a first step, chains orient perpendicular to TD, which implies that lamellar planes tend to orient parallel to TD, possibly due to their high aspect ratio (denoted as 'Rigid Lamella' model). In a second step, beyond the yield, a major fraction of crystallites then reorients normal to TD, i.e. chains themselves become parallel to TD, while a minor fraction remains oriented along TD. A highly oriented fibrillar morphology is ultimately obtained in all cases.

KEYWORDS: polyamide 6, WAXS, SAXS, in-situ tensile test, elastic domain, plastic domain, phase transformation

Résumé

Notre étude a porté sur la compréhension microscopique des mécanismes de déformation du polyamide 6 (PA6) à l'état massif. Par des traitements thermiques appropriés, on a obtenu un jeu d'échantillons présentant des microstructures semi-cristallines variées, avec différentes formes cristallographiques (allotropes : α , γ ou β), différents taux de cristallinité (de 24 à 35%), différentes périodes de l'empilement des lamelles cristallines (de 7 à 12nm), ceci pour deux masses moléculaires différentes. Les propriétés mécaniques en traction ont été caractérisées au-dessus et au-dessous de la transition vitreuse de la phase amorphe (T_g). Les différents matériaux présentent des différences notables de comportements. Le taux de cristallinité semble être le facteur prédominant au-dessus de T_g , mais d'autres facteurs sont à prendre en compte en dessous de T_g , comme la forme cristalline et la morphologie lamellaire (épaisseur et facteur de forme). Grâce à un dispositif expérimental fabriqué sur mesure, des essais de traction ont été suivis par diffusion des rayons X aux petits (SAXS) et grands angles (WAXS) sur la ligne D2AM, ESRF, pour caractériser les déformations à l'échelle des empilements lamellaires et à l'échelle de la maille cristalline. Dans les échantillons présentant principalement de la phase cristalline β , les lamelles tendent à s'orienter perpendiculairement à la direction de traction (TD). Ce mécanisme d'orientation local (que nous appelons « modèle de réseau de chaînes ») est induit par la transmission des contraintes par les chaînes amorphes reliant les lamelles cristallines adjacentes. L'allongement local est plus faible que l'allongement macroscopique dans les lamelles perpendiculaire à TD, ce qui implique que les lamelles inclinées doivent être cisailées. De plus, la phase β se transforme en phase α aux fortes extensions. Dans les échantillons présentant principalement de la phase α (la plus rigide), au-dessus de T_g , dans le régime élastique, les chaînes tendent d'abord à s'orienter perpendiculairement à TD, ce qui implique que les lamelles s'orientent parallèlement à TD (« modèle de lamelles rigides »). Ensuite, dans le régime plastique, une majeure partie des lamelles se réoriente perpendiculairement à TD, comme dans le « modèle de réseau de chaînes », tandis qu'une fraction mineure reste orientée parallèlement à TD. Une morphologie fibrillaire fortement orientée est finalement obtenue pour tous les échantillons quelle que soit la température.

MOTS-CLES : polyamide 6, WAXS, SAXS, traction in-situ, domaine élastique, domaine plastique, transformation de phases

Remerciements

On en arrive maintenant à la dernière page que l'on rédige lors d'une thèse et qui, bizarrement, est la première que les gens lisent... Pourtant, il s'en passe des choses en 3 ans, la thèse est loin d'être un long fleuve tranquille et, quand plus rien ne fonctionne, il est bon de se rappeler que la patience est une vertu... mais ça y est, j'ai enfin atteint la lumière au bout du tunnel !!

Commençons d'abord par récapituler un peu : ma thèse est issue d'une collaboration entre deux laboratoires, celui de MATEIS et du LPMA. Je tiens donc à remercier les directeurs de ces laboratoires pour m'avoir accueillie au sein de leurs unités : Joël Courbon et Jérôme Chevalier, directeurs successifs de MATEIS et Ludovic Odoni et Jean-Yves Delannoy, directeurs successifs du LPMA.

Je tiens à remercier mes encadrants, Olivier (je retiens l'EPF et je vais donc continuer à faire attention pour ne pas refaire un 2^{ème} « Pise »...) et Paul (j'ai apprécié nos échanges et ta pédagogie, merci aussi pour être resté jusqu'à la fin des essais à l'ESRF et ce, même un samedi à 20h passé). Un grand merci également à Roland car même si tu ne faisais pas officiellement partie de l'encadrement, tu as été là du début à la fin et as toujours été disponible pour toutes mes questions, mais aussi les différentes manips que ce soit à l'INSA, au LPMA, à l'ESRF ou bien même durant notre virée à Lille. J'espère que tu vas pouvoir profiter de ta retraite pour aller découvrir les chênes du monde et les planter dans ton jardin !! Merci aussi à Louise-Anne, je pense que le message-clé et la vue d'avion sont passés...

Je souhaite également remercier l'ensemble des membres du jury : Noëlle Billon qui l'a présidé, mes deux « rapportrices », Valérie Miri avec qui j'ai beaucoup échangé lors des congrès où nous nous sommes croisées ou bien lors de ma venue à Lille et Finizia Auriemma venue spécialement d'Italie, ainsi que Cyrille Rochas. Cyrille, j'ai été honorée que tu viennes assister à la finalité du travail mais j'aimerais aussi te remercier pour ton aide et ton implication lors des deux sessions d'essais à l'ESRF car même si le « dieu » faisceau nous en a fait voir des toutes les couleurs, tu es venu à bout de toutes les situations et j'ai ainsi pu réaliser et analyser toutes les expériences nécessaires au bon déroulement de ma thèse.

Dans la partie essais in-situ, je souhaite évidemment remercier l'ESRF pour avoir alloué du temps de faisceau mais aussi Grégory Stoclet et les « filles » de Lille (Julie, avec qui j'ai partagé pas mal de moments en particulier durant les congrès avec pour apothéose le DEPOS 25, Juliette, Lise et Saadia)

pour le prêt de leur machine de traction in-situ durant la première session mais aussi leur aide durant les différentes sessions.

Je souhaiterais également remercier l'équipe d'électroniciens de MATEIS, composée de José, Nicolas et Christophe pour leur aide dans la conception et réalisation de la machine X-JICO, pierre centrale de mes essais de traction in-situ. Je n'oublie évidemment pas Ilias, qui a lui aussi admirablement participé à ce projet, mais aussi à la conception de tous mes moules, qui m'ont permis de «façonner » mes matériaux, merci aussi pour le thé à la menthe et les traductions de recettes !!

Merci à la région Rhône-Alpes et à l'Arc Energie qui ont financé cette thèse.

Je remercie l'ensemble des membres permanents du « LPMA » et de MATEIS dont Florence, Lise, Anthony, Sylvie, Olivier G. pour m'avoir formé sur la Schenck, Didier, Léo, Séverine pour ton aide pour les colonnes à gradients, Clémence, Magalie et Rémi (merci pour ton accueil à Shanghai), Pierre-Yves mais aussi Jean-Marc P., Jean-Marc C., Jean-Yves (encore merci pour les souvenirs du Japon), Gérard pour les discussions et les jeux de mots, Renaud (j'espère que tu continueras à mettre la « raclée » au ping-pong à ceux de Bretagne...). Merci aussi à l'ensemble des « non-permanents », i.e. doctorants et post-docs passés et présents du LPMA et de MATEIS dont Florentina (le secret c'est les M&M'S... courage pour la fin !), Congyu (謝謝 et désolée d'avoir été une aussi mauvaise élève en chinois... j'ai été ravie de faire ta connaissance), mes conscrits depuis l'A7 Caro et Chloé, Mathieu, Ashkan, Luca mais aussi Nicolas du 1^{er}, Marta, Malgorzata, Rabia (une sacrée épopée ce DYFP... merci pour les conseils pour le Maroc et d'être revenu pour ma soutenance, cela m'a touché), Bijin et Cyril V. (merci pour m'avoir formée aux X et à ce satané Fit2D...).

Merci à Erika, Antonia qui assurent pour tout ce qui touche à l'administratif ainsi qu'à Sandrine Gonnet avec qui j'ai partagé de nombreux éclats de rire !! (Fais quand même attention avec le sport et n'oublie pas de boire ^^)

Un grand merci également à Sandrine Rossi qui m'a chaleureusement accueillie au sein du LPMA et ce, dès mon stage de fin d'études, ainsi qu'à Simona, j'ai beaucoup apprécié nos soirées filles !!

Je tiens maintenant à saluer les différents membres de mon bureau à l'Insa (pour reprendre la formule) : Nolwenn, Tais et surtout Nicolas !! Mon petit Nico, tu as été là du début à la fin et il faut dire qu'on a bien commencé l'aventure avec notre trip à Amsterdam ou tes essais à Soleil et au final ce n'est pas le co-bureau « exemplaire » que tu as été que je retiens mais l'ami que tu es devenu.

Un grand merci aussi à Millán, mon conscrit de thèse mais surtout mon pote de galère !! Grâce à toi, les pauses ont pris une autre tournure mais aussi mon travail !! En effet, grâce à ton talent de communication avec Igor, ma vie s'est simplifiée et j'ai ainsi pu mener à bien toute l'analyse de DRX et d'ailleurs ma thèse (sans oublier ma santé mentale) t'en remercie car sans toi je pense que j'y serais encore...

Merci à ma bande de prépa (Sam, Pilou & cie) et mes amis pour les tranches de rigolade que l'on partage depuis pas mal d'années et, en particulier, à ma petite Sophie, venue tout spécialement pour moi afin de m'encourager jusque dans la dernière ligne droite.

Merci à Cathy et Jean-Marie pour leurs soutien et venue à ma soutenance qui m'ont fait très plaisir. Merci à Melwin, à l'ensemble de ma famille (Papy, Mémé, mes oncles, tantes, cousins et cousines) et, surtout à mes parents pour m'avoir encouragée depuis ma naissance et aidé de quelle que manière que ce soit tout au long de ces années. Les choses ne se sont pas toujours passées comme on l'aurait espéré mais avoue Maman que je suis une super post-dog !! D'ailleurs, merci à Hélios, mon louloup qui m'a supportée et forcée à sortir afin de me changer les idées pendant les derniers mois de rédaction. Son soutien, parfois envahissant, et ses grands yeux m'ont été d'un grand secours quand je sentais poindre l'impatience...

Enfin, Ronan, ma moitié, qui me supporte (quasi) sans failles depuis tant d'années, tu m'as finalement fort surprise vis-à-vis de ta compréhension approfondie de mon sujet. Après, pour tout ce que tu m'as apporté, j'ai peur que ce ne soit pas l'endroit pour le faire... Quoï qu'il en soit, à nous deux, on fait une sacrée paire !!

Sur ce, je crois que j'ai épuisé mon cota de mots en français alors place à la lecture, all in English !!

Contents

Introduction	1
---------------------	----------

Chapter I: Structure and mechanical properties of polyamide 6

I. Polyamide 6: structure of a semi-crystalline polymer	4
I.1. General points and synthesis	4
I.2. Crystalline phase	5
I.2.1. Description of the different crystalline forms	5
I.2.2. Organization of crystals, from lamellae to spherulites	9
I.3. Amorphous phase	10
I.3.1. Mechanical relaxations: mobility of amorphous phase	10
I.3.2. Heterogeneity of the amorphous phase	11
I.4. Linking between crystalline and amorphous phases	12
II. Mechanical behavior	13
II.1. Elastic behavior	14
II.1.1. Mechanisms at the crystalline lamella scale	14
II.1.2. Elastic modulus versus crystallinity index	15
II.2. Plastic behavior	17
II.2.1. Crystal shear	17
II.2.2. Cavitation	19
II.2.3. Fibrillation.....	20
II.2.4. Effect of phase nature in the case of PA6	21
II.3. Failure behavior.....	22
References	23

Chapter II: Experimental techniques

I. Physico-chemical analysis	30
I.1. Karl Fischer titration: measure of water content.....	30

I.2.	Gel Permeation Chromatography	30
II.	Microstructural analysis	31
II.1.	Optical microscopy	31
II.2.	Differential scanning calorimetry	32
II.2.1.	Protocol and experimental set up	32
II.2.2.	Crystallinity index X_c	32
II.2.3.	Estimation of α/γ ratio	33
II.2.4.	Physical ageing	33
II.2.5.	Density measurements	34
II.3.	Small angle X-ray scattering	35
II.3.1.	Experimental set up and data collection	35
II.3.2.	About the Lorentz correction	37
II.3.3.	Determination of the long period L_p	39
II.3.4.	Estimation of the crystalline lamellar thickness L_c	42
II.4.	Wide angle X-ray scattering	42
II.4.1.	Experimental set up	44
II.4.2.	Corrections and adjustment of WAXS data	44
II.4.3.	Identification of PA6 crystalline phases	45
III.	Mechanical investigations	46
III.1.	Dynamic mechanical analysis	46
III.1.1.	Principle	46
III.1.2.	Experimental set up	46
III.2.	Monotonic tensile test	47
III.2.1.	Experimental set up	47
III.2.2.	Determination of the Young's modulus E	48
III.2.3.	Determination of the yield stress σ_y	48
III.3.	In-situ tensile test (ESRF)	50
	References	52

Chapter III: Thermal treatments and materials

I.	State of the art	56
I.1.	Models of polymer crystallization	56
I.1.1.	Nucleation	57

I.1.2.	Growth: Hoffman-Lauritzen theory.....	58
I.2.	Memory effects	59
I.3.	Quenching	61
I.4.	Isothermal crystallization	61
I.4.1.	Principle.....	61
I.4.2.	Kinetics of isothermal crystallization.....	62
I.4.3.	Effect of the temperature of isothermal crystallization on microstructure.....	63
I.5.	Annealing.....	64
I.5.1.	Principle.....	64
I.5.2.	Effect of annealing on microstructure	65
I.6.	Issues	65
II.	Materials and processing	67
II.1.	Virgin pellets.....	67
II.2.	Injection molding process	67
II.3.	Compression molding process	68
III.	Results: effects of thermal treatments	69
III.1.	Determination of a condition to erase memory effects	69
III.2.	Isothermal crystallization	71
III.2.1.	Crystallization kinetics.....	71
III.2.2.	Isotherm characterization	73
III.3.	Annealing.....	75
III.3.1.	Adapted principle	75
III.3.2.	Annealing characterization.....	75
III.4.	Quenching	78
III.5.	Time–Temperature–Crystallization (TTC) diagram of PA6.....	80
IV.	Final choice of materials.....	81
	References.....	86

Chapter IV: Macroscopic mechanical properties

I.	Dynamic Mechanical Analysis (DMA).....	92
II.	Tensile tests.....	96
II.1.	Above the glass transition at $T = T_g + 65^\circ\text{C} = 120^\circ\text{C}$	96
II.2.	Below the glass transition at $T = T_g - 65^\circ\text{C} = -10^\circ\text{C}$	99

III. Discussions	102
III.1. Effect of molecular mass	102
III.2. Poisson's coefficient	104
III.3. Issues	105
References.....	106

Chapter V: Microscopic study – Elastic strain domain

Introduction.....	111
I. Elastic strain domain at the scale of lamellae, studied by SAXS	114
I.1. SAXS protocol	114
I.2. Local strain of horizontal lamellae ($\psi = 0^\circ$)	115
I.2.1. Experimental data	115
I.2.2. Discussion	117
I.3. Local strain as a function of orientation.....	119
I.3.1. Experimental data	119
I.3.2. Analysis of local strain	122
I.4. Orientational distribution of lamellae (SAXS investigation).....	126
I.4.1. Experimental data	127
I.4.2. Analysis of orientational distributions of lamellae.....	128
II. Elastic strain domain at the scale of crystalline unit cell, studied by WAXS	131
II.1. WAXS protocol	132
II.2. Crystal strain in vertical scattering direction ($\psi = 0^\circ$)	133
II.3. Azimuthal distribution of crystal strain (WAXS investigation)	135
II.3.1. Experimental results.....	135
II.3.2. Analysis of the results.....	136
II.4. Orientational distribution of crystalline planes, studied by WAXS	138
II.4.1. Case of INJ sample, with β crystalline phase.....	138
II.4.2. Case of sample I213, with α crystalline phase	140
III. Discussion: deformation mechanisms under stretching in the elastic regime	142
III.1. Models.....	142
III.1.1. "Chain network" model (CN)	142
III.1.2. "Rigid Lamella" model (RL).....	143
III.2. Comparison to experimental data.....	146

III.2.1.	Case of β phase.....	146
III.2.2.	Case of α phase	146
III.2.3.	Case of $\alpha+\gamma$ phases	149
III.2.4.	Additional information	149
III.3.	Conclusion	150
References.....		151

Chapter VI: Microscopic study – Plastic strain domain

Introduction.....		154
I.	Deformation mechanisms at the scale of the crystalline lattice, investigated by WAXS.....	155
I.1.	Injected (INJ) sample: predominant β phase	155
I.1.1.	Evolution in the plastic domain above T_g	155
I.1.2.	Evolution in the plastic domain below T_g	160
I.1.3.	Discussion: temperatures and deformation mechanisms of the β phase in the plastic strain domain	161
I.2.	Annealed (A215) and isotherm-treated (I213) samples: pure α phase	166
I.2.1.	Evolution in the plastic strain domain above T_g	167
I.2.2.	Evolution in the plastic strain domain below T_g	170
I.2.3.	Discussion: temperatures and deformation mechanisms of the plastic strain domain for α phase	171
I.3.	Discussion on A200 sample: mixture of α and γ phases	175
I.4.	Conclusion on ductility	176
II.	Deformation mechanisms at the scale of lamellae, investigated by SAXS	177
II.1.	Fibrillar transformation	178
II.2.	Cavitation	180
References.....		181

Conclusion & Perspectives 183

Appendix:

Article: "Assessment of polyamide-6 crystallinity by DSC: the temperature dependence of the melting enthalpy" 187

Introduction

Polyamides are semi-crystalline thermoplastic polymers largely used in industries as in the automotive field or home appliances and in applications such as gears due to their high mechanical and thermal resistance properties. These mechanical properties are related to the fact that polyamides are polar polymers with a “dense” network of intermolecular hydrogen bonds, in contrast to commodity plastics such as polyethylene and polypropylene. In the aim of improving the thermo-mechanical performances for structural applications at high temperature, it is of prime importance to understand the mechanisms of deformation and how they rule the macroscopic behavior in relation to the semi-crystalline microstructure. Polyolefins have been widely studied in this aim, which is not the case of polyamides. The aim of this thesis is to understand the mechanisms of deformation of polyamide 6 (PA6). This work focuses on the following issues:

- Bulk material, as few studies has been done in contrast to the case of fibers or thin films.
- A multi-scale investigation of the mechanisms of deformation. Macroscopic tensile tests as well as in-situ tensile tests investigated by X-ray scattering have been performed.
- The influence of the state of the amorphous (i.e. glassy or rubbery), in contrast to usual works where mechanical properties are studied at room temperature without taking into account the mechanical relaxations of the amorphous phase. Indeed, in PA6, the amorphous phase represents nearly 70% of the polymer meaning that its mechanical behavior plays a major role. In this work, tensile tests were carried out below and above the glass transition (T_g).
- The microstructure. In a semi-crystalline polymer, a large amount of parameters like the crystallinity index, the crystalline phase, the long period, the molecular mass, etc. can impact the mechanical behavior. The microstructure was modified thanks to thermal treatments.

Thus, the strategy of this thesis can be summed up as depicted in Figure 1. We aim to study the mechanical properties of PA6, a semi-crystalline polymer, and more precisely its mechanisms of deformation. These mechanical properties are influenced by the mechanical coupling between the amorphous and crystalline phases: working at temperatures below or above to the glass transition allows a better understanding of the mechanisms. In addition as this coupling relies upon both the amorphous and the crystalline phase, we have chosen to affect it by working on the microstructure of the crystalline phase thanks to thermal properties. In this way, it allows us to link the microstructure to the mechanical properties and their consequence of the mechanisms of deformation below and above T_g .

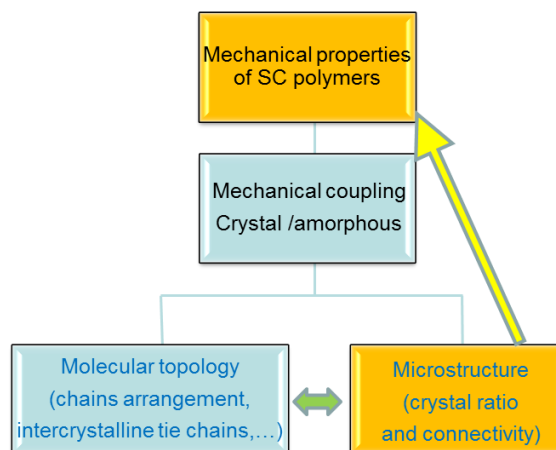


Figure 1: Global strategy

The first chapter deals with a state of art on PA6. It is divided into two main parts. The first one deals with the structure of PA6, meaning the structure of both amorphous and crystalline phases. Indeed, PA6 is a polymorph polymer exhibiting several crystalline structures. The second part introduces the mechanisms of deformation usually encountered in semi-crystalline polymers. This review allowed us to define a strategy in order to achieve our objective on the understanding of deformation mechanisms in PA6.

In the second chapter, an overall description of the techniques used for the physico-chemical and microstructural analyses as well as the mechanical investigations is reported.

The third chapter is in the heart of the cogitation concerning the choice of materials. Thermal treatments and their influence on microstructure are presented as well as our own studies on PA6. Thus, according to the thermal treatments, the crystalline phase, the crystallinity index, the long period or the crystalline perfection can be modified. A panel of samples presenting various microstructures is selected.

The fourth, fifth and sixth chapters deal with mechanical properties at various scales and at two temperatures (one below and another one above T_g). Macroscopic scale is approached in chapter IV and mainly concerns the Young modulus and the yield during tensile tests. The effects of microstructure on the mechanical behavior are also discussed but for explaining the difference of behaviors, the fifth and sixth chapters are of main importance, they deal at a microscopic scale. The study of tensile tests investigated by x-ray scattering is divided into two parts: the elastic and plastic strain domains, studied in chapter V and chapter VI respectively. Deformation at the scale of lamella stacks have allowed to characterize the elastic strain domain while the study on crystalline phases transformation and texturing phenomena has informed us on the plastic strain domain. Finally, the general conclusion and perspectives finish the present work.

Chapter I: Structure and mechanical properties of polyamide 6

I.	Polyamide 6: structure of a semi-crystalline polymer	4
I.1.	General points and synthesis	4
I.2.	Crystalline phase	5
I.2.1.	Description of the different crystalline forms	5
I.2.2.	Organization of crystals, from lamellae to spherulites	9
I.3.	Amorphous phase	10
I.3.1.	Mechanical relaxations: mobility of amorphous phase	10
I.3.2.	Heterogeneity of the amorphous phase	11
I.4.	Linking between crystalline and amorphous phases	12
II.	Mechanical behavior	13
II.1.	Elastic behavior	14
II.1.1.	Mechanisms at the crystalline lamella scale	14
II.1.2.	Elastic modulus versus crystallinity index	15
II.2.	Plastic behavior	17
II.2.1.	Crystal shear	17
II.2.1.1.	Definition of slip systems	17
II.2.1.2.	Twinning	18
II.2.1.3.	Shear banding.....	18
II.2.1.4.	Stress transmitters	19
II.2.2.	Cavitation	19
II.2.3.	Fibrillation.....	20
II.2.4.	Effect of phase nature in the case of PA6	21
II.3.	Failure behavior.....	22
	References.....	23

I. Polyamide 6: structure of a semi-crystalline polymer

W. H. Carothers from Dupont was the inventor of polyamide synthesis in 1929. Polyamide 6-6 (PA6-6) was first made in 1936 with adipic acid and hexamethylene. P. Schlack directly polymerized ϵ -caprolactam from aminocaproic acid and water and the patent for polyamide 6 (PA6) was recorded in 1938. Polyamides are usually called nylons because of the commercial name given by the Dupont Company to the former polyamides. Industrial developments of PA6 and PA6-6 were accelerated during World War II because these materials were good replacements to the lack of silk that was essential for military applications like parachute [1].

I.1. General points and synthesis

Polyamides were the first synthetic semi-crystalline polymers having high mechanical and thermal performances. In the 1940s, polyamides were widely used in applications such as gears, bearings and the shaping of coils. Since then, many other areas have taken interest in such polymers : automotive industry (parts covers such as air intake manifolds, water pumps, water tanks, radiator and external parts such as wheel covers), home appliances (boxes contactors, isolators, coil bobbins, switches, connectors, clamps, collars), mechanical (cages bearings, bushings), and sports and leisure (cradles of bicycle saddles, ski components, climbing ropes ...).

Poly- ϵ -caprolactam, also called PA6, is a commercial homopolyamide and belongs to the category of semi-crystalline aliphatic polyamides. Its synthesis is really specific because contrary to most of the other polyamides, it is not a polycondensation but a polymerization by cycle opening. Pure ϵ -caprolactam is used as monomer in this synthesis. It is a lactam with 6 carbon atoms in its cycle. Indeed, the reason why poly- ϵ -caprolactam is called PA6, it is because the unit repeat in the polymer is composed of 6 carbon atoms.

The polymerization of PA6 takes place by heating a mix of ϵ -caprolactam and water at about 270°C. This temperature is hold until equilibrium conditions are reached.

There are three main reactions:

- The cycle opening, when lactam is hydrolyzed into amino acid, as shown in Figure I.1.
- The addition, when a lactam molecule is directly grafted at the end of the growing chain
- The condensation, when the carboxyl and amine groups of the chain end react in order to eliminate water molecules.

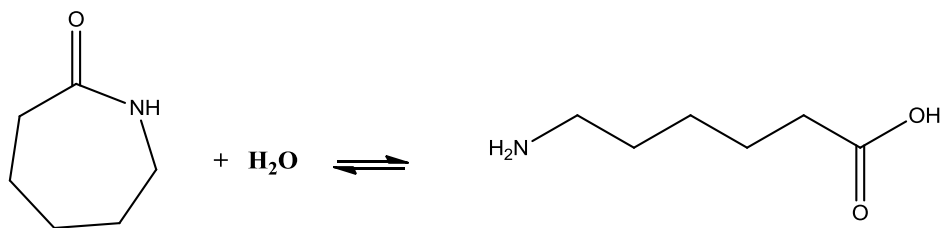


Figure I.1: Opening of caprolactam cycle leading to the formation of PA6

Because of its chemical structure composed of polar groups, polyamides are really sensitive to water. However, this water absorption is reversible. The amount of absorbed water depends on relative humidity, environment temperature, exposition time as well as polyamide type and crystallinity [2].

I.2. Crystalline phase

Polymers having a regular chain architecture are able to crystallize. However, the mechanism of crystallization by chain-folding from the quiescent melt makes the crystallization process partial. Indeed, an amorphous phase is generated between adjacent crystals that have the form of lamellae. The extent of crystallization and the crystal structural habits depend both on intrinsic and extrinsic factors. Intrinsic factors such as the chain stiffness, the stable chain conformation, the presence of statistical chain defects, ... can reduce the crystallization ability. In the case of polyamides, the presence of intermolecular H-bonds is one of the reasons of the limited crystallinity as compared to polyolefins, in spite of a perfect chain regularity. Extrinsic factors that may affect the crystallinity are the crystallization conditions: the cooling rate for an-isothermal crystallization, the temperature for isothermal conditions, the thermo-mechanical history for crystallization in processing... (detailed in chapter III) [3] [4].

Polyamide 6 exhibits several crystal forms depending on the crystallization conditions. These different crystalline structures are described in this part. The characteristics of the amorphous phase will be described in section I.3.

The primary structure of aliphatic polyamides consists of two amid groups separated by methylene sequences. The amid group is essentially planar due to the C=O double bond. The capacity of NH groups to form strong hydrogen-bonds (H-bonds) with CO groups is at the origin of polyamide high melting point in comparison with polyolefins, and to the sheet-like structure similar to that of keratin. Chains in the crystalline phase are indeed oriented in a way to maximize intermolecular H-bonds [2] so as to form planar sheets which contain the H-bonds.

I.2.1. Description of the different crystalline forms

Polyamides can crystallize into various crystal forms depending on their molecular architecture. Moreover, every polyamide may display polymorphic forms denoted α , β , γ , δ . Two specific notions need to be defined for polyamides.

The first one is the parity, i.e. the number of carbon atoms in the chain. PA6 contains 6 carbon atoms meaning an even polyamide. For PA6-6, its chemical structure consists of two segments of 6 carbon atoms: it is an even-even polyamide. Other categories of parity for polyamides:

- Odd polyamide like PA11 (contains 11 carbon atoms)
- Odd-odd polyamide like PA9-11
- Even-odd polyamide like PA6-9
- Odd-even polyamide like PA5-6

The second notion concerns the direction of the chains in the crystal lattice. According to the crystalline phase, chains do not fold the same way: they can fold either in parallel or in anti-parallel way, as depicted in Figure I.2. The chain conformation is planar zigzag in the α form and chain-twisted in the γ form.

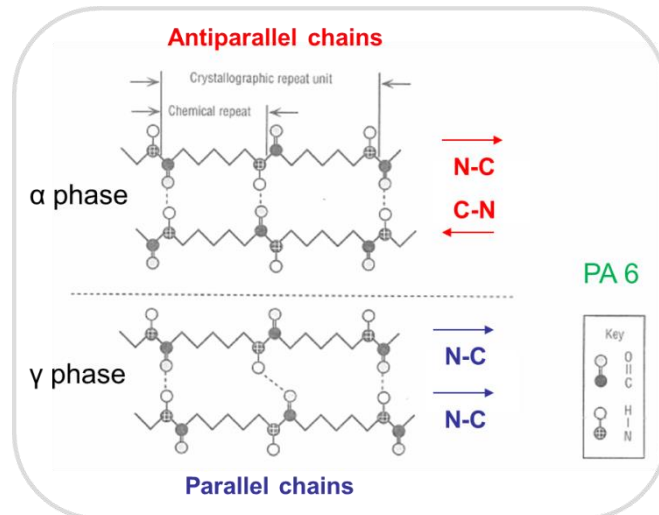


Figure I.2 : Molecular arrangement in the α and the γ crystal lattices of PA 6 [2]

With these notions, a classification of the different crystalline structures observed in PA is proposed in Table I.1.

Table I.1 : Kinds of crystalline structures observed in polyamides

Parity of PA	Chains direction	
	Parallel	Antiparallel
Even (<7C)	γ	α
Even (>7C)	γ	γ
Odd	α	α
Even/Even	α (centro-symmetric)	
Odd/Odd	γ	γ
Even/Odd	γ	γ
Odd/Even	γ	γ

In the case of PA6, there is another crystalline form which is however mesomorphic and metastable: the β phase.

The crystalline lattices of α and γ phases are shown in Figure I.2 and Figure I.3 for PA6. The following difference between α and γ phases are observed:

- In the case of α phase, intermolecular H-bonds between anti-parallel neighbor chains are arranged in the plane of the planar zigzag of the aliphatic segment and they are collinear. Sheets containing H-bonds are stacked upon each other thanks to van der Waals interactions.
- In the case of γ phase, intermolecular H-bonds between parallel chains are no longer collinear with the zigzag conformation of the methylene segments. The chains are twisted about the amid group. This twist gives a contraction of the repeat unit along chains axis. The energetic cost spent to twist the amid groups is compensated by the gain of stability of the H-bonds [5] [6].

To sum up, the main difference between α and γ occurs in the conformation of amid groups which are either coplanar to the carbon chain for α phase or rotated by 67° for γ phase [7]. As a consequence, there is shrinkage of the unit cell parameter along the chain axis.

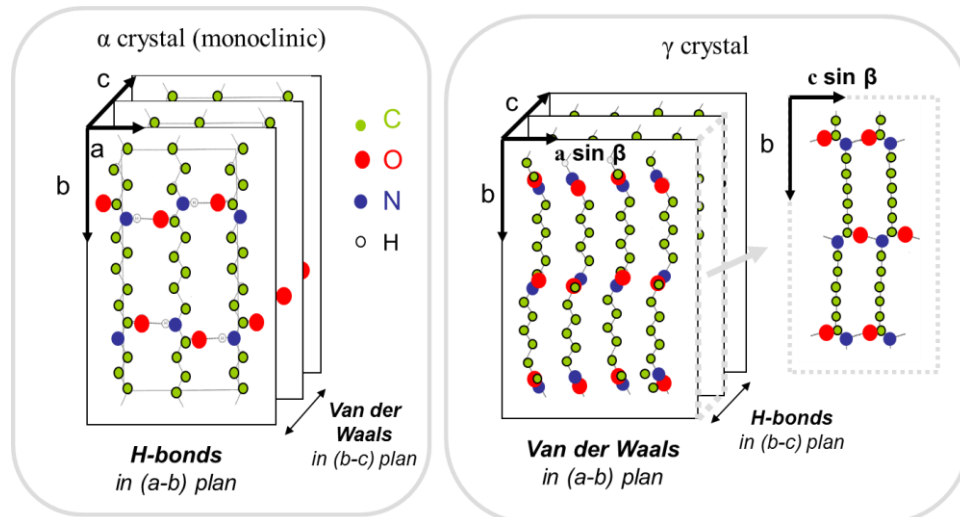


Figure I.3 : Scheme of the various crystalline lattices in PA6: monoclinic α and γ (adapted from [2])

The assignment of the α and γ crystal forms to the planar zig-zag and the chain twisted chain conformation is a general rule for polyamides. The symmetry of the α crystal form is monoclinic for even polyamides like PA6. Concerning the γ crystal, it is usually monoclinic but it can be sometimes labeled as pseudo-hexagonal.

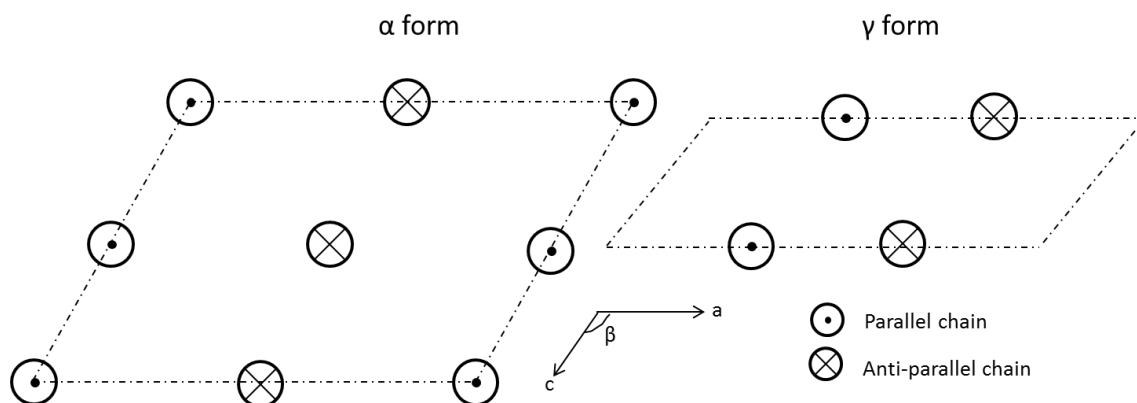


Figure I.4: Lattices of α and γ for PA6, top view

In PA6, the α form has four chains by lattice whereas they are only two for γ form, as shown in Figure I.4. The α phase is the thermodynamically stable form whereas γ is favored by kinetics. These two phases can be easily generated:

- regarding the α form, by slow cooling from the melt or by crystallization from a solvent
- regarding the γ form, by fast cooling from the melt.

The α/γ ratio can be estimated with various techniques, such as differential scanning calorimetry (see chapter II).

The α phase can be converted into γ phase thanks to an iodine treatment [8]. The γ phase can be transformed into α phase thanks to a phenol treatment [9] or by stretching [10].

Concerning the β phase, several authors have tried to describe it but no consensus was established. The most representative models are shown in Figure I.5.

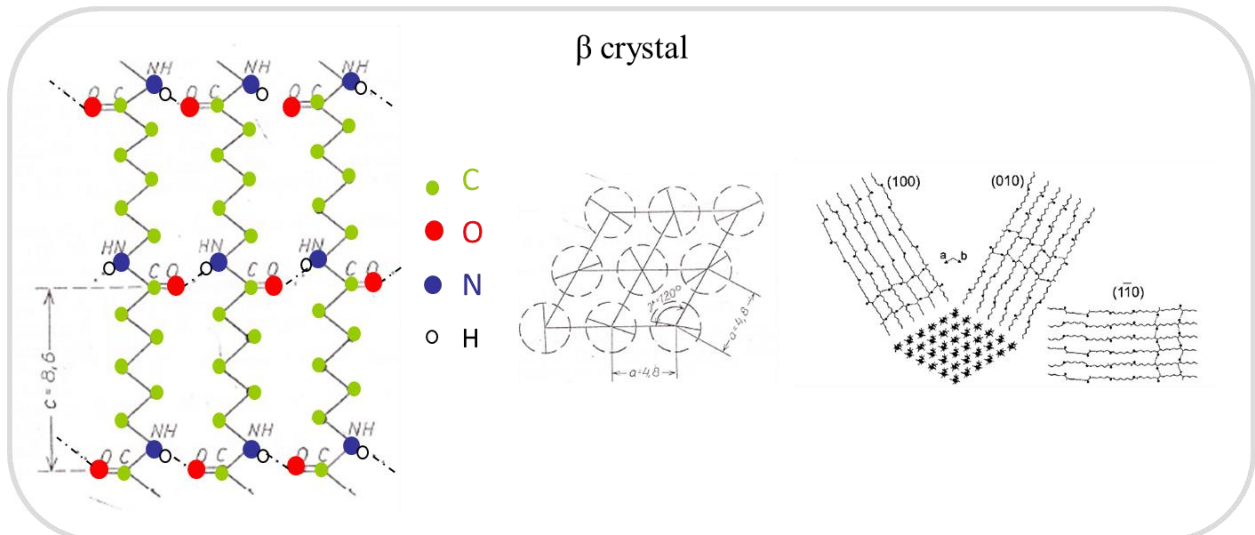


Figure I.5 : Propositions of β phase representation from Ziabicki [11] and Auremma et al. [12] (right). Dotted circles in the middle scheme stand for random orientation of chains.

In 1955, Ziabicki [11] proposed a hexagonal or pseudo-hexagonal structure with random distribution of the H-bonds around the chains axis. This metastable phase can transform into α upon annealing. For Auremma et al. [12], the β phase is composed of small mesomorphic chain aggregates where axes are arranged on a hexagonal lattice. H-bonds form along $[100]$, $[010]$ and $[\bar{1}10]$ directions, forcing chains to adjust their conformation in a way that nearly 100% of H-bonds are formed.

Characteristics of the different crystalline structures are summarized in Table I.2.

Table I.2: Characteristics of the different structures α , β and γ

	α	γ	β
Lattice parameters (* = axis // to the chains)	$a=9.56 \text{ \AA}$ $b^*=17.24 \text{ \AA}$ $c=8.01 \text{ \AA}$ $\beta=67.5^\circ$ [13]	$a=9.33 \text{ \AA}$ $b^*=16.88 \text{ \AA}$ $c=4.78 \text{ \AA}$ $\beta=59^\circ$ [14]	$a=4.8 \text{ \AA}$ $c^*=8.6 \text{ \AA}$ $\gamma=120^\circ$ [11]
Bragg's indices ($\lambda=1.542$)	$(200) \ 2\theta=20.21^\circ$ $(002) \ 2\theta=23.09^\circ$ $(20\bar{2}) \ 2\theta=24.36^\circ$ $(202) \ 2\theta=37.36^\circ$ $(0 \ 14 \ 0) \ 2\theta=77.42^\circ$ [15]	$(200) \ 2\theta=21.69^\circ$ $(002) \ 2\theta=22.23^\circ$ $(202) \ 2\theta=38.73^\circ$ $(0 \ 14 \ 0) \ 2\theta=79.39^\circ$ [8]	$(020) \ 2\theta=10.47^\circ$ (low) $(200) \ 2\theta=21.66^\circ$ $(002) \ 2\theta=21.66^\circ$ $(\bar{2}02) \ 2\theta=21.34^\circ$ (broad) [7]
Density (at 23°C)	$1.235 \pm 0.002 \text{ g/cm}^3$ [13]	$1.18 \pm 0.02 \text{ g/cm}^3$ [8]	$1.14 \pm 0.02 \text{ g/cm}^3$ [16]
Melting temperature	222°C	214°C	Transformation $\beta \rightarrow \alpha$
Enthalpy of melting ΔH_f°	241 J/g [17]	239 J/g [17]	

Concerning the amorphous phase, its density is estimated at $1.09 \pm 0.01 \text{ g/cm}^3$, at 23°C [18].

I.2.2. Organization of crystals, from lamellae to spherulites

There are four major different morphologies [19] in which n-polyamides (with $n > 2$) use to crystallize depending on the crystallization mode:

- from dilute solutions [20]: single crystals,
- from the quiescent homogeneous melt: stacks of lamellar crystals,
- from melt spinning: fibers display a cylindrical chain-extended texture that has been largely exploited in the domain of textile industry since the discovery of polyamides,
- from the molten state in confined geometries such as thin films [21] or in the presence of nucleating agents or fillers: transcrystallinity is a typical texture arising from the heterogeneous nucleation on a foreign surface [22].

The case on which we focus in this study is the second one. Indeed, single crystals are useful for purely academic studies but do not exhibit worthy mechanical properties. In contrast, textured materials display local or global anisotropic effects that make difficult the analysis of macroscopic mechanical properties. Thus, quiescent crystallization provides isotropic bulk samples in order to study the relationship between mechanical properties and structure at various scale levels, as presented in the general introduction.

When crystallization occurs from the molten state, n-polyamides prefer to develop spherulitic structures. These structures are constituted of large crystalline lamellae, growing from a unique nucleus for each spherulite (Figure I.6). However, secondary growth of additional lamellae is frequently observed: it took place in spaces between the primary lamellae. The periodicity of lamellae stacking is around 10 nm but the length can reach a few micrometers (equivalent to the spherulite radius). When spherulites growth from the molten state, in particular out of equilibrium conditions during the cooling, they can lack perfection and also grow on each other, giving a fragmented and segmented appearance.

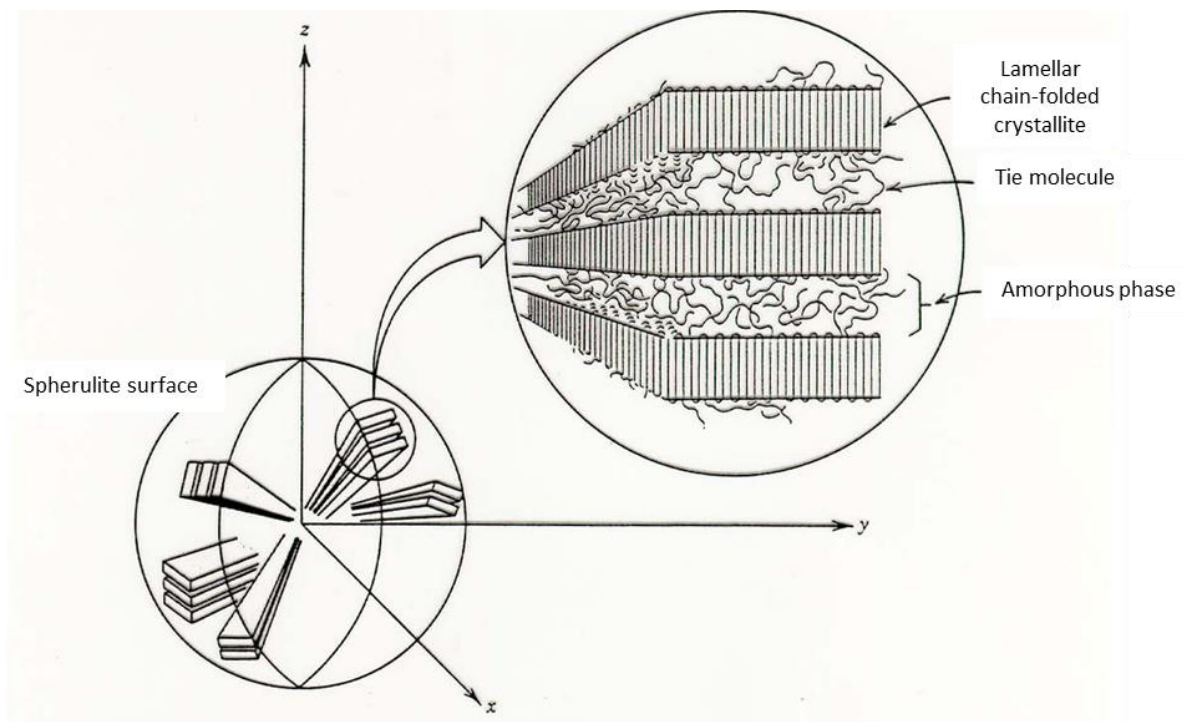


Figure I.6: Scheme of the structure of a spherulite [23]

In polyamides, different kinds of spherulites are observed [24] [25] [26] [27] [28]. Indeed, the characterization of spherulites is based on the nature of their birefringence which is detected by means of optical microscopy under crossed polarizers (see chapter II §II.1). Birefringence is the physical property of a material in which light propagates in an isotropic way. In a birefringent environment, the refractive index is not unique but depends on the directions of propagation and polarization of the light ray. As the birefringence is the difference between refractive indices measured in two different directions, it can be positive or negative. In practice, for the observation of spherulites under polarized light in microscopy, there will be roughly equal light and dark sectors yielding the familiar « Maltese cross » appearance, as shown in Figure I.7.

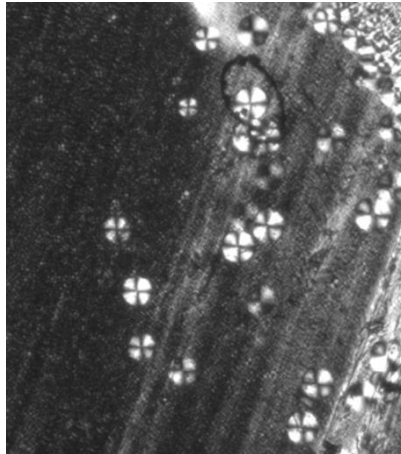


Figure I.7: Specific spherulites of PA-6, showing the characteristic appearance of « Maltese cross » (or tie bow according to the light orientation), observed under polarized light

In the case of polyamide 6, only positive spherulites are observed [29] [30] due to the crystallization process that promotes the H-bond arrangement along the growth axis of the crystallites [31]. Furthermore, it was established that the spherulites of PA6 consist of untwisted and narrow ribbon-like lamellae. The lamellae stacks do not exceed three to four parallel lamellae, in contrast to high crystallinity polyolefins [32]. This structural feature involves the presence of a significant content of amorphous phase out of the lamellae stacks. This is at the origin of inter- and extra-lamellar amorphous phase with suspected different properties [33].

I.3. Amorphous phase

In contrast to the crystalline phase, the amorphous phase is a disordered structure. It is yet well known that most of the H-bonds are formed [34]. Molecular mobility in the amorphous phase may strongly influence the material properties. Indeed, as the crystallinity index of PA6 is low (maximum 40%), the amorphous phase should have a significant contribution.

I.3.1. Mechanical relaxations: mobility of amorphous phase

The origin of mechanical relaxations is the mobility of chains at the molecular scale in the amorphous phase. These relaxations can be detected by mechanical spectroscopy (DMA see chap II §III.1) or dielectric spectroscopy, as shown in Figure I.8. Three amorphous relaxations were clearly identified in PA6: γ , β and α , with increasing temperature, as shown in Figure I.8 in the case of isochronal measurements at 1Hz. This labeling of the mechanical relaxations should not be confused with the various crystal forms. Chain mobility in the crystalline phase proved to be hardly activated due to the presence of hydrogen-bonds.

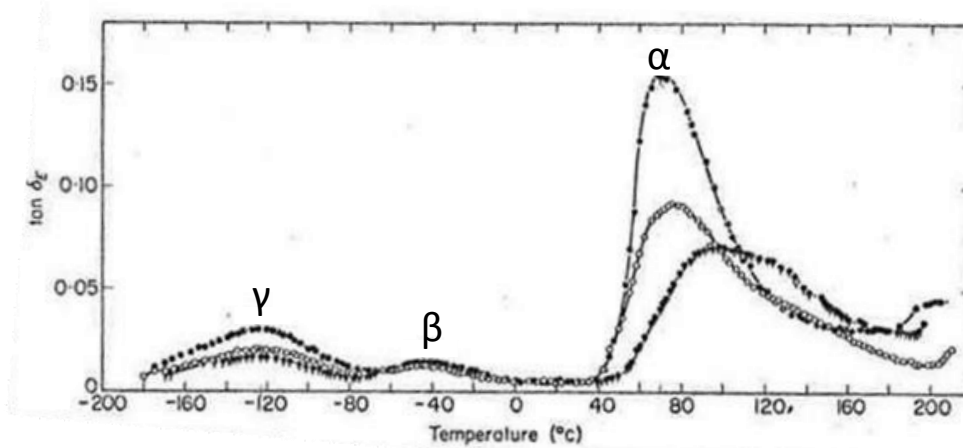


Figure I.8: Temperature dependence of the mechanical loss tangent, $\tan \delta_\epsilon$, at 100c/s for PA6 samples of different crystallinity. (●) sample quenched from the melt to -78°C ; (○) sample crystallized at 200°C ; (●) ϵ -caprolactam removed [35]

The γ relaxation is located around $[-140^\circ\text{C} / -100^\circ\text{C}]$ at 1 Hz. In the presence of water, the relaxation intensity decreases and moves to higher temperature. The existence of γ is probably related to the relaxation motions associated with the amide group itself (mechanism known as "crank") and may involve the twist or kink of the amide groups, which could explain the effects of humidity on relaxation, but not only [19] [36]. In addition to the motion of polar groups, the motions of methylene units could also be involved [37].

The β relaxation is usually between $[-50^\circ\text{C} / -10^\circ\text{C}]$ at 1Hz. The peak intensity is rather low but increases in the presence of humidity or residual monomers. Its position does not change but its amplitude does [19]. The β relaxation involves motions of chain segments including amide groups which are not hydrogen bonded to neighboring chains as well as the motions of a water-polymer-complex [9] [19] [37] [36].

The α relaxation is usually associated to the glass transition of the amorphous phase. The relaxation moves to lower temperature when the quantity of residual monomers as well as the water content increases [38]. It is assumed to involve motions of long chain segments comparable in length to the one between entanglements [19] [37].

In addition to these relaxations, cryogenic relaxations have also been investigated by Papir et al. [37]. These relaxations are the followings: δ at -220°C , ϵ at -268.8°C and ζ at -253°C . Their presence reveals that local chain mobility still exists below the γ relaxation. However, the origin of these cryogenic relaxations has not been determined.

Regarding the crystalline phase, a specific relaxation called α_c has been observed by dielectric spectroscopy close to the melting point [35]. By analogy with polyolefins it has been speculatively attributed to the chain mobility in crystalline phase thanks to the diffusion of defects [9] [39].

1.3.2. Heterogeneity of the amorphous phase

As said previously, polyamide 6 is a semi-crystalline polymer and its morphology could be considered as a 2-phase system of crystalline and amorphous phases. However, several authors have proposed the existence of a third intermediate phase located at the interface between crystalline and amorphous phases [19] [40] [41] [42] [43]. This phase is known as the Rigid Amorphous Fraction (RAF) due to its reduced mobility in comparison to the usual Mobile Amorphous Fraction (MAF). The chains

belonging to the RAF are indeed constrained by their anchoring to the crystallites. This 3-phase system is depicted in Figure I.9.

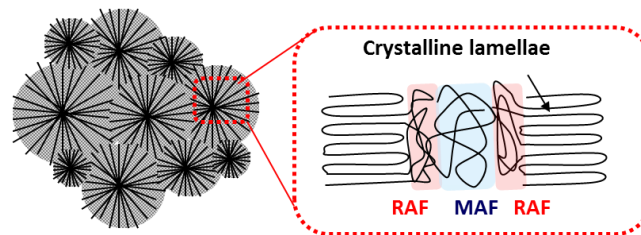


Figure I.9 : Scheme of 3-phase system

I.4. Linking between crystalline and amorphous phases

Amorphous and crystalline lamellae are physically linked by various elements. During crystallization and chains folding, chains can go out of the crystal to cross the amorphous phase in order either to go back to the crystal, fold in amorphous phase or go in an adjacent crystal. Various topological elements can form like loops, pending chains, tie molecules, etc... as depicted in Figure I.10 [44] [45]. The thickness of the crystalline phase is referred as L_c and the thickness of the amorphous phase as L_a . The long period L_p is defined as the thickness of both a crystalline lamella and the amorphous phase contained between two successive crystalline lamellae.

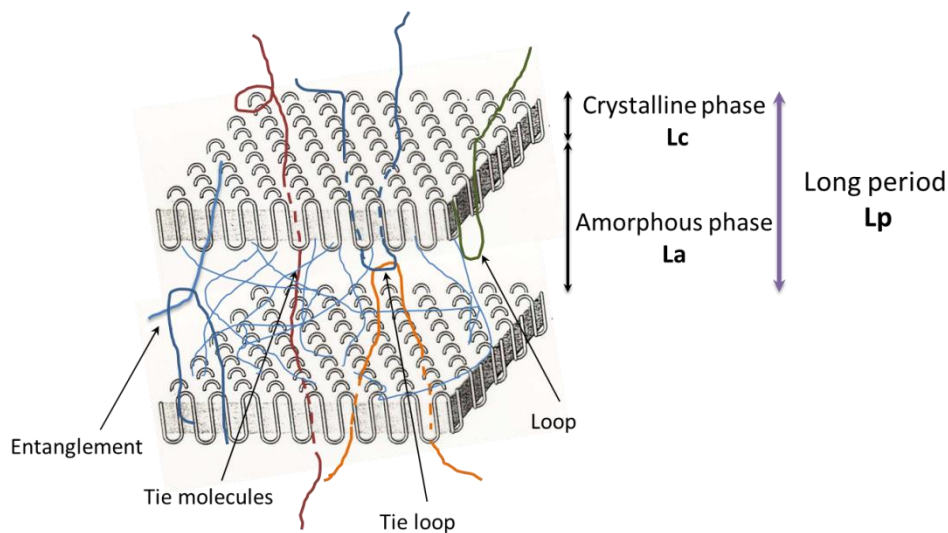


Figure I.10 : Scheme of crystalline and amorphous phase with the various linking elements

Tie molecules are long molecules going through two successive crystalline lamellae. It is also possible to define tie molecules when two loops going out of two neighboring lamellae entangle each other. Under stress, tie molecules can only be destroyed by breaking, in contrast to entangled chains that can slide on each other and disentangle, owing to the chain relaxation in the crystalline lamellae to which the tie chains are anchored on. Nonetheless, disentanglement needs more or less time depending on temperature and stress level [46].

All these elements (loops, tie molecules, entanglements...) allow mechanical coupling between amorphous and crystalline phases because they transmit the stresses between the two phases. Thus, they are named stress transmitters. The numbers of entangled molecules depends to the molecular mass of the polymer. Below a critical molecular mass M_c , no entanglement can form [19] [44] [47]

[48]. This restriction also applies to the tie molecules since the longer is the chain the greater is its probability to span the amorphous layer and the two adjacent crystalline lamellae. From a theoretical standpoint, it was computed the following value [49] :

$$M_{c\ th} = 5180\ g/mol$$

whereas the following value was reported from experiments [50] :

$$M_{c\ exp} = 4380\ g/mol$$

II. Mechanical behavior

At macroscopic scale, the characteristic mechanical behavior of a semi-crystalline, including PA6, can be described by the stress-strain curve of Figure I.11 in the case uniaxial tensile loading [51] [52] [53].

This stress-strain curve can be divided into four domains:

- The first one is the elastic as well as viscoelastic strain domain. The Young's modulus E can be determined by the slope of the stress/strain curve in the initial elastic domain.
- The yield stress σ_Y corresponds to the border between the elastic and plastic strain domains. It is the threshold of the plastic behavior. At this stage, macroscopic necking usually starts in the sample. Plastic deformation is irreversible contrary to the elastic behavior.
- The stress plateau corresponds to the spreading of the neck over the whole sample length. This stage corresponds to the chain-unfolding process. After complete propagation of the neck, a hardening stage appears before failure.
- The strain-hardening corresponds to the orientation of macromolecules along the tensile direction giving rise to the so-called fibrillar structure. Depending on the ductility or fragility of the material, in relation to its molecular weight, this domain can exist or not. The breaking stress σ_R corresponds to the stress at which the polymer breaks.

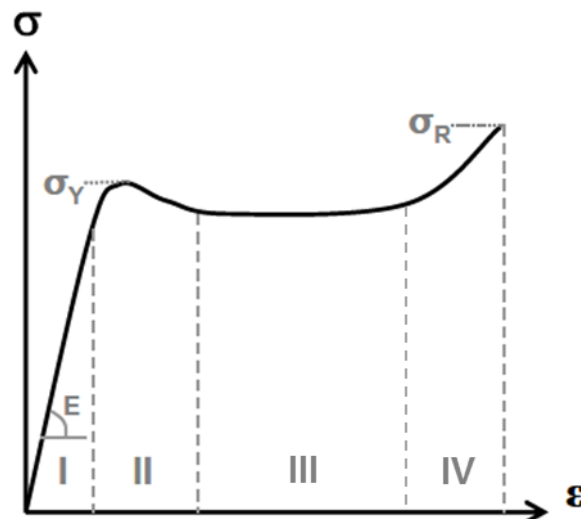


Figure I.11 : Nominal stress-strain curve for a semi-crystalline polymer: (I) elastic-viscoelastic domain, (II) plastic domain, (III) neck propagation, (IV) strain-hardening; adapted from [54]

Usually, for dry PA6, the following characteristic values are found for tensile test following the ASTM D-638 norm [55]:

- At 23°C (below T_g) : $\sigma_Y = 79\ MPa$, $\epsilon_Y = 7\ %$ and $\epsilon_R = 70\ %$
- At 121°C (above T_g) : $\sigma_Y = 21\ MPa$, $\epsilon_Y = 15\ %$ and $\epsilon_R > 300\ %$

It is easier to determine global properties as Young's modulus or yield stress for a material, than to link macroscopic behavior to its microstructural parameters. Indeed, during a tensile test, local strains and stresses on the microstructure are complex, as it will develop below. As said earlier, in a semi-crystalline, the matter organizes at different scale levels: staking of crystalline lamellae at microscopic scale, spherulitic arrangement of the lamellae at mesoscopic scale, polymer sample at the macroscopic scale. The following parts focus on the deformation mechanisms at different scales occurring in the different domains of the stress-strain curve (i.e. elastic, plastic and breaking), as well as the connection between mechanical properties and microstructure.

II.1. Elastic behavior

These different mechanisms are presented below from smaller to larger scale, as well as correlation between mechanical properties and microstructure.

II.1.1. Mechanisms at the crystalline lamella scale

At low deformation corresponding to the viscoelastic behavior, mainly the amorphous phase deforms. At the scale of crystalline lamella stacks, three types of deformation are observed:

- Interlamellar shear
- Interlamellar separation
- Lamella rotation or flip

These deformations have been studied by Bowden and Young [56] under uniaxial tensile testing and are depicted in Figure I.12. The implication of one mechanism depends on the orientation of lamellae stacks versus the load direction as well as the crystalline network.

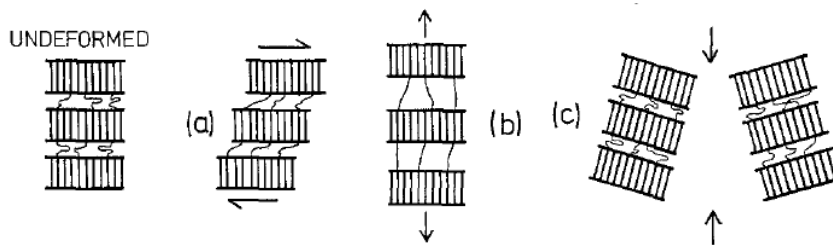


Figure I.12 : Deformation of the amorphous phase in lamella stacks under uniaxial tensile testing: a) interlamellar shear, b) interlamellar separation, c) lamella rotation [56]

The interlamellar separation is due to a tension component normal to the lamella surface. It increases the distance between two crystalline lamellae. It is effective for stacks whose normal is parallel to the tensile direction. These mechanisms have been studied for polyethylene [57] and polyamide 66 [58]. Reciprocally, lamellae oriented parallel to the tensile stress display transverse contraction owing to the Poisson's effect.

The interlamellar shear corresponds to the slip of the crystalline lamellae parallel to each other, with the interlamellar amorphous phase undergoing a simple shear deformation. This solicitation is essentially effective for lamellae inclined with respect to the tensile direction. This mechanism should be relatively easy above T_g when the amorphous phase is expected to behave like a rubber and deform at a relatively low stress level [56].

Interlamellar shear is generally concomitant with lamellar stack rotation in the diagonal regions of the spherulites.

Considering the usual spherulitic structure of semi-crystalline polymers various regions should be distinguished concerning lamellae orientation with regard to the applied stress under uniaxial tensile testing, as depicted in Figure I.13. In polar regions where the lamellae are mainly aligned parallel to the tensile direction, the chains axis is normal to tensile axis. In the equatorial region, lamellae may have their larger surface (see the sketch of Figure I.13a) either parallel or normal to the main stress: concomitantly the chain axis may be either normal or parallel to the tensile direction (TD).

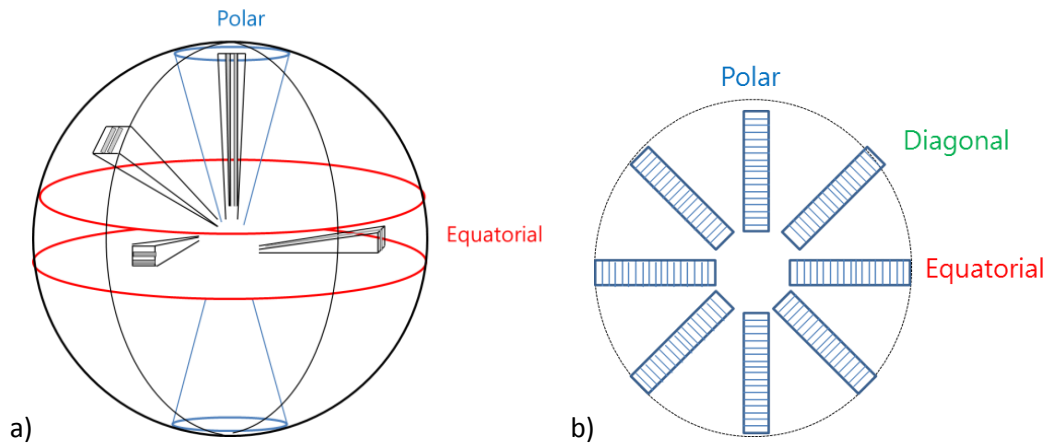


Figure I.13: a) 3D and b) 2D spherulite picture (Tensile direction is vertical).

Due to the complex morphology of the spherulites, it is difficult to analyze their global deformation and the resulting complex state of stress in the various regions [59]. Under tensile loading, equatorial lamellae stacks are submitted to tensile stress either normal to the lamella surface meaning a separation of the stacks or parallel to the lamella surface meaning an elastic stretching of the crystalline lattice. Lamella rotation also occurs with increasing strain. In polar region, lamella stacks undergo stretching along their major direction and transverse compression due to the Poisson's effect. In diagonal regions, interlamellar shear is the more favorable process.

II.1.2. Elastic modulus versus crystallinity index

In semi-crystalline polymers, it has been shown in the literature that the Young's modulus E generally increases with the crystallinity index X_c . This trend was observed for PA6 by Bessel et al. [60] as shown in Figure I.14 concerning a rather large range of X_c and for tensile tests at 23°C.

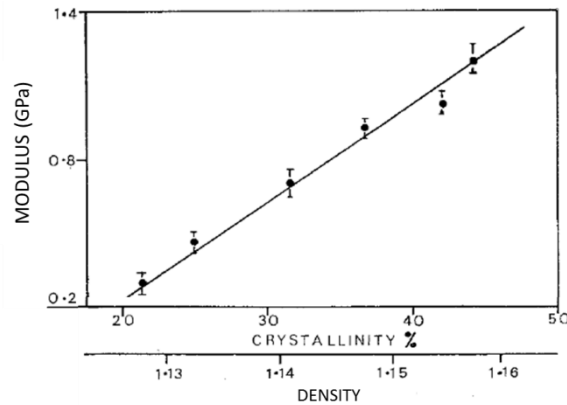


Figure I.14: Evolution of elastic modulus as a function of crystallinity index in PA 6 [60]

Using the connection between E and X_c , parallel and series models can be used. These models are based on the fact that in semi-crystalline polymers, both amorphous and crystalline phases contribute to E . In literature, the modulus of heterogeneous systems is often modeled via two mixing laws based on very simple coupling models: in the parallel model, the stiff component predominates the overall behavior whereas in the series model, it is the softer phase that dominates. The Young's modulus of a semi-crystalline polymer can be described by the following relationships:

$$E_{\parallel} = X_c \cdot E_c + (1 - X_c)E_a \quad \text{for the Parallel model} \quad (\text{E I.1})$$

$$E_{\infty} = \frac{1}{\frac{X_c}{E_c} + \frac{(1-X_c)}{E_a}} \quad \text{for the Series model} \quad (\text{E I.2})$$

With X_c the crystallinity index

E_c the modulus of the crystalline phase

E_a the modulus of the amorphous phase

However, in reality the mechanical behavior of semi-crystalline polymer generally corresponds to a combination of these two models. Evidence of this intermediate situation has been given by Humbert [46] in the case of polyethylene (PE). This is shown in Figure I.15. In PE, different domains have been pointed out depending on crystallinity index. Figure I.15 shows that with increasing X_c the Young's modulus gradually shifts from *close to the series model* to *close to the parallel model*. This observation suggests that the crystalline network made of more or less interconnected lamella plays a determining role in the elastic deformation mechanisms: for low X_c , the amorphous phase accommodates a large part of the strain whereas for high X_c more of the load is sustained by the percolating crystalline network. Regarding PA6, for $20\% < X_c < 50\%$, the relationship between E and X_c is fairly linear (Figure I.14). This linear trend suggests a parallel coupling according to Equation E.1. However, lacking data for the moduli of the crystal and the amorphous phases, it is not possible to conclude at the present moment.

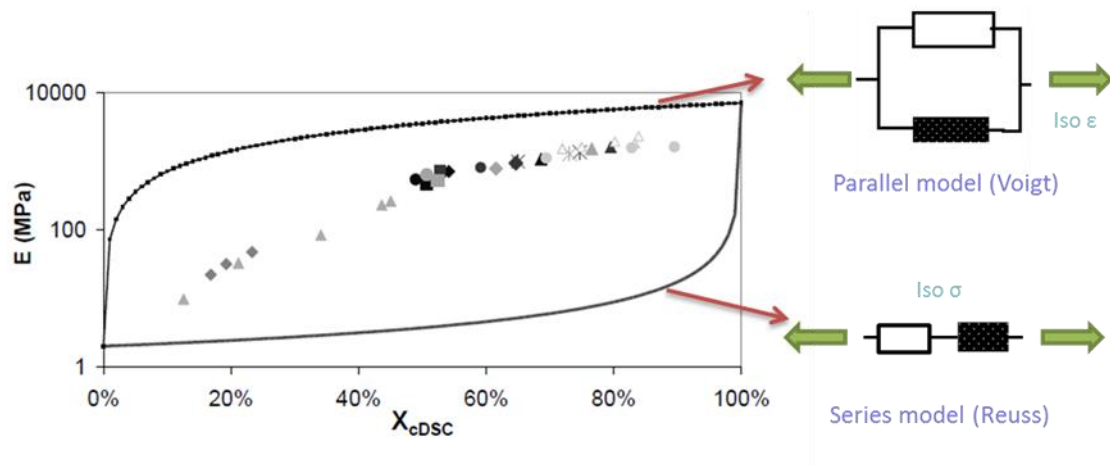


Figure I.15 : Young's modulus E (in log scale) plotted as a function of crystallinity index X_c measured by DSC for several PE [61], with the corresponding theoretical curves for parallel and series mechanical models.

II.2. Plastic behavior

This part describes the phenomena occurring in the domains II and III of the Figure I.11, at different scales. Indeed, plastic deformation is a complex process involving crystal shear, stack rotation, cavitation, phase transformation, allowing the transition between lamellar and fibrillar structure. These different mechanisms are presented below from smaller to larger scale.

II.2.1. Crystal shear

II.2.1.1. Definition of slip systems

The global motion of dislocations corresponds to a plastic deformation, which can be observed at a larger scale. In semi-crystalline polymers, the motion of dislocations is limited by the foldings of chains at the surface of the lamellar crystals and by the presence of amorphous phase between crystals. It is admitted that the only active slip systems are the ones containing the chains axis [62]. Usually, slip systems are of the type $\{hk0\} \langle uvw \rangle$, where $\{hk0\}$ holds for the slip plane and $\langle uvw \rangle$ holds for the slip direction –with c axis being the chains axis [63]. However in the case of polyamide 6, the chains axis corresponds to the b axis because the main crystalline lattices are monoclinic (crystallographic convention for monoclinic lattices), so that the slip systems are of the type $\{h0l\} \langle uvw \rangle$. Experimental observations allow determining precisely the slip direction:

- Chain slip is of the kind $\{h0l\} [010]$
- Transverse slip is of the kind $\{h0l\} \langle u0w \rangle$

The two kinds of slip systems are schematized in Figure I.16.

In the case of PA6, the main slip modes are $(001)[010]$, $(100)[010]$ and $(001)[100]$. It is the $(001)[010]$ slip system that is the easiest one to activate [15]. In the case of α phase of PA6, this system corresponds to the chain slip in the H-bond planes [15] [64].

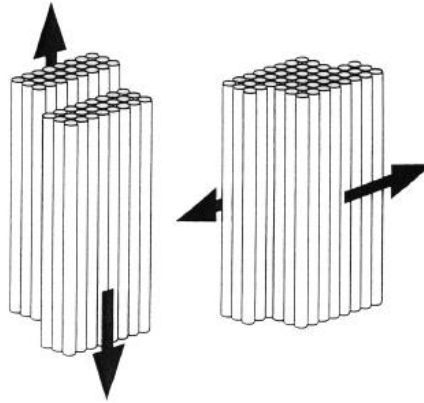


Figure I.16 : Chain and transverse slips in crystalline lamellae [62]

II.2.1.2. Twinning

Twining is a kind of plastic deformation mode to occur in semi-crystalline polymers. It is a collective shear process which generates a disorientation of a part of the crystalline lattice with respect to the original one. The two lattices are fitted together on a common crystallographic plane called the twinning plane. This is sketched in Figure I.17. The induced shear strain is given by the geometry of the twinning system, i.e. the crystallographic plane and direction of the twinning process in the crystalline lattice. This phenomenon has been reported for PE [65] [66], PP [67] and PA66 [65].

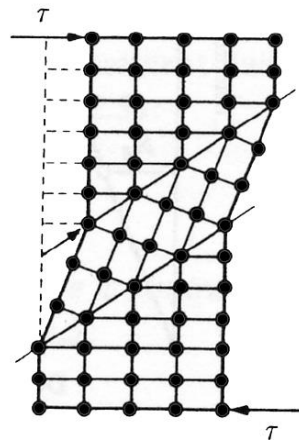


Figure I.17: Illustration of twinning mechanism

II.2.1.3. Shear banding

Shear banding is a localized plastic deformation mechanism commonly observed in semi-crystalline polymers. It occurs in the direction of maximum shear stress, i.e. at an angle close to 45° relative to the main stress in case of uniaxial tensile test. Bowden and Young [56] have demonstrated this phenomenon by combined wide-angle and small-angle X-ray scattering.

More recent observations by Atomic Force Microscopy have been reported regarding PA6 [68]:

- Above T_g , interlamellar shear allows the rotation of lamellae even for weak deformations. For intermediate deformations, shear bands cross the crystalline lamellae and move uniformly throughout the spherulite volume.

- Below T_g , interlamellar shear is much more difficult and the propagation of shear bands is more heterogeneous.
- Above the critical temperature of 160°C, spherulites deform homogeneously.

In Ferreiro et al.'s study [68], it is shown that, whatever the temperature, shear bands appear at a shear angle of 52° with respect to the tensile direction. For strains below 10%, no shear bands were detected. Ferreiro [69] was also able to image both amorphous and crystalline phase thanks to AFM. He reported that for PA6 stretched beyond the elasticity limit at $T < 160^\circ\text{C}$, shear bands nucleate and propagate in the amorphous phase before to expand into the crystalline lamellae.

II.2.1.4. Stress transmitters

Japanese teams have led studies on semi-crystalline polymer, having the capacity to form spherulitic structure, and proposed a new mechanical model which describes the strain-stress relation at an intermediate scale which corresponds to a stack of several lamellae linked by tie molecules. These studies have been carried out in consideration of polypropylene data [70] [71].

During tensile tests, semi-crystalline polymers usually show a distinct yield point. Below the yield point, the material undergoes viscoelastic deformations, essentially localized into the amorphous phase. Crystal shear takes place beyond the yield point. Mechanical linking between amorphous and crystalline phase is of primary importance during this transition. The linking is carried out thanks to stress transmitters, meaning tie molecules, entangled chain loops... (cf. §1.4).

Nitta et al. [70] have built the following model, depicted in Figure I.18. It takes into account the influence of tie molecules between the adjacent lamellae in stack. During a tensile test, lamellae are subjected to bending around the anchoring points of the tie molecules due to the pulling force that generates stress concentration on the lamellae. As tie molecules sustain the bending effect, the closer are these tie chains, the most difficult is the breaking of the lamellae. In other words, the higher the tie chain density, the higher the lamella resistance to breaking.

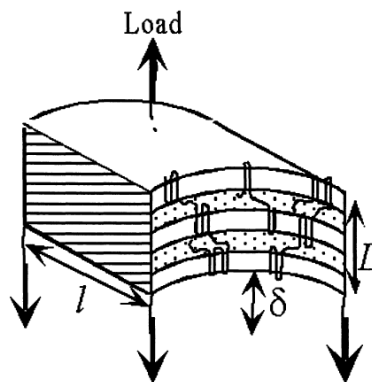


Figure I.18: Scheme of a bending lamellae stacks [70]

II.2.2. Cavitation

Cavitation is one of the micro-mechanisms of plastic deformation of semi-crystalline polymers during tensile loading. This phenomenon is also considered as a damaging process since it significantly affects the plastic yielding and failure of the material [72].

Generally, cavities appear into equatorial regions of spherulite as depicted in Figure I.19b, because these regions are subjected to a local tensile stress, leading to interlamellar separation.

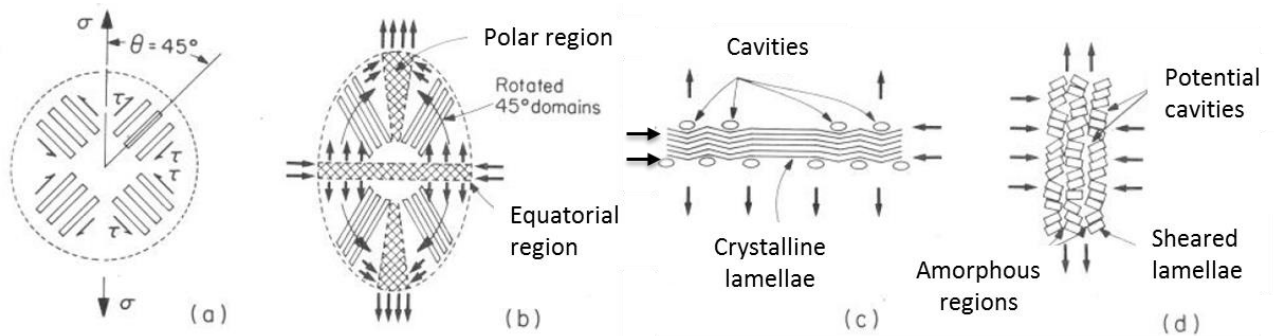


Figure I.19: Steps of cavities formation into equatorial regions of spherulites [59]: a) undeformed state; b) rotations due to simple shear; c) kink of undeformed lamellae in equatorial regions; d) instabilities due to chain slip for lamellae in polar regions

Pawlak and Galeski [72] have compared the influence of crystalline shear and cavitation in the amorphous phase leading to the breaking of semi-crystalline polymers: cavitation appears for polymers having crystals with high plastic resistance whereas polymers having crystal with weak plastic resistance deform by crystalline shears. For PA6, cavities are unstable and tend to heal upon unloading but in any case the cavities generate damage of the material. The diameter of the incipient cavities is around 4-5 nm, as measured by X-ray scattering, which is close to the interlamellar distance [72]. Observations by electronic microscopy have allowed Galeski to locate these cavities within the interlamellar and interspherulitic amorphous phase [59] [73].

II.2.3. Fibrillation

At higher deformation, the plastic deformation is supposed to proceed in three steps: the plastic deformation of the original spherulitic structure, the discontinuous transformation of the spherulitic into fibril structure by micronecking and the plastic deformation of the fibril structure [74].

The first step has already been described above (stack rotation, sliding of lamellae, twinning...). The second step consists in the transformation of every lamella into a bundle of microfibrils thanks to micronecks. The microfibrils, the basic elements of the structure, contain folded chain crystal blocks alternating with amorphous layers, as depicted in Figure I.20a. In the fibril structure, the chains are nearly perfectly oriented along the tensile direction (see also Figure I.20b).

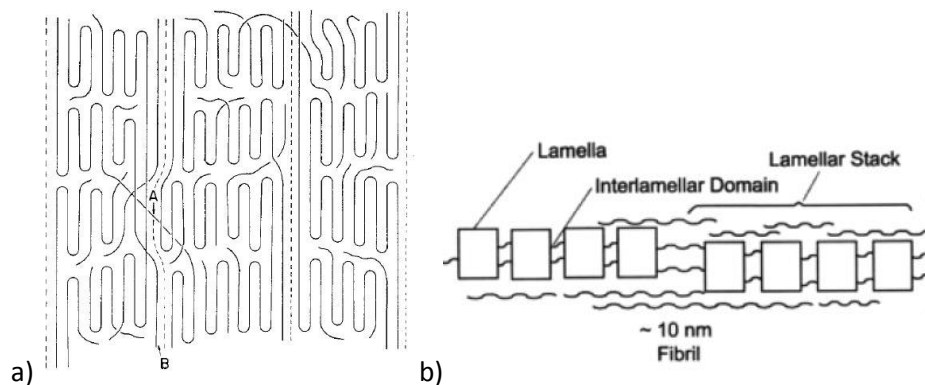


Figure I.20: a) Microfibrillar model of the fibril structure: A interfibrillar and B intrafibrillar tie molecule [74]
b) Fibril structure, tensile direction is horizontal [75]

In bulk samples, a striking change of long period can occur during the fibrillation process without any connection with the long period of the initial material. Indeed, the long period of the fibril structure mainly depends on the temperature of drawing. Such a structural adjustment requires a high chain mobilization involving eventually strain-induced melting [74].

Finally, the plastic deformation of the fibril structure can occur only by sliding motion of the microfibrils or fibrils. It corresponds to the strain hardening which proceeds up to the final break.

II.2.4. Effect of phase nature in the case of PA6

As previously mentioned, PA6 is a polymorphic polymer. Three crystalline lattices can be observed. Having different crystalline phases has an effect on the mechanical behavior. During a preliminary study of Penel-Pierron and al [16], tests of mechanical stability have been performed on the different crystalline phases for 80 μ m thick films: α phase was obtained thanks to a hot water treatment, γ phase by an iodine treatment and β phase was obtained thanks to quenching. It was shown that β phase turned into α phase upon stretching whatever the temperature. The γ phase, stable until 200°C, was more stable than β but finally reorganized into α phase when it was stretched at high temperature.

In another study, the above authors have shown that β phase was more ductile than α phase [64]. Indeed, film containing a predominant the α phase is less ductile than films containing either the γ or the β phase, as judged from the yield stress level and strain at break and shown in Figure I.21 (left). The yield stress as a function of strain rate is reported in Figure I.21 (right), where a steeper dependence is shown for α phase. As the tensile tests are performed at 80°C, the amorphous phase is rubbery and the observed difference can be mainly attributed to the crystalline structure. The difference of ductility between the α and β phases could be due to the higher cohesion and reduced number of available slip planes of the H-bonded sheet-like structure of the α phase compared to the β phase [64]. In addition, under uniaxial tensile loading, most of the β phase transforms into α phase accompanied by a hardening of the material. The degree of $\beta \rightarrow \alpha$ transformation increases when the stretching is performed above 120°C, due to additional thermal reorganization.

Ito and al [76] [77] have also reported that the deformability of PA6 depends on the crystalline structure: γ phase is more ductile than α in the temperature range [100-180°C].

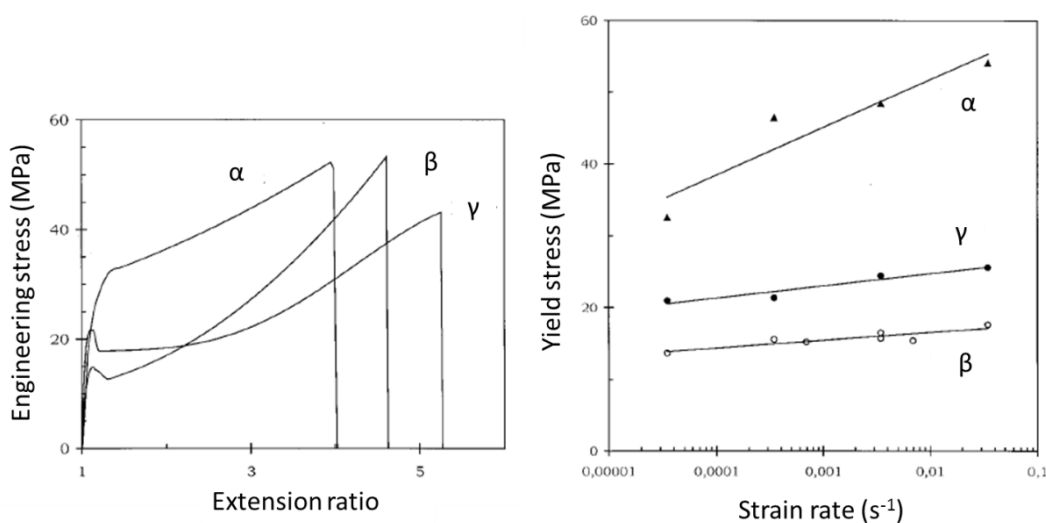


Figure I.21: Strain-stress curves for tests at $T=120^{\circ}\text{C}$ and crosshead speed of 50 mm/min on PA 6 (left) ; Yield stress as a function of initial strain rate at $T=80^{\circ}\text{C}$ (right) [64]

However, one should keep in mind that all these studies were done ex-situ, meaning that the possibility of relaxation phenomena is not taken into account. In addition, only tensile tests at the macroscopic scale above T_g have been performed and the α and especially γ phases of the sample were obtained thanks to chemical treatments.

II.3. Failure behavior

The failure of polymers has been often studied under tensile testing conditions at room temperature, using notched samples [53] [78]. Regarding PA6, Bessel et al. [60] reported the following features of the failure process at the spherulite scale under tensile testing of un-notched samples:

- Fine cracks start to form inside the spherulite normal to the tensile direction.
- As the deformation increases, more cracks form and the previous ones continue to grow.
- During last steps of deformation, cracks in neighboring spherulites begin to coalesce to form voids.
- Finally, the polymer breaks due to propagation of cracks and/or voids.

The influence of the crystallinity index ($20\% < X_c < 44\%$) on the mechanical behavior and failure at room temperature of PA6 has also been studied by Bessel et al. [60]. The stress-strain curves are shown in Figure I.22. It has been observed that:

- For high crystallinity ($X_c = 44\%$), the failure is typically brittle. Cracks appear very soon at the yield point. Crack propagation is fast with a low interaction between the spherulitic structure and the crack path.
- For low crystallinity ($X_c < 30\%$), PA6 does not show a defined yield point but displays a large elongation at break. Failure takes place after fibrillation due to coalescence of small voids in a stress whitened zone.
- For intermediate crystallinity, the tensile behavior is characterized by a well-defined yield point and an elongation at break around 50-80%. The fracture surface of the material displays two distinct regions: a central fibrillated zone and an outer zone with interspherulitic failure. This is evidence that failure occurs in a highly heterogeneous state of strain in the material.

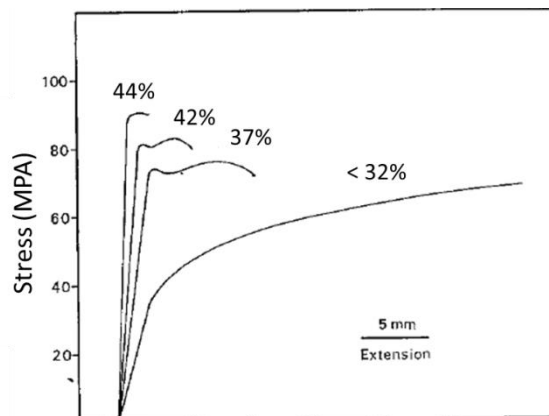


Figure I.22: Stress-elongation behavior for various crystallinity index on PA 6 [60]

References

- [1] B. Guerin, "Polyamides PA," *Techniques de l'Ingénieur*, p. A 3360, 1994.
- [2] M. Kohan, *Nylon Plastics handbook*, Wilmington: Hanser, 1995.
- [3] B. Wunderlich, *Macromolecular Physics*, vol.1 : Crystal structure, morphology, defects, New York: Academic Press, 1973.
- [4] C. De Rosa and F. Auriemma, *Crystals and crystallinity in polymers: diffraction analysis of ordered and disordered crystals*, New York: John Wiley & Sons, 2013.
- [5] Y. Li and W. Goddard, "Nylon 6 crystal structures, folds and lamellae from theory," *Macromolecules*, vol. 35, pp. 8440-8455, 2002.
- [6] N. S. Murthy, "Hydrogen bonding, mobility and structural transitions in aliphatic polyamides," *Journal of Polymer Science: Polymer Physics*, vol. 44, pp. 1763-1782, 2006.
- [7] L. Penel-Pierron, "Transition de phase induite par déformation dans les polymères à liaisons hydrogène : cas des polymères éthylène/alcool vinylique et du polyamide 6," USTL, Lille, 1998.
- [8] H. J. Arimoto, "Alpha-gamma transition of nylon 6," *Journal of Polymer Science Part A*, vol. 2, pp. 2283-2295, 1964.
- [9] K. Hoashi and R. D. Andrews, "Morphological changes in nylon 6 and effect on mechanical properties. II. Dynamic mechanical properties," *Journal of Polymer Science: Part C: Polymer Symposia*, vol. 38, pp. 387-404, 1972.
- [10] K. Miyasaka and K. J. Makishim, "Transition of nylon 6 γ -phase crystals by stretching in the chain direction," *Journal of Polymer Science Part A*, vol. 5, pp. 3017-3027, 1967.
- [11] A. Ziabicki, "Über die mesomorphe β -Form von Polycapronamid und ihre Umwandlung in die kristalline Form α ," *Kolloid-Zeitschrift*, vol. 167, pp. 132-141, 1959.
- [12] F. Auriemma, V. Petraccone, L. Parravicini and P. Corradini, "Mesomorphic form (β) of Nylon 6," *Macromolecules*, vol. 30, pp. 7554-7559, 1997.
- [13] D. R. Holmes, C. W. Bunn and D. J. Smith, "The crystal structure of polycaproamide: nylon 6," *Journal of Polymer Science*, vol. 17, pp. 159-177, 1955.
- [14] H. Arimoto, M. Ishibashi and M. Hirai, "Crystal structure of the γ form of Nylon 6," *Journal of Polymer Science, Part A*, vol. 3, pp. 317-326, 1965.
- [15] L. Lin and A. Argon, "Deformation resistance in oriented nylon 6," *Macromolecules*, vol. 25, pp. 4011-4024, 1992.

- [16] L. Penel-Pierron, C. Depecker, R. Seguela and J.-M. Lefebvre, "Structural and mechanical behavior of nylon 6 films. Part I: Identification and stability of the crystalline phases," *Journal of Polymer Science: Part B: Polymer Physics*, vol. 39, pp. 484-495, 2001.
- [17] K.-H. Illers, "Polymorphie, Kristallinität und Schmelzwärme von Poly(ϵ -caprolactam), 2)," *Makromolekulare Chemie*, vol. 179, pp. 497-507, 1978.
- [18] S. Gogolewski, M. Gasiorek, K. Czerniawska and A. J. Pennings, "Annealing of melt-crystallized nylon 6," *Colloid & Polymer Science*, vol. 260, pp. 859-863, 1982.
- [19] S. Aharoni, *n-Nylons : their synthesis, structure and properties*, John Wiley & Sons, 1997, pp. 284-296.
- [20] P. Geil, "Nylon single crystals," *Journal of Polymer Science*, vol. 44, pp. 449-458, 1960.
- [21] O. Muratoglu, A. Argon and R. Cohen, "Crystalline morphology of polyamide-6 near planar surfaces," *Polymer*, vol. 36, pp. 2143-2152, 1995.
- [22] Y. Kojima, A. Usuki, M. Kawasumi, A. Okada, T. Kurauchi, O. Kamigaito and K. Kaji, "Fine-structure of nylon-6-clay hybrid," *Journal of Polymer Science Part B: Polymer Physics*, vol. 32, pp. 625-630, 1994.
- [23] W. Callister, *Materials science and engineering: an introduction*, John Wiley & Sons, 1997, p. 459.
- [24] E. Boasson and J. Woestenenk, "Negative spherulites in 66 Nylon ((Polyhexemethylene adipamide)," *Journal of Polymer Science*, vol. 21, no. 97, pp. 151-153, 1956.
- [25] F. Khoury, "The fibrillar structure of spherulites in polyhexemethylene adipamide," *Journal of Polymer Science*, vol. 26, no. 114, pp. 375-379, 1957.
- [26] C. Lindegren, "Spherulites in Nylon 610 and Nylon 66," *Journal of Polymer Science*, vol. 50, no. 153, pp. 181-189, 1961.
- [27] J. Mann and L. Roldan-Gonzalez, "Orientation in nylon spherulites: a study by X-Ray diffraction," *Journal of Polymer Science*, vol. 60, no. 169, pp. 1-20, 1962.
- [28] J. Magill, "Formation of spherulites in polyamide melts: Part III. Even-even polyamides," *Journal of Polymer Science*, vol. 4, pp. 243-265, 1966.
- [29] B. Burnett and W. McDevit, "Kinetics of spherulite growth in high polymers," *Journal of Applied Physics*, vol. 28, pp. 1101-1105, 1957.
- [30] J. Magill, "Melting behaviour and spherulitic crystallization of polycapramide (nylon 6)," *Polymer*, vol. 3, pp. 43-51, 1962.

- [31] R. Huisman and H. Heuvel, "Quantitative information from X-Ray diffraction of Nylon-6 yarns. II. Physical aspects of some quantitative parameters," *Journal of Polymer Science: Polymer Physics Edition*, vol. 14, pp. 941-954, 1976.
- [32] A. Galeski, A. Argon and R. Cohen, "Morphology of nylon 6 spherulites in bulk," *Die Makromolekulare Chemie*, vol. 188, pp. 1195-1204, 1987.
- [33] B. Sauer and B. Hsiao, "Effect of the heterogeneous distribution of lamellar stacks on amorphous relaxations in semicrystalline polymers," *Polymer*, vol. 36, pp. 2553-2558, 1995.
- [34] D. Skrovanek, S. Howe, P. Painter and M. Coleman, "Hydrogen bonding in polymers: infrared temperature studies of an amorphous polyamide," *Macromolecules*, vol. 18, pp. 1676-1683, 1985.
- [35] M. Takayanagi, "Crystallized state of polymer in its dispersion behaviour," *Pure and applied Chemistry*, vol. 15, pp. 555-586, 1967.
- [36] "Chap. 12: Polyamides and Polyurethanes," in *Anelastic and dielectric effects in polymeric solids*, John Wiley & Sons, 1967, pp. 478-497.
- [37] Y. S. Papir, S. Kapur and C. E. Rogers, "Effect of orientation, anisotropy, and water on the relaxation behavior of nylon 6 from 4.2 to 300°K," *Journal of Polymer Science: Part A-2*, vol. 10, pp. 1305-1319, 1972.
- [38] M. Laurati, P. Sotta, D. Long, L.-A. Fillot, A. Arbe, A. Alegria, J. Embs, T. Unruh, G. Schneider and J. Colmenero, "Dynamics of water absorbed in polyamides," *Macromolecules*, vol. 45, pp. 1676-1687, 2012.
- [39] C. Ibanes, "Relations structure-propriétés mécaniques de fibres de polyamide 6 renforcées de nanoparticules organiques ou minérales," Ecole doctorale Matériaux, INSA, Lyon, 2003.
- [40] J. D. Menczel and M. Jaffe, "How did we find the rigid amorphous phase ?," *Journal of Thermal Analysis and Calorimetry*, vol. 89, pp. 357-362, 2007.
- [41] D. C. Prevorsek, Y. D. Kwon and R. K. Sharma, "Structure and properties of nylon 6 and PET fibres: the effects of crystallite dimensions," *Journal of Materials Science*, vol. 12, pp. 2310-2328, 1977.
- [42] I. Kolesov and R. Androsch, "The rigid amorphous fraction of cold-crystallized polyamide 6," *Polymer*, vol. 53, pp. 4770-4777, 2012.
- [43] H. Chen and P. Cebe, "Investigation of the rigid amorphous fraction in nylon-6," *Journal of Thermal Analysis and Calorimetry*, vol. 89, pp. 417-425, 2007.
- [44] H. Keith, F. Padden and V. R.G., "Intercrystalline links in polyethylene crystallized from the melt," *Journal of Polymer Science Part A-2: Polymer Physics*, vol. 4, no. 2, pp. 267-281, 1966.

- [45] P. J. Flory and Y. D.Y., "Molecular morphology in semicrystalline polymers," *Nature*, vol. 272, pp. 226-229, 1978.
- [46] S. Humbert, "Influence de la topologie moléculaire et de la microstructure sur les propriétés mécaniques des polyéthylènes," Ecole doctorale Matériaux, INSA, Lyon, 2009.
- [47] N. Brown and I. Ward, "The influence of morphology and molecular weight on ductile-brittle transitions in linear polyethylene," *Journal of Materials Science*, vol. 18, pp. 1405-1420, 1983.
- [48] Y. Huang and N. Brown, "The effect of molecular weight on slow crack growth in linear polyethylene homopolymers," *Journal of Materials Science*, vol. 23, pp. 3648-3655, 1988.
- [49] P. J. Flory and A. D. Williams, "Configurational statistics of polyamide chains," *Journal of Polymer Science: Part A-2: Polymer Physics*, vol. 5, pp. 399-415, 1967.
- [50] S. Aharoni, "On entanglements of flexible and rodlike polymers," *Macromolecules*, vol. 16, pp. 1722-1728, 1983.
- [51] J.-L. Halary, F. Laupretre and L. Monnerie, *Mécanique des matériaux polymères*, Paris: Belin, 2008.
- [52] J.-L. Halary, F. Laupretre and L. Monnerie, *Polymer materials: macroscopic properties and molecular interpretations*, New York: John Wiley & Sons, 2011.
- [53] J. M. Schlutz, "Microstructural aspects of failure in semicrystalline polymers," *Polymer Engineering & Science*, vol. 24, pp. 770-785, 1984.
- [54] E. Mourglia Seignobos, "Compréhension des mécanismes physiques de fatigue dans le polyamide vierge et renforcé de fibres de verre," Ecole doctorale Matériaux, Lyon, 2009.
- [55] "Polymer Data Handbook," Oxford University Press, 1999.
- [56] P. B. Bowden and R. J. Young, "Review : Deformation mechanisms in crystalline polymers," *Journal of Materials Science*, vol. 9, pp. 2034-2051, 1974.
- [57] S. Humbert, O. Lame, J. Chenal, C. Rochas and G. Vigier, "Small strain behavior of polyethylene: In situ SAXS measurements," *Journal of Polymer Science: Part B: Polymer Physics*, vol. 48, pp. 1535-1542, 2010.
- [58] E. Mourglia-Seignobos, D. Long, L. Odoni, L. Vanel, P. Sotta and C. Rochas, "Physical mechanisms of fatigue in neat polyamide 6,6," *Macromolecules*, vol. 47, pp. 3880-3894, 2014.
- [59] A. Galeski, A. S. Argon and R. E. Cohen, "Changes in the morphology of bulk spherulitic nylon 6 due to plastic deformation," *Macromolecules*, vol. 21, pp. 2761-2770, 1988.

- [60] T. J. Bessel, D. Hull and J. B. Shortall, "The effect of polymerization conditions and crystallinity on the mechanical properties and fracture of spherulitic nylon 6," *Journal of Materials Science*, vol. 10, pp. 1127-1136, 1975.
- [61] S. Humbert, O. Lame, R. Seguela and G. Vigier, "A re-examination of the elastic modulus dependence on crystallinity in semi-crystalline polymers," *Polymer*, vol. 52, pp. 4899-4909, 2011.
- [62] C. G'Sell and J.-M. Haudin, *Introduction à la mécanique des polymères*, INPL, 1995.
- [63] Y. Chastel, "Mécanismes physique de la déformation," in *Matériaux pour l'ingénieur*, Paris, Transvalor - Presses des Mines, 2010.
- [64] L. Penel-Pierron, R. Seguela, J.-M. Lefebvre, V. Miri, C. Depecker, M. Jutigny and J. Pabiot, "Structural and mechanical behavior of nylon-6 films. Part II: Uniaxial and biaxial drawing," *Journal of Polymer Science: Part B: Polymer Physics*, vol. 39, pp. 1224-1236, 2001.
- [65] I. Hay and A. Keller, "Mechanically induced twinning and phase transformations," *Journal of Polymer Science: Part C: Polymer Symposia*, vol. 30, pp. 289-296, 1970.
- [66] J. Preedy and A. Wheeler, "A study of twinning in polyethylene," *Journal of Materials Science*, vol. 12, pp. 810-815, 1977.
- [67] P. Cerra, D. Morrow and J. Sauer, "Deformation of polypropylene single crystals," *Journal of Macromolecular Science-Physics*, vol. B3, pp. 33-51, 1969.
- [68] V. Ferreiro, Y. Pennec, R. Seguela and G. Coulon, "Shear banding in polyamide 6 filmss as revealed by atomic force microscopy," *Polymer*, vol. 41, pp. 1561-1569, 2000.
- [69] V. Ferreiro and G. Coulon, "Shear banding in strained semicrystalline polyamide 6 films as revealed by atomic force microscopy: Role of the amorphous phase," *Journal of Polymer Science: Part B: Polymer Physics*, vol. 42, pp. 687-701, 2004.
- [70] K. Nitta, "Structural factors controlling tensile yield deformation of semi-cristalline polymers," *Macromolecular Symposium*, vol. 170, pp. 311-319, 2001.
- [71] K. Nitta and M. Takayanagi, "Tensile yield of isotactic polypropylene in terms of lamellar-cluster model," *Journal of Polymer Science: Polymer Physics*, vol. 38, pp. 1037-1044, 2000.
- [72] A. Pawlak and A. Galeski, "Plastic deformation of crystalline polymers: the role of cavitation and crystal plasticity," *Macromolecules*, vol. 38, pp. 9688-9697, 2005.
- [73] A. Rozanski and A. Galeski, "Controlling cavitation of semicrystalline polymers during tensile drawing," *Macromolecules*, vol. 44, pp. 7273-7287, 2011.
- [74] A. Peterlin, "Molecular model of drawing polyethylene and polypropylene," *Journal of Materials Science*, vol. 6, pp. 490-508, 1971.

- [75] N. Murthy and D. Grubb, "Deformation of lamellar structures: simultaneous Small and Wide-Angle X-ray Scattering studies of polyamide-6," *Journal of Polymer Science: Part B: Polymer Physics*, vol. 40, pp. 691-705, 2002.
- [76] M. Ito, K. Mizuochi and T. Kanamoto, "Effects of crystalline forms on the deformation behaviour of nylon-6," *Polymer*, vol. 39, pp. 4593-4598, 1998.
- [77] M. Ito, A. Takahashi, N. Araki and T. Kanamoto, "Effects of molecular weight on the drawing and the draw efficiency of nylon-6," *Polymer*, pp. 241-248, 2001.
- [78] I. Narisawa and M. Ishikawa, "Crazing in semicrystalline thermoplastics," *Advances in Polymer Science*, vol. 91/92, pp. 353-391, 1990.

Chapter II: Experimental techniques

I.	Physico-chemical analysis	30
I.1.	Karl Fischer titration: measure of water content.....	30
I.2.	Gel Permeation Chromatography	30
II.	Microstructural analysis	31
II.1.	Optical microscopy	31
II.2.	Differential scanning calorimetry	32
II.2.1.	Protocol and experimental set up	32
II.2.2.	Crystallinity index X_c	32
II.2.3.	Estimation of α/γ ratio	33
II.2.4.	Physical ageing	33
II.2.5.	Density measurements.....	34
II.3.	Small angle X-ray scattering	35
II.3.1.	Experimental set up and data collection.....	35
II.3.2.	About the Lorentz correction	37
II.3.2.1.	Case of an isotropic system	37
II.3.2.2.	Case of a non-isotropic system, case of uniaxial system.....	38
II.3.3.	Determination of the long period L_p	39
II.3.4.	Estimation of the crystalline lamellar thickness L_c	42
II.4.	Wide angle X-ray scattering	42
II.4.1.	Experimental set up.....	44
II.4.2.	Corrections and adjustment of WAXS data.....	44
II.4.3.	Identification of PA6 crystalline phases	45
III.	Mechanical investigations	46
III.1.	Dynamic mechanical analysis	46
III.1.1.	Principle	46
III.1.2.	Experimental set up.....	46
III.2.	Monotonic tensile test	47
III.2.1.	Experimental set up.....	47
III.2.2.	Determination of the Young's modulus E	48
III.2.3.	Determination of the yield stress σ_y	49
III.3.	In-situ tensile test (ESRF).....	50
	References.....	52

The samples with various microstructures were obtained thanks to thermal treatments, which will be described in chapter III. Indeed, different thermal treatments are used in order to modify the crystalline microstructure. Two kinds of samples referred as 15K and 31K, corresponding to different molecular masses, were employed.

In the first part, the techniques to evaluate the physico-chemical analysis are described. In the second part, the employed techniques used for the microstructural analysis are listed. Several techniques have been used in combination for determining the crystalline phase and their ratio, the crystallinity index, the stacking long period of the lamellae, etc... The third part displays the techniques used for the mechanical investigations.

I. Physico-chemical analysis

I.1. Karl Fischer titration: measure of water content

The method of Karl Fischer is an analytical chemistry method for measuring the amount of water into a sample by titration. It is particularly adapted to measure very faint amounts of water in PA6 samples, as low as parts-per-million (ppm) order.

The principle is based on the oxidation of sulfur dioxide by iodine, originally observed by Robert Bunsen. A very low amount of sample is required, around 0.01 to 1 g depending on the amount of water inside the sample. Indeed, when a sample contains a high water amount, a really low quantity of sample is required in order to be more precise and also to reduce the time of analysis. On the contrary, when a sample is dry, a higher quantity of material is needed.

The titration was carried out on a Karl Fischer apparatus from Mettler society. This apparatus is associated with an oven where the PA6 samples are melted at 180°C in order to release water. It turned out that all of our samples contained less than 0.3% of water, when stored under “dry” atmosphere which allows us to say that our samples are “dry”.

I.2. Gel Permeation Chromatography

Gel Permeation Chromatography (GPC) otherwise size exclusion chromatography (SEC) is a liquid phase chromatographic method, which allows separating macromolecules as a function of their hydrodynamic volume. In the case of polymer samples, it is used to evaluate the molecular mass distribution thanks to a calibration using standard samples.

A mass of 100 mg of the polyamide 6 sample is dissolved into a solvent composed of 95% dichloromethane (DCM) and 5% trifluoroacetic anhydride (TFAA) under stirring at room temperature. After 4 hours, the solution is filtrated and injected into the 4 PLGEL MIXTE C columns of the GPC apparatus. Experiments were carried out at Solvay Analysis Department, using a PL GPC 120.

From the molecular mass distribution, the number-average molecular mass M_n and the weight-average molecular mass M_w were calculated as follows:

$$M_n = \frac{\sum_i N_i M_i}{\sum_i N_i} \quad (\text{E II.1})$$

$$M_w = \frac{\sum_i N_i M_i^2}{\sum_i N_i M_i} \quad (\text{E II.2})$$

With N_i the number of macromolecules of mass M_i ,

The dispersity index I_p is a measure of the molecular mass width of the distribution in the polymer and is defined as:

$$I_p = \frac{M_w}{M_n} \quad (\text{E II.3})$$

II. Microstructural analysis

The characterization of microstructure is of prime importance in this work. It implies several scales and mainly concerns the global morphology of the sample, the crystallinity index, the crystalline phases and the long period. However, several techniques are needed to characterize all these parameters and in this aim, they are described below.

II.1. Optical microscopy

The aim of the optical microscopy is to characterize the global crystalline microstructure and in the specific case of semi-crystalline polymers to observe or not the characteristic presence of spherulites.

Spherulites can be observed by optical microscopy benefiting from the birefringence of the crystal which is detected by means of crossed polarizers, as shown in Figure II.1a [1]. The birefringence is the difference between refractive indices measured in two different directions of the wave plane.

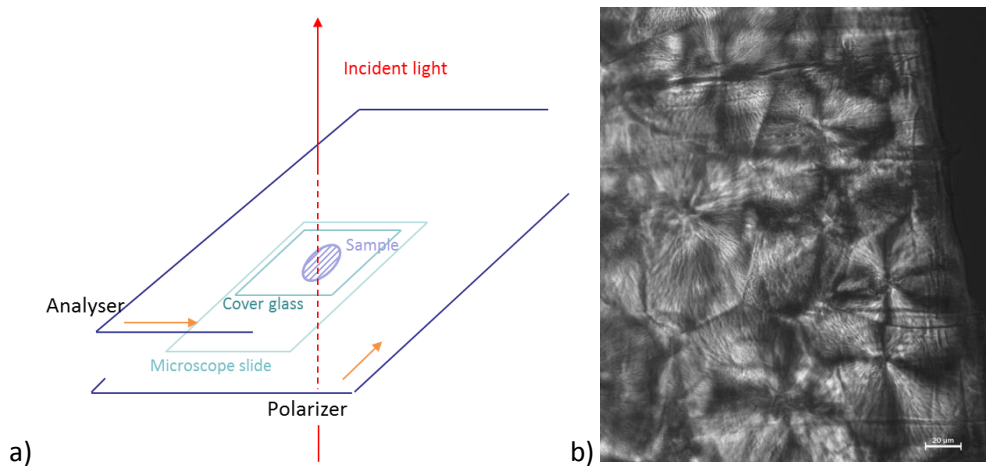


Figure II.1: a) Diagram of the optical microscopy under polarized light; b) Example of observed PA6 spherulites (right)

In practice, the observation of spherulites under polarized light in microscopy consists in transmission and extinction sectors yielding the familiar « Maltese cross », as shown in Figure II.1b.

II.2. Differential scanning calorimetry

Differential Scanning Calorimetry (DSC) is a thermoanalytical technique, used to measure crystallization temperature T_c , melting temperature T_f , glass transition temperature T_g ... It measures the difference in the amount of heat required to increase the temperature of both a sample and an empty reference as a function of temperature, both the sample and the reference following the same temperature ramp during the experiment time [2].

II.2.1. Protocol and experimental set up

The DSC Q2000 device and the analysis software 'Universal Analysis from TA Instruments were used. Experiments have been carried out according to two DSC modes:

- Standard DSC
- Modulated DSC (MDSC)

Standard DSC gives us a heat flow curve as a function of temperature. Characteristic peaks of fusion and crystallization are respectively endothermic and exothermic. What is measured is the crystallinity index (X_c). Thermal analyses were performed on samples of 5-8 mg under nitrogen atmosphere; pellets and sheets of polymers were cut, weighed and put into aluminum non-hermetic cans. The apparatus was calibrated with indium and sapphire.

The curves of fusion and crystallization were recorded between 0 and 270°C at a heating rate of 10°C/min.

As the glass transition of polyamide is hardly detectable by standard DSC, the modulated DSC (MDSC) was used instead [3]. In this case, samples were heated from -20°C to 110°C, at a heating rate of 3°C/min, with a modulation of $\pm 2^\circ\text{C}$ every 60 seconds. The glass transition temperature (T_g) is determined at the inflexion point of the heat capacity jump.

MDSC was also employed to investigate the physical ageing effect with the same temperature ramp as for the measurement of T_g . In the case of following the crystallization after melting in order to find a condition to erase memory effect, MDSC was used as well as standard DSC. However in order to correctly follow the non-isothermal crystallization which is a very fast process in the case of polyamide, this time a modulation of $\pm 0.159^\circ\text{C}$ every 60 seconds and a heating rate of 1°C/min were used.

II.2.2. Crystallinity index X_c

The crystallinity index (χ_c) is calculated from the following formula:

$$\chi_c = \frac{\Delta H_f}{\Delta H_f^0} \quad (\text{E II.4})$$

Where ΔH_f is the melting enthalpy of the material and ΔH_f^0 is the specific melting enthalpy of infinite perfect crystal. For polyamide 6, data from literature suggest the following value:

$$\Delta H_f^0 = 230 \pm 30 \text{ J.g}^{-1} \quad [4]$$

which applies to both α and γ phases [5].

As β phase transforms into α phase upon heating beyond 150°C (see chapter I §I.2.1 and §II.2.4), the β crystallinity index was determining from the melting enthalpy of α phase after transformation, using the above mentioned ΔH_f^0 value.

In order to measure the enthalpy in a same way for all samples, the integration limits of the melting endotherm were set between 190 and 240°C.

II.2.3. Estimation of α/γ ratio

As polyamide 6 is a polymorph polymer, a mixture of different phases can be observed. A common case in our study is a mixture of α and γ phases. When this kind of sample is heated in DSC, two peaks of melting are observed; each of them corresponds to a specific crystalline form owing to their different melting points. An estimation of the α/γ ratio can be done by integrating separately each peak. A typical thermogram is shown in Figure II.2, together with a schematic integration profile of the two melting peaks. The thermodynamic melting temperature of the two crystal forms is $T_m^\circ(\alpha)\approx 240^\circ\text{C}$ and $T_m^\circ(\gamma)\approx 225^\circ\text{C}$ [4]

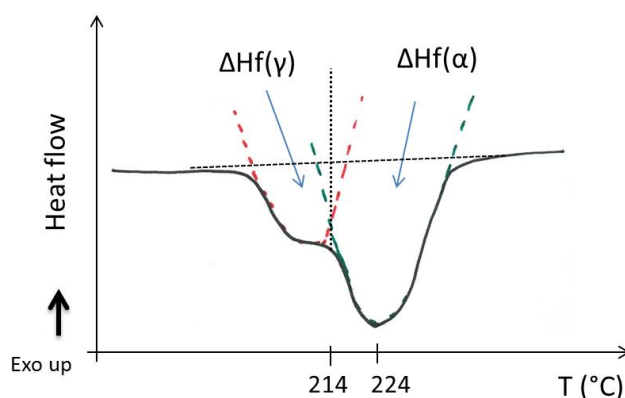


Figure II.2: Estimation of α/γ ratio by DSC mean

In Figure II.2, the γ melting endotherm spans from 190°C to 214°C [6] and the α melting endotherm from 214°C to 240°C. By integrating the various components of the DSC curve, the total crystallinity index X_c , as well as $X_c(\alpha)$ and $X_c(\gamma)$, can be assessed.

It is to be mentioned that the methodology described above could be incorrect in case of partial recrystallization of γ crystals. However, this is unlikely due to the proximity of the two endotherms. Indeed, only very unstable γ crystals exhibiting very early melting can actually recrystallize into α crystals.

In case of mixture of β and γ phases, an annealing of the β phase is performed in order to promote its transformation into α phase. Then, a similar analysis, as for the previous case of γ - α mixture, can be carried out, the amount of α phase being attributed to the initial β phase.

II.2.4. Physical ageing

Physical and chemical ageing are the two types of possible ageing. In the first case, there is no alteration of chemical structure of the macromolecule: only their spatial configuration or material compositions are affected. Concerning the second case, there is modification of the chemical structure. Only physical ageing interests us. As there is no interaction of the environment (samples are sealed into impervious bags), only processes of structural relaxations can happen [7]. Our aim is not to study physical ageing but to avoid it. Indeed, physical ageing can alter mechanical properties. MDSC is used in order to evidence it.

The total heat flow is depicted in Figure II.3. Endotherms peaks after T_g can be seen for the aged samples. Those endotherms are proof that injected samples aged.

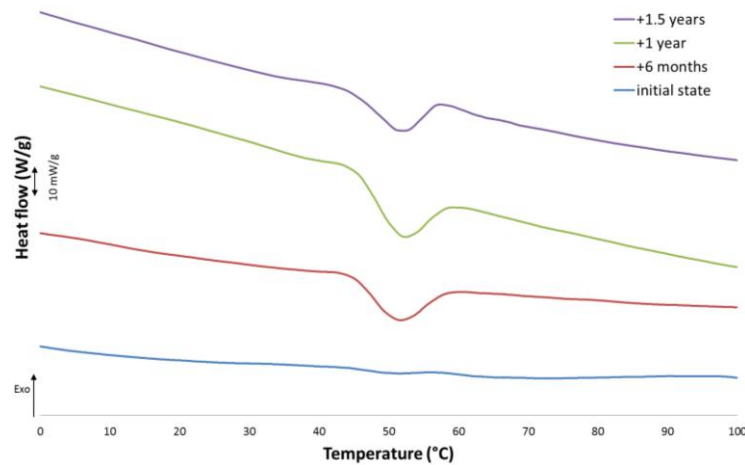


Figure II.3: MDSC total heat flow traces of injected PA6 at various ageing times

The specificity of MDSC is that the total heat flow can be divided into reversing and non reversing heat flows, allowing better separations of various thermal transitions. Reversing flows of the various samples are shown in Figure II.4a: it stands for the glass transition. Ageing acts on the distribution of the temperature of glass transition. Indeed T_g falls from 58.5°C to 52.5°C, i.e. a shift of 6°C. Non reversing heat flows are shown in Figure II.4b: the endotherms after T_g are the direct proofs that evidence physical ageing. It seems that most of the ageing happens during the first 6 months.

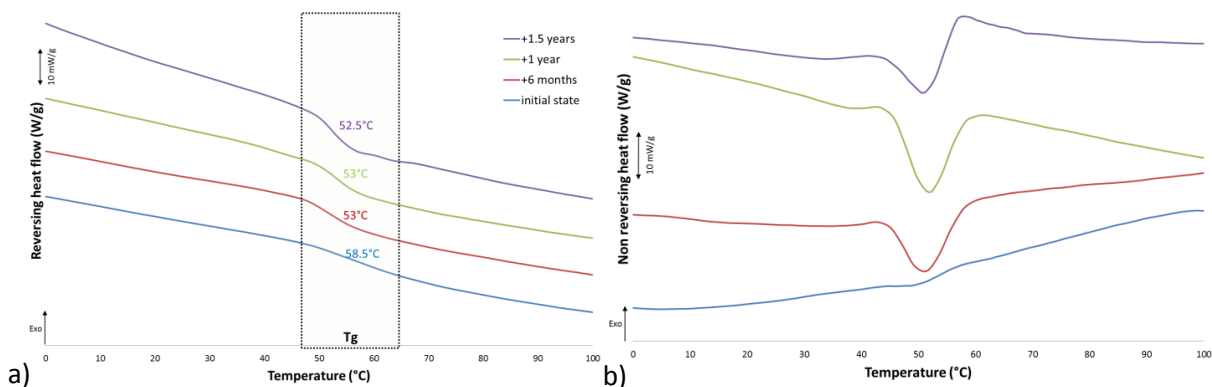


Figure II.4: MDSC a) reversing heat flow and b) non reversing heat flow of injected PA6 at various ageing times

However, as said previously, the aim is not study ageing but to assure that our samples are not aged. That is why, after thermal treatments, samples were sealed into impervious bags and put into the fridge at 5°C. MDSC tests were carried out on these samples and no ageing was checked. Concerning injected samples, they were the most sensitive to ageing but by putting them into an oven at 110°C during 10min, it was possible to suppress the ageing and rejuvenate the samples. For the following of the thesis, all the samples must be considerate as “young” (i.e. not aged) except mention.

II.2.5. Density measurements

An alternative method to evaluate the crystallinity index is based on precise measurement of the density of a given sample thanks to difference of densities of the crystalline and amorphous phases.

The density gradient column is filled with two miscible liquids of different densities. It is possible to obtain a vertical gradient calibrated with hollow glass beads having a density accuracy of 10^{-4} . The sample immersed in the column gradually drops to reach its equilibrium position in the region having the same density according to Archimedes' principle.

In our case, the density measurements were performed with a gradient column made of solutions of

- Dichloromethane $\rho_L=1.325$
- propylene-2-glycol $\rho_I=1.036$

The weight fraction crystalline index χ_c can be determined with the following formula:

$$\chi_c = \frac{\frac{1}{\rho} - \frac{1}{\rho_a}}{\frac{1}{\rho_c} - \frac{1}{\rho_a}} \quad (\text{E II.5})$$

In the case of PA6, $\rho_a=1.09 \text{ g.cm}^3$ for the amorphous density [8] and $\rho_c=1.24 \text{ g.cm}^3$ for the crystalline density of the α phase [9] and $\rho_c=1.18 \text{ g.cm}^3$ for the crystalline density of the γ phase [10].

This relationship only works for a two phase model, i.e. amorphous and crystalline phases. In case of several crystal forms, their relative proportions must be determined by an independent method. It also does not work if there is presence of an interphase between the crystalline and amorphous phases.

II.3. Small angle X-ray scattering

Small Angle X-ray Scattering (SAXS) are used to characterize the crystalline morphology at the scale of crystalline lamellar stackings in semi-crystalline polymers. The periodicity (so-called long period) of crystalline lamella stackings can be measured, as well as the possible anisotropy (orientation) of the morphology. In some circumstances, the size of crystalline lamellae may be estimated. The geometry of the experiment is schematized in Figure II.5.

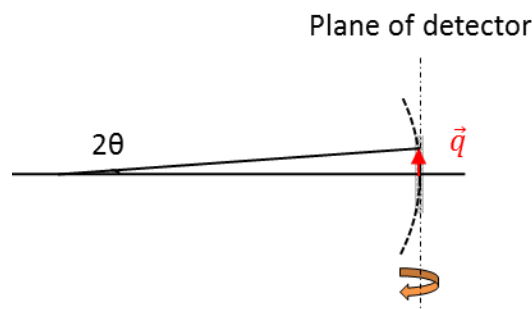


Figure II.5: SAXS conditions: \vec{q} is in the plane of the detector

II.3.1. Experimental set up and data collection

The scattered intensity is collected on a 2D detector. In the small angle limit, \vec{q} is within the plane of the detector. The range of accessible scattering vectors q (or equivalently of scattering angles 2θ) is determined by choosing the sample-to-detector distance D : q_{max} is given by $\sin 2\theta_{max} \approx d/D$ (d : radius of the detector) while q_{min} is given by the radius of the beam stop.

SAXS experiments were performed both at the MATEIS laboratory and at the D2AM beamline at ESRF (European Synchrotron Radiation Facility, Grenoble). The laboratory apparatus at MATEIS is equipped with an RU-300 X-ray generator with rotating Cu anode (CuK α radiation, wave length $\lambda=1.54 \text{ \AA}$) and a CCD camera from Princeton Instrument. The sample to detector distance is 60 cm. The patterns were obtained with an accumulation time of 10 min. This equipment was used for the characterization of the samples described in chapter III, as obtained from the various thermal treatments.

In-situ tensile tests at a constant drawing rate with simultaneous SAXS acquisition require a significantly shorter accumulation time. These experiments were done at D2AM beamline (ESRF). The setup is equipped with a CCD camera from Princeton Instrument. The chosen wavelength λ was 1.54 \AA corresponding to 8keV energy. The sample-detector distance was about 90 cm, the radius of the detector is 3 cm, the size of the beam stop is 1.5 mm, which gives access to a q range from 0.1- 1.51nm^{-1} .

The collected raw 2D SAXS pattern must be corrected from detector imperfection and background. The corrected intensity I is corrected as follows:

$$I = \frac{I_S - \mu \cdot I_F}{\mu \cdot e} \times q^2 \quad (\text{E II.6})$$

where I_S is the raw measured intensity, I_F the measured intensity in the absence of sample (empty beam pattern), μ the coefficient of transmission of the sample (the ratio of X-ray photon counters after and before the sample), and e the thickness of the sample. The thickness e varies during tensile tests. For small strain values $\varepsilon < 1$, the thickness e varies according to the following equation:

$$e = e_0(1 - \nu\varepsilon) \approx e_0\lambda^{-\nu} \quad (\text{E II.7})$$

With e_0 the initial thickness of the sample,
 $\lambda = 1 + \varepsilon$ the drawing ratio
 and ν the Poisson coefficient, taken equal to 0.39 [11].

The scattering vector q is defined as a function of the scattering angle 2θ as (see Figure II.10 raw data):

$$q = \frac{4\pi}{\lambda} \sin \theta \quad (\text{E II.8})$$

The q scale on the 2D pattern is precisely calibrated using a reference sample, in our case silver behenate (BeAg) whose narrow scattering ring has a perfectly known position ($d=2\pi/q=58,33\text{\AA}$). Given that, in SAXS, the scattering angle is very small, the scattering vector \vec{q} is in the plane of the detector (see Figure II.5) and no further geometrical correction is needed.

For isotropic samples, the intensity $I(q)$ as a function of the scattering vector q is obtained by averaging the 2D SAXS pattern over all azimuthal angles ψ . This is the so-called 'regrouping' of the data. For anisotropic samples, the scattering is modulated as a function of the azimuthal angle, and the intensity $I(q)$ must be calculated for each angle ψ in order to allow an analysis of the azimuthal distribution. In this case, the 2D pattern files were divided into 72 sectors of 5° and the intensity was averaged in each sector.

II.3.2. About the Lorentz correction

The general problem which is addressed here is to determine or reconstruct the orientation distribution of scattering objects (for example, stacks of amorphous/crystalline lamellae) from the measured intensity pattern.

Let us consider a system made of an ensemble of identical uniaxial scattering objects, for example, stacks of amorphous/crystalline lamellae, which are defined uniquely without ambiguity by the orientation of their normal vectors \vec{n} . The number $dn(\Omega)$ of objects oriented within a solid angle $d(\Omega)$ is $dn(\Omega) = D(\vec{n})d\Omega$. This is the definition of the distribution of orientation $D(\vec{n})$.

The corresponding distribution of intensity in the reciprocal space is:

$$i(\vec{q}) \approx i_0(q) \frac{D(\vec{n})}{4\pi q^2} \quad (\text{E II.9})$$

in which the vector \vec{q} is in the same direction as \vec{n} since objects (lamellar stacks) scatter in the direction of their normal \vec{n} (this is imposed anyway by their assumed uniaxial symmetry). There is of course a proportionality coefficient (not indicated here) related to the overall sensitivity of the experimental setup. $4\pi q^2$ represents the surface area of the sphere of radius q . Separation in one factor $D(\vec{n})$ depending only on the orientation \vec{n} and one factor $i_0(q)$ depending only on q holds only if all objects are identical (but with different orientations). It is no longer valid if, for instance, the long periods of the lamellar stacks vary as a function of their orientation, which will actually be the case in stretched samples. This more general case will be discussed below.

II.3.2.1. Case of an isotropic system

Let us first consider the case of an isotropic system. Scattering objects (for example, stacks of amorphous/crystalline lamellae) are oriented randomly, isotropically in all directions. Then, in the reciprocal space, the intensity is distributed uniformly on a sphere. It depends only on $q = \|\vec{q}\|$ and not on the orientation of \vec{q} .

The detected intensity comes from objects which are in Bragg condition, or equivalently, it corresponds to the intersection of the reciprocal space with the Ewald sphere, which, in the small angle limit, is the same as the plane of the detector, as shown in Figure II.6. The relative number of objects which are in Bragg conditions depend on \vec{q} , this is why this so-called 'Lorentz' correction is needed. Let us denote ξ the 'thickness' of the Ewald sphere (related essentially to the dispersion in wavelength $\delta\lambda/\lambda$ of the incident beam).

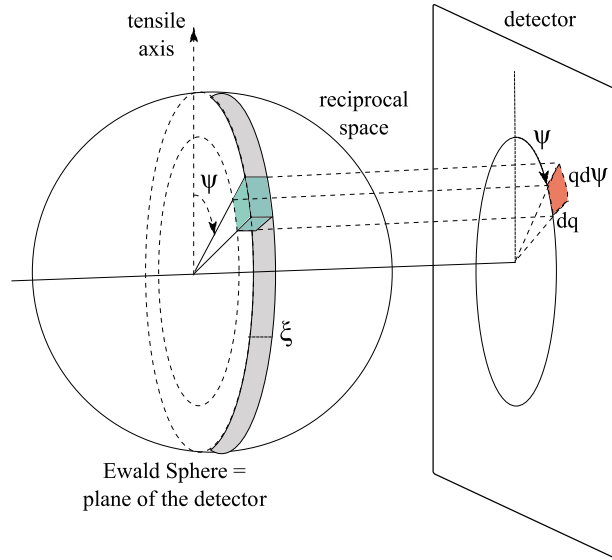


Figure II.6: The fraction of reciprocal space which is detected corresponds to scattering elements (lamellar stacks) which are in Bragg conditions. In other words, the detected intensity corresponds to the intersection of the reciprocal space by the Ewald sphere, depicted here as a plane of thickness ξ (in grey on the scheme). This fraction depends on q .

The total collected intensity (number of photons) in a small zone of the detector defined by $q \rightarrow dq$, $\psi \rightarrow d\psi$ (where ψ is the azimuthal angle in the plane of the detector) is (see Figure II.6):

$$d^2 I_{mes}(q) = i(q) \xi q dq d\psi \quad (\text{E II.10})$$

$d^2 S = q dq d\psi$ is a small surface element in the plane of the detector (in polar coordinates). $i(q)$ is the 'density' of intensity in the reciprocal space (for an isotropic system, it depends only on q , or equivalently, it is a constant for a given value of q). $i(q)$ is given by Eq. II.9.

The measured intensity in the detector (number of photon per pixel at position of the surface element dS) is thus (combining Eqs. II.9 and II.10):

$$I_{mes} \approx \frac{d^2 I_{mes}(q)}{dS^2} \approx \frac{i(q)}{q^2} \quad (\text{E II.11})$$

and $i(q)$ is recovered by taking the corrected measured intensity $q^2 I_{mes}(q)$. It is $i(q) \approx q^2 I_{mes}(q)$ which contains the 'true' information on the structure of the sample.

II.3.2.2. Case of a non-isotropic system, case of uniaxial system

We consider here only the case when the symmetry axis of the system (tensile direction) is perpendicular to the incident beam direction. In a non-isotropic system, the "cloud" of the intensity in the reciprocal space can no longer be expressed in a separate way $I_0(q)D(\vec{n})i_0(q)$ as in Eq. II.9. This does not change Eq. II.11, except that $i(q)$ depends now on both the modulus q of the scattering vector and on its orientation.

For a uniaxial system, $i(\vec{q})$ has a cylindrical symmetry, it depends on q and on the polar angle ψ with respect to the direction of symmetry (e. g. the tensile direction in case of a uniaxially stretched system). Note that, since \vec{q} is in the plane of the detector, the polar angle ψ between \vec{q} and the tensile direction is identical to the azimuthal angle ψ in the plane of the detector. This will not be

strictly the case in WAXS (see below). $i(\vec{q})$ is related to the number $D(\vec{n})$ of lamellae which have their normal at \vec{n} (in the same direction as \vec{q}):

$$i(\vec{q}) \approx \frac{D(\vec{n})}{q^2} \quad (\text{E II.12})$$

The number of lamellae oriented in the solid angle $d\Omega = \sin \psi d\psi d\varphi$ in the direction \vec{n} defined by the polar angle ψ and the meridian angle φ is $dn(\psi, \varphi) = D(\vec{n})d\Omega$.

Given the cylindrical symmetry, the orientation distribution $D(\vec{n})$ does not depend on the meridian angle φ . The orientation distribution is conveniently described by the number of lamellar stacks within the interval $[\psi, \psi + d\psi]$, given by $n(\psi)d\psi = 2\pi D(\vec{n})\sin \psi d\psi$. It is $n(\psi)$ which contains the relevant information on the system anisotropy. We need here to determine $n(\psi)$ from the measured intensity $I_{mes}(\psi)$:

$$n(\psi) = q^2 I_{mes}(q, \psi) \sin \psi \quad (\text{E II.13})$$

One should be careful not to confuse the intensity $i(\vec{q})$ (or equivalently the orientation distribution $D(\vec{n})$) as expressed in Eq. II.9 and the uniaxially averaged distribution $n(\psi)$ as expressed in Eq. II.13. In case of uniaxial system (with axis of symmetry perpendicular to incident beam direction) $n(\psi)$ is related to $i(\vec{q})$ by $n(\psi) = \sin \psi i(\vec{q})$ (where ψ is the polar angle of \vec{q}).

II.3.3. Determination of the long period L_p

The scattered intensity contains two distinct contributions (see the so-called raw data curve in Figure II.10). First, there is some increase of intensity as the scattering vector q tends to zero. This is associated to large scale inhomogeneities in the samples. Then, a semi-crystalline polymer is composed of lamellae stacks. Each lamellar stack scatters in the plane containing its normal as shown in Figure II.7a. Regular stacking gives rise to an interference with maximum $q = 2\pi/L_p$ where L_p is the stacking long period. Owing to the random distribution of the stacks in the material, the overall scattering result is a uniform SAXS ring, as depicted in Figure II.7b.

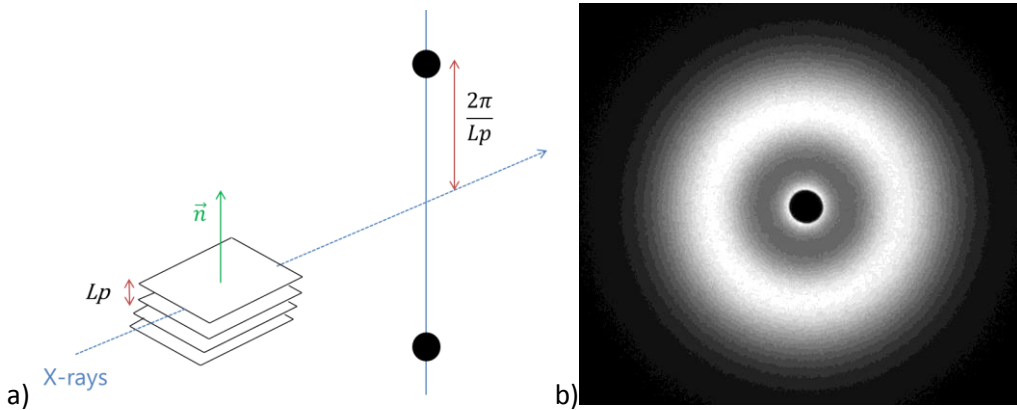


Figure II.7: a) Correspondence between lamellar stacks and L_p in SAXS; b) Example of PA6 SAXS pattern taken at 23°C

To model the intensity in the ring, various contributions must be taken in to account. The intensity scattered by a periodic structure is the product of the form factor of the unit cell and the peaks associated to the periodic lattice:

$$I(q) = F(q)P(q) \quad (\text{E II.14})$$

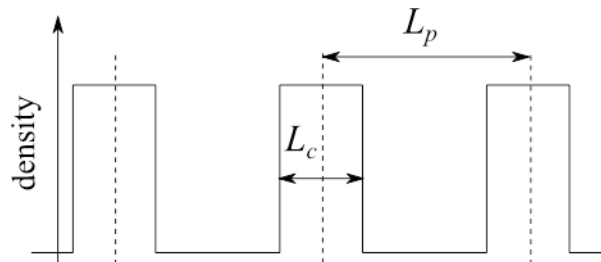


Figure II.8: The density modulation in a lamellar stack.

The unit cell is the stacking of a crystalline and an amorphous lamella. To estimate the form factor, the corresponding density may be modeled by a step function as schematized in Figure II.8. This gives the following form factor (normalized to one as $q \rightarrow 0$):

$$F(q) = \frac{\sin^2\left(\frac{qL_c}{2}\right)}{\left(\frac{qL_c}{2}\right)^2} \quad (\text{E. II.15})$$

The lattice function gives peaks at $q = m2\pi/L_p$ (m integer).

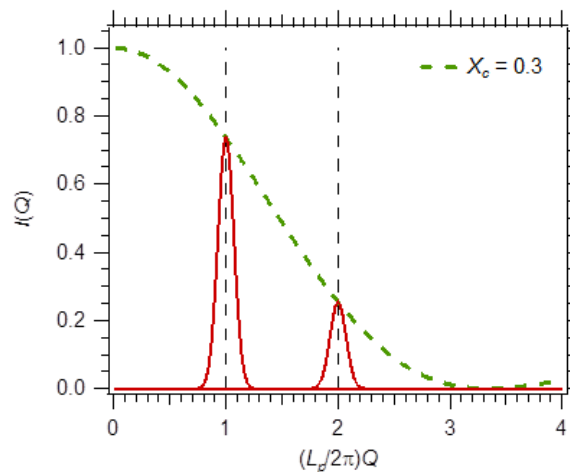
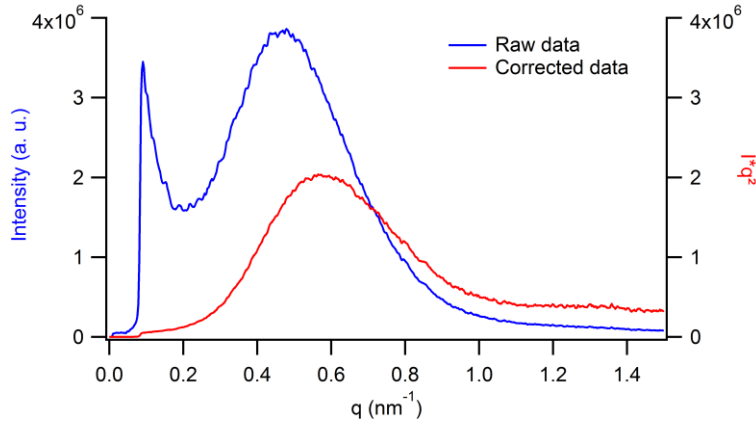


Figure II.9: Peaks correspond to the lattice function; L_p is the period of the lamellar stacking. The dashed curve is the form factor of the crystalline lamella (calculated here for crystallinity $L_c/L_p = 30\%$), which modulate the intensity of the peaks.

In practice, only the first order peak at $q = 2\pi/L_p$ is observed and it is very broad (see Figure II.9). L_c may deduced from L_p assuming that the crystalline ratio L_c/L_p within the lamellar stack is equal to the overall average crystallinity of the sample, as measured from DSC, which is a strong assumption however.

The broadness of the peak indicates that the crystalline order of lamellar stackings is imperfect. This may be due to:

- The small size of lamellae;
- The relatively large fluctuations of the distance L_p ;
- The presence of a relatively high density of defects, etc.


 Figure II.10: Raw and corrected intensities a function of the scattering vector q

Thus, we did not attempt to fit using a form factor. However, in order to extract quantitative information, namely the variation of the long period as a function of the macroscopic strain and of the azimuthal angle, as well as the variation of the intensity as a function of the azimuthal angle for a given strain value, we need to fit the peak. We have chosen to use an empirical function. Thus, the Lorentz-corrected intensity is plotted as a function of the scattering vector q , as shown in Figure II.10 (corrected data) and the peak is fitted with a log-normal function:

$$f(q) = I_0 + \frac{A}{qw\sqrt{\pi}} \exp\left(-\left(\frac{\ln q/q_{max}}{w}\right)^2\right) \quad (\text{E II.16})$$

The amplitude of the peak (integrated intensity) is given by the parameter A (I_0 was set to zero). An example of fit is shown in Figure II.11.

The long period is computed as:

$$Lp = \frac{2\pi}{q_{max}} \quad (\text{E II.17})$$

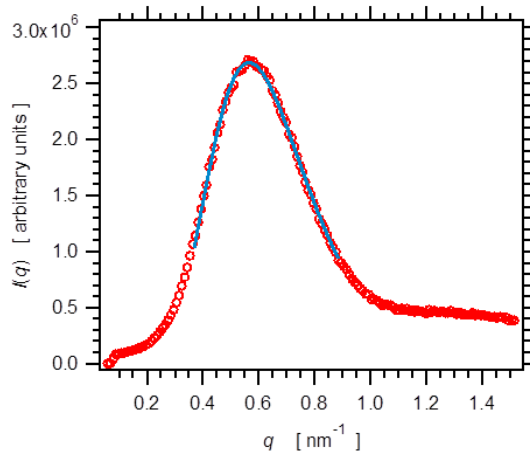


Figure II.11: Example of experimental points (red circles) fitted by the log-normal function of Eq. II.16 (blue curve)

II.3.4. Estimation of the crystalline lamellar thickness L_c

The crystalline lamellar thickness L_c can be estimated with the following relation which assumes very large and long lamellae as compared to their thickness:

$$L_c = L_p \times \frac{\rho}{\rho_c} \times \chi_c \quad (\text{E II.18})$$

With L_p , the long period as determined previously with SAXS

ρ , the density of the material

$\rho_c = 1.235 \pm 005 \text{ g.cm}^{-3}$, the density of the crystalline phase

χ_c , the crystallinity index determined by DSC

The density of the material can be calculated as follow:

$$\frac{1}{\rho} = \frac{\chi_c}{\rho_c} + \frac{1 - \chi_c}{\rho_a} \quad (\text{E II.19})$$

With $\rho_a = 1.009 \pm 001 \text{ g.cm}^{-3}$, the density of the amorphous phase of PA6

This allows estimating L_c for PA6 in the assumption that all the amorphous phase is distributed within the lamellae stacks. Some evidence has been given that part of the amorphous phase is located around the stacks so that L_c is actually underestimated [12].

II.4. Wide angle X-ray scattering

Wide Angle X-ray Scattering (WAXS) gives information at the scale of the crystalline unit cell. It allows identifying structural and crystalline phases, measuring crystalline parameters, crystalline index, and in some cases the crystallite size. When a material is stretched, information on the distribution of orientation of crystal lattice planes may be obtained.

A graphical representation of X-ray diffracting from crystal planes is shown in Figure II.12. Diffracted beams interfere constructively when the following relation is satisfied:

$$2d \sin \theta = n\lambda \quad (\text{E II.20})$$

Where n is an integer, λ is the wavelength of incident wave (X-ray radiation), d is the spacing between the planes in the atomic lattice and θ the angle between the incident ray and the scattering planes. This is the Bragg's law, which is the basic relation in X-ray scattering. The angle between the incident beam and the diffracted beam is 2θ . Thus, for a given family of periodic crystal planes, only the directions defined by the angle θ given by Bragg's law give scattering. This ensemble of directions is called the reciprocal space of the given family of planes.

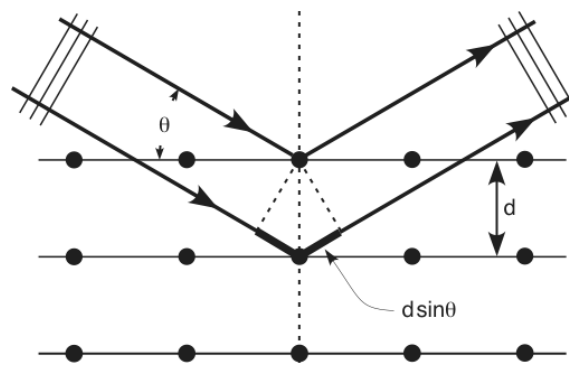


Figure II.12: Graphical representation of X-ray diffracting from crystal planes

The scattering vector \vec{q} is defined as $\vec{q} = \vec{k} - \vec{k}_0$, where \vec{k}_0 and \vec{k} are the wave vectors of the incident and diffracted beams respectively. The ensemble of all possible wave vectors is called the Ewald's sphere (Figure II.13).

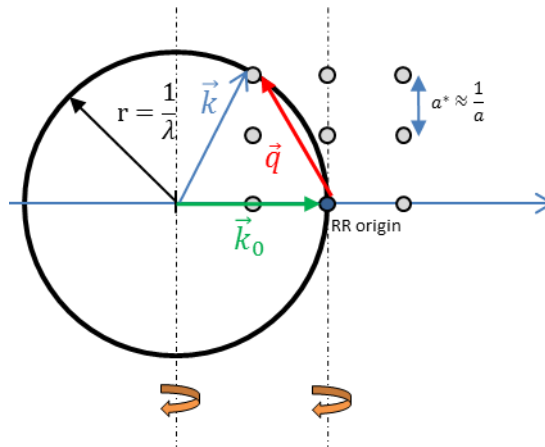


Figure II.13: Construction of Ewald's sphere where $\vec{q} = \vec{k} - \vec{k}_0$

Finally, the condition of diffraction is that directions satisfying the Bragg's law (i.e the reciprocal space) must correspond to possible scattering vectors (i.e. the Ewald's sphere), which gives the so-called Ewald construction [13] (Figure II.13). Indeed, it allows determining graphically which nodes of the reciprocal lattice (RR), i.e. the families of crystalline planes given diffraction, as depicted in Figure II.13. All hkl nodes of the RR, meeting the Ewald's sphere ($r = 1/\lambda$) answer to Bragg's law (Eq. II.20). In a crystal lattice, planes are denoted by their Miller indices (see Figure II.14).

For a monoclinic lattice, it is possible to index the spots of WAXS with the corresponding planes thanks to the following formula:

$$\frac{1}{d_{hkl}} = \sqrt{\frac{h^2}{a^2 \sin^2 \beta} + \frac{k^2}{b^2} + \frac{l^2}{c^2 \sin^2 \beta} - \frac{2hl \cos \beta}{ac \sin^2 \beta}} \tag{E II.21}$$

With d_{hkl} the distance between planes of the crystalline lattice
 h, k and l: indices of Miller
 a, b, c : parameters of lattice, $a=9.56 \text{ \AA}$, $b=17.24 \text{ \AA}$ and $c=8.01 \text{ \AA}$ [9]
 β the angle of lattice, $\beta=112.5^\circ$ [9]

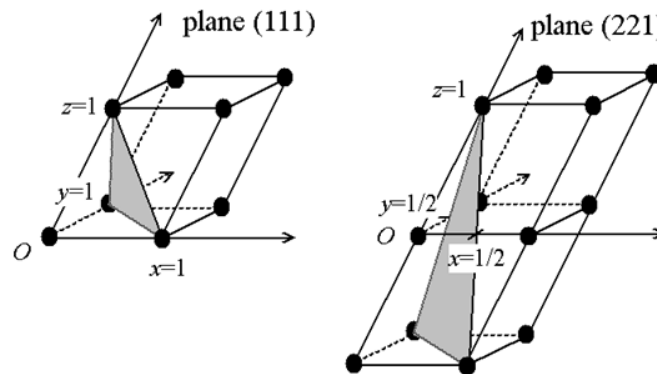


Figure II.14: Miller's indices (hkl) of a family of planes.

The detected intensity is projected on the plane of the detector. In WAXS, the vector \vec{q} is not contained in the plane of the detector. As a result, the problem of reconstructing orientation

distribution from scattering patterns is quite complex (see for instance [14]). This difficulty comes from the fact that only a limited part of the reciprocal space, corresponding to a circle which does not intersect the reciprocal space along a meridian circle, is detected as depicted in Figure II.15. In SAXS conditions (see above), this problem simplifies because \vec{q} is in the plane of the detector (to a very good approximation) and thus a meridian plane is detected, as depicted in Figure II.5.

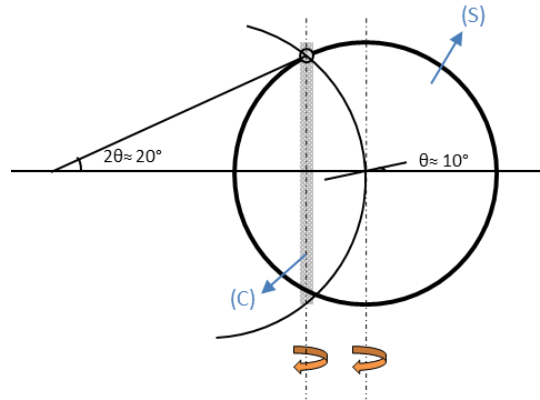


Figure II.15: It is the distribution of intensities in all directions in the reciprocal space (i.e. on the whole sphere (S)) which gives the full information on the distribution of orientation of objects in the real space. This distribution of intensity must be inferred from the measured intensity, which is only the circle (C).

II.4.1. Experimental set up

The same experimental set up was used (see §II.3.1). Concerning static experiments, the sample-detector distance was 5cm in order to obtain 2θ observation range from 5° to 35° for $\lambda=1.54 \text{ \AA}$. The patterns were obtained with an accumulation time of 5 min.

At ESRF, the chosen wavelength was 0.55 \AA corresponding to 24keV energy. The sample-detector distance was enough short in order to also obtain 2θ observation range from 5° to 35° calculated for $\lambda=1.54 \text{ \AA}$.

II.4.2. Corrections and adjustment of WAXS data

The same kinds of files, as SAXS data, were generated. WAXS patterns consist of plotting intensity as a function of 2θ . Nevertheless, as for SAXS, the data concerning intensity need correction, as follow:

$$I = \frac{I_S - \mu \cdot I_F}{\mu \cdot e} \quad (\text{E II.22})$$

Indeed, the collected data are already corrected from all noises, electronic noise specific to the detector (white noise) and noises due to the cumulated signal of direct beam and to the diffusion of air and kapton (dark noise).

Concerning the position of the peaks in WAXS patterns, they were adjusted thanks to a reference. The reference used is a sample of polyoxymethylene (POM) whose diffraction ray ($2\theta=22.16^\circ$) is perfectly known. With this reference, we can determine the distance between the sample and the detector and so adjust the position of the peaks.

II.4.3. Identification of PA6 crystalline phases

The representation of the WAXS patterns of the different crystalline phases is shown in Figure II.16.

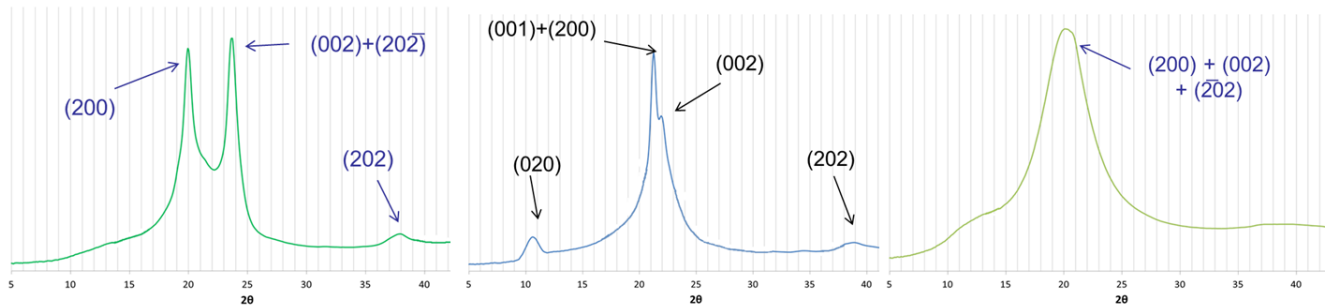


Figure II.16: PA6 crystalline phase patterns as observed by WAXS at 23°C: α , γ and β phases (from left to right)

The atomic planes are identified for each of the peaks of the different phases. Atomic planes are indicated in Figure II.17. The values of 2θ angles are listed in Table II.1.

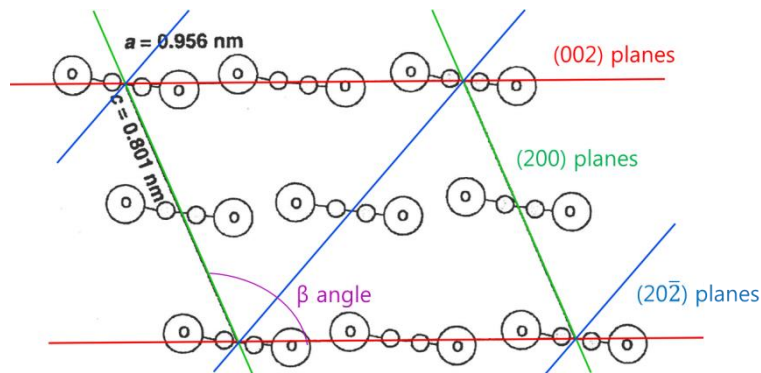


Figure II.17: Schematics of the lattice planes for the α phase, associated to the main peaks in the diffraction pattern shown in Figure II.16

Table II.1: 2θ values for PA6 crystalline phases as observed in WAXS patterns

	α	γ	β
Bragg index ($\lambda=1.542$)	(200) $2\theta=20.21^\circ$	(200) $2\theta=21.69^\circ$	(200) $2\theta=21.66^\circ$
	(002) $2\theta=23.09^\circ$	(002) $2\theta=22.23^\circ$	(002) $2\theta=21.66$
	(20 $\bar{2}$) $2\theta=24.36^\circ$	(202) $2\theta=38.73^\circ$	($\bar{2}02$) $2\theta=21.34^\circ$ (large)
	(202) $2\theta=37.36^\circ$	[10]	[16]
	[15]	(020) $2\theta=10.47^\circ$	
		(001) $2\theta=21.66^\circ$	
		[16]	

It is easy to differentiate α phase from γ phase. However it is more complicated to identify γ phase from β phase except for $2\theta=10.5^\circ$ which is present only in γ phase. For our study we have samples which are a mix of different phases. In this case, the help of DSC is also used as described in the previous paragraph II.2.3.

III. Mechanical investigations

In order to understand the deformation mechanisms and how they rule the macroscopic behavior in relation to the semi-crystalline microstructure, several techniques used for mechanical investigations were used. They are described below as well as the employed protocols.

III.1. Dynamic mechanical analysis

III.1.1. Principle

Dynamic mechanical spectroscopy (DMA) allows studying the viscoelastic properties of a material by measuring its dynamical modulus as a function of temperature. The sample is submitted to a sinusoidal strain of the form:

$$\varepsilon^* = \varepsilon_0 \exp(i\omega t) \quad (\text{E II.23})$$

In the linear stress-strain regime, the sinusoidal stress response displays a retardation phase angle φ such as:

$$\sigma^* = \sigma_0 \exp(i\omega t - \varphi) \quad (\text{E II.24})$$

The complex dynamical modulus G^* is defined by:

$$G^* = G' + iG'' \quad \text{with} \quad G' = \frac{\sigma_0}{\varepsilon_0} \cos \varphi \quad \text{and} \quad G'' = \frac{\sigma_0}{\varepsilon_0} \sin \varphi$$

$$\tan \varphi = \frac{G''}{G'} \quad \text{and} \quad |G| = \sqrt{G'^2 + G''^2} \quad (\text{E II.25})$$

G' is named the elastic or storage modulus whereas G'' is named the viscous or loss modulus.

The phase angle between the stress and the strain allows determining the coefficient of internal friction ($\tan \varphi$), representing the dissipated energy as a form of heat over the elastic energy used. $\tan \varphi$ defines the loss factor.

III.1.2. Experimental set up

Tests have been carried out on a home-made torsion pendulum, as depicted in Figure II.18. Dumbbell specimens have been cut from molded sheets with a cutting die. The type of dumbbell is H3, with a gauge length of 17 mm, a width of 4 mm and a thickness from 1.4 to 1.8 mm depending on the samples. Measurements have been performed at 1Hz frequency, using a temperature ramp from -170°C to 200°C at a heating rate of 1°C/min.

Absolute values of G' and G'' are not really precise but this technique allows to follow their evolution as a function of temperature. Furthermore, by following $\tan \varphi$ during the temperature ramp, DMA is able to evidence α , β and γ relaxations (not to be mingled with crystalline phases).

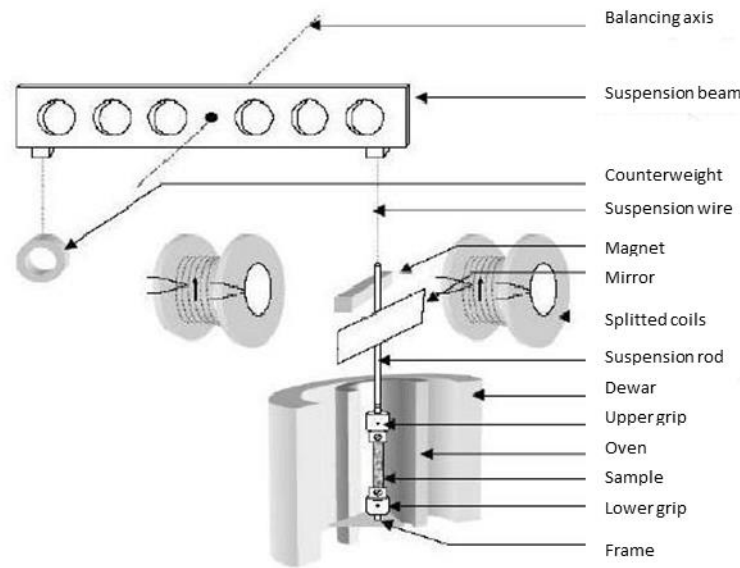


Figure II.18: Scheme of the torsion pendulum built at MATEIS [17]

III.2. Monotonic tensile test

III.2.1. Experimental set up

Uniaxial macroscopic tensile tests have been carried out on a Schenck device with a load cell of 5 kN. The same samples H3 were used, as described above.

Tensile tests were performed at a controlled crosshead speed of 3 mm/min corresponding to an initial strain rate of $3 \cdot 10^{-3} \text{ s}^{-1}$, until failure of the specimen.

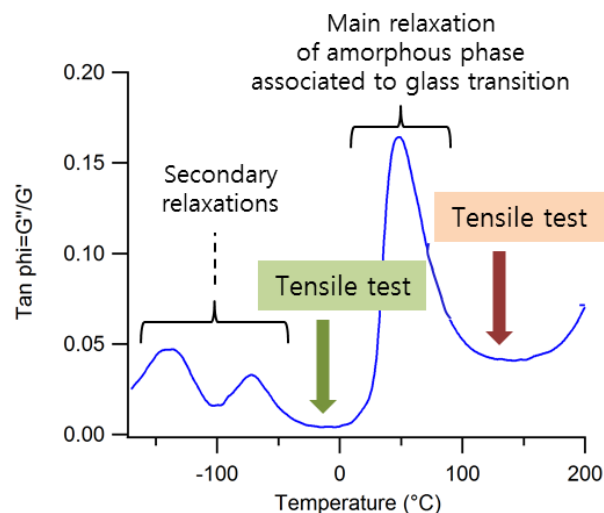


Figure II.19: Temperature choice for the tensile tests of PA6 according to the $\tan \varphi=f(T)$ damping curve at 1Hz

In order to get an insight on the influence of the state of the amorphous (i.e. glassy or rubbery), tests were carried out at temperatures below and above the glass transition. Thanks to the DMA data of Figure II.19, the choice made was for -10°C ($= T_g - 65^\circ\text{C}$) and 120°C ($= T_g + 65^\circ\text{C}$), i.e. at the location of

the minima of the $\tan \varphi$ curve on both sides of the main amorphous phase relaxation. This choice enables minimizing energy dissipation as compared to elastic behavior in both situations. The machine was equipped with a temperature chamber fed by liquid nitrogen for the cold temperature experiments.

The recorded stress-strain curves allowed determining the yield stress σ_y and the Young modulus E thanks to Imetrum system. The determination of these two parameters is now described.

III.2.2. Determination of the Young's modulus E

The Imetrum video gauge (IVG) system was employed in order to determine the Young's modulus. It consists in a non-contact precision measurement by means of a video camera and a specific software, as shown in Figure II.20a. Pattern recognition and sub-pixel interpolation enable the exact location of a user-defined target in the image. Targets are first selected by the user as seen in Figure II.20b and are then tracked in real time, outputting measurements frame-by-frame. This technology allows multi-point measurements of strain, rotation and displacements. The principles involved in this technique are often referred to as Digital Image Correlation (DIC).

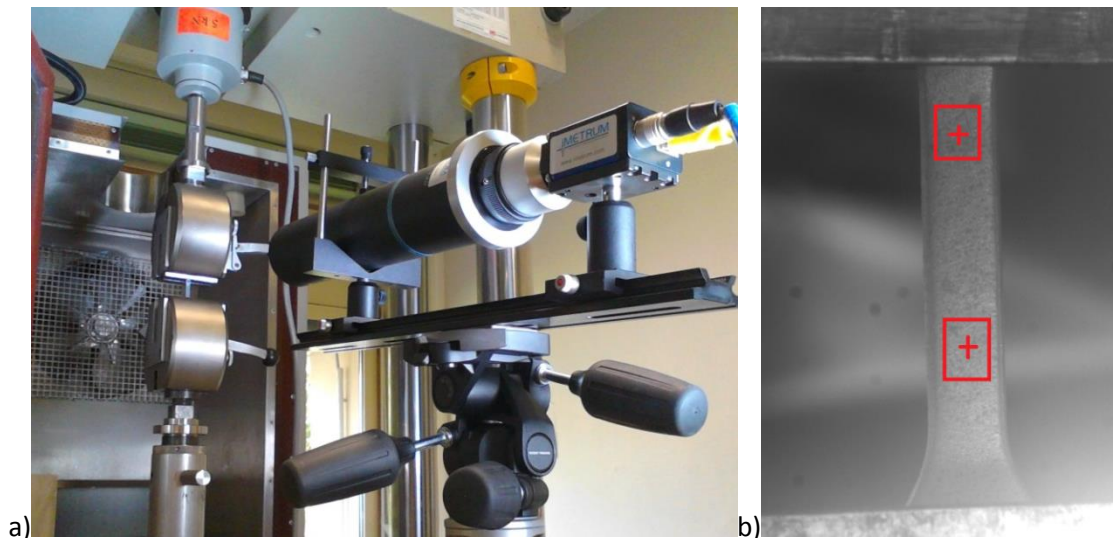


Figure II.20: a) Tensile test with Imetrum device ; b) Targets system for the displacement measurement

In our case, measurements have been restricted to vertical and transversal displacements, in order to determine the tensile strain and the Poisson's coefficient ν . For each sample, two measurements defined by two sets of targets were done. The software has a voltage input/output mode that was used to record the load given by the Schenck device. This was possible after having made a calibration in order to have equivalence between voltage in volts and load in newtons. This output mode allows synchronizing between Imetrum and Schenck devices.

Finally when we record a tensile test, it gives us a strain-stress curve for a deformation domain of maximum 10% as depicted in Figure II.21.

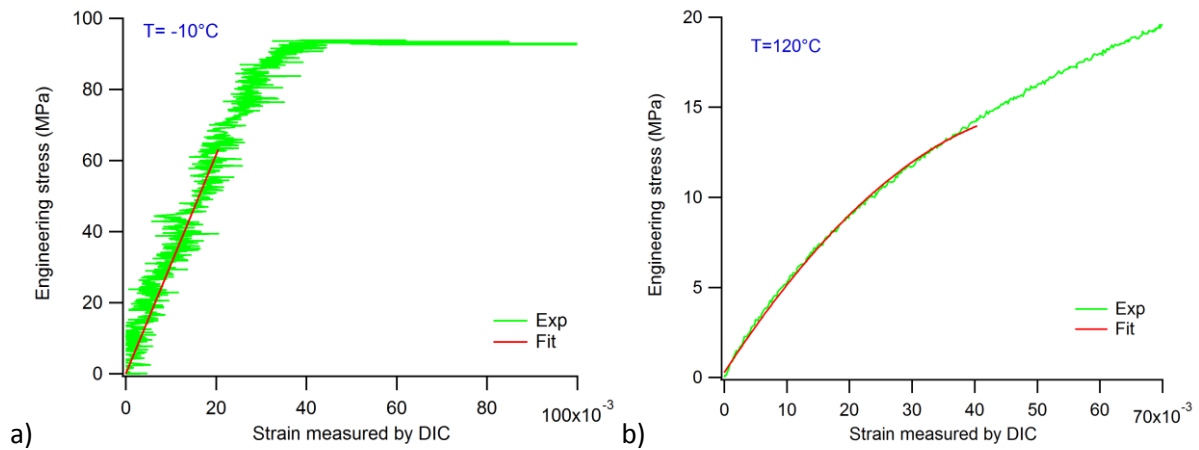


Figure II.21: Stress-strain curves obtained by DIC a) at -10°C and b) at 120°C ; red line holds for the fitting procedure for the E determination (see text for details)

For $T = -10^{\circ}\text{C}$ (Figure II.21a), the Young’s modulus was determined with a linear fit “ $K1 x$ ” on the strain domain $[0-0.02]$. The coefficient $K1$ gives the Young’s modulus. The noise is due to the low resolution of the high focal camera.

In the case of $T=120^{\circ}\text{C}$ (Figure II.21b), the Young’s modulus was determined with a second order polynomial regression $K0 + K1 x + K2 x^2$ on the strain domain $[0-0.04]$. The coefficient $K1$ (slope at the origin) was taken as the Young’s modulus value. The use of the camera with short focal allowed a better resolution.

III.2.3. Determination of the yield stress σ_y

The determination of the yield stress σ_y from the stress-strain curves was different for the two tensile test temperatures as shown in Figure II.22. The initial strain rate was 3.10^{-3} s^{-1} in all cases.

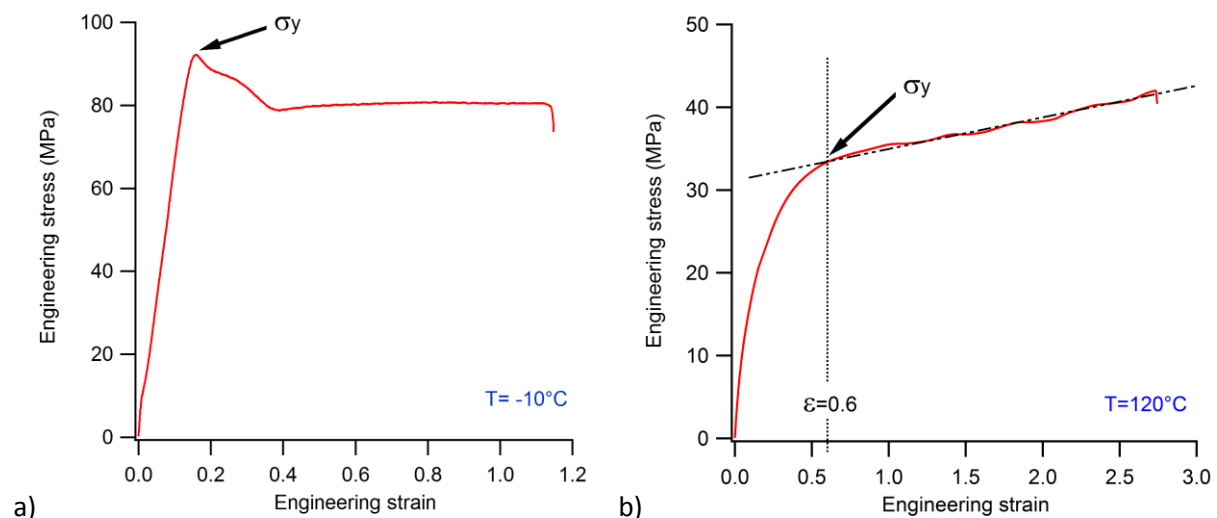
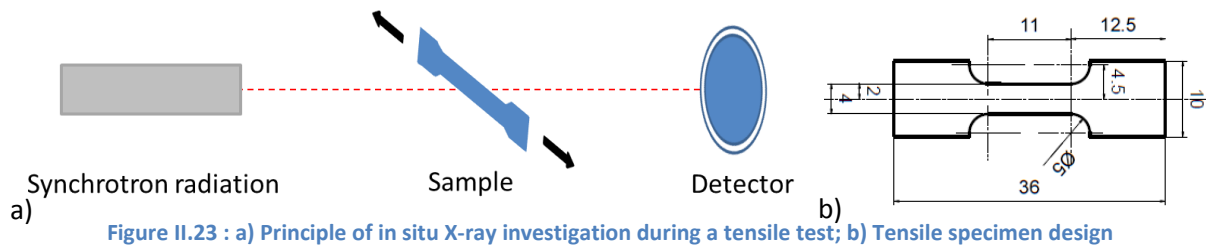


Figure II.22: Stress-strain curves obtained with Schenck device at a) $T=-10^{\circ}\text{C}$ and b) $T=120^{\circ}\text{C}$

In the case of $T = -10^{\circ}\text{C}$ (Figure II.22a), the yield stress is well defined at the maximum stress. However, for the case of $T=120^{\circ}\text{C}$ (Figure II.22b), no clear maximum was observed, so that the stress corresponding to an arbitrary strain of 0.6 was taken as the yield stress value.

III.3. In-situ tensile test (ESRF)

The tests were carried out on D2AM beam at European Synchrotron Radiation Facility (ESRF) at Grenoble (see §II.3.1 and §II.4.1). The aim of the experiments was to perform a tensile test and to take WAXS and SAXS patterns during the tests to follow up the evolution of the crystals during deformation, as sketched in Figure II.23a.



Dumbbell samples were cut with a gauge length of 11mm as seen in Figure II.23b. The home-made tensile device X-JICO used for these experiments is depicted in Figure II.24. X-JICO allows running tensile tests at crosshead speed from $6\mu\text{m}/\text{min}$ to $15\text{mm}/\text{min}$. Furthermore, X-JICO is equipped with a 2 kN load cell and temperature regulated chamber, which enables either heating or cooling down thanks to an Intracooler apparatus. Temperature can be regulated from -20°C to 200°C .

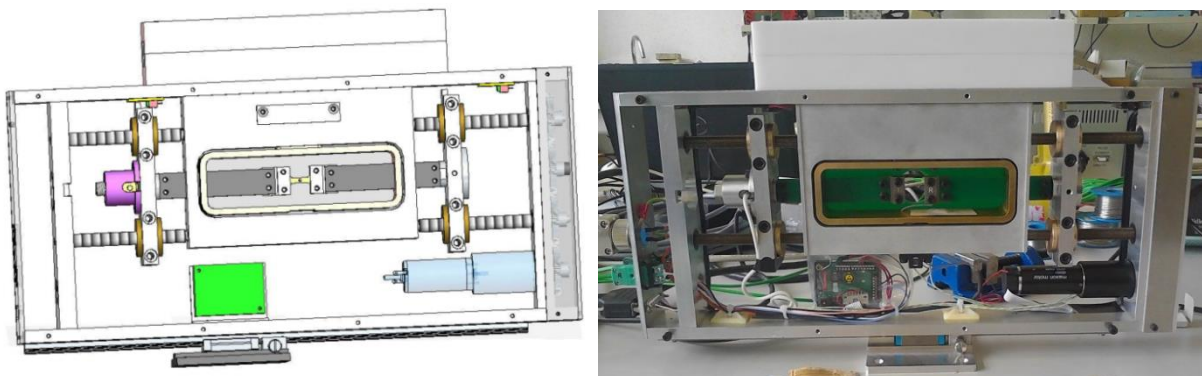


Figure II.24: X-JICO, homemade X-ray in-situ tensile device

SAXS and WAXS tests were both performed at 120°C . Tensile test were performed at -10°C for WAXS and at 0°C for SAXS. Due to the difficulty of cooling and specifically of ice formation and condensation, a dry airflow was injected during the tests in the X-JICO stage, as shown in Figure II.25a. The sliding rail at the bottom of the device allows moving the stage out of the scattering bench for changing samples, as depicted in Figure II.25b.

Studying both elastic and plastic strain domains of the strain-stress curves required using different strain rates due to the quite different extents of the two domains:

- Concerning the plastic strain domain, the same strain rate of $3 \cdot 10^{-3} \text{ s}^{-1}$ as macroscopic tensile tests was used for every temperature. It corresponds to a crosshead speed of $0.035 \text{ mm} \cdot \text{s}^{-1}$.
- Concerning the elastic strain domain, a strain rate of $5 \cdot 10^{-4} \text{ s}^{-1}$ – corresponding to a crosshead speed of $0.006 \text{ mm} \cdot \text{s}^{-1}$ – was used at $T=120^\circ\text{C}$ whereas a strain rate of $1.25 \cdot 10^{-4} \text{ s}^{-1}$ – corresponding to a crosshead speed of $0.0015 \text{ mm} \cdot \text{s}^{-1}$ – was used at $T=[-10^\circ\text{C} - 0^\circ\text{C}]$ due to the reduced elastic strain domain at low temperature.

For SAXS tests, an exposure time of 15s was used whereas for WAXS, exposure times of 2 or 5s depending on the crosshead speed were chosen. Whatever the exposure time, a transfer time of 5s must be added to the exposure time of each pattern, in every instance.

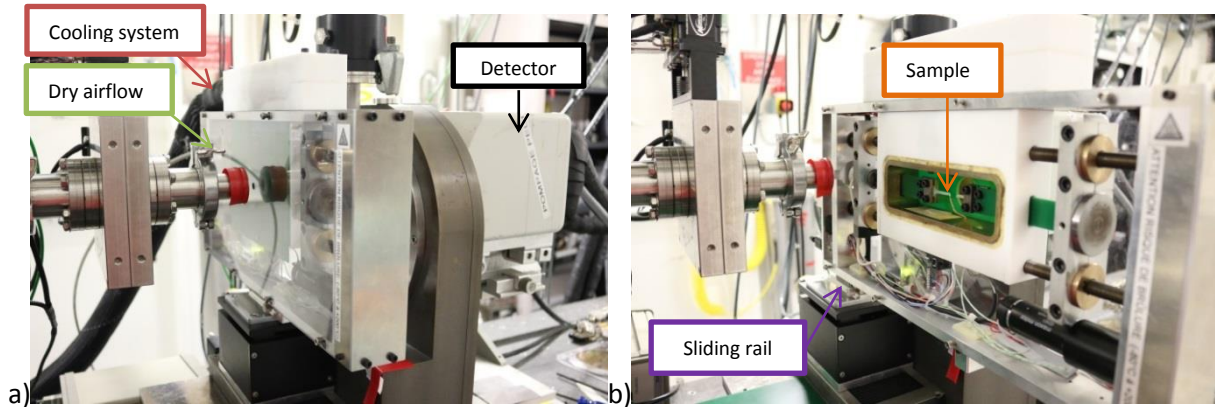


Figure II.25: X-JICO device with cooling system and dry airflow on the D2AM bench at ESRF:
a) WAXS disposition and b) setting up of the sample after tensile test

References

- [1] G. Roblin, "Microscopie optique," *Techniques de l'Ingénieur*, p. R 6 712, 1999.
- [2] J. Grenet and B. Legendre, "Analyse calorimétrique différentielle à balayage (DSC)," *Techniques de l'Ingénieur*, p. P 1205, 2010.
- [3] J. Grenet and B. Legendre, "Analyse calorimétrique différentielle à balayage à température modulée (DSC-TM)," *Techniques de l'Ingénieur*, p. P 1206, 2011.
- [4] B. Wunderlich, *Macromolecular Physics*, vol. 3 : Crystal melting, New York: Academic Press, 1980.
- [5] K.-H. Illers, "Polymorphie, Kristallinität und Schmelzwärme von Poly(ϵ -caprolactam), 2)," *Makromolekulare Chemie*, vol. 179, pp. 497-507, 1978.
- [6] N. S. Murthy, S. M. Aharoni and A. B. Szollosi, "Stability of the gamma form and the development of the alpha form in nylon 6," *Journal of Polymer Science: Polymer Physics Edition*, vol. 23, pp. 2549-2565, 1985.
- [7] B. Fayolle and J. Verdu, "Vieillessement physique des matériaux polymères," *Techniques de l'Ingénieur*, no. AM3150.
- [8] S. Gogolewski, M. Gasiorek, K. Czerniawska and A. J. Pennings, "Annealing of melt-crystallized nylon 6," *Colloid & Polymer Science*, vol. 260, pp. 859-863, 1982.
- [9] D. R. Holmes, C. W. Bunn and D. J. Smith, "The crystal structure of polycapromamide: nylon 6," *Journal of Polymer Science*, vol. 17, pp. 159-177, 1955.
- [10] H. J. Arimoto, "Alpha-gamma transition of nylon 6," *Journal of Polymer Science Part A*, vol. 2, pp. 2283-2295, 1964.
- [11] "Goodfellow," [Online]. Available: <http://www.goodfellow.com/F/Polyamide-Nylon-6.html>. [Accessed 16 Juillet 2014].
- [12] B. Sauer and B. Hsiao, "Effect of the heterogeneous distribution of lamellar stacks on amorphous relaxations in semicrystalline polymers," *Polymer*, vol. 36, pp. 2553-2558, 1995.
- [13] "Construction d'Ewald," Université Le Mans, [Online]. Available: <http://ressources.univ-lemans.fr/AccesLibre/UM/Pedago/physique/02/cristallo/ewald.html>. [Accessed 2 Juin 2014].
- [14] P.-A. Albouy, A. Vieyres, R. Perez-Aparicio, O. Sanseau and P. Sotta, "The impact of strain-induced crystallization on strain during mechanical cycling of cross-linked natural rubber," *Polymer*, vol. 55, pp. 4022-4031, 2014.

- [15] L. Lin and A. Argon, "Deformation resistance in oriented nylon 6," *Macromolecules*, vol. 25, pp. 4011-4024, 1992.
- [16] L. Penel-Pierron, "Transition de phase induite par déformation dans les polymères à liaisons hydrogène : cas des polymères éthylène/alcool vinylique et du polyamide 6," USTL, Lille, 1998.
- [17] J. Cavaillé, M. Salvia and P. Merzeau, "Un nouvel outil d'analyse de spectrométrie mécanique : le Micromecanalyser. Application à la caractérisation dynamique des matériaux métalliques, polymères et composites," *Spectro 2000*, vol. 16, no. 133, pp. 37-45, 1988.

Chapter III: Thermal treatments and materials

I.	State of the art	56
I.1.	Models of polymer crystallization	56
I.1.1.	Nucleation	57
I.1.2.	Growth: Hoffman-Lauritzen theory.....	58
I.2.	Memory effects	59
I.3.	Quenching	61
I.4.	Isothermal crystallization	61
I.4.1.	Principle.....	61
I.4.2.	Kinetics of isothermal crystallization.....	62
I.4.3.	Effect of the temperature of isothermal crystallization on microstructure.....	63
I.5.	Annealing.....	64
I.5.1.	Principle.....	64
I.5.2.	Effect of annealing on microstructure	65
I.6.	Issues	65
II.	Materials and processing	67
II.1.	Virgin pellets.....	67
II.2.	Injection molding process	67
II.3.	Compression molding process	68
III.	Results: effects of thermal treatments	69
III.1.	Determination of a condition to erase memory effects	69
III.2.	Isothermal crystallization	71
III.2.1.	Crystallization kinetics.....	71
III.2.2.	Isotherm characterization	73
III.3.	Annealing.....	75
III.3.1.	Adapted principle	75
III.3.2.	Annealing characterization.....	75
III.4.	Quenching	78
III.5.	Time–Temperature–Crystallization (TTC) diagram of PA6.....	80
IV.	Final choice of materials.....	81
	References.....	86

In chapter I, we have displayed the multi-scale structure of PA6 as well as some mechanical properties and behaviors. This multi-scale structure has an impact on mechanisms, which is why we wanted to control the parameters of the microstructure like the crystallinity index, the crystalline phase, the long period. As we want to set a specific panel of samples, it is important for us to first focus on the microstructure and the way to obtain it. We have chosen to affect the microstructure thanks to thermal treatments, and not by chemical processes. As for the metals, thermal treatments can be used on polymers in order to modify the microstructure.

The first part allows us to explain why and how thermal treatments change the microstructure. In the second part, the initial materials used for the thermal treatments are depicted. In the third part, the effects of thermal treatments on bulk PA6 are discussed. In the purpose of this thesis, employed thermal treatments were focused on isotherms and annealing. A particular annealing treatment was also studied and performed: it concerns memory effects of polyamides. The control parameters we have used for our thermal treatments are time and temperature.

Finally, the last part (part IV) describes the panel of samples that we have used for our mechanical study.

I. State of the art

Some knowledge on the physical processes involved during thermal treatments is needed. As the microstructure involves different scales -crystalline lattices with different perfection degrees, long period L_p of lamellae, crystallite and spherulite sizes from smallest to largest- models of polymer crystallization are first described and followed by literature knowledge on thermal treatments (quenching, isothermal crystallization and annealing).

I.1. Models of polymer crystallization

Nucleation and growth are the recognized mechanisms for the phase transition of a metastable liquid of small molecules into a crystal. In the case of crystallization of polymer chains from the molten state, the process of crystallization can be developed as well into two steps: nucleation and growth. Different crystallization theories have been developed. The Hoffman-Lauritzen theory is one of the theories which explains the differences of obtained microstructures. We will discuss only crystallization from the melt in quiescent conditions under the effect of temperature and not in solution under shear or stretching.

From a kinetic point of view, two types of experiments of crystallization are reported: isothermal and non-isothermal crystallizations. An isothermal crystallization has a constant rate of growth whereas a non-isothermal crystallization (cooling from the molten state) has a variable growth rate.

For our thermal treatments, isothermal crystallization was favored. Indeed, isothermal crystallization consists in the melting of the polymer and the crystallization at a unique temperature of crystallization whereas non-isothermal crystallization consists in the melting of the polymer and the cooling (at a defined cool rate) until the crystallization happens and finishes. Non-isothermal crystallization happens during a cooling scan of DSC.

I.1.1. Nucleation

When a liquid is quenched to a temperature below its melting temperature, small nuclei of different sizes and shapes are initially born. Nonetheless, in order to have the growth of these nuclei, they need to be larger than a critical size r^{crit} otherwise they will dissolve back. This means that they need to reach a nucleation barrier as depicted in Figure III.1. In this theory, the nucleus is usually described as a parallelepiped with a rectangular basis, defined by a thickness r , a width basis a_0 and length basis b_0 .

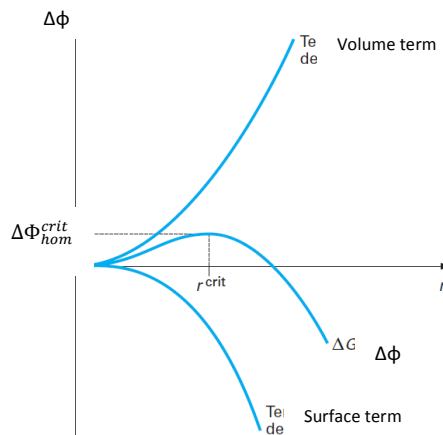


Figure III.1: Free enthalpy (ΔG) of homogeneous nucleation activity as a function of nucleus radius [1]

The free enthalpy which is necessary to form a nucleus is:

$$\Delta\Phi = -V \cdot \Delta G + 2\sigma_e S_b + 4\sigma S_L \quad (\text{E III.1})$$

With V the volume of crystal, S_b the surface of crystal basis, S_L the lateral surface of crystal, σ_e the surface energy of folding and ΔG the free enthalpy:

$$\Delta G = \frac{\Delta H_m \times \Delta T}{T_m^0} \quad (\text{E III.2})$$

Where ΔH_m is the enthalpy of fusion, T_m^0 the melting temperature of a perfect crystal and ΔT is called undercooling.

$$\Delta T = T_m - T_x \quad (\text{E III.3})$$

With T_m the melting temperature of a perfect crystal and T_x the temperature of isothermal crystallization.

The dimension of the nucleus critical size r^{crit} , as shown in Figure III.1, is given by:

$$\frac{\partial \Phi}{\partial r} = 0 \quad (\text{E III.4})$$

And then,

$$r^{crit} = \frac{2\sigma_e T_m^0}{\Delta H_m \cdot (\Delta T)} \quad (\text{E III.5})$$

The nucleation is really dependent of the undercooling and when doing thermal treatments, this is one of the control parameter. Indeed, the nucleation and the growth are influenced by the temperature of crystallization, as below in §I.1.2.

There are different kinds of nucleation:

- Primary nucleation when nuclei are directly formed. It can be:
 - o Homogeneous nucleation when active nuclei are part of the melted polymer.
 - o Heterogeneous nucleation when active nuclei are formed from the surface contact of external bodies (impurities, cavities, surfaces), playing the role of nucleant agents.

- Secondary nucleation when nuclei are formed from the contact of pre-existing nuclei, being part of the polymer.

Nucleation can also be qualified as sporadic when the rate of nucleation is constant.

I.1.2. Growth: Hoffman-Lauritzen theory

The basic premise of the Hoffman-Lauritzen theory is that the lamellar growth is assumed to occur by successive attachment of polymer stems to crystallites. In this model, polymer molecules are assumed to attach at the growth front in terms of stems, each of length comparable to the lamellar thickness l^* .

The first step of the growth is to place a first stem at the growth crystal surface, whose lateral dimension is taken as L and corresponds to the width of the growth front (the length) which the nucleation and growth covers. Indeed this step is associated with nucleation. After this step, the secondary nucleus spreads out laterally with the lateral covering rate g , corresponding to the growth rate parallel to the growth plane that covers the growth front after the surface nucleation.

Other notations are also needed for the following understanding, they are:

- The growth rate perpendicular to the growth plane G
- The surface nucleation rate i
- The undercooling noted ΔT

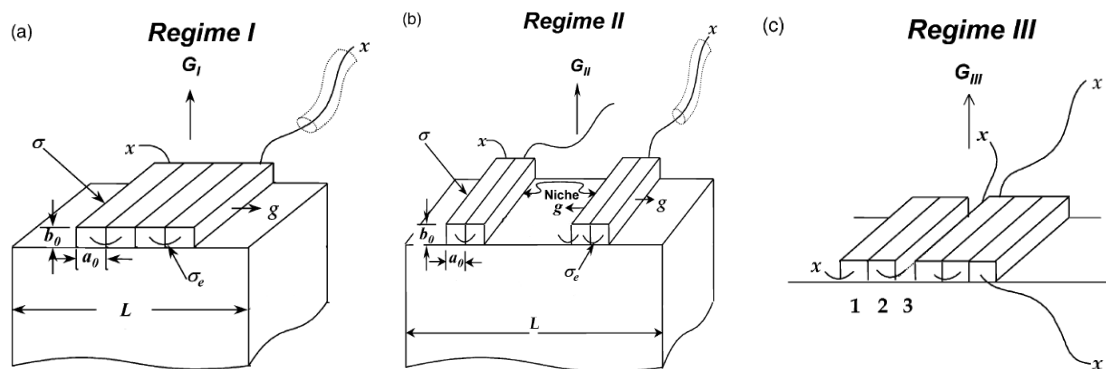


Figure III.2: Schemes of the different crystal growth regimes: a) regime I, b) regime II and c) regime III. The 'x' represents chain ends [2]

Here, the size a_0 is the monomer size (mesh size of the crystal), around 3 to 4 Å.

The Hoffman-Lauritzen theory predicts three growth regimes, as depicted in Figure III.2:

- At low ΔT s, regime I takes place when the growth from a single nucleus covers the entire growth plane L , as show in Figure III.2a, meaning that the lateral growth rate (g) is significantly greater than the secondary nucleation rate (i). For $g \gg i$, the whole substrate is covered by stems as soon as a first one is nucleated. Then, monolayers are added one by one. The analytical expression for the growth rate in regime I is given by:

$$G_I = i b_0 L \quad (\text{E III.6})$$

Where b_0 is the thickness of the molecular layer crystallized on the surface

In regime I, each secondary nucleation leads to the formation of a full monolayer of thickness b_0 [3].

- At intermediate ΔT s, the lateral growth rate g is comparable to or smaller than the nucleation rate i . In this case, the second regime applies: further nuclei are deposited before the first layer is fully formed as shown in Figure III.2b. The linear growth rate is given by:

$$G_{II} = b_0 \sqrt{i g} \quad (\text{E III.7})$$

- At high ΔT s, the multiple nucleation of stems is so prolific that the spreading rate is irrelevant, $i \gg g$, as sketched in Figure III.2c. The growth rate is exactly of the same form as in regime I:

$$G_{III} = ib_0L \quad (\text{E III.8})$$

This means that the growth of a crystalline lamella is almost achieved by stem covering, as a new stem is nucleated before the previous one is fully achieved.

Thus, according to the type of growth regimes, the growth of the crystal changes and so the microstructure of the crystal can be impacted.

I.2. Memory effects

An effect of the thermal history on crystallization exists in polyamides, as well as in other polymers [4] and it is usually called “crystalline memory effect”. Memory effects reflect the thermal history of the sample and they mean that a certain temperature above the bulk melting point has to be reached in order to remove any influence of thermal history on the crystallization kinetics of a sample. As we want to use thermal treatments on materials, it is important to erase this memory effect in order to only see the consequence of the treatments on PA6.

Memory effects depend on the melt temperature T and the time spent in the molten state t , as depicted in Figure III.3. Meares [5] has described the general nature of these effects by these words: “The higher the degree of molecular order in a crystallite the higher is its melting point. After most of the crystallites have melted, tiny regions which have an unusually high degree of order may persist in the melt. If these are sufficiently large, they act as predetermined nuclei for immediate recrystallization on cooling. Even though such nuclei may be below the critical size they probably build up more quickly to give growing centers than the subcritical nuclei which form spontaneously on cooling.” The number and size of the nuclei which remain in the melt depend on three factors:

- 1) The temperature of any previous crystallization, since higher is this temperature, higher is the perfection degree of crystallites, and so higher is their melting point.
- 2) The temperature of melting T because higher is this temperature, more complete is the destruction of the crystallites formed previously.
- 3) The period of time spent in the molten state t since the melting of the crystallites is not an instantaneous process.

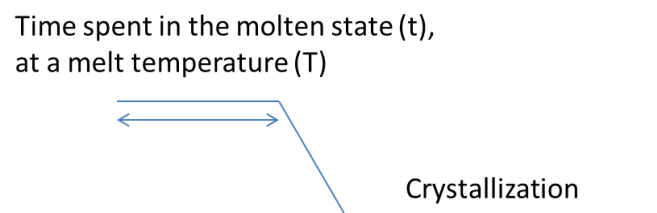


Figure III.3: Scheme of the influence of memory effects on the crystallization

Further than the T and t conditions, Aharoni [6] has also emphasized the fact that concerning the crystallization, the cooling rate from the molten state has a more drastic effect on crystallization kinetics than the choice of the temperature of melting T when the influence of the memory effect is studied.

Nonetheless, memory effects being linked inherently to the material and its thermal history, they can be induced or influenced by the molding process. Khanna et al [7] have noticed a temperature shift of 15°C of the crystallization temperature T_c for a PA6 with and without memory, as shown in Figure III.4. A shift of 15°C (peak to peak) is observed between a virgin pellet ($T_c = 169^\circ\text{C}$) and an extruded

pellet ($T_c = 184^\circ\text{C}$), due to the process. However, with a closer look on the DSC onset, it can be noticed that the onset of crystallization on cooling is nearly the same, around 190°C , meaning that it is important to focus on the global DSC scan.

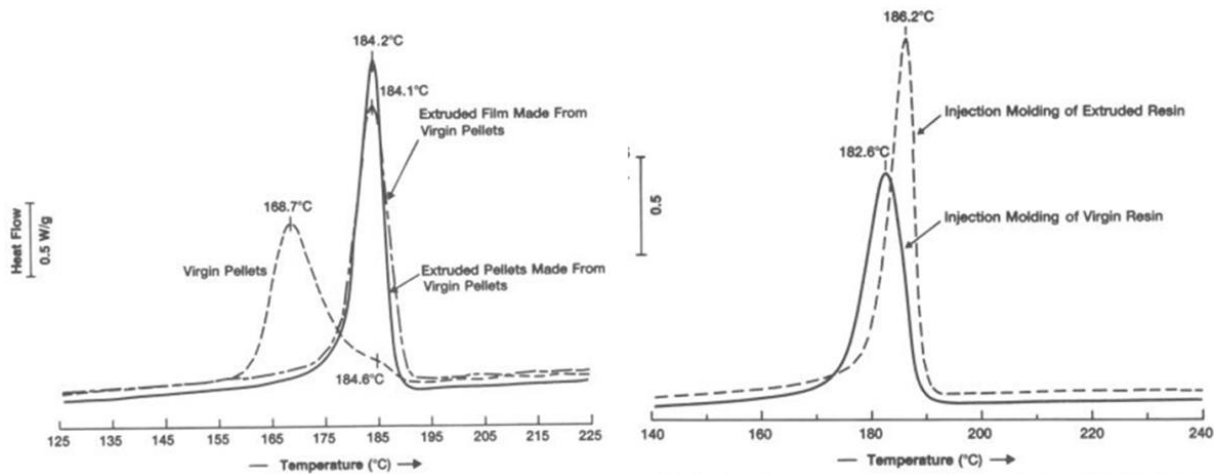


Figure III.4: Crystallization curves from the molten state for virgin and extruded pellets of PA6 (left); Curves for injection molding from virgin and extruded resin (right), extract from [7]

Many studies [8] [9] [7] [6] [10] [11] [12] have been performed on memory effects. However no consensus has been found. The following results were reported in order to erase memory effects:

- 260°C during 20 min for Tidick et al [13]
- 261°C during 30 min for Turska and Gogolewski [14] [15]
- 270°C during 30 min for Magill [16] [17] [18]
- 280°C for Illers [19].
- Avramova and Fakirov considered that at 260°C , there are still active centers (nuclei) but their numbers decrease with the spent time t [8]. They have also demonstrated that complete annihilation of nuclei was reached at $T=280^\circ\text{C}$ (melting equilibrium point of PA6) for $t>80$ min [9]. However, it is also possible to rise T at 290°C or 300°C and in this case t only needs to be inferior to 40 min but as a consequence the polymer undergoes thermal degradations.
- According to Gurato et al [20], polyamide loses its structural 'memory' after $t=15$ min at 280°C . A critical annealing temperature T should exist where all the crystallization centers are destroyed:
 - o $T_{\text{crit}}=281^\circ\text{C}$ during 15 min according to Gurato et al [20] in order to erase thermal and morphological past of the sample
 - o $T_{\text{crit}}=284^\circ\text{C}$ according to Avramova and Fakirov [8] (precisely $T_m^\circ=278^\circ\text{C}\pm 6^\circ\text{C}$)

Finally, by compiling literature data, melt temperatures of polyamides are in the following temperature range $T=[260-281^\circ\text{C}]$ [6] in order to erase memory effect. This lack of consensus could be related to the fact that in polyamide 6, no specific equilibrium melting temperature has been detected [7]. Furthermore, in case of polyamides, the erase of the "memory" of the polymer should correspond to the entirely random disposition of locally chain-folded segments and to the rupture of most H-bonds between these chains. This induces that erasing process has to be a very slow process [6].

I.3. Quenching

Quenching consists in heating the material above its melting point before cooling it rapidly down to ambient temperature or below, in every case far below the crystallization temperature as shown in Figure III.5a. Quenches are usually achieved by dipping samples into water or air. Nevertheless, other types of fluids can also be employed in order to perform variable cooling speeds (from the fastest to the slowest): salty water, water, oil, gas (air, argon, nitrogen, etc.). The cooling speed and/or the final quench temperature are of a primary importance for polymer microstructure.

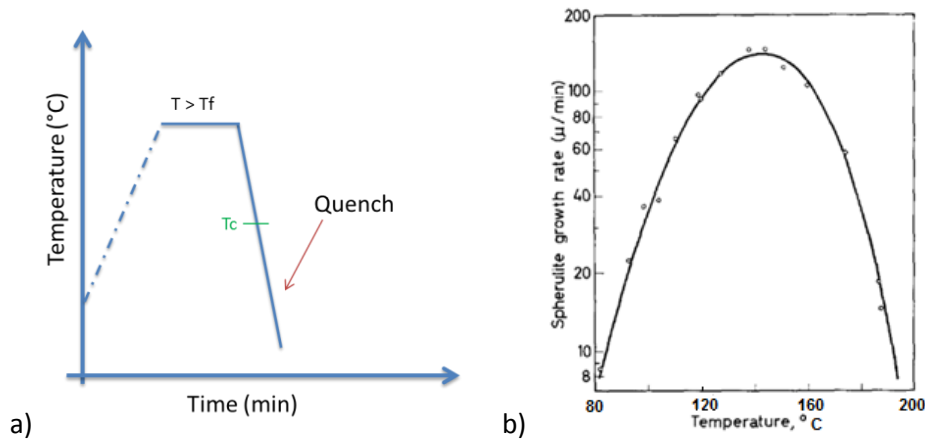


Figure III.5: a) Scheme of a quench; b) Spherulite growth rates as a function of T_c for PA6 [18]

In the case of quenching from the molten state down to $T_c = 23^{\circ}\text{C}$ or 0°C , the crystallization regime can be assimilated to the third regime of crystallization, according to the Lauritzen-Hoffman theory [21]. At this temperature T_c , the undercooling ($\Delta T = T_f^{\circ} - T_x$) is really high. Indeed, growth rate of spherulite exhibits a maximum as shown in Figure III.5b and at low temperature (well under 80°C), this means that nucleation is the predominant effect. Because of this high undercooling, the critical size of the nuclei is very small (i.e. 1.1.2), as well as the crystalline lamellar thickness L_c . Because having a fast crystallization has consequence on reptation, this means that crystallinity index X_c decreases as the cooling speed increases. Furthermore, the melt temperature of the polymer is also lower in the case of quenching due to the non-perfection of the crystals and their low thermal stability.

I.4. Isothermal crystallization

I.4.1. Principle

In the case of isothermal treatment, the aim is to bring the material above its melting point in order to be in the molten state and then to maintain it at a chosen temperature, taken into the temperature range of PA6 crystallization, noted T_c . The length of time spent at T_c depends on T_c : higher is T_c , longer the time spent at T_c has to be in order to let the polymer fully crystallized. The protocol is shown in Figure III.6.

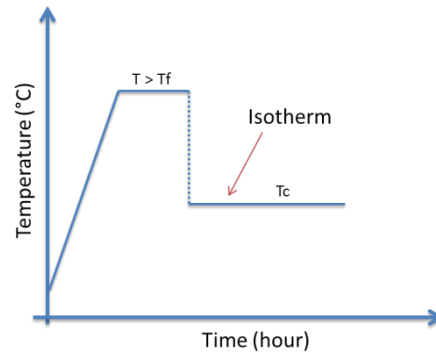


Figure III.6: Diagram of an isotherm

In the case of isothermal crystallization from the molten state, the crystallization is carried out at small undercooling ($\Delta T = T_f^\circ - T_c$), which means that the nucleation process is slow. It corresponds to the first regime of crystallization, according to the Lauritzen-Hoffman theory [21]. This regime gives a relatively large initial thickness of crystal. It also globally allows the crystals to grow independently isolated and so to reduce the numbers of connections between them. This means that a chain will tend to belong only to one lamella.

I.4.2. Kinetics of isothermal crystallization

For polymers, the kinetics of isothermal crystallization is usually described by the Avrami equation [22] [23]. This equation describes how solids transform from one phase to another at constant temperature. In our case, this corresponds to an isotherm where the polymer crystallizes and so transforms from the molten to the crystalline state. It describes the beginning of crystallization:

$$\alpha(t) = 1 - \exp(-kt^n) \quad (\text{E III.9})$$

Where $\alpha(t)$ is the crystalline volume fraction of the polymer, n the Avrami index and k a kinetic constant.

In general, n and k characterize the nucleation type and the crystal growth geometry.

The crystallization transformation follows a sigmoidal profile. Furthermore, there is often an induction time at the beginning, corresponding to the needed time for critical nuclei to appear. This induction time is a function of crystallization temperature T_c for a given material.

In this form, the n factor gives information on the mechanism involved in the crystallization process, according to its values. The meaning of n values is reported in Table III.1.

Table III.1: Mechanism of crystallization and the value of n (6) (7)

Growth	Crystal growth shape	Homogeneous nucleation	Heterogeneous nucleation
Three-dimensional	Sphere	4	$3 \leq n \leq 4$
Two-dimensional	Disc	3	$2 \leq n \leq 3$
One-dimensional	Rod	2	$1 \leq n \leq 2$

One should take note that secondary crystallization and crystal perfecting processes are not taken into account.

In the case of polyamide 6, Inoue [24], has shown that Avrami's equation could be applied but only to describe the first half of crystallization curve. In the second part of the curve, the relaxation of the

entanglements and the perfection of crystals take place, and the change of density increases with crystallization temperature. The following conditions were reported:

- $n=4$ at $T_c = [210-215^\circ\text{C}]$
- $n < 2.5$ for $T_c < 207^\circ\text{C}$
- n value changes rapidly between 207 and 210°C

Above 210°C , it is said that the crystallization occurs as three-dimensional growth and homogeneous nucleation, and there should be heterogeneous (and instantaneous) nucleation below 210°C [24].

Furthermore, Inoue has shown that melting points increase with crystallization temperature but this rising was also higher for a crystallization temperature above 210°C .

I.4.3. Effect of the temperature of isothermal crystallization on microstructure

In case of isothermal crystallization, it has been observed that the long period L_p increases as a function of crystallization temperature for polymers like polyethylene or polyamide 6, as reported in Figure III.7. However, the possibility of performing different crystalline phases was not taken into account.

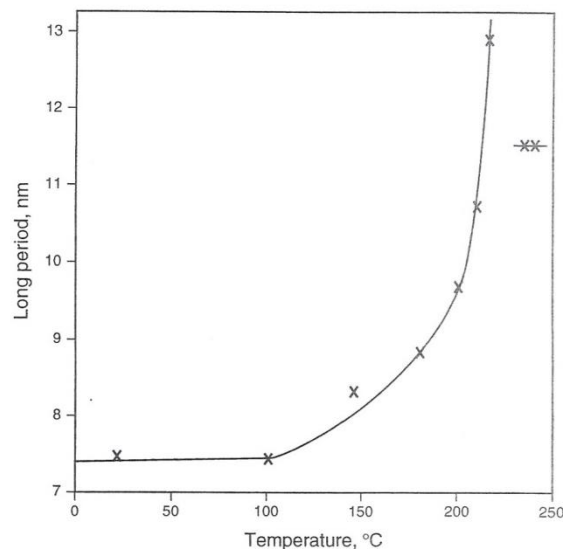


Figure III.7: Dependence of L_p measured in SAXS versus crystallization isotherm temperature [6] (with data of [25])

That is why, a few years later, Hiramani conducted a study on 0.3 mm thick bulk PA6 and this time took into account α and γ phases (no β phase) [26]. Samples were melted at 270°C during 10min before being rapidly transferred to an oil bath. Isothermal crystallization was performed at different temperatures during 1h except for $T_c = 210^\circ\text{C}$, which was held during 10h in order to overpass induction time. The results are shown in Figure III.8, where L_p is plotted as a function of $T_m/\Delta T$, equivalent to $\Delta H_f/\Delta G$, meaning more it increases more perfect the crystal is. It was shown that depending on crystallization temperature (equivalent to a quench for low temperatures), γ phase could be formed.

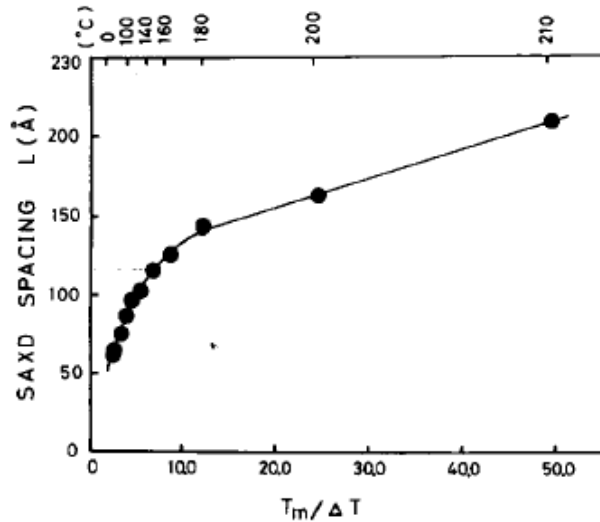


Figure III.8 : Evolution of L_p as a function of crystallization temperature for bulk PA6 [26] where $\Delta T = T_m - T$ and $T_m = 220^\circ\text{C}$

I.5. Annealing

I.5.1. Principle

Annealing consists in maintaining the sample at a temperature T_a (between T_f and T_g) in order to allow it to crystallize further. This is related to the growth of nuclei which were formed during the quench but did not have time to grow. The thermal way is illustrated in Figure III.9.

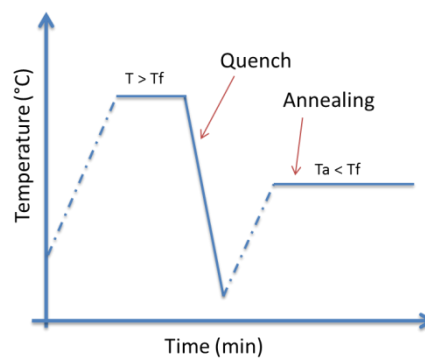


Figure III.9 : Diagram of an annealing

According to the choice of the annealing temperature, observed phenomena may be different. Furthermore, they can depend on the crystalline structure of the polymer obtained by quenching. Indeed, as said before, polyamide 6 has different crystalline phases and these phases do not possess the same thermal stability nor the same conditions of formation. That is why some phase transformations can occur depending on the temperature range. Crystal growth can also happen in some specific temperature ranges, especially when annealing temperature T_a is higher than the crystallization temperature. Gogolewski et al [27] have also found that the annealing process was characterized by an induction period.

I.5.2. Effect of annealing on microstructure

In a study led by Hiramí [28], samples were fibers and thick films. The films consist of 0.5 mm thick non-oriented samples quenched from the melt and then annealed for 1 hour into an oil bath, with temperature range between 100°C and 215°C. In the case of fibers, the annealing treatment was carried out on free or tension loaded samples.

The results are depicted in Figure III.10. In the case of films, the long period L_p is considered equal to the thickness of lamellae due to the fine structure. The rising of L_p for high temperatures corresponds to a thickening phenomenon of lamellae. One should take care that during the study the presence of different crystalline structures was not taken into account neither their possible transformations into other crystalline phases, which could explain the huge difference of L_p at higher temperatures between the films and the fibers (yarns).

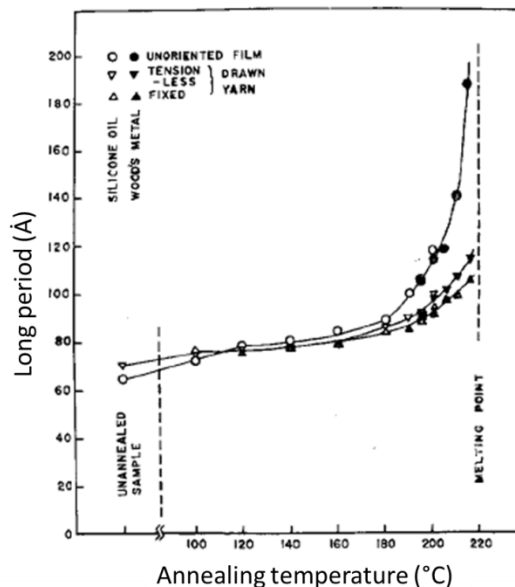


Figure III.10 : Dependence of L_p as a function of annealing temperature for PA6 [28]

Let us now compare the Figure III.7 and Figure III.10, meaning the increase of L_p as a function of T_c or T_a . From the literature, it seems that doing an isotherm or an annealing at the same temperature has the same effect on the long period. However, this does not mean that there is the same effect on the crystal thickness L_c : indeed the effect on the crystallinity index X_c is not reported in both case. In addition, isotherm and annealing treatments cannot have the same effect on the density of stress transmitters.

I.6. Issues

This state of art has allowed us to explain why and how thermal treatments change the microstructure. However there are still some lacks in the literature that we need to fill in as well as the absence of consensus. These points are developed below and only concern the issues on microstructure.

Indeed, generally, few studies have been published on bulk polyamides and on their crystalline microstructure. The existence of α and γ phases are widely accepted but the existence of a metastable phase is disputed [29]. Furthermore even if this existence is taken into account, authors

do not agree on its structure or name [30] [31] [32]. As our work is not to precisely define the crystallographic part of crystalline phases, we accept this phase as β phase [33]. According to Penel-Pierron [34] cast films promote β phase but what for bulk material. Thus, one of our objectives is to study the conditions allowing obtaining β phase as well as the conditions allowing the transformation of β into α phase thanks to thermal treatments. This would allow us to better apprehend the β phase.

Back to α and γ phases, even if they are widely described, there are still some lacks in the literature on the way to obtain them, especially by doing thermal treatments. Indeed, it is said that α phase can be converted into γ phase thanks to an iodine treatment [35]. Inversely, γ phase can be converted into α phase with phenol treatment [36] or by drawing [37]. However by using only thermal treatments, the conditions are not a consensus:

- For Kyotani and Mitsuhashi [38] γ is supposed to be predominant for crystallization at 100°C and α predominant at 200°C. In addition, the presence of α increases with annealing at 200°C whatever the crystallization temperature was.
- Hu and Zhao [39] say that whatever the annealing temperature, α phase is always preferred.
- On the contrary Zhao and Zhang [40] pretend that at 195°C, fast cooling speeds promote α formation whereas longer annealing times promote γ phase.
- For Zhang et al [41], amorphous phase converts into γ phase for $T < 180^\circ\text{C}$ but between 180 and 200°C it converts into α phase. However, one can wonder if they do not mix β phase with amorphous phase.

This is to prove that the limit of domains between α and γ phases are not well-defined, and β is even not part of it. Thus, it is important to check the literature with our own experiments. One way to display the different domains and their interactions is to plot a time-temperature-crystallization (TTC) diagram. Indeed, TTC diagram is used to study the transitions of phases or states, especially during thermal treatments. Labour has made a schematic TTC diagram for iPP, as shown in Figure III.11 and one of our goals would be to do the same for PA6. It would allow us displaying according to time and temperature in which state or phase the material is.

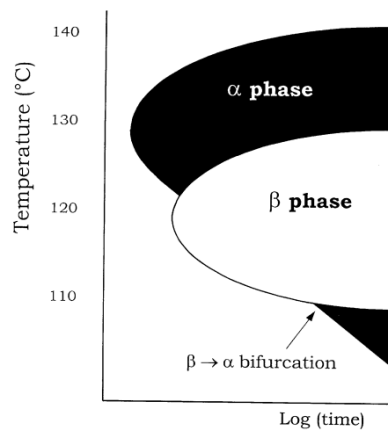


Figure III.11: Schematic time-temperature-crystallization diagram of iPP [42]

Concerning the global microstructure, one of the biggest lacks in literature is the presence of all microstructural parameters. Indeed, studies can be done on the influence of the crystallinity index but without considering if all the samples are constituted of the same crystalline phase. The same can go on with the study of L_p or else... By characterizing our samples, it will allow us to take into account the influence of the crystallinity index, the long period but also the crystalline phase, morphology... and thus observe the real influence of the crystalline microstructures on the mechanical properties.

II. Materials and processing

II.1. Virgin pellets

Two grades of virgin pellets were provided by Solvay (Gorzow's plant). They are commercial grades; having different molecular masses but both of them are linear polymers. They are reported in Table III.2, M_n and I_p were determined by GPC (chapter II, §I.2). The virgin pellets contain no additive nor nucleant agent, nor lubricant.

Table III.2: Commercialized PA6 at our disposal

Sample name	M_n (Kg/mol)	I_p	Structure
31K	30.3	1.86	linear
15K	19.3	1.63	linear

The virgin pellets are mainly composed of α phase but there is also a presence of γ phase. However, the molecular mass has an effect on the crystalline structure and the crystallinity index as shown in Figure III.12. Indeed, there is a higher percent of γ phase into the 15K than into the 31K. This seems that having a higher molecular mass favor stable phase like α .

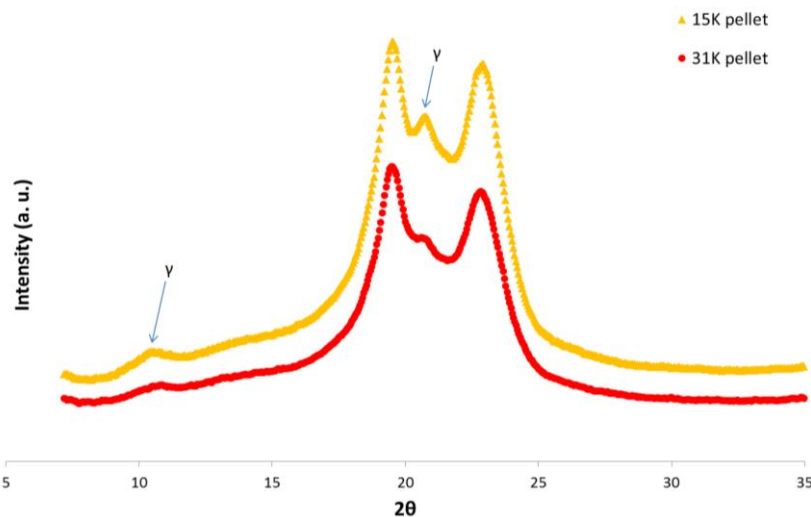


Figure III.12: DRX patterns of PA6 virgin pellets (15K and 31K)

II.2. Injection molding process

The injection was carried out in the Belle-Etoile plant of the Solvay group for each grade. The process is schematized in Figure III.13. The obtained sheets are 102*102 mm squares of thickness 1.6 mm. The injection pressure is around 2000 bar, injection time is of the order 0.5 sec and cooling time is of order 10 seconds.

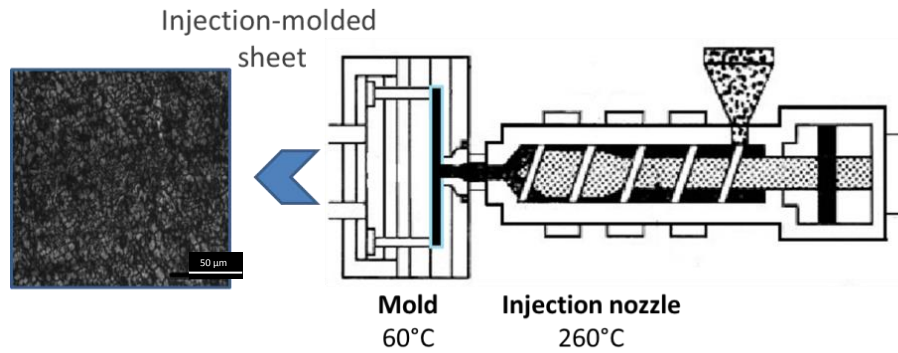


Figure III.13: Scheme of the injection molding process

The sheets exhibit an absence of large well-formed spherulites but a large number of small crystallites, which indicates that a very high density of nuclei is generated in the process. This could be due to the introduction of impurities by the process, or to an effect of the high rate shear during the process. Concerning the crystalline structure, β and γ phases are found in different ratios in the injection molding sheets, according to the molecular masses, as shown in Figure III.14. The β/γ ratio seems to correspond to the initial α/γ ratio present in the virgin pellets. This would mean that during the injection process, γ phase is conserved but α phase is transformed into β phase. As the pellets are melted at 260°C, this could mean that memory effects are conserved, meaning a conservation of the initial nuclei. In this way, only the cooling speed could affect the crystallization: as γ phase is favored by kinetics, the initial corresponding nuclei grow as γ phase; however concerning α phase, the conditions do not favor its growth and β phase could grow instead.

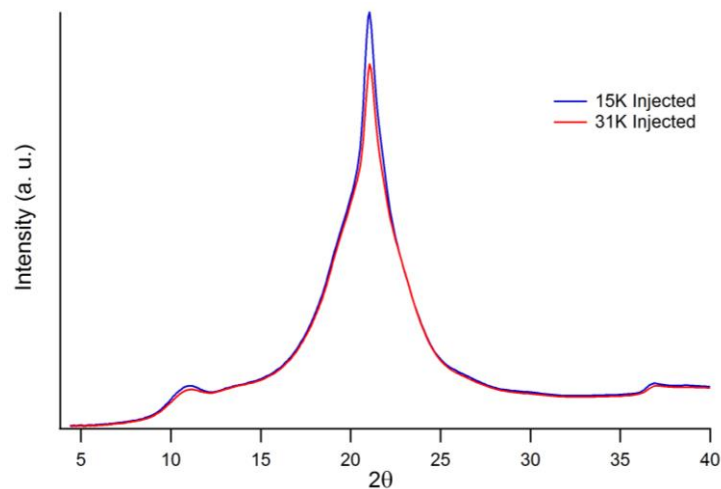


Figure III.14: DRX patterns of PA6 injected sheets (15K and 31K)

II.3. Compression molding process

In order to study the effect induced by the process, a compression molding process was employed. It consists in melting the virgin pellets in a press, under load. There are three main differences between the two processes: no high shear rate is applied in compression molding, cooling down is much slower (of order 10 min) and there is no introduction of impurities by the process. The final microstructure is very different from that obtained with injection molding. It consists in a stack of layers of transcrystalline zones and spherulites, possibly due to thermal gradients. Transcrystallinity is crystallization from a stranger surface in a particular structure. Its structure is characterized by a

columnar growth of spherulites along a stranger surface (often fibers) [43]. There is a lateral growth limitation and a development normal to the stranger surface, as visible in the optical microscopy pattern in Figure III.15. Transcrystallinity has an influence on mechanical properties of materials [44].

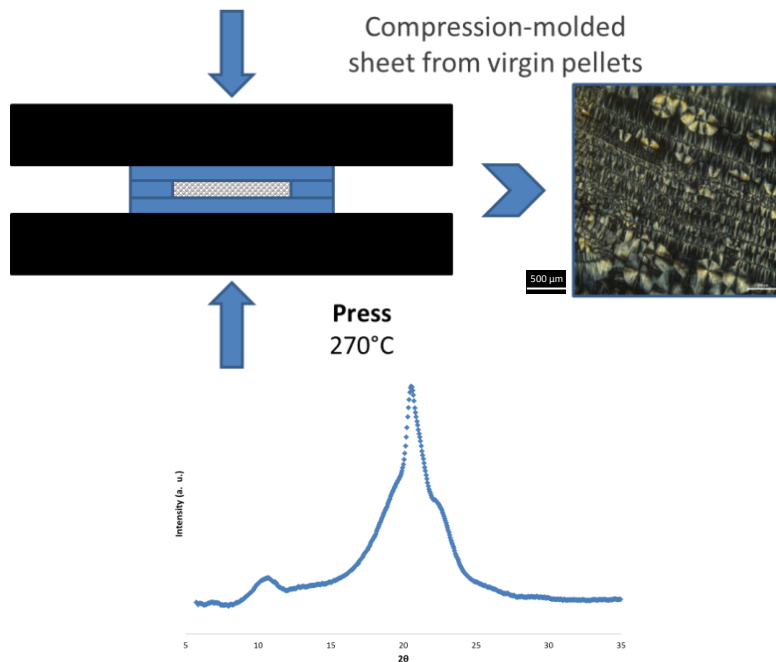


Figure III.15: Representation of the compression molding process (left), DRX pattern of a compression molded sheet (right)

For our study, we have chosen to use only the higher molecular mass sample (31K), since it seems to give the most stable crystalline structure. In Figure III.15 (right), the DRX pattern informs us that the compression molded sheet contains a mix of γ and α phases and maybe a little bit of β phase.

III. Results: effects of thermal treatments

Literature has given us the basis of thermal treatments however due to a lack of consensus concerning all the microstructural parameters, it is of prime importance to perform the thermal treatments and entirely characterize the obtained samples (in particular the crystallinity index, the crystalline phase and the long period).

III.1. Determination of a condition to erase memory effects

In order to find the conditions to erase memory effects, we have investigated them by changing the temperature of melting (T) and the length of time spent in the molten state (t). In addition to this set of control parameters, the full previous thermal history of the material may have an impact. The thermal history depends on the process and is not appropriately controlled. That is why, virgin pellets have also been studied in order to overcome the process effect (i.e. injection molding).

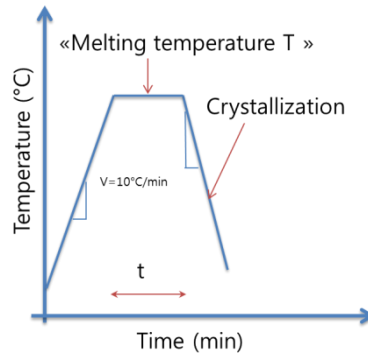
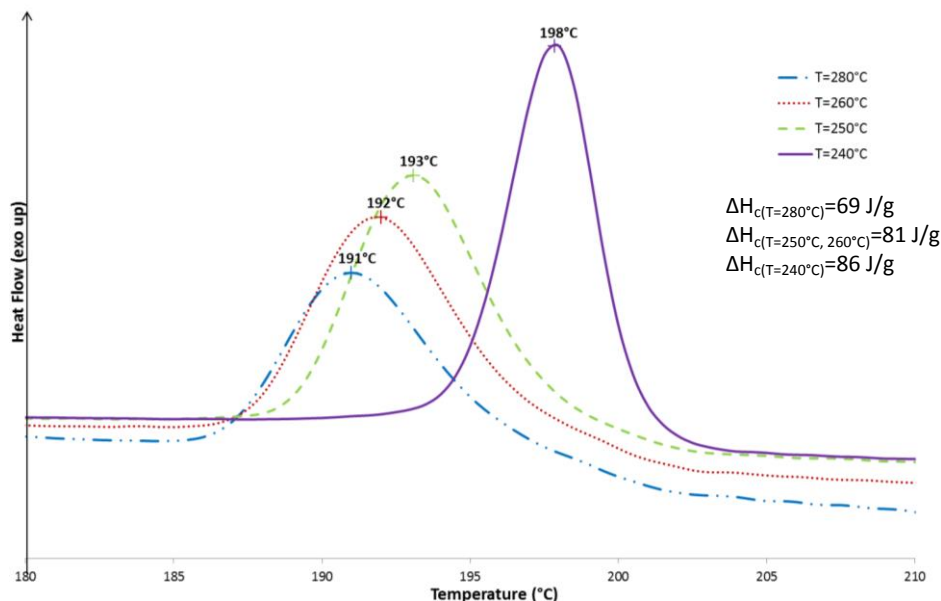


Figure III.16: DSC protocol to study memory effect

To study these effects, differential scanning calorimetry (DSC) can be employed. The DSC protocol is depicted in Figure III.16: it consists in melting the sample at a chosen temperature T during a chosen time t and then observing the DSC crystallization curve concerning the peak crystallization and its onset. In the case of non-isothermal crystallization upon cooling from the molten state, memory effects are clearly observed in the fact that the onset and the crystallization peak of samples with memory effect appear at higher temperatures than those without “memory”.

Figure III.17: Effect of the melting temperature (T) on the crystallization for 18K virgin pellets (MDSC, $v=1^\circ\text{C}/\text{min}$)

Starting with the virgin pellets, Figure III.17 shows the effect of the melting temperature T on the crystallization temperature T_c and how the material is affected by the memory effect. Indeed, because memory effect means the survivals of remaining crystalline nuclei, this means also that when the material is cooled down, the crystallization starts earlier when these crystallites are present, due to secondary nucleation. It can be noted in Figure III.17, that a melting temperature T of 240°C is clearly not high enough to suppress these memory effect, as there is a gap of 6°C between the peaks and also the onset temperature is shifted to lower temperature when the melting temperature is increased. Above $T=250^\circ\text{C}$, the shift between the peaks is nearly insignificant and the onset temperature is also identical.

This gives us precious information on the fact that the melting temperature has to be higher than 250°C . If we also take into account the small temperature gap between the peaks, it is also better to be above 260°C . Furthermore, if we consider the crystallization enthalpies for the different melting

temperature, it should be noted that there is a significant gap of value between $T=280^{\circ}\text{C}$ and the other melting temperatures (a ΔH_c shift of at least 12 J/g). This could be due to the presence of homogeneous nucleation or to the presence of degradation perturbing the crystallization process.

After studying virgin pellets, the study has been transposed to the materials injected from these virgin pellets. It was found that the onsets and the crystallization peaks were the same between $T=240^{\circ}\text{C}$ and 270°C . There was a very small effect when the melting temperature was increased to $T=300^{\circ}\text{C}$. However, the polymer at this temperature undergoes degradation: PA6 is highly sensitive to oxidation, which results in chain breaking and the loss of mechanical properties. Thus, $T=300^{\circ}\text{C}$ was considered as too high.

Because the polymer is sensitive to oxidation and degradation at high temperature, a compromise has been set and a melting temperature of 270°C has been decided. Concerning the length of time spent in the molten state, the time $t=10\text{min}$ was chosen. This set of conditions was checked by doing an isotherm at 203°C after melting the polymer. The observed results are shown in Figure III.18.

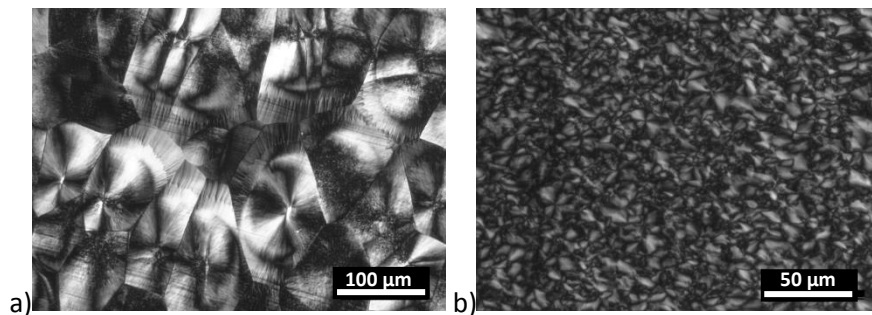


Figure III.18: Spherulites in PA 6 after erasing memory effects at 270°C (10 min) and followed by an isotherm at 203°C observed under transmitted polarized light for a) virgin pellets and b) injected sheet

Indeed, optical microscopy observations of PA 6 indicate that samples exhibiting memory effects are characterized by a multitude of nuclei and small fragments of spherulites. In contrast, for virgin samples (having no “memory”), the crystallized spherulites are in a few number but are remarkably large and well-developed [6]. The thermal treatments on virgin pellets clearly show that 270°C (10 min) is a sufficient condition to erase the memory effect: the initial spherulites (before treatments) had a $10\text{-}20\mu\text{m}$ diameter whereas after suppressing memory effect, the spherulites were in a fewer number and their diameter had increased to $100\mu\text{m}$ (Figure III.18a). Concerning the injected materials, no change was observed before and after the thermal treatment was performed (Figure III.18b). It confirms us that the presence of impurities in the injected sheets and also that the impurities play a major role in the nucleation process and lead to presence of fragments and small spherulites as well as crystallites.

III.2. Isothermal crystallization

III.2.1. Crystallization kinetics

In order to establish the best parameters (time and temperature), a crystallization kinetics study has been performed by DSC. As mentioned earlier, there is a correlation between T_c and t_c which is important to know in order to achieve crystallization at only one temperature. Indeed, the crystallization must be over before the cooling at room temperature in order to have only one population of crystallites. The study was performed on 15K and 31K injected samples (cf. Table III.1).

The crystallization temperature range was set between 200 and 210°C as shown in Figure III.19. The half time of crystallization depends on the crystallization temperature. Its value increases when the crystallization temperature is increased as depicted in Figure III.19a. For a same crystallization temperature, the half time increases as the average molecular mass increases, as shown in Figure III.19b. Thus, the induction and length time were based on the higher molecular mass, in order to be sure that crystallization is over for all the polymers, included the ones with lower molecular masses.

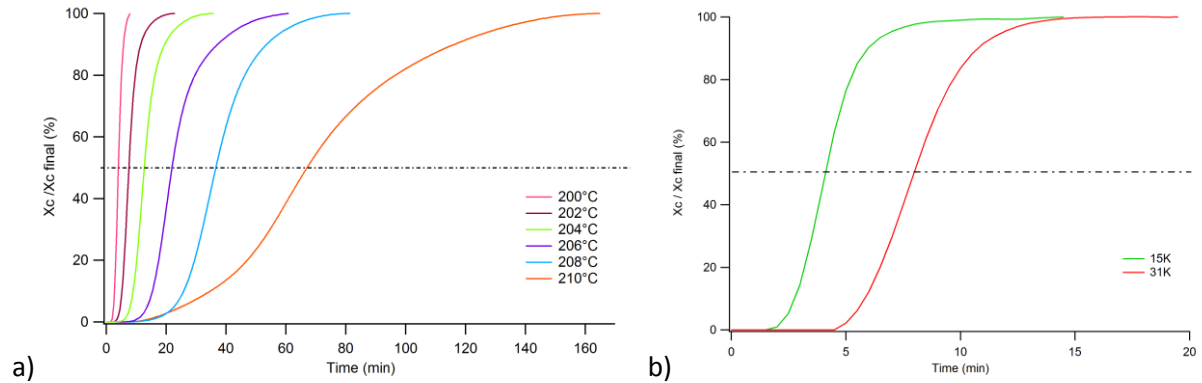


Figure III.19 : a) Crystallization kinetics of PA6-31K in function of time for different isothermal crystallization temperatures; b) Crystallization kinetics for 15K and 31K samples at the same crystallization temperature, i.e. $T_c = 203^\circ\text{C}$

Our data were compared with the literature, as depicted in Figure III.20, and we are in a good accordance. Inoue’s data can be used for higher crystallization temperatures.

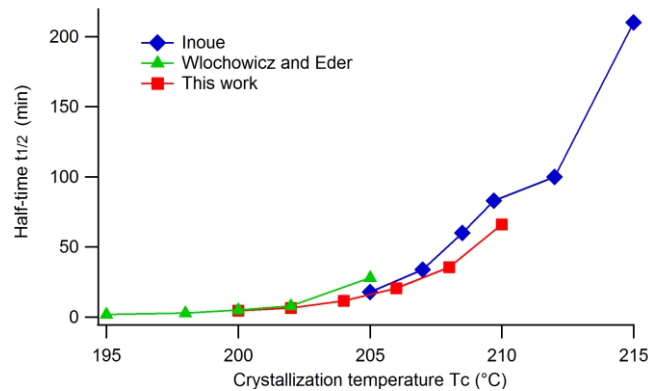


Figure III.20: Comparison between literature data [24] [45] and this work concerning the half time of crystallization (PA6-31K)

In order to better understand the nucleation processes during the isotherms at different temperatures, the crystallization kinetics were fit by Avrami’s law and the exponent n was determined, as reported in Figure III.21. The Avrami parameters are listed in Table III.3.

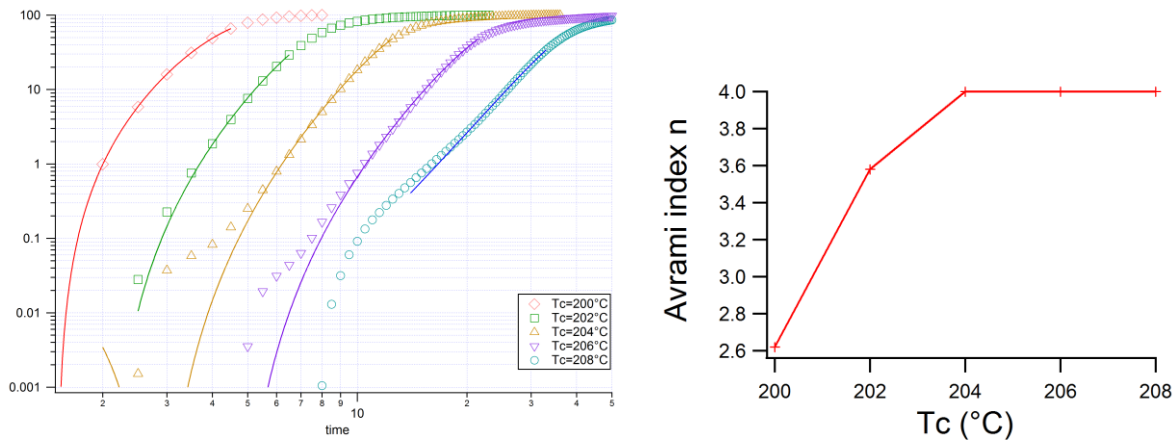


Figure III.21: Fit for crystallization kinetics by using Avrami's law

With these parameters, we found as in Inoue's work [24] that over $T_c = 204^\circ\text{C}$, the nucleation is homogeneous and the growth is three-dimensional, meaning spherulites are spheres. At $T_c = 202^\circ\text{C}$, the nucleation is heterogeneous but with a three-dimensional growth. Finally at $T_c = 200^\circ\text{C}$, the growth is two-dimensional, meaning having discs, with heterogeneous nucleation. $T_c = 200^\circ\text{C}$ is definitely not an advantageous crystallization temperature because it impacts the spherulite structures. Thus, in order to compare our results it is better to only perform spherulites in form of sphere than disc.

Table III.3: Avrami parameters determined by the fit

T_c ($^\circ\text{C}$)	n	τ (min) ($t_{1/2}$)	t_0 (min) (induction)
200	2.6	2.9	1.5
202	3.6	6	2
204	4	10.7	2.8
206	4	18.8	4.6
208	4	35	11.5

Concerning our study and in order to have the better conditions of reproducibility, it seems important to work with isotherm at $T_c > 204^\circ\text{C}$.

III.2.2. Isotherm characterization

Thanks to the crystallization kinetics, the time and temperature were determined. Let us now focus on the microstructure and in particular the crystallinity index, the crystalline phase and the long period. As the previous study was performed on small molding devices (DSC pans), the process is now transposed to macroscopic scale. In this aim, a special mold was designed because of the huge dilation/retraction of the polymer during its melting/crystallization. In order to take into account the polymer change of volume, the design implies a dynamic mold with springs which act on a piston. A non-adhesive coating was also added on the metallic parts of the mold, as depicted in Figure III.22a.

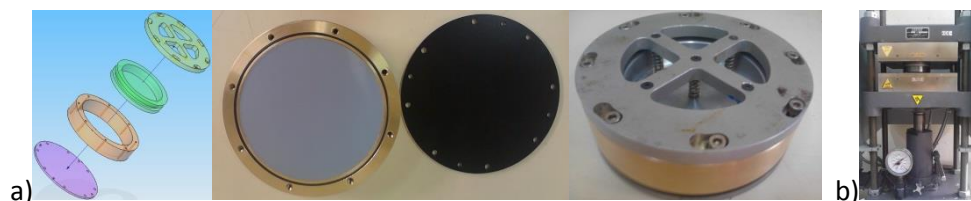


Figure III.22: a) Isotherm mold and b) press at 270°C containing the mold

Finally, the isotherm process consists in maintaining the mold in the press at 270°C during 10min (see Figure III.22b) before transferring it to a silicon oil bath regulated at the chosen crystallization temperature.

Different molecular masses (15K and 31K) were tested. The employed time and T_c temperatures ($\pm 0.5^\circ\text{C}$) are described below, according to the kinetics crystallization study:

- 202°C during 1h
- 205°C during 1h30
- 209°C during 3h
- 213°C during 24h
- 216°C during 72h

WAXS patterns were performed: the crystalline structure was pure α phase for all these isotherms as shown in Figure III.23. One can notice that depending on the isotherm temperature, the angular gap between the two α peaks changes: this angular gap can be defined as an index of crystalline perfection (ICP) [46] [47]. The ICP increases for higher temperatures which correspond to a higher crystalline perfection. It is also confirmed by DSC where a higher melting temperature is observed for higher isotherm temperature: the more stable is the structure, the higher it melts. Any special influence of the molecular mass has been observed on the structure for an isotherm at a same temperature.

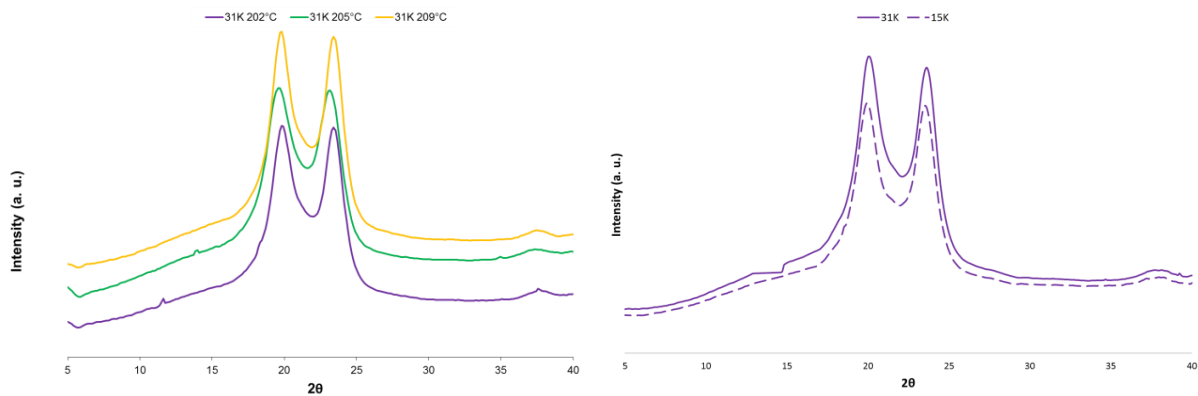


Figure III.23: DRX patterns for isotherms at different T_c for PA6 31 K (l.) and for PA6 15K and 31K at $T_c = 202^\circ\text{C}$ (r.)

SAXS and DSC were also carried out in order to determine L_p and L_c (with Lorentz correction). The results are sum up in the Table III.4. These results confirm us that it was possible to obtain significant changes of the crystallinity index and the long period.

Table III.4: DRX and DSC combined data for PA6 isotherms

Sample name	Crystalline phase	L_p (nm)	X_c (%)	L_c (nm)(with DSC)
15K iso 202°C	α	10.9	27	2.7
31K iso 202°C	α	9.8	24	2.1
15K iso 205°C	α	11.0	31	2.9
31K iso 205°C	α	10.2	32	3.2
31K iso 209°C	α	10.8		
15K iso 213°C	α	11.2	35	3.6
31K iso 213°C	α	11.3	35	3.7
31K iso 216°C	α	11.8	31	3.5

As a conclusion, the aim of isotherm is to produce a stable phase and to have a high crystallinity. In our case, in order to have only α phase, the crystallization conditions are:

- $202^{\circ}\text{C} < T_c < 216^{\circ}\text{C}$
- $1\text{h} < \text{time} < 72\text{h}$

The obtained microstructures are summarized in Figure III.24. The initial state corresponds to injection molded sheets. One can notice that $T=213^{\circ}\text{C}$ corresponds to an inflexion point for X_c .

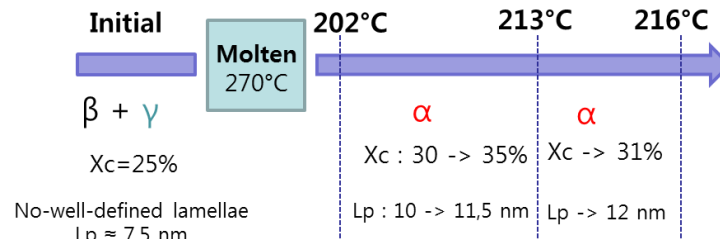


Figure III.24: Isotherm consequences on PA6 microstructure

III.3. Annealing

III.3.1. Adapted principle

For our study, we have chosen to work from the injected molding sheets. Indeed even if there are presence of defaults due to impurities induced by the process, as the process is the same for each molecular mass, we can suppose that the impurities density is the same for every sample. The annealing was performed at different temperatures T_a in order to obtain various but stable crystalline phases, as well as various lamella thicknesses. The used diagram is shown in Figure III.25.

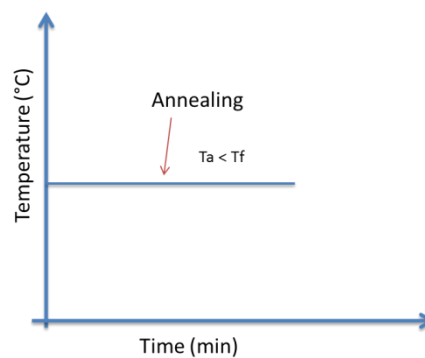


Figure III.25 : Diagram of an annealing on injected molding sheet

III.3.2. Annealing characterization

As said previously, one of the aims of this thesis is to study the mechanical behaviors of PA6 under the influence of the microstructure. Annealing treatment allows changing the long period as well as the crystalline phase. Indeed, as reported in literature, β and γ phases can transform into α phase under specific conditions. These specific conditions are studied in this part. The scheme of the annealing treatment was depicted in Figure III.25: it allows studying both the influence of annealing temperature and time spent at T_a .

The influence of temperature with sufficient hold times is exhibited in Figure III.26. It clearly shows that annealing temperatures under 195°C do not allow the total transformation of β into α phase. On the contrary, above 195°C we clearly observed the presence of the two α phase peaks ((200) at $2\theta=20.21^\circ$ and (002)+(20 $\bar{2}$) at $2\theta\approx 24^\circ$).

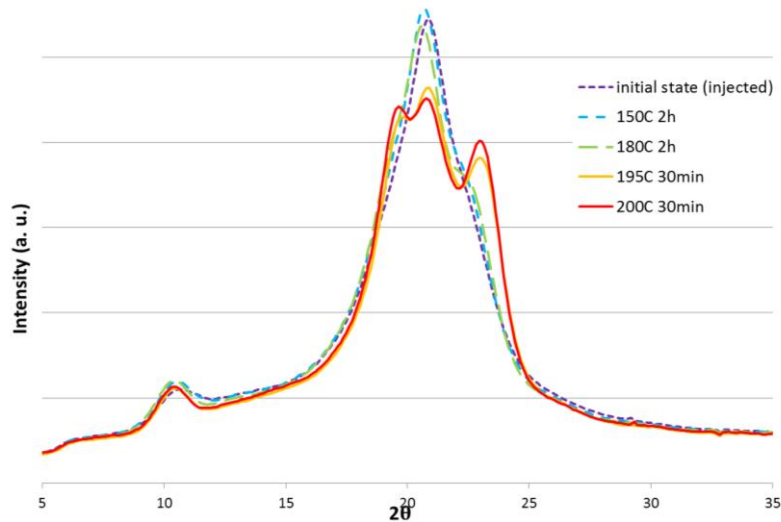


Figure III.26: WAXS patterns at 23°C concerning PA6 for different annealing temperatures

The influence of hold time was also studied, as shown in Figure III.27. The chosen annealing temperature was 200°C. It can be noted that 30 seconds is a too short time but from 2min, no crystalline change can be observed, meaning that all the β phase has been transformed into α phase. An annealing temperature of $T_a = 215^\circ\text{C}$ has also been examined and at this temperature another phase transformation has been reported: the $\gamma \rightarrow \alpha$ phase transformation. Indeed, on the WAXS pattern, only α phase was observed for this temperature and this was valid for all the molecular masses. Thus, depending on the annealing temperature, we are able to transform our initial injected molding sheet containing a mixture of $\beta + \gamma$ into a mixture of $\alpha + \gamma$ or into pure α phase.

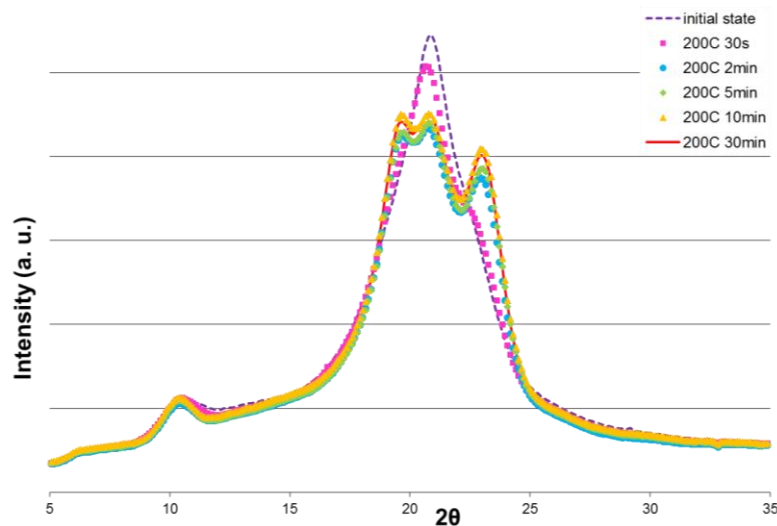


Figure III.27: WAXS patterns at 23°C concerning PA6 for different annealing times at $T_a = 200^\circ\text{C}$

The same samples have also been examined under SAXS. The effect of the annealing on the long period is depicted in Figure III.28. During the annealing at 200°C, we know that the $\beta \rightarrow \alpha$ transformation occurred thanks to WAXS. Concerning SAXS, it can be noted that the initial injected

sample has a broad halo and a large size of scattering ring, corresponding to a small L_p . For $T_a = 200^\circ\text{C}$, the scattering ring is much more focused, meaning a lower distribution lamellae size and as the size of the scattering ring decreases, it means that the long period has increased.

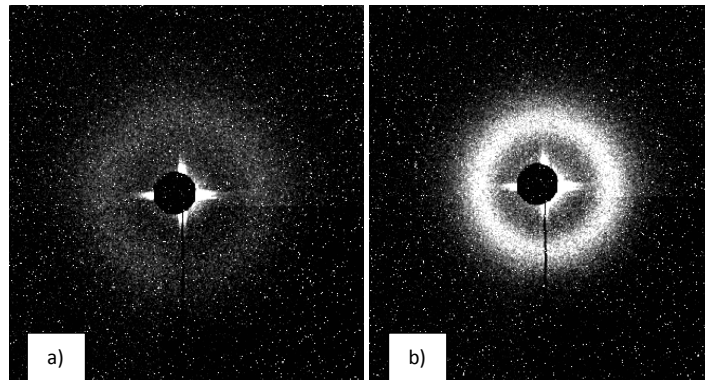


Figure III.28 : SAXS patterns of PA6 at 23°C : a) after injection and b) after an annealing at $T_a = 200^\circ\text{C}$ (30min)

The evolution of L_p as a function of T_a is shown in Figure III.29. L_p increases as well as T_a . However, one has to keep in mind that the increase of the long period is not necessary only connecting to the thickening of crystal because the crystalline phase is not always identical: above 180°C , the $\beta \rightarrow \alpha$ transformation occurs (detection by WAXS). Concerning the influence of the molecular masses, it seems that higher molecular mass has a higher L_p for a same annealing temperature. If we now compare with literature, Figure III.10 and Figure III.29 show the same trend: the evolution of L_p seems to show a change of slope around 180°C . It could be explained by the presence of the $\beta \rightarrow \alpha$ transformation at this temperature.

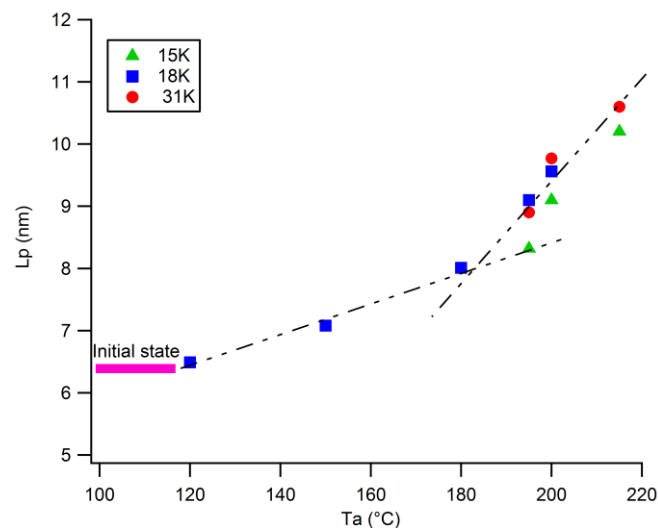


Figure III.29: Dependence of the long period (L_p) as a function of annealing temperature (T_a) for several PA6 molecular masses (15K, 18K and 31K)

The influence of time spent at the same annealing temperature was also investigated. It was found that increasing the time increases L_p however the impact on L_p was less important than the change of annealing temperature. It is more efficient to change the annealing temperature than the length of time spent at T_a in order to increase the long period. Thus, the thickening mechanism of L_p still remains difficult to understand.

In conclusion, annealing thermal treatments allow phase transformations ($\beta \rightarrow \alpha$ and $\gamma \rightarrow \alpha$) depending on temperatures. Furthermore, according to the temperature, the increase of L_p is more or less stronger depending if the temperature is below or above the temperature of $\beta \rightarrow \alpha$ starting transformation, i.e. around 180°C . To sum up, the obtained microstructures are described in Figure III.30. The initial state corresponds to injected molding sheets.

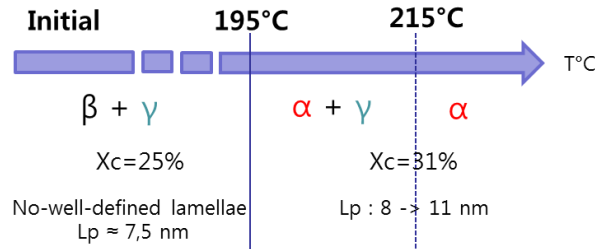


Figure III.30: Annealing consequences on PA6 microstructure

It is worth noticing that in the case of PA6, the annealing process can also be considered as a way to identify β phase. Indeed, as reported in chapter II, the WAXS pattern of β and γ phases are quite similar which makes difficult to identify the crystalline phases in particular in case of mixture (as for the injected sheets). The difficulty of identifying β phase happens also for DSC thermograms because due its transformation, the thermograms of α and β phases are quite similar. Finally, by performing an annealing above 195°C , the presence or absence of β phase can be validated.

III.4. Quenching

In Figure III.31a, the principle of a quench is depicted. In our case, the study was done on DSC hermetic pans in order to have the better thermal conduction between the sample and the desired quenching temperature. The samples were melted at 270°C during 10 min in order to erase memory effects and then plunged into iced water at 0°C in less than 5 seconds. The structures obtained by WAXS are shown in Figure III.31b.

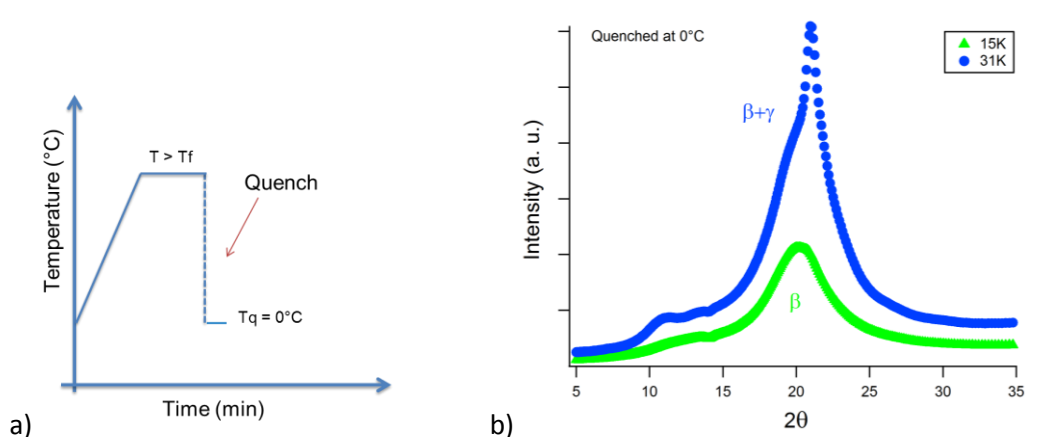


Figure III.31: a) Principle of quench; b) Influence of the molecular masses on microstructure after quenching treatment for bulk PA6

At this temperature and whatever the molecular mass, it was impossible to obtain a pure amorphous phase. Indeed, polyamide 6 needs a faster cooling rate to entirely be amorphized [48]. Generally, for bulk PA6, the polymer structure is changed by incorporating aromatic groups in order to facilitate the amorphization. Nonetheless, even if quenching allows a low X_c , the structure is not stable and when

the sample goes through its glass transition, a cold crystallization is induced as depicted on DSC thermograms of Figure III.32.

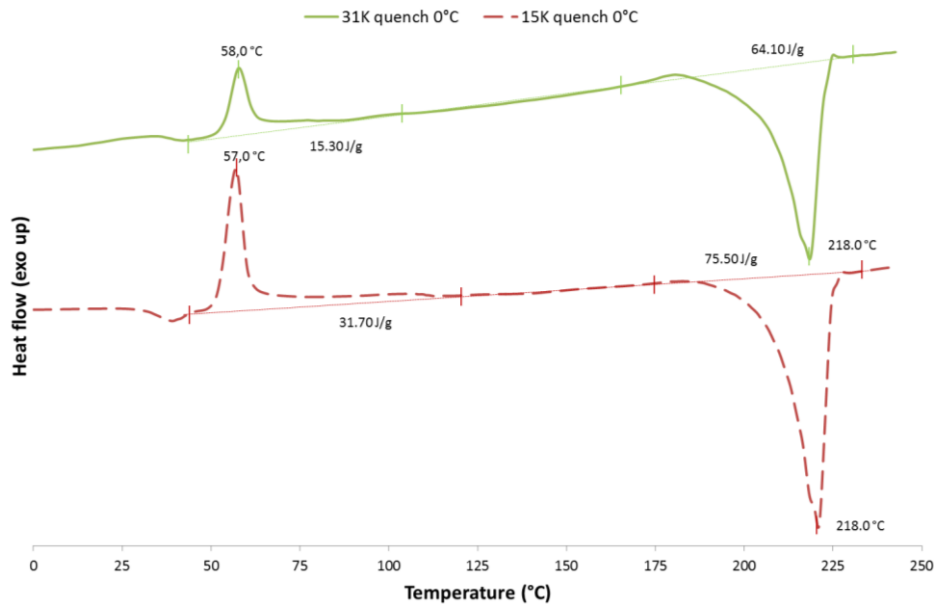


Figure III.32: Influence of molecular mass and structure on X_c upon a quenched sample followed by a cold crystallization

Let us now focus on Figure III.32 and the way to estimate the crystallinity index in the case of cold crystallization. Thanks to the method presented in annex (“Assessment of polyamide-6 crystallinity by DSC: structural changes and temperature dependence of the melting enthalpy”), the X_c calculations are the following:

$$\Delta H_f(58^\circ\text{C}) = 142 \text{ J/g}$$

For 31K:

$$X_c = \frac{64.1}{230} - \frac{15.30}{142} = 17 \%$$

For 15K:

$$X_c = \frac{75.5}{230} - \frac{31.70}{142} = 10.5 \%$$

Concerning the influence of the molecular mass, it seems that high molecular mass (31K) prefers to form ordered phase (γ) unlike the low molecular mass (15K), which exhibits only β phase as observed in Figure III.31b. 15K sample has also a lower crystallinity index than 31K. However, at the moment our kinetic studies (§III.2.1 and non-isothermal crystallizations non exhibited) do not allow us reporting these observations.

In conclusion, different kinds of quench have been tried but in the case of polyamide 6, the β metastable phase was present in every crystalline structure as well as cold crystallization. However, the presence of cold crystallization is inadequate with our first goal: study mechanical behavior below and above the glass transition temperature. Indeed, depending on the temperature, the structure is affected. Furthermore, the influence of speed and quench temperature had a real impact on microstructure and a slight difference could induce a big change in microstructure, giving us a difficult repeatability. However, it has allowed us to bring out the molecular mass effect on crystalline structure (Figure III.31). Likewise, the observation of cold crystallization after quench (Figure III.32) has allowed us to spotlight a problem of characterization of the absolute fusion

enthalpy (ΔH_f) and so a bad approximation of crystallinity rate (χ_c) in the case of low crystallized PA6. Furthermore, doing quench from DSC pans to macroscopic scale brought out a technology lock. Indeed, it was impossible for us to obtain the same results because we did not have a mold sufficiently strong to resist to the melting deformation and also waterproof. Usually, quenching is performed on thin films whereas our samples are thick, which increases the difficulty of cooling. Thus, the quenching was not kept for our final selection of materials.

III.5. Time-Temperature-Crystallization (TTC) diagram of PA6

One of the objectives of §I.6 was to be able to plot a TTC diagram of PA6, like for iPP polymer. Thanks to our experiments, we were able to learn more on the influence of thermal treatments on the crystalline microstructure. A summary of the observed consequences on isotherm and annealing treatments is shown in Figure III.33. It allows us to better know the condition necessary for phase transformation thanks to thermal treatments. Indeed, β phase can be converted into α phase thanks to annealing. A time-temperature dependence has been pointed out. The transformation or fusion then recrystallization of γ into α phase has also been demonstrated.

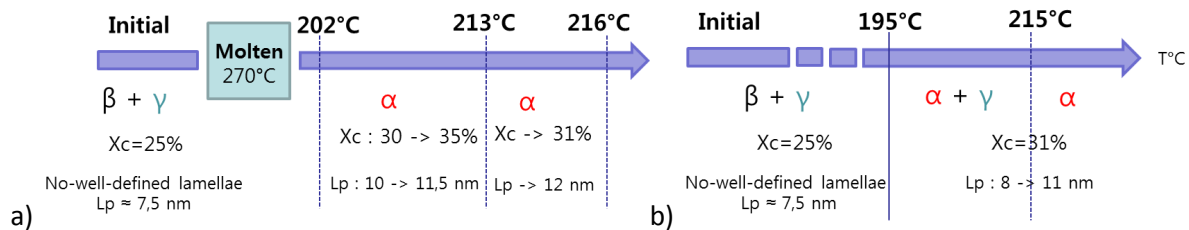


Figure III.33: a) Isotherm and b) annealing consequences on PA6 microstructure

A proposition of TTC diagram is plotted in Figure III.34, thanks to our experiments and data of literature. It is possible to obtain α phase from the melt state by cooling down the sample at high crystallization temperatures (way 1). If the crystallization temperature is colder, γ phase can appear alone or depending on the temperature with α phase (way 3). Finally if crystallization temperature is really low, as it is the case in the injection process for our material (mold at 60°C) or rolled cast films, the formation of β is possible (way 5). Now if the sample is melted and then immediately quenched, by doing an annealing treatment, we can either have pure α phase for high temperature (way 2), γ phase for intermediate temperature (way 4) or β phase at low temperature (way 6). Indeed, on quenched sample after cold crystallization, the presence of β phase was proved by WAXS. Note that this TTC diagram is pertinent for kinetics but not for the stability limits of the different phases. For example, if β crystals are present after quenching, doing an annealing at 150°C will not transform the β phase into γ . When performing annealing on pre-crystallized samples, the data depicted in Figure III.33b may be used in order to determine the temperature range of the phase transformations.

Anyway, this diagram shows us how difficult it can be to obtain one given pure phase except for α phase. A lot of precautions and special conditions have to be taken. Furthermore, from the melting state, the cooling speed and temperature play an important parameter. As easy it is to control the temperature, the same does not go for the cooling speed and constitutes for us a technological issue, in particular for preparing “macroscopic” samples.

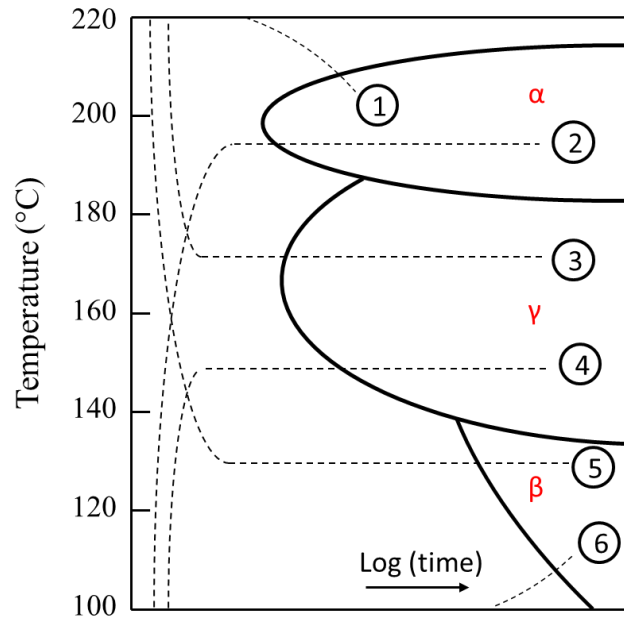


Figure III.34: Schematic TTC diagram for PA6: 1) Slow cooling from the molten state at high crystallization temperature, 2) Isotherm at high temperature from a quenching state, 3) Isotherm from the melting state, 4) Isotherm from a quenching state at intermediate crystallization temperature, 5) Fast cooling from the melting state at low crystallization temperature, 6) Heating from a quenching state

IV. Final choice of materials

In order to work on the multi-scale structure of PA6, the aim of the materials choice is to have different materials with various molecular mass, crystallinity rate, long period L_p , crystalline phases, crystalline perfection ... via thermal treatments as described previously.

For better understanding of the coupling between amorphous and crystalline phase, initially the aim was to have “model” materials. This means having materials with iso-crystalline phases (α , γ and β only) and for each crystalline phases having a range of various crystallinity index and long period. However as described previously and sum up in Figure III.34, the interaction between parameters (crystallinity rate, long period L_p , crystalline phases) is complex and unfortunately it was impossible for us to perform materials at a macroscopic scale with only one crystalline phase except in the case of pure α phase. Thus, the choice of material was adapted in order to still have a large panel of various samples.

Furthermore, previously, we have exhibited two ways of processing a sample: by injection molding or thermo-compression molding. However, concerning the thermo-compression way, the crystalline structure of the sample was highly sensitive to the cooling speed and environmental temperature. The repeatability of the process, as well as the effect that the process can have on the microstructure, were too hard to deal with. In addition, as transcrystallinity has an impact on mechanical properties, like the increase of the yield stress and the Young's modulus during stretching [43], this could introduce a bias for our study concerning the influence of the microstructure on these mechanical properties. As it is difficult to separate the effects of transcrystallinity and the crystalline phases, we have finally chosen to work only on the injected samples. Concerning the presence of defaults due to impurities induced by the process, we supposed that the impurities density was the same for every sheet, as the process was the same for every sheet.

Thus, the final choice of thermal treatments is reported in Table III.5. It allows a large panel of microstructures: various crystalline phases, a large range of crystallinity index and long period... as it is further described below and in Table III.7.

Table III.5: 15K and 31K selection for macroscopic study

Sample name	Thermal treatment	Symbol for 15K	Symbol for 31K
INJ	Initially injected	▲	●
A200	Annealed at 200°C during 30 min	▲	●
A215	Annealed at 215°C during 10 min	▲	●
I213	Isotherm at 213°C during 24 h	▲	●

The impact of thermal treatments on molecular masses has been checked by GPC. The results are shown in Figure III.35.

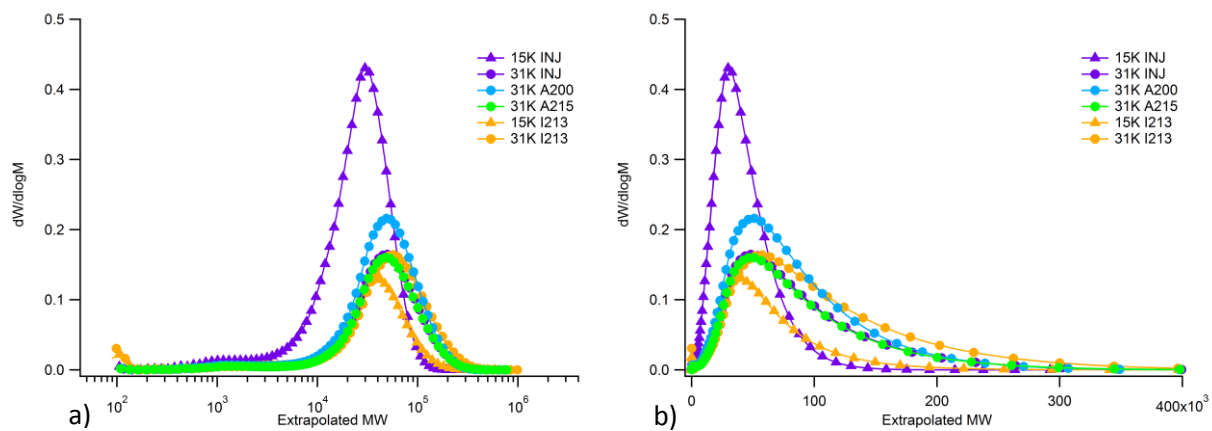


Figure III.35: GPC curves for PA6 samples a) with log scale and b) with linear scale

The values in absolute mass for a truncation of oligomers at 2000g/mol (classical truncation for polyamides) for the different thermal treatments are given in Table III.6.

Table III.6 : GPC data of our PA6 samples with oligomers truncation at 2000g/mol

Sample	Symbol	Mn	Mw	Ip (dispersity)	Bulk IV
15K INJ	▲	19341	31516	1.629	0.7202
31K INJ	●	30279	56478	1.865	1.1286
31K A200	●	30289	56479	1.865	1.1698
31K A215	●	30195	56152	1.860	1.1480
15K I213	▲	24238	43004	1.774	0.8263
31K I213	●	32027	67444	2.106	1.2477

It has allowed us to check that during thermal treatments, the molecular mass of our samples is nearly not affected and remains constant. A little bit of post-condensation is observed for the samples having undergone an isotherm.

The microstructure observed in microscopy under polarization light is depicted in Figure III.36 for 15K and in Figure III.37 for 31K PA6. The scale bar corresponds to 50 μm . The observations are made on a cut of 5 μm across the injected sheet perpendicular to the surface. This means that we observe what happened on a thickness section.

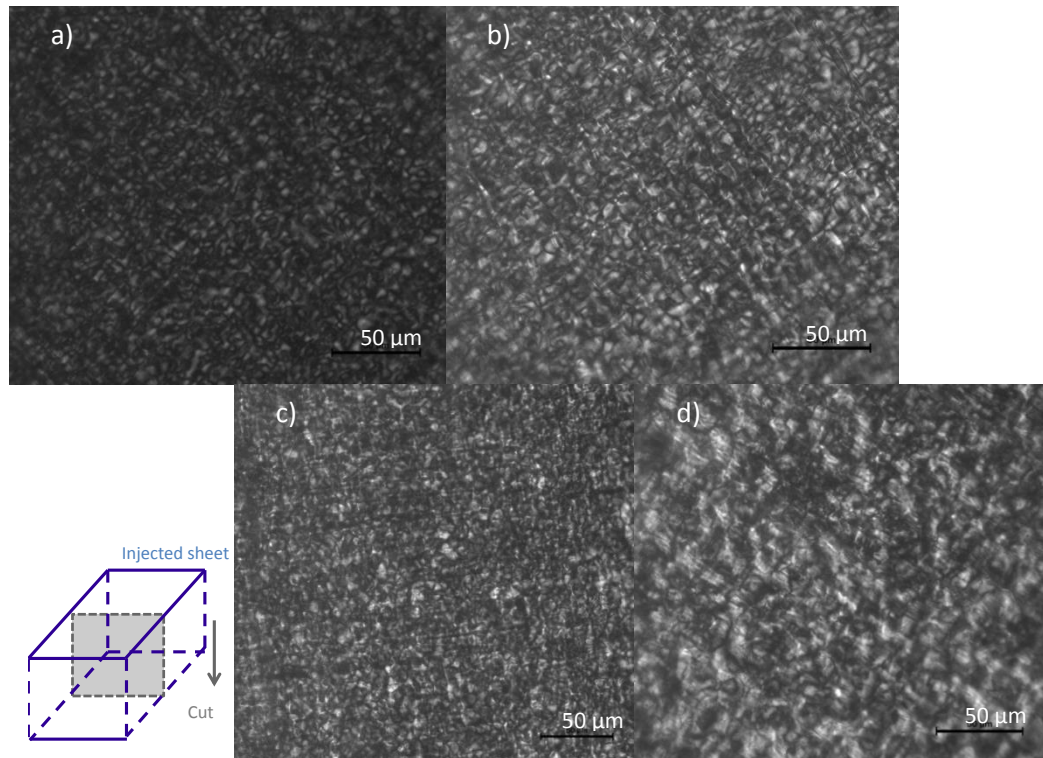


Figure III.36: Microstructures of 15K PA 6 samples observed in optical microscopy under polarized light: a) INJ, b) A200, c) A215 and d) I213 samples ; Scale bar = 50 μm

The skin-core effect has been taken into account: for J sample there is a layer of 60 μm at each side of the sheet, meaning 120 μm of skin for 1480 μm of core corresponding to 8% of the sample. When the polymer is annealed the skin is reduced to less than 20 μm , which corresponds to a skin effect of 2%. That is why the skin effect will not be taken into account during tensile tests. For a film this could have an influence however on bulk material, this is clearly negligible.

Back to the microstructure, a few spherulites are visible on the injected sheet but most of the crystalline structure is composed of small crystallites. Annealing does not seem to really affect the microstructure, maybe the crystallites grow a little bit. Isotherm is the only thermal treatment which is different from the other ones: larger crystallites and spherulites are visible (increase from ≈ 10 to ≈ 25 μm). However most of the microstructure does not seem to be composed of spherulites but of crystallites. These remarks apply for both molecular masses. Indeed, on the micro scale, molecular mass does not seem to affect the microstructure.

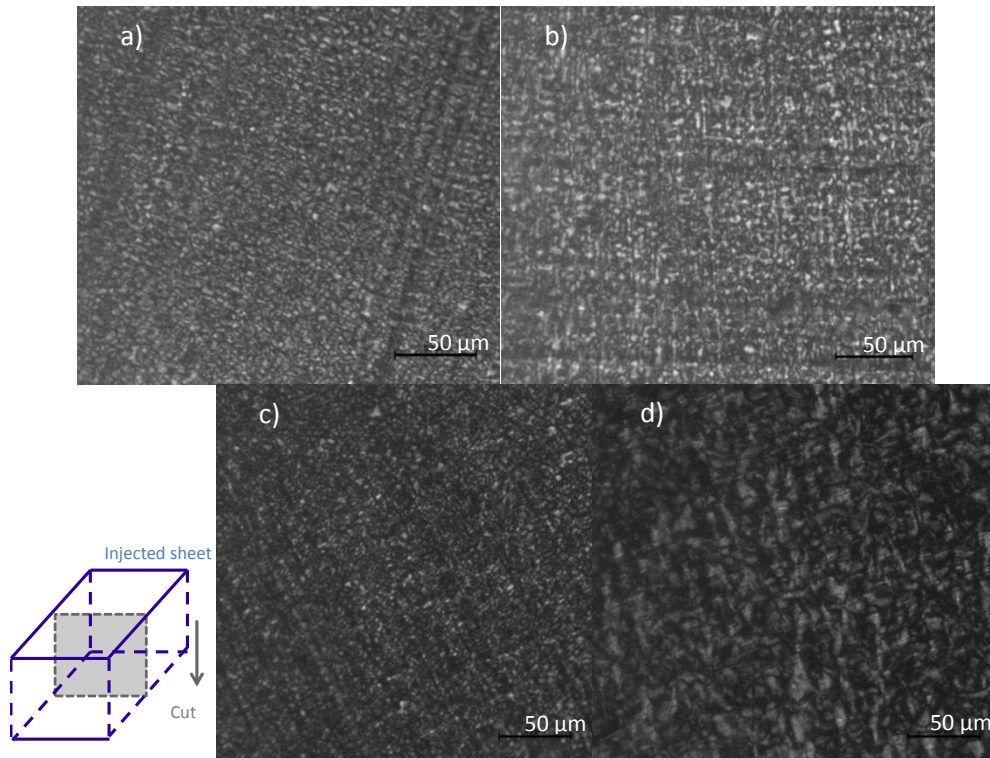


Figure III.37: Microstructures of 31K PA 6 samples observed in optical microscopy under polarized light: a) INJ, b) A200, c) A215 and d) I213 samples ; Scale bar = 50 μm

Let us now focus on the characterization of the crystalline phase for the various samples, meaning its crystalline phase, crystallinity index X_c , crystalline perfection, long period L_p , crystalline thickness L_c or melting point T_f . These characteristics were determined thanks to DSC, WAXS and SAXS, as explained in chapter II, and are reported in Table III.7. Our set of samples exhibits a widely microstructure with various crystalline phases: a mixture of $\beta+\gamma$ phases for INJ samples, a mixture of $\alpha+\gamma$ phase for A200 samples and finally pure α phase for A215 and I213 samples whatever the molecular mass. X_c increases from 24% to 35%, meaning a relative increase of 46%, which for a polyamide 6 is really impressive. L_p has increased of 57%, from 7.2 to 11.3 nm.

Table III.7: Sample characteristics (angular gap corresponds the α peaks gap, and an estimation of the crystalline perfection)

Sample name (Mn thermal treatment)	Crystalline phase	Ratio α/γ (DSC)	Angular gap ($^\circ$) for α	L_p (nm)	L_c (nm) (with DSC)	X_c (%)	T_f (peak $^\circ\text{C}$)
15K INJ	$\beta+\gamma$			7.2	1.6	29	
31K INJ	$\beta+\gamma$			7.4	2	24	
15K A200	$\alpha+\gamma$	70/30	3.2	9.1	2.8	34	224
31K A200	$\alpha+\gamma$	60/40	3.2	10	2.8	31	223
15K A215	α	100	3.7	10.2	3.3	35	225
31K A215	α	100	3.7	10.7	3.0	31	225
15K I213	α	100	3.8	11.2	3.6	35	230
31K I213	α	100	3.9	11.3	3.4	33	230

Concerning the effect of the molecular mass, we observe that for a same given process or heat treatment the same crystalline structure is obtained, as shown in Figure III.38. Concerning I213 samples (Figure III.38a), only α phase is encountered for both molecular masses. However, if we focused on A200 samples (Figure III.38b), even if the same mixture $\alpha+\gamma$ phases is displayed, one can notice that the ratio of α/γ phases seems to be affected. This was confirmed by the estimation made in DSC. Furthermore, for a same annealing temperature, higher molecular mass has a higher long period L_p , as seen previously in Figure III.29. On the contrary, lower molecular mass, whatever the treatment is, has always a higher crystallinity index.

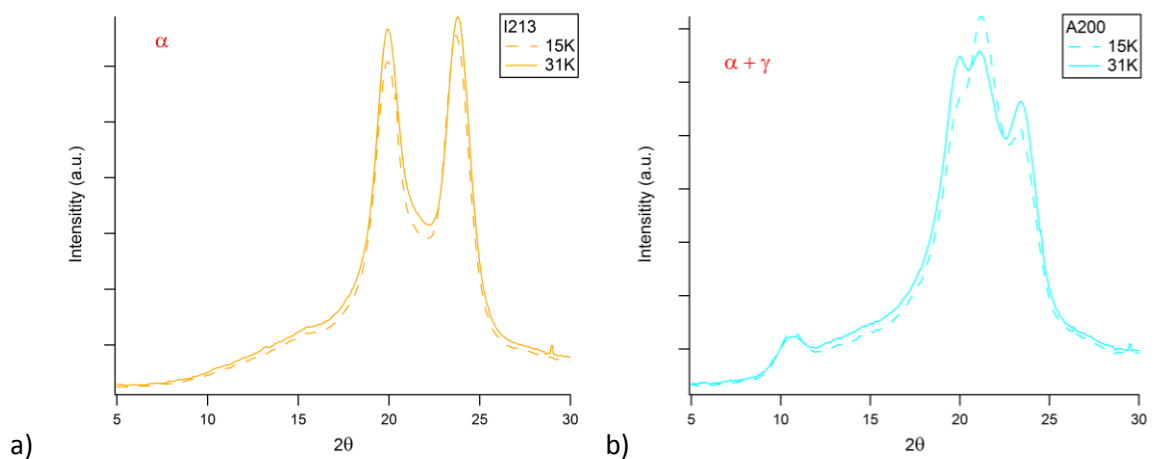


Figure III.38: DRX patterns for PA6 low (15K) and high (31K) molecular masses for a) I213 and b) A200 samples

Finally, with this choice of samples, we are able to exhibit a large panel of microstructure. It will allow us to better understand the effect of the microstructure on some specific mechanical properties as well as the deformation mechanisms. The multi-scale mechanical investigations on these materials are displayed in the following chapters (IV, V and VI).

References

- [1] F. Puel, S. Veessler and D. Mangin, "Cristallisation : Aspects théoriques," *Techniques de l'Ingénieur*, p. J 2710, 2005.
- [2] S. Cheng and B. Lotz, "Enthalpic and entropic origins of nucleation barriers during polymer crystallization: the Hoffman-Lauritzen theory and beyond," *Polymer*, vol. 46, pp. 8662-8681, 2005.
- [3] M. Muthukumar, "Nucleation in polymer crystallization," *Advances in Chemical Physics*, vol. 128, pp. 1-63, 2004.
- [4] A. Maus, E. Hempel, T. Thurn-Albrecht and K. Saalwächter, "Memory effect in isothermal crystallization of syndiotactic polypropylene - role of melt structure and dynamics ?," *The European Physical Journal E*, vol. 23, pp. 91-101, 2007.
- [5] P. Meares, *Polymers : structure and bulk properties*, London: Van Nostrand, 1965, pp. 149-151.
- [6] S. Aharoni, *n-Nylons : their synthesis, structure and properties*, John Wiley & Sons, 1997, pp. 284-296.
- [7] Y. P. Khanna, A. C. Reimschuessel, A. Banerjee and C. Altman, "Memory effects in polymers. II. Processing history vs. crystallization rate of nylon 6 - Observation of phenomenon and product behavior," *Polymer Engineering and Science*, vol. 28, pp. 1600-1606, 1988.
- [8] N. Avramova and S. Fakirov, "Cumulative "memory" effect in nylon-6," *Journal of Polymer Sciences: Polymer Physics Edition*, vol. 21, pp. 311-313, 1984.
- [9] N. Avramova and S. Fakirov, "Cumulative erasing effect in the melt memory," *Journal of Polymer Science: Part B: Polymer Physics Edition*, vol. 24, pp. 761-768, 1986.
- [10] Y. P. Khanna and A. C. Reimschuessel, "Memory effects in polymers. I. Orientation memory in the molten state - Its relationship to polymer structure and influence on recrystallization rate and morphology," *Journal of Applied Polymer Science*, vol. 35, pp. 2259-2268, 1988.
- [11] Y. P. Khanna, R. Kumar and A. C. Reimschuessel, "Memory effects in polymers. III. Processing history vs. crystallization rate of nylon 6 - Comments on the origin of memory effect," *Polymer Engineering and Science*, vol. 28, pp. 1607-1611, 1988.
- [12] Y. P. Khanna, R. Kumar and A. C. Reimschuessel, "Memory effects in polymers. IV. Processing history vs. crystallization rate - Effect of polymer structure," *Polymer Engineering and Science*, vol. 28, pp. 1612-1615, 1988.

- [13] P. Tidick, S. Fakirov, N. Avramova and H. Zachmann, "Effect of the melt annealing time on the crystallization of nylon-6 with various molecular weights," *Colloid & Polymer Science*, vol. 262, pp. 445-449, 1984.
- [14] E. Turska and S. Gogolewski, "Study on crystallization of nylon-6 (polycapramide): Part I. Isothermal crystallization," *Polymer*, vol. 10, pp. 616-628, 1971.
- [15] E. Turska and S. Gogolewski, "Study on crystallization of nylon-6 (polycapramide): Part 2. Effect of molecular weight on isothermal crystallization kinetics," *Polymer*, vol. 10, pp. 629-641, 1971.
- [16] J. Magill, "Melting behaviour and spherulitic crystallization of polycaproamide (nylon 6)," *Polymer*, vol. 3, pp. 43-51, 1962.
- [17] J. Magill, "Crystallization kinetics study of nylon 6," *Polymer*, vol. 3, pp. 655-664, 1962.
- [18] J. Magill, "Crystallization of polyamides. II-Nylon 6 and nylon 66," *Polymer*, vol. 6, pp. 367-371, 1965.
- [19] K.-H. Illers, "Polymorphie, Kristallinität und Schmelzwärme von Poly(ϵ -caprolactam), 2)," *Makromolekulare Chemie*, vol. 179, pp. 497-507, 1978.
- [20] G. Gurato, D. Gaidano and R. Zannetti, "Influence of nucleating-agents on crystallization of 6-polyamide," *Makromolekulare Chemie*, vol. 179, pp. 231-245, 1978.
- [21] J. Hoffman and R. Miller, "Kinetic of crystallization from the melt and chain folding in polyethylene fractions revisited: theory and experiment," *Polymer*, vol. 38, no. 13, pp. 3151-3212, 1997.
- [22] M. Avrami, "Kinetics of phase change. I General theory," *Journal of Chemical Physics*, vol. 7, pp. 1103-1112, 1939.
- [23] M. Avrami, "Kinetics of phase change. II Transformation-time relations for random distribution of nuclei," *Journal of Chemical Physics*, vol. 8, p. 212, 1940.
- [24] M. Inoue, "Crystallization kinetics of polycapramide," *Journal of Polymer Science*, vol. 55, pp. 753-766, 1961.
- [25] K. K. H. Hess, "Zur Kenntnis der Feinstruktur der Polyamidfasern," *Zeitschrift für Physikalische Chemie*, vol. 193, p. 196, 1944.
- [26] M. Hiram, "SAXD studies on bulk crystallization of nylon 6. I. Changes in crystal structure, heat of fusion, and surface free energy of lamellar crystals with crystallization temperature," *Journal of Macromolecular Science. Part B Physics*, vol. 23, pp. 397-414, 1984-85.
- [27] S. Gogolewski, M. Gasiorek, K. Czerniawska and A. J. Pennings, "Annealing of melt-crystallized nylon 6," *Colloid & Polymer Science*, vol. 260, pp. 859-863, 1982.

- [28] M. Hirami, "Dependence of the long period of nylon 6 on annealing temperature," *Die Makromolekulare Chemie*, vol. 105, pp. 296-299, 1967.
- [29] N. S. Murthy, S. M. Aharoni and A. B. Szollosi, "Stability of the gamma form and the development of the alpha form in nylon 6," *Journal of Polymer Science: Polymer Physics Edition*, vol. 23, pp. 2549-2565, 1985.
- [30] F. Auriemma, V. Petraccone, L. Parravicini and P. Corradini, "Mesomorphic form (β) of Nylon 6," *Macromolecules*, vol. 30, pp. 7554-7559, 1997.
- [31] N. S. Murthy, "Hydrogen bonding, mobility and structural transitions in aliphatic polyamides," *Journal of Polymer Science: Polymer Physics*, vol. 44, pp. 1763-1782, 2006.
- [32] I. Kolesov, D. Mileva, R. Androsch and C. Schick, "Structure formation of polyamide 6 from the glassy state by fast scanning chip calorimetry," *Polymer*, vol. 52, pp. 5156-5165, 2011.
- [33] A. Ziabicki, "Über die mesomorphe β -Form von Polycapronamid und ihre Umwandlung in die kristalline Form α ," *Kolloid-Zeitschrift*, vol. 167, pp. 132-141, 1959.
- [34] L. Penel-Pierron, "Transition de phase induite par déformation dans les polymères à liaisons hydrogène : cas des polymères éthylène/alcool vinylique et du polyamide 6," USTL, Lille, 1998.
- [35] H. J. Arimoto, "Alpha-gamma transition of nylon 6," *Journal of Polymer Science Part A*, vol. 2, pp. 2283-2295, 1964.
- [36] K. Hoashi and R. D. Andrews, "Morphological changes in nylon 6 and effect on mechanical properties. II. Dynamic mechanical properties," *Journal of Polymer Science: Part C: Polymer Symposia*, vol. 38, pp. 387-404, 1972.
- [37] K. Miyasaka and K. J. Makishim, "Transition of nylon 6 γ -phase crystals by stretching in the chain direction," *Journal of Polymer Science Part A*, vol. 5, pp. 3017-3027, 1967.
- [38] M. Kyotani and S. Mitsuhashi, "Studies on crystalline forms of nylon 6. II. Crystallization from the melt," *Journal of Polymer Sciences: Polymer Physics*, vol. 10, pp. 1497-1508, 1972.
- [39] X. Hu and X. Zhao, "Effects of annealing (solid and melt) on the time evolution of polymorphic structure of PA6/silicate nanocomposites," *Polymer*, vol. 45, pp. 3819-3825, 2004.
- [40] X.-Y. Zhao and B.-Z. Zhang, "The effects of annealing (solid and melt) on the time evolution of the polymorphic structure of polyamide 6," *Journal of Applied Polymer Science*, vol. 115, pp. 1688-1694, 2010.
- [41] Y. Zhang, Y. Zhang, S. Liu, A. Huang, Z. Chi, J. Xu and J. Economy, "Phase stability and melting behavior of the alpha and gamma phases of nylon 6," *Journal of Applied Polymer Science*, vol. 120, pp. 1885-1891, 2011.

- [42] T. Labour, C. Gauthier, R. Seguela, G. Vigier, Y. Bomal and G. Orange, "Influence of the β crystalline phase on the mechanical properties of unfilled and CaCO₃-filled polypropylene. I. Structural and mechanical characterisation," *Polymer*, vol. 42, pp. 7127-7135, 2011.
- [43] C. Magnet, "Cristallisation du polyamide 66 utilisé en filage textile," Thèse ENS des Mines de Paris, 1993.
- [44] M. Raimo, "'Kinematic' analysis of growth and coalescence of spherulites for predictions on spherulitic morphology and on the crystallization mechanism," *Progress in Polymer Science*, vol. 32, pp. 597-622, 2007.
- [45] A. Wlochowicz and M. Eder, "The effect of TiO₂ on the kinetics of polyamide 6 crystallization," *Colloid & Polymer Science*, vol. 261, pp. 621-625, 1983.
- [46] N. Murthy, H. Minor and R. Latif, "Effect of annealing on the structure and morphology of nylon 6 fibers," *Journal of Macromolecular Science, Part B: Physics*, vol. 26, no. 4, pp. 427-446, 1987.
- [47] N. Murthy, R. Bray, S. Correale and R. Moore, "Drawing and annealing of nylon-6 fibres: studies of crystal growth, orientation of amorphous and crystalline domains and their influence on properties," *Polymer*, vol. 36, no. 20, pp. 3863-3873, 1995.
- [48] D. Cavallo, L. Gardella, G. Alfonso, P. G., L. Balzano and R. Androsch, "Effect of cooling rate on the crystal/mesophase polymorphism of polyamide 6," *Colloid Polymer Science*, vol. 289, pp. 1073-1079, 2011.

Chapter IV: Macroscopic mechanical properties

I.	Dynamic Mechanical Analysis (DMA).....	92
II.	Tensile tests.....	96
II.1.	Above the glass transition at $T = T_g + 65^\circ\text{C} = 120^\circ\text{C}$	96
II.2.	Below the glass transition at $T = T_g - 65^\circ\text{C} = -10^\circ\text{C}$	99
III.	Discussion	102
III.1.	Effect of molecular mass	102
III.2.	Poisson's coefficient	104
III.3.	Issues	105
	References.....	106

All mechanical tests were carried out on dry PA6 samples. Water uptake was not expected to occur during the time of the experiments under ambient conditions with relative humidity $10 < RH < 50\%$, in the case of the bulk samples 1.5 mm thick of the present study. Indeed, the equilibrium time for water uptake for 0.25 mm thick samples is about 5 days at 20°C for a large relative humidity range [1] [2]. For that reason, it is assumed that the PA6 water content is maintained at its original low value for the duration of the experiments so as to obtain reproducible results during mechanical testing [3].

In this chapter, macroscopic mechanical properties are evaluated and discussed. The list of samples for the two polymers of molecular masses 15K and 31K is reminded in Table IV.1.

Table IV.1: Details on the “15K” and “31K” PA6 samples for the macroscopic tensile study

Name	Sample	Crystalline phase	Symbol for 15K	Symbol for 31K
INJ	Injected	$\beta+\gamma$	▲	●
A200	Annealed at 200°C	$\alpha+\gamma$	▲	●
A215	Annealed at 215°C	α	▲	●
I213	Isotherm at 213°C	α	▲	●
JA	Injected then aged	$\beta+\gamma$		●

In the first part of this chapter, the mechanical relaxations are studied by dynamical experiments in the linear regime, whereas in the second part, we are interested in the tensile properties. Finally, in the third part, the effects of the molecular mass and microstructure are discussed, as well as associated models.

I. Dynamic Mechanical Analysis (DMA)

Dynamic mechanical analysis allows studying the viscoelastic properties of a material by measuring its dynamical modulus at a given frequency as a function of temperature. Each DMA analysis was carried out twice for each sample. The measurements are reproducible and only one curve of each sample is plotted. The storage (elastic) modulus G' is plotted as a function of temperature in Figure IV.1 for all samples. The large drop of G' around 50°C is associated to the glass transition of the amorphous phase of the materials. The transition temperature seems to be a function of the crystallinity.

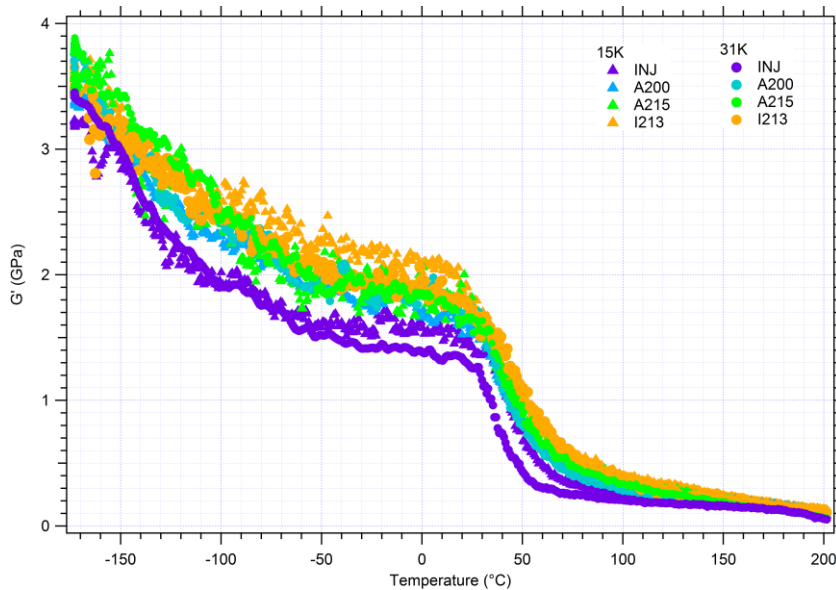


Figure IV.1 : Storage modulus G' as a function of temperature for PA6 samples at 1Hz

Regarding the elastic modulus, in the temperature range 80/150°C i.e. above T_g , the G' values are increasing in the order of increasing crystallinity, as depicted in Figure IV.2. Indeed, above T_g , the amorphous phase is much softer than the crystalline phase, so that the global stiffness of the material is dominated by the stiff crystalline volume fraction. In the temperature range -150/20°C, i.e. below T_g , the G' values are also sorted in the same increasing order as a function of crystallinity. This is somewhat surprising in consideration that the amorphous phase is in the glassy state. Though very stiff, the glassy state of polymers is generally not as stiff as the corresponding crystal [4]. This is the reason for the sensitivity of the macroscopic modulus to crystallinity at $T < T_g$. These points will be further discussed at the end of this chapter.

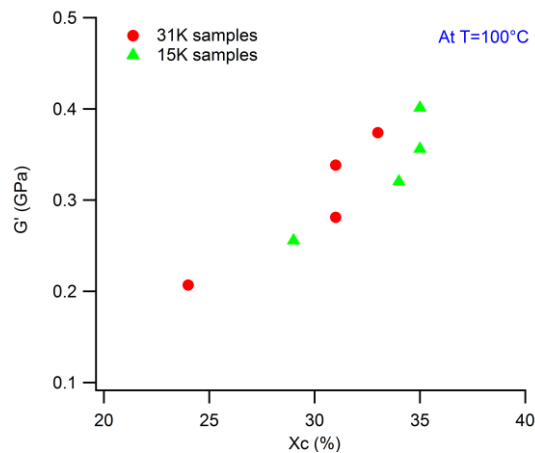


Figure IV.2: Storage modulus G' value as a function of crystallinity index for PA6 samples at $T=100^\circ\text{C}$

The loss factor $\tan\phi$ is also plotted in Figure IV.3. It provides better observation of the various relaxations processes, as described in §I.3.1 of chapter I. The main relaxation peak around 50°C, namely α relaxation, is associated with the glass transition of the amorphous phase. The other relaxations, β and γ , are secondary relaxations in the amorphous phase, corresponding to localized motions of functional groups along the polyamide chain as described in chapter I.

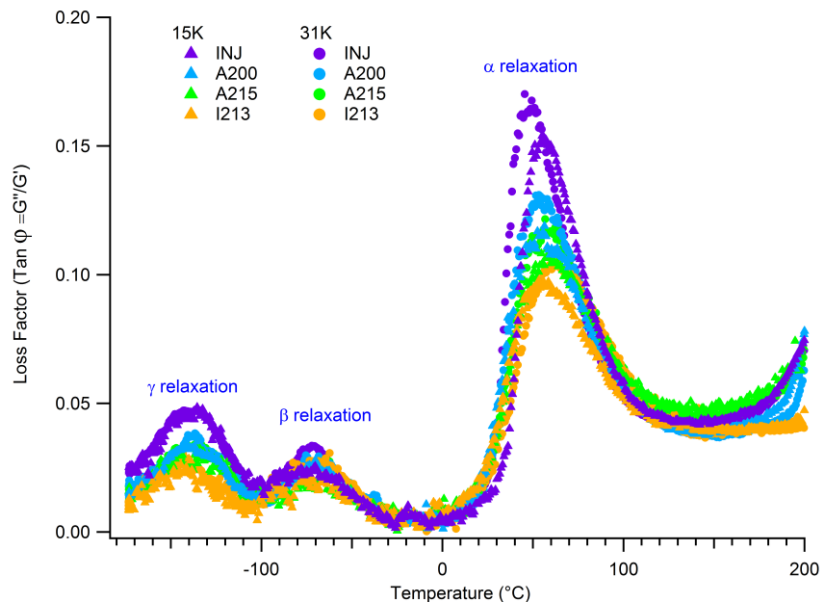


Figure IV.3: Loss factor $\tan \phi = G''/G'$ measured in DMA curves for 15K and 31K PA6 samples at 1Hz

The amplitude of the $\tan \phi$ peaks of these relaxations decreases as crystallinity increases. Looking more precisely at the amplitude of the α relaxation peak, one can notice that its drops with increasing X_c is not quantitatively consistent with the concomitant decrease in amorphous phase volume fraction. Indeed, when computing $\tan \phi = G''/G'$, the storage modulus G' is not the one of the amorphous phase but of the whole material, meaning it also takes into account the crystalline phase. Furthermore, we observed that the amplitude of the α relaxation peak for G'' does not change significantly, as depicted in Figure IV.4. A broadening of G'' peak on the high temperature side is observed on the samples having high crystallinity index. Thus, it means that the decrease of $\tan \phi$ is essentially due to the decrease of G' .

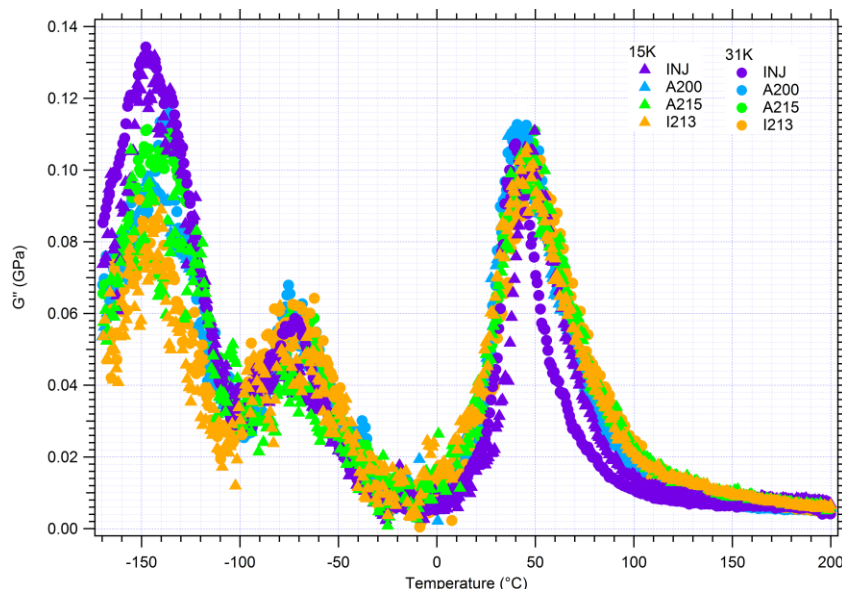


Figure IV.4: Loss modulus G'' as a function of temperature for PA6 samples at 1Hz

The temperature of α relaxation at 1 Hz corresponding to the maximum of the $\tan \phi$ peak, T_{α} , is plotted as a function of crystallinity index in Figure IV.5 (left). In agreement with Aharoni's data [5], this figure reveals a significant T_{α} shift to higher temperature with increasing crystallinity. This means

that the higher is X_c , the higher is the restriction of the cooperative molecular motions in the amorphous phase due to the amorphous chain anchoring onto the crystalline lamella surface. This is a rather common feature of semi-crystalline polymers, noticeably polyesters [6], though not systematic [4]. The reason may be an increasing confinement of the amorphous phase between the crystalline lamellae when the volume fraction of the latter ones increases.

In order to probe more specifically which structural factor of the semi-crystalline structure controls the amorphous chain mobility, the T_α temperature at 1 Hz has been reported as a function of the amorphous layer thickness L_a in Figure IV.5 (right). It is to be reminded here that only the long period of lamellar stacks is directly measured in SAXS. The L_c and L_a values are calculated by assuming that the crystalline fraction within lamellar stacks is equal to the overall crystallinity index (which is directly measured in DSC). Note that this hypothesis may not be fully verified for PA6 (see §II.3.3 and §II.3.4 of chapter II). It is found that T_α increases monotonically with L_a . This finding is somewhat surprising since the increase of the interlamellar distance would intuitively reduce the confinement effect and thus would induce a reduced influence of the crystal on the amorphous chain mobility. So, the observed phenomenon could be a consequence of another feature of the lamellar morphology, namely the change of form factor of the crystalline lamellae. Indeed, since crystallinity increases as a result of high temperature annealing, the crystalline lamellae are expected not only to thicken but also to increase both in width and length. This might result in an increase of the volume fraction of interlamellar amorphous phase within the lamella stacks at the expense of the amorphous phase out of the stacks. Therefore, as X_c increases, the increase of the amorphous phase fraction constrained between stiff crystalline lamellae would be the main reason for the upward shift of T_α . In such instance, the measured T_α would be an average value of the inter- and extra-lamellar fractions of the amorphous phase.

Androsch and Wunderlich [7] have reported that constraints on amorphous chains in semi-crystalline poly(ethylene-terephthalate) are partly released upon annealing together with increasing crystallinity and crystal perfectness. If this phenomenon would also apply to semi-crystalline PA6, it reinforces our assignment of the global increase of T_α with increasing X_c to an increase of the fraction of constrained amorphous phase.

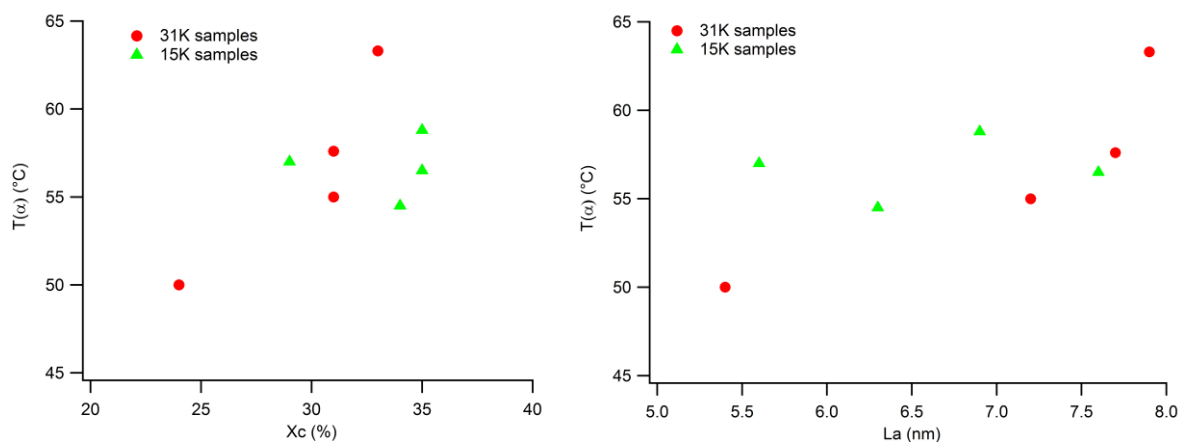


Figure IV.5: Temperature of the main relaxation $T(\alpha)$ as a function of crystallinity index X_c (left) and L_a (right) for 15K and 31K polymers

II. Tensile tests

From a practical standpoint, the previous DMA analyses have allowed us to set two different temperatures for tensile testing experiments, either above or below the α relaxation, in order that the amorphous phase is either rubbery or glassy. The temperatures that have been chosen are respectively $T = 120^\circ\text{C} = T_g + 65^\circ\text{C}$ and $T = -10^\circ\text{C} = T_g - 65^\circ\text{C}$. They correspond to a minimum of the loss factor on both sides of the α relaxation, so that the amorphous phase is the less mechanically dissipative as possible, as already pointed out in the experimental part (see §III.2.1 of chapter II). This makes dynamic experiments little sensitive to strain rate.

Regarding macroscopic tensile testing that is presently under consideration, the mechanical coupling of the amorphous and crystalline phases is expected to be significantly different depending on the rubbery or glassy state of the amorphous component and this should impact the macroscopic properties.

Each tensile test was carried out 5 times above T_g for both 15K and 31K polymers. Below T_g , 31K polymers were tested 3 times for each sample but concerning 15K polymers, only some samples were tested two times. Measurements are reproducible but only one curve of each sample is represented.

II.1. Above the glass transition at $T = T_g + 65^\circ\text{C} = 120^\circ\text{C}$

The PA6 samples with different microstructures generated by thermal treatments have been submitted to tensile testing. The stress-strain curves for the two PA6 polymers 15K and 31K are shown in Figure IV.6 for temperature above the glass transition at $T=120^\circ\text{C}$. It has to be pointed out that 15K and 31K INJ samples did not break but reached the limit displacements of the tensile machine, corresponding to 500% elongation.

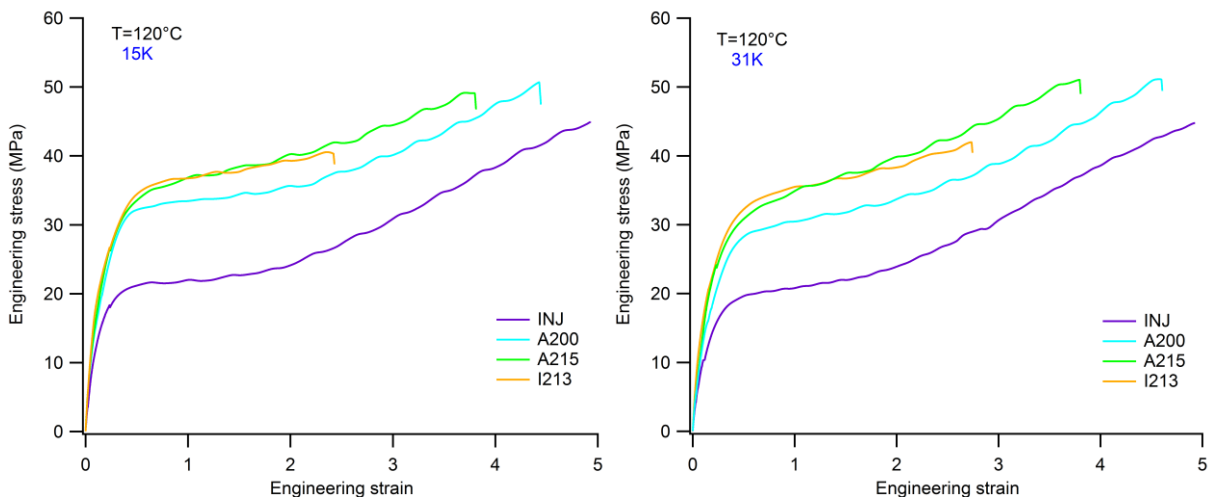


Figure IV.6: Tensile tests at $T=120^\circ\text{C}$ for 15K and 31K polymers,

If we look only at the influence of the microstructure as depicted in Figure IV.6, the same trend is observed for both 15K and 31K polymers. There is a large difference between the injected samples (INJ) and the thermally treated samples (A200, A215 and I213). Indeed, a yield stress value of 20 MPa is found for the first samples whereas the other ones have a yield stress value around 30-35 MPa.

The elongation at break is correlated with the crystallinity index: lower X_c gives higher elongation at break, as reported by Bessel [8] for room temperature experiments.

In order to better compare the effect of the molecular mass, tensile stress-strain curves of both polymers for various samples are represented in Figure IV.7. It shows that, for each thermal treatment, the stress-strain curve of the 15K samples is above that of the corresponding 31K samples. However, this effect may not be directly attributed to the difference in molecular mass but to the difference in crystallinity index induced by each thermal treatment on the respective samples. This point will be further discussed below.

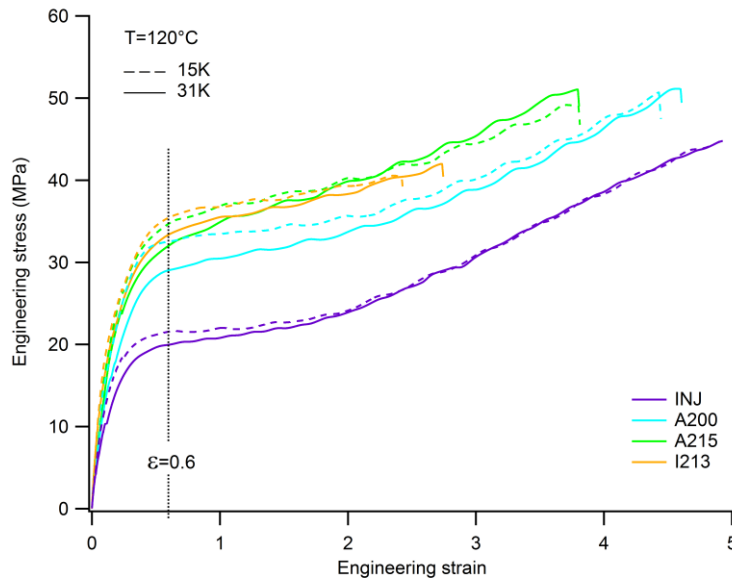


Figure IV.7: Tensile tests at $T=120^{\circ}\text{C}$ for 15K and 31K PA6 samples: influence of the molecular mass

Now if we look into details about the effect of the crystalline microstructure, the injected sample (INJ) contains both β and γ phase crystals, with β being predominant, whereas all the thermally treated samples contain either pure α phase (A215 and I213) or predominant α phase (A200). So one can wonder whether the differences of behavior and ductility could be due in part to the intrinsic properties of the crystalline phase itself, and not only to the crystallinity index. Indeed, it has been reported in literature that the β phase is the most ductile phase of PA6 [9]. Furthermore, it has also been shown that the γ phase is more ductile than the α phase in the temperature range of $[100-180^{\circ}\text{C}]$ [10] [11].

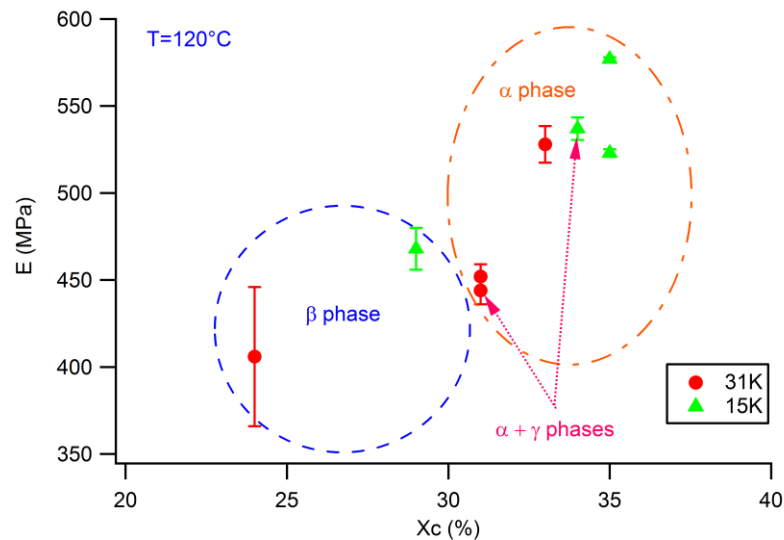


Figure IV.8: Young's modulus E at $T=120^\circ\text{C}$ for 15K and 31K polymers as a function of crystallinity index X_c .

Figure IV.8 represents the Young's modulus E as a function of crystallinity index for both 15K and 31K polymers. It clearly shows that molecular mass has little incidence (if any at all) on the Young's modulus at $T = 120^\circ\text{C}$. It seems that the Young's modulus is mainly correlated with crystallinity as already reported in the literature [8]. This may be simply due to the increasing volume fraction of the stiff crystalline phase. The modulus of the crystalline phase itself may also have an influence on the global Young's modulus. Indeed, when the crystallinity index increases above 30%, the crystalline phase changes from the β form to the α form, with a corresponding increase of cohesiveness. As a matter of fact, higher thermal stability and density of the α phase compared to β phase strongly suggest higher cohesiveness and therefore higher intrinsic stiffness.

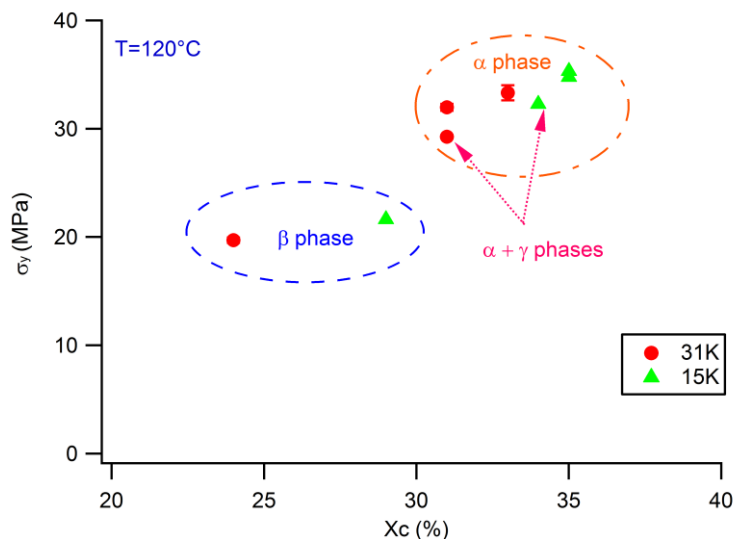


Figure IV.9: Yield stress σ_y at $T=120^\circ\text{C}$ for 15K and 31K polymers as a function of crystallinity index X_c .

Figure IV.9 represents the yield stress σ_y as a function of crystallinity index for both 15K and 31K polymers. It clearly shows that, similarly to the Young's modulus, molecular mass has no significant impact on the yield stress at $T = 120^\circ\text{C}$ but that the crystallinity plays a major role on this mechanical property. This is consistent with the sensitivity of the Young's modulus to X_c . However, the yield

stress proved to be much more sensitive to X_c than the Young's modulus: indeed, over the whole X_c range, σ_y increases by 75% whereas the Young's modulus increases by 42 % only.

This fact that σ_y is more sensitive to X_c than the Young's modulus may be explained via the dislocation approach of the plastic yielding of semi-crystalline polymers above T_g or T_α [12] [13]. The dislocation model for yield was developed in order to explain the temperature dependence on the critical resolved shear stress for chain direction slip in polyethylene [12]. Thus, the yield can then be explained in term of energy required to nucleate screw dislocations within the crystalline lamellae, with Burgers vectors parallel to the chain direction. Moreover, in this approach, the yield stress not only depends on the crystal stiffness but also on the crystal thickness [14]. Considering that L_c increases as X_c increases, this additional dependence of the yield stress may account for the surprisingly strong sensitivity to X_c .

II.2. Below the glass transition at $T = T_g - 65^\circ\text{C} = -10^\circ\text{C}$

The results for the different samples of the 15K and 31K polymers are depicted in Figure IV.10 and Figure IV.11 for tensile tests below the glass transition.

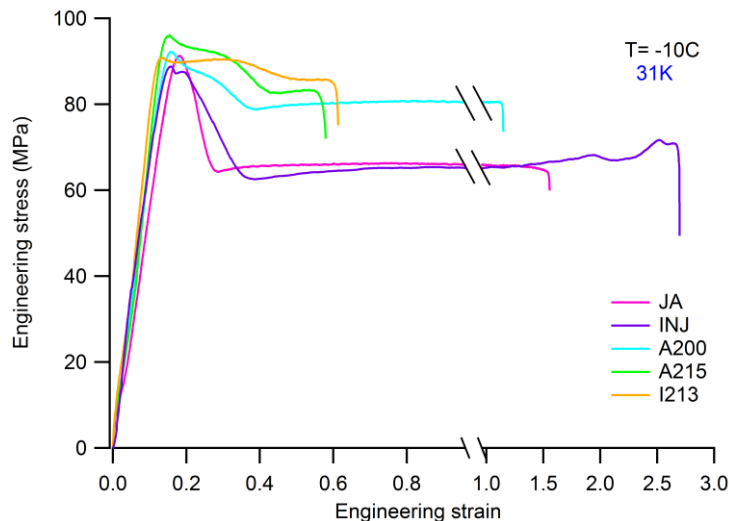


Figure IV.10: Stress-strain curves in tensile tests at $T = -10^\circ\text{C}$ for 31K PA6 samples

Figure IV.10 represents the tensile tests for the 31K samples with different microstructures. The effect of ageing has also been taken into account for the injected material. Indeed, the yield is double or simple if the sample is “young” (INJ) or aged (JA). The double yielding phenomenon is presented below.

Back to the “normal” samples (JA sample being out of the discussion), one can notice that at first glance, the elastic part of the curves and the yield stress values are similar for all samples. However, if we look further into detail, we can notice that the amplitudes of stress overshoot, defined as the difference between the maximum stress at yield point and the stress value on the plateau, differ according to the thermal treatments. Some samples exhibit a double yield. The first yield corresponds to the usual, well-defined yield at which the stress reaches its maximum value. The second yield is more a zone than a precise point and it goes from the first yield to the reaching of a constant stress, which marks a plateau until the final failure. This double yield effect will be further discussed below.

Concerning the ductility and the elongation at failure, the results depend on the nature of the crystalline phase. Again, it is found that it is the injected sample (INJ), containing majority β phase, which is the most ductile. It is then the one with γ phase, meaning that γ plays a significant role even if it is not the predominant phase, as A200 has exactly the index of crystallinity as A215. Again, the difference in ductility between the crystalline phases is emphasized.

The strain-stress curves for both 15K and 31K polymers are plotted in Figure IV.11. It is clear that samples with a lower molecular mass have a lower elongation at break.

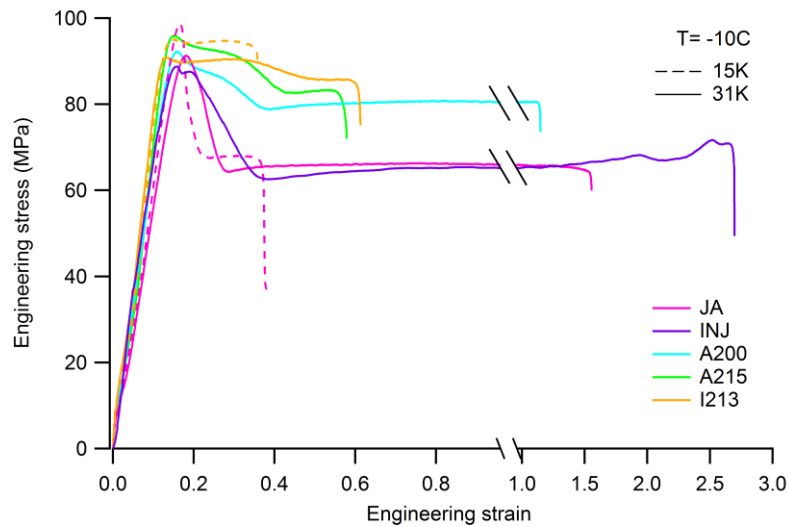


Figure IV.11: Stress-strain curves for tensile tests at $T=-10^{\circ}\text{C}$ for 15K (dotted lines) and 31K (full lines) PA6 samples

The Young's modulus is plotted versus crystallinity in Figure IV.12. In spite of a rather large dispersion of the data, a linear increasing trend can be observed. As for tests performed at $T = 120^{\circ}\text{C}$, the molecular mass by itself does not seem to play a role on the Young's modulus at $T = -10^{\circ}\text{C}$, at a given value of the crystallinity index. However, more data would be needed to give a clear conclusion on that point.

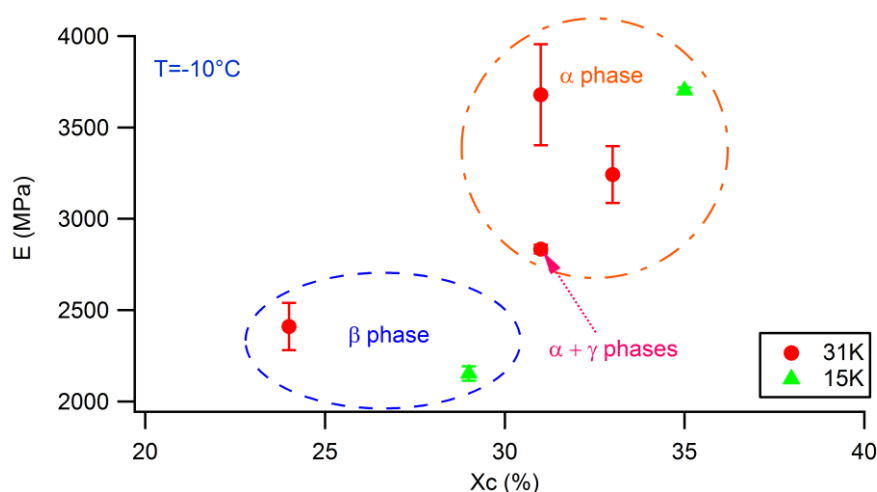


Figure IV.12: Young's modulus E at $T = -10^{\circ}\text{C}$ for 15K and 31K polymers as a function of crystallinity index X_c

The yield stress σ_y is plotted as a function of crystallinity index in Figure IV.13 for both 15K and 31K polymers. In contrast to the behavior of the Young's modulus, neither crystallinity nor molecular mass have a significant effect on the yield stress at $T = -10^\circ\text{C}$, the values being nearly the same for all samples within the experimental accuracy. This suggests that at this temperature, the plastic behavior of the glassy amorphous phase is very close to that of the crystal. The reason may be that yielding at such low temperature, i.e. far below both the melting point and the glass transition temperature, is not only controlled by conventional plastic processes such as micro shear bands but also by damaging processes such as cavitation and crazing. This hypothesis is thoroughly confirmed in Chapter VI via SAXS experiments. Therefore one can feature out that nanovoids initiate first in the amorphous, owing to its lower cohesiveness compared to the crystal, then propagate through the adjacent crystal lamellae thanks to local stress concentration. This latter process is not likely to depend on the morphology, but on the critical stress for cavitation in the amorphous phase. The resulting macroscopic indicator, i.e. the yield stress, then does not depend on the crystallinity.

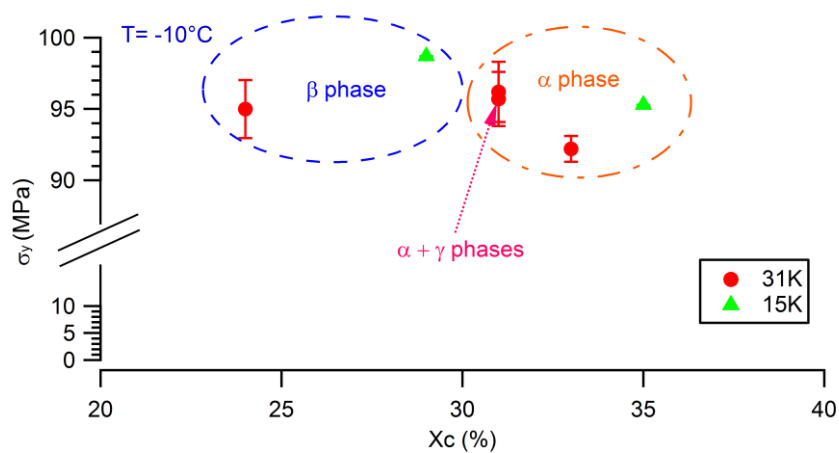


Figure IV.13: Yield stress σ_y at $T = -10^\circ\text{C}$ for 15K and 31K polymers as a function of crystallinity index X_c

Figure IV.14 presents the stress-strain curves for 31K PA6 samples at room temperature. This is useful for our discussion about the double yielding phenomenon.

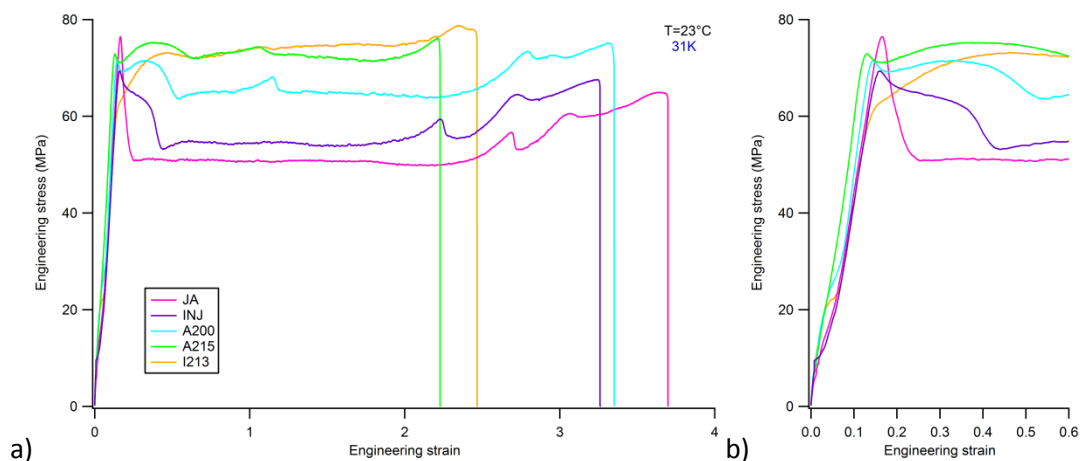


Figure IV.14: a) Stress-strain curves for tensile tests at room temperature ($T = 23^\circ\text{C}$) for 31K PA6 samples, showing double yield and b) zoom of the yielding zones

Double yielding has been reported by Shan et al. [15] [16] [17] [18] in polyamide 6. However no explanation of this phenomenon has been proposed. Seguela and coworkers have previously

observed the same effect on polyethylene and have put forward a theory based on two plastic processes operating competitively [19] [20]. Indeed, if we look at Figure IV.10 and Figure IV.14, we can see that the double yielding phenomenon depends on the drawing temperature – strain rate being identical - indicating a combination of two thermally activated rate processes. The most striking difference of behavior is observed for the isothermally treated material (I213): at room temperature, the second yield is predominant whereas at -10°C , the first yield is better defined. Seguela [19] suggested that the two processes governing the plastic deformation of the crystalline lamellae are closely related to the viscoelastic relaxations in the crystal. Accordingly, crystal shear and crystal block sliding are proposed to be the two plastic processes, on the basis of the concept of the mosaic block structure of the crystalline lamellae [20] that has been largely studied by Takayanagi et al. [21] and Hosemann et al. [22].

III. Discussion

III.1. Effect of molecular mass

The molecular mass is well known to influence the mechanical properties of thermoplastic polymers. This was the major reason for studying two PA6 samples of different molecular masses. Indeed, after performing different thermal treatments in order to change the crystalline microstructure and/or the nature of the crystalline phase, we have observed that, for a given thermal treatment, the molecular mass has only an impact on the crystallinity index.

Bessel et al. [8] have shown that an increase of the number average molecular mass, at least in the range $9.5 < M_n < 39.1$ kg/mol, could result in an increase of ductility for PA6, at room temperature. Ito et al. [11] have also studied the effect of molecular mass on the tensile mechanical behavior in relation with the crystalline structure of PA6. Data from Ito et al. are shown in Figure IV.15 for the drawing temperature 180°C . At a given strain level, the stress increases as a function of chains length, for samples having about the same crystallinity. The authors ascribed this effect to the increase of the number of entanglements per chain that reduce chain slippage. This is true for tensile tests in the temperature range $120\text{-}200^{\circ}\text{C}$. However, in this study, the macroscopic deformability (extension at break) of PA6 was little affected by chain length.

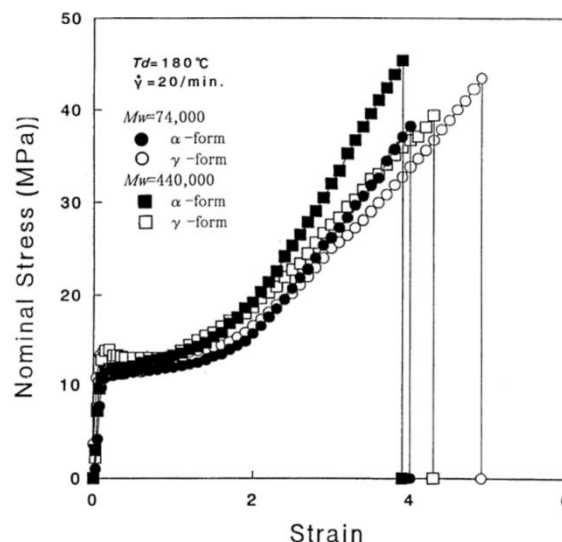


Figure IV.15 : Tensile stress-strain curves for PA6 films of various M_w and crystalline forms, at 180°C and $\dot{\epsilon} = 20\text{min}^{-1}$ [11]

Our experimental results apparently disagree with Ito et al.'s data for drawing above T_g . Indeed, for a given strain level, the stress is not sensitive to the molecular mass, in the limit of the experimental accuracy. It is to be noticed that in our case the range of molecular mass under investigation ($30 < M_w < 70$ kg/mol) is significantly narrower than that of Ito et al. study.

Regarding the experiment below T_g , no significant influence of molecular mass on the tensile drawing behavior is observed. This finding is in agreement with previous data from Bessel et al., for an equivalent molecular mass.

In order to understand the effect of molecular weight, it is worth pointing out that intercrystalline tie molecules play an important role in the mechanical properties of semi-crystalline polymers, in addition to, or together with, chain entanglements. A schematic of the molecular topology of a semi-crystalline polymer is shown in Figure IV.16 (left). It indicates that the requirement for generation of intercrystalline tie molecules is that a chain in random coil conformation should enfold at least one amorphous layer and the two adjacent crystalline lamellae as expressed by the following relation:

$$R_c \geq L_a \quad (\text{E IV.1})$$

where R_c is the square root of the average squared end-to-end distance of the chain and L_a the amorphous layer thickness (see Figure IV.16 (right)).

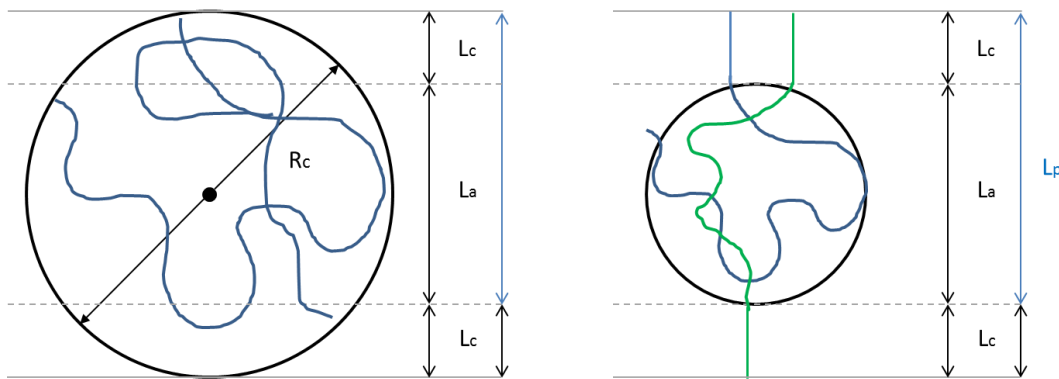


Figure IV.16: Schematic molecular topology of a semi-crystalline polymer (left); Schematic illustrated the conditions expressed in Eq. IV.1 (right)

The average squared end-to-end distance of a polymer chain in random coil (gaussian) conformation obeys the following relation:

$$R_c^2 = \alpha^2 M \quad (\text{E IV.2})$$

where the tabulated value is $\alpha^2 = 0.853$ nm for PA6 (with M given in g/mol) [23]

Thanks to Equations IV.1 and IV.2, various values of the average end-to-end distance of the chains have been calculated in the case of A215 samples for the two molecular masses 15K and 31K and compared to the distance L_a , corresponding to the right hand side in Eq.IV.1. $R_{c(Mn)}$ and $R_{c(Mw)}$ are the average end-to-end distances corresponding to the chains having molecular mass equal to the actual values of M_n and M_w given in Table III.2. The results are reported in Table IV.2

Table IV.2: Calculation of 2 R_g for the A215 samples of the 15K and 31K polymers

	L_p (nm)	L_c (nm)	L_a	$R_{c(Mn)}$	$R_{c(Mw)}$
15K	10.2	3.3	6.9	12.8	16.3
31K	10.7	3	7.7	16.2	21.8

For each molecular mass, both R_{cMn} and R_{cMw} are significantly larger than L_a , which means that a large fraction of the chains are able to go from one crystalline lamella to another, i.e. form tie molecule. Indeed, given the length of a monomer and the thickness crystalline lamella (around 3 to 4 monomers to form a crystalline lamella), most of the chain length is localized into the amorphous phase (around 300 monomers for a chain length of 31K PA6 and 190 monomers for 15K PA6). Obviously, this probability of forming tie molecules is greater for 31K PA6 samples than for 15K PA6 samples. Moreover, it should be mentioned that these conclusions also apply to the samples submitted to other thermal treatments since the amorphous thickness for A215 samples considered in this discussion, is the highest one among all samples.

Another major parameter regarding the mechanical properties is the average molecular mass between entanglements, M_e . In the literature, the tabulated value for PA6 is $M_e = 2470$ g/mol [24]. In the present case, the average number of entanglements per chain has been estimated and is reported in Table IV.3 for both 15K and 31K polymers, irrespective of thermal treatment.

Table IV.3: Average number of entanglement per chain for the 15K and 31K samples

	M_n (g/mol)	Entanglement number for M_n	M_w (g/mol)	Entanglement number for M_w
15K	19340	≈ 7	31516	≈ 12
31K	30280	≈ 12	56478	≈ 22

In any case, the rather low influence of the molecular mass on the mechanical properties could be due to the rather small difference in molecular mass between the two series of samples. Indeed, in both cases, the molecular mass value is much higher than the minimum distance required to connect two adjacent lamellae, meaning that tie molecules can be formed. Significant effect of the mechanical behavior could be observed in case of molecular mass close to or lower than the critical molecular mass defined as $M_c \approx 2M_e$.

Finally, in the present study, no clear evidence of the molecular mass on the mechanical properties has been observed, at small to medium elongation ratios. Indeed it seems that the effect of chain length on the mechanical behavior may be rather attributed to the change in morphology and in particularly the crystallinity index. However, it seems that the chain molecular mass may have an effect on the elongation at break. For temperature above the glass transition, no effect has been evidenced. Below the glass transition, the elongation at break seems indeed to depend on the chain length (Figure IV.12 and Figure IV.13). Additional, more systematic experiments should be performed in order to confirm and quantify this effect.

One may also wonder about the long term properties. Even if the molecular mass does not affect the short-term properties such as Young's modulus or yield stress under uniaxial tensile testing, it does not mean that fatigue or creep resistance may not be affected by the molecular mass. This was not the topic of the present study but it is of course a major issue for the usage properties of engineering plastics and composites [25].

III.2. Poisson's coefficient

When a material is stretched in one direction, it usually exhibits a contraction effect in the directions transverse to the stretching axis. This phenomenon is called the Poisson's effect. The Poisson's coefficient, ν , is defined by the expression:

$$\nu = -\frac{\varepsilon_{\perp}}{\varepsilon_{\parallel}} \quad (\text{E IV.3})$$

Where ε_{\parallel} is the axial strain parallel to stretching and ε_{\perp} is the transverse strain, in the linear regime.

The Poisson's coefficient at $T = 120^\circ\text{C}$ is plotted in Figure IV.17 as a function of crystallinity index for the various 31K PA6 samples of the present study.

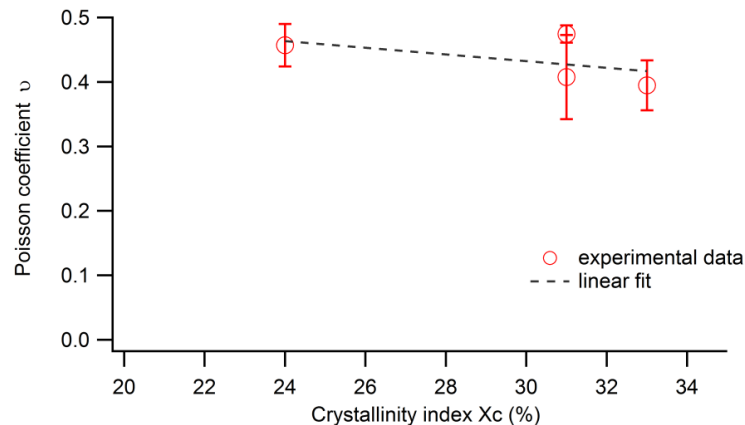


Figure IV.17: Poisson's coefficient ν as a function of crystallinity index for 31K samples at $T = 120^\circ\text{C}$

The Poisson's coefficient of PA6 is reported to be $\nu = 0.39$ at room temperature [26]. For tensile tests above T_g , the present data for the Poisson's coefficient are in the range $0.35 < \nu < 0.5$ and seem to depend linearly of the crystallinity index (Figure IV.17). For low X_c , the Poisson's coefficient is close to 0.5, meaning that the mechanical behavior is close to that of a rubber. This is consistent with the fact that at this temperature, the amorphous state is in rubbery state and that crystallinity is rather low. For high X_c , the Poisson's coefficients decreases to an average value $\nu \approx 0.4$. In this case, the crystalline network affects the mechanical behavior at small deformations. Indeed, depending on the crystallinity index, the crystalline fraction in the sample may form or not a percolating network and thus affect differently the mechanical behavior.

Due to a problem of freezing over the window of chamber of the tensile machine at $T = -10^\circ\text{C}$, capturing the sample image by the videometric device turned out to be very difficult, preventing accurate measurements of the Poisson's coefficient at this temperature.

III.3. Issues

Differences of mechanical behavior have been observed depending on temperature and processing conditions. Above T_g , the crystallinity index seems to be of prime importance. However it does not seem to be the only criteria. The nature of the crystalline phase could indeed have an important part to play. Furthermore, for tensile tests below T_g , crystallinity index is no more the major criteria. The differences of mechanical behavior of the various samples can no longer be explained by a difference of crystallinity index only. The nature of the crystalline phase as well as the morphology of the structure (difference of long period for example) should also be included in the discussion. Indeed, as reported in the literature, it seems that the β phase is more ductile than the α phase, probably due to a lower density and a lower cohesiveness. In order to progress in the understanding of the mechanical behavior of PA6 in relation to microstructure, different scales of the microstructure should be investigated during tensile tests. In this aim Small- and Wide-Angle X-ray Scattering experiments (SAXS and WAXS) have been performed in-situ during tensile tests, as reported in chapters V and VI.

As said above, as no clear influence of the molecular mass has been evidenced, further work has been focused only on the higher molecular mass samples, i.e. the 31K PA6 samples.

References

- [1] E. L. V. Lewis and I. M. Ward, "Anisotropic mechanical properties of drawn nylon 6. I. The alpha phase," *Journal of Macromolecular Science, Part B: Physics*, vol. 18, pp. 1-46, 1980.
- [2] D. Hunt and M. Darlington, "Accurate measurement of creep of nylon-6,6 at constant temperature and humidity," *Polymer*, vol. 19, pp. 977-983, 1978.
- [3] L. Lin and A. Argon, "Deformation resistance in oriented nylon 6," *Macromolecules*, vol. 25, pp. 4011-4024, 1992.
- [4] R. Boyd, "Relaxation processes in crystalline polymers: Experimental behaviour - A review," *Polymer*, vol. 26, pp. 323-347, 1985.
- [5] S. Aharoni, "Increased glass transition temperature in motionally constrained semicrystalline polymers," *Polymers for Advanced Technologies*, vol. 9, pp. 169-201, 1998.
- [6] M. Arnoult, E. Dargent and J. F. Mano, "Mobile amorphous phase fragility in semi-crystalline polymers: Comparison of PET and PLLA," *Polymer*, vol. 48, pp. 1012-1019, 2007.
- [7] R. Androsch and B. Wunderlich, "The link between rigid amorphous fraction and crystal perfection in cold-crystallized poly(ethylene terephthalate)," *Polymer*, vol. 46, pp. 12556-12566, 2005.
- [8] T. J. Bessel, D. Hull and J. B. Shortall, "The effect of polymerization conditions and crystallinity on the mechanical properties and fracture of spherulitic nylon 6," *Journal of Materials Science*, vol. 10, pp. 1127-1136, 1975.
- [9] L. Penel-Pierron, C. Depecker, R. Seguela and J.-M. Lefebvre, "Structural and mechanical behavior of nylon 6 films. Part I: Identification and stability of the crystalline phases," *Journal of Polymer Science: Part B: Polymer Physics*, vol. 39, pp. 484-495, 2001.
- [10] M. Ito, K. Mizuochi and T. Kanamoto, "Effects of crystalline forms on the deformation behaviour of nylon-6," *Polymer*, vol. 39, pp. 4593-4598, 1998.
- [11] M. Ito, A. Takahashi, N. Araki and T. Kanamoto, "Effects of molecular weight on the drawing and the draw efficiency of nylon-6," *Polymer*, pp. 241-248, 2001.
- [12] R. J. Young, "Screw dislocation model for yield in polyethylene," *Materials Forum*, vol. 11, pp. 210-216, 1988.
- [13] N. W. Brooks, M. Ghazali, R. A. Duckett, A. Unwin and I. Ward, "Effects of morphology on the yield stress of polyethylene," *Polymer*, vol. 40, pp. 821-825, 1999.

- [14] O. Darras and R. Seguela, "Tensile yield of polyethylene in relation to crystal thickness," *Journal of Polymer Science: Part B: Polymer Physics*, vol. 31, pp. 759-766, 1993.
- [15] G.-F. Shan, W. Yang, B. Xie, Z. Li, J. Chen and M. Yang, "Double yielding behaviors of polyamide 6 and glass bead filled polyamide 6 composites," *Polymer Testing*, vol. 24, pp. 704-711, 2005.
- [16] G.-F. Shan, W. Yang, M. Yang, B. Xie, Z. Li and J. Feng, "Effect of crystallinity level on the double yielding behavior of polyamide 6," *Polymer Testing*, vol. 25, pp. 452-459, 2006.
- [17] G.-F. Shan, W. Yang, X.-G. Tang, M. Yang, B. Xie and Q. Fu, "Double yielding in PA6: Effect of mold temperature and moisture content," *Journal of Polymer Science: Part B.: Polymer Physics*, vol. 45, pp. 1217-1225, 2007.
- [18] G.-F. Shan, W. Yang, M. Yang, B. Xie, J. Feng and Q. Fu, "Effect of temperature and strain rate on the tensile deformation of polyamide 6," *Polymer*, vol. 48, pp. 2958-2968, 2007.
- [19] R. Seguela and O. Darras, "Phenomenological aspects of the double yield of polyethylene and related copolymers under tensile loading," *Journal of Materials Science*, vol. 29, pp. 5342-5352, 1994.
- [20] V. Gaucher-Miri and R. Seguela, "Tensile yield of polyethylene and related copolymers: mechanical and structural evidences of two thermally activated processes," *Macromolecules*, vol. 30, pp. 1158-1167, 1997.
- [21] M. Takayanagi and T. Kajiyama, "Structural factors in deformation of crystalline polymers," *Journal of Macromolecular Science, Part B: Physics*, vol. 8, no. 1-2, pp. 1-27, 1973.
- [22] R. Hosemann, W. Wilke and F. Calleja, "Twist-korngrenzen und andere parakristalline gitterstorungen in polyathylen-einkristallen," *Acta Crystallographica*, vol. 21, pp. 118-123, 1966.
- [23] L. Fetters, D. Lohse, D. Richter, T. Witten and A. Zirkel, "Connection between polymer molecular weight, density, chain dimensions, and melt viscoelastic properties," *Macromolecules*, vol. 27, no. 17, pp. 4637-4647, 1994.
- [24] L. Fetters, D. Lohse and R. Colby, "Chapter 25 : Chain dimensions and entanglement spacings," in *Physical properties of polymers handbook*, J. E. Mark, Ed., 2006, Springer, pp. 447-454.
- [25] E. Mourglia Seignobos, "Compréhension des mécanismes physiques de fatigue dans le polyamide vierge et renforcé de fibres de verre," Ecole doctorale Matériaux, Lyon, 2009.
- [26] "Goodfellow," [Online]. Available: <http://www.goodfellow.com/F/Polyamide-Nylon-6.html>. [Accessed 16 Juillet 2014].

Chapter V: Microscopic study – Elastic strain domain

Introduction.....	111
I. Elastic strain domain at the scale of lamellae, studied by SAXS	114
I.1. SAXS protocol	114
I.2. Local strain of horizontal lamellae ($\psi = 0^\circ$)	115
I.2.1. Experimental data	115
I.2.2. Discussion.....	117
I.3. Local strain as a function of orientation.....	119
I.3.1. Experimental data	119
I.3.2. Analysis of local strain	122
I.4. Orientational distribution of lamellae (SAXS investigation).....	126
I.4.1. Experimental data	127
I.4.2. Analysis of orientational distributions of lamellae.....	128
II. Elastic strain domain at the scale of crystalline unit cell, studied by WAXS	131
II.1. WAXS protocol	132
II.2. Crystal strain in vertical scattering direction ($\psi = 0^\circ$)	133
II.3. Azimuthal distribution of crystal strain (WAXS investigation)	135
II.3.1. Experimental results.....	135
II.3.2. Analysis of the results.....	136
II.4. Orientational distribution of crystalline planes, studied by WAXS	138
II.4.1. Case of INJ sample, with β crystalline phase.....	138
II.4.2. Case of sample I213, with α crystalline phase	140
III. Discussion: deformation mechanisms under stretching in the elastic regime	142
III.1. Models.....	142
III.1.1. “Chain network’ model (CN)	142
III.1.2. “Rigid Lamella” model (RL).....	143

III.2. Comparison to experimental data.....	146
III.2.1. Case of β phase.....	146
III.2.2. Case of α phase	146
III.2.3. Case of $\alpha+\gamma$ phases	149
III.2.4. Additional information	149
III.3. Conclusion	150
References.....	151

Introduction

The results of tensile tests reported in the previous chapter have shown that there are major differences of behavior between samples, and especially between samples containing predominantly β or α phase. The effect of the crystallinity index was also discussed. Thus, an in-situ characterization in “real time” was performed: tensile tests were investigated by combining Small and Wide Angle X-ray Scattering (SAXS and WAXS) in order to understand the differences observed at the macroscopic scale. Results concerning the elastic strain domain are reported in this chapter.

As no major effect of the molecular mass has been evidenced in the previous chapter, this study is focused on 31K samples. The list of samples is summarized below in Table V.1.

Table V.1: 31K selection for microscopic in-situ study

Name	Sample	Crystalline phase	Symbol
INJ	Injected	$\beta+\gamma$	
A200	Annealed at 200°C	$\alpha+\gamma$	
A215	Annealed at 215°C	α	
I213	Isotherm at 213°C	α	
JA	Injected then aged	$\beta+\gamma$	

As for macroscopic tensile tests, in-situ tests were done at two temperatures. Above T_g , the choice was 120°C. Below T_g , the choice was initially -10°C and this is this temperature which was used for WAXS in-situ tensile tests. Due to technical problems (scattering of rime), SAXS experiments were done at 0°C. However, using -10°C or 0°C does not change the mechanical behavior. Indeed, as explained in chapter II and depicted in Figure II.19, the whole temperature interval [-30°C; 0°] can be considered to correspond to a minimum of loss factor. Working with the same temperature allows comparing the results obtained at macroscopic and microscopic scales.

As said, this chapter is focused on the elastic strain domain. The plastic strain domain (beyond the yield) will be discussed in chapter VI. The in-situ tensile study is performed in the aim of understanding the deformation mechanisms. However X-ray techniques do not allow following all the morphology scales: lamellae and crystalline planes can be analyzed but not the spherulite structure. Indeed, information on orientation of lamellae planes are obtained but not their location in spherulites.

In order to follow the different parts of the material which are deformed, the following convention has been adopted. Lamellae in general are defined by three distinct directions, the direction of their normal \vec{n} and two growth directions, \vec{g}_1 and \vec{g}_2 (not necessarily orthogonal), in the plane of the lamella. In general, growth is faster in one direction called \vec{g}_1 and lamellae have biaxial shape as depicted in Figure V.2 and Figure V.3.

Equatorial and polar directions are linked to the lamellae distribution in the spherulite as shown in Figure V.1, with the tensile direction (TD) being vertical. 2D SAXS (and WAXS) pattern are oriented in a way that vertical and horizontal respectively correspond to the vertical and horizontal zones in WAXS and SAXS patterns, with the tensile axis being vertical. Polar lamellae are restricted to conic zone whereas equatorial lamellae are located in a discoid zone.

In SAXS, detected intensity corresponds to intersection of reciprocal space (scattering) with the plane of the detector (see chapter II).

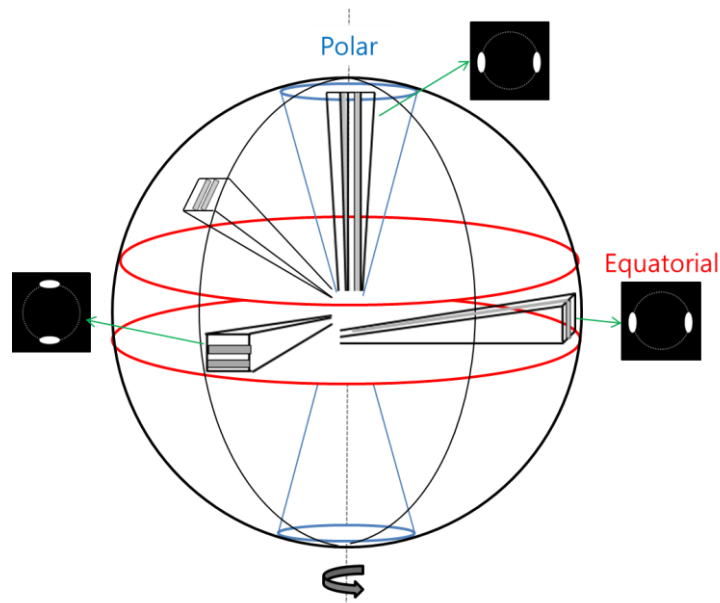


Figure V.1: Lamellae distribution in a spherulite and correspondence to 2D SAXS patterns

Lamellae stacks scatter in the direction of their normal. Thus, polar lamellae which have horizontal normals \vec{n} only scatter horizontally as depicted in Figure V.2.

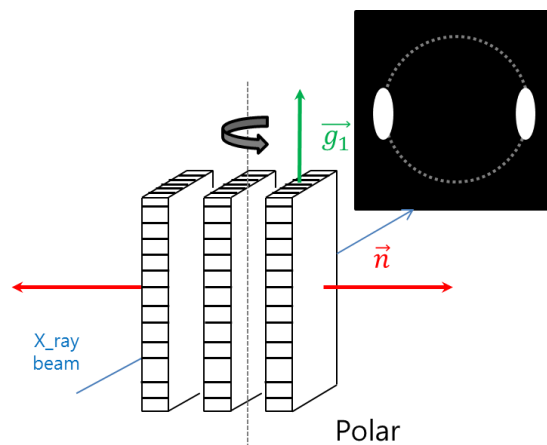


Figure V.2: SAXS pattern for polar lamellae

Concerning equatorial lamellae, depending on the orientation of their normals, the scattering pattern differs, as shown in Figure V.3. It is very important to notice that, in a lamellae stack, chains are oriented along the normal. This allows doing a distinction between equatorial lamellae: this distinction corresponds to different orientation of chains with respect to the tensile direction. For vertical scattering, chains axis is parallel to TD (Figure V.3a) whereas for horizontal scattering, chains axis is perpendicular to TD (Figure V.3b) and only lamellae oriented with their normal \vec{n} perpendicular to the beam are detected (for other orientations, Bragg's conditions are not respected). These two families may thus have different mechanical response and/or be affected differently by mechanical sollicitation.

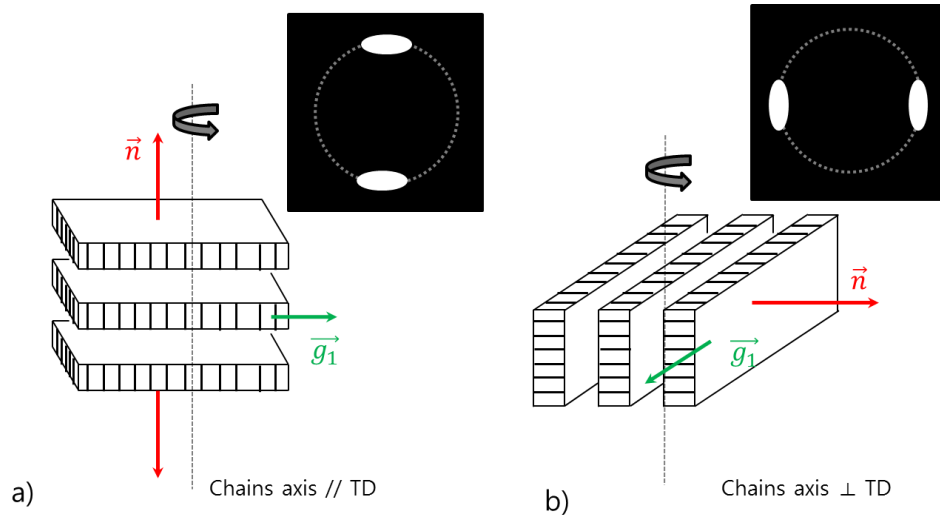


Figure V.3: SAXS patterns for equatorial lamellae oriented with a) chains axis parallel to TD and b) chains normal to TD

As mentioned earlier, the study is focused on the elastic strain domain. It was taken as the strain region below the yield stress for tensile tests at 0°C as shown in Figure V.4a. At 120°C, it corresponds to the strain domain denoted elastic domain, below $\epsilon_{\text{macro}}=0.2$ as shown in Figure V.4b.

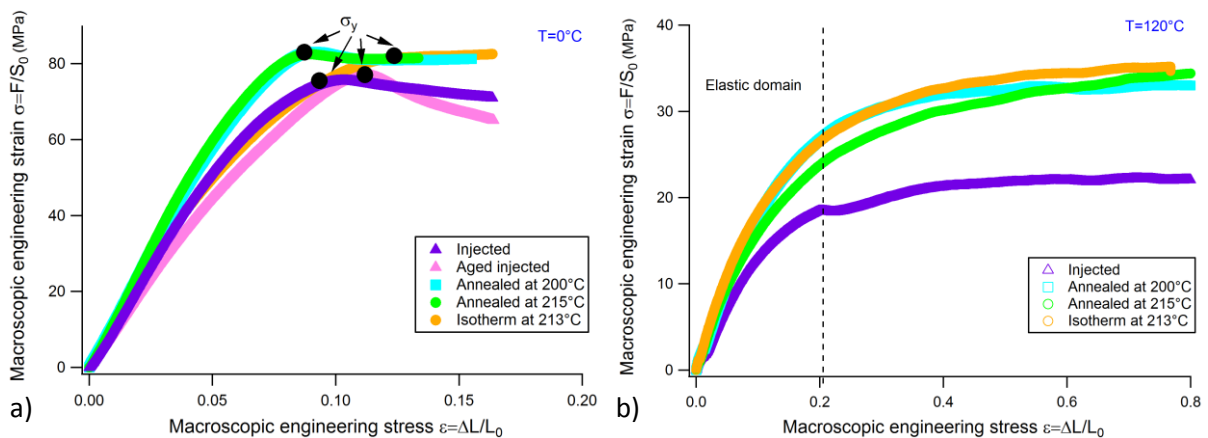


Figure V.4: Strain-stress curves of in-situ tensile tests at a) $T=0^{\circ}\text{C}$ and b) $T=120^{\circ}\text{C}$

At 0°C, the yield stress corresponds to different values of engineering stress in different samples. Concerning PA6, we have seen in the chapter IV that the temperature has an effect on the yield stress value: it changes by a factor 3 to 4 depending on the thermal treatments (for example in the case of INJ sample, σ_y decreases from 80 MPa to 20 MPa as the temperature increases). Let us now see what is happening at a microscopic scale.

In the first part, deformation mechanisms are first studied at the scale of crystalline lamellae by SAXS. Two aspects are discussed, which give access to a description of the local structure under stretching: the variation of the long period of the lamellar stacking, related to the local strain, and the distribution of lamella orientations. In the second part, the deformation mechanisms are studied at the scale of the crystalline unit cell by WAXS. The deformation of the unit cell under stress and the distribution of orientation of crystalline lattice planes are discussed. Finally, in the third part, models of deformation mechanisms reuniting both SAXS and WAXS observations are discussed.

I. Elastic strain domain at the scale of lamellae, studied by SAXS

In SAXS experiments, only the orientation of normals to lamellae stacks are detected since lamellae scatter only along their normal. The structure within the plane (crystallographic unit cell, growth direction) is not detected. Thus, in a first step, lamellae may be described as planes with no preferred direction or no shape anisotropy within the plane, assuming lamellae planes are large enough with respect to the period of the lamellae stacks. With this assumption, they have the symmetry of cylindrical disk. This assumption will be discussed when discussing WAXS patterns.

The reference direction of the problem is the tensile direction (denoted TD in what follows). The overall (macroscopic) deformation is uniaxial around this direction. The orientation of a lamella is described completely and without ambiguity by the orientation of its normal \vec{n} which is described by the azimuthal angle ψ only, due to the overall cylindrical (uniaxial) symmetry of the deformed sample, as schematized in Figure V.5. For a stack of lamellae with a normal \vec{n} , the scattered intensity is in the direction of \vec{n} (see Figure V.2 or Figure V.3).

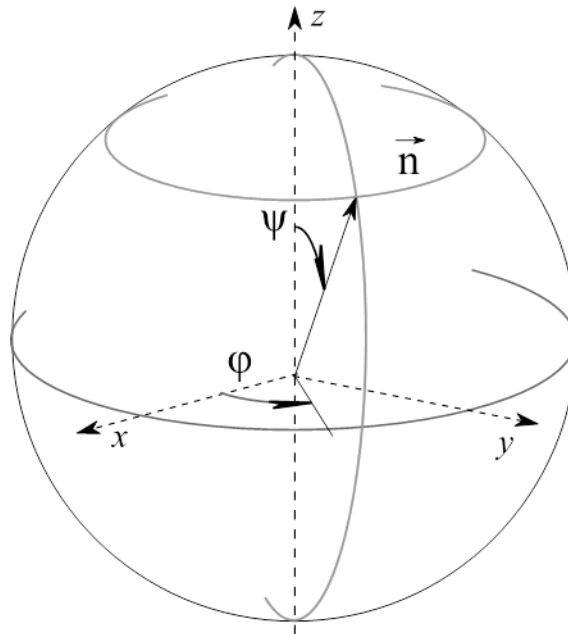


Figure V.5: Description of the orientation of a lamella normal n . Due to uniaxiality, the distribution of orientation depends on the azimuthal angle ψ only, not on the angle ϕ .

I.1. SAXS protocol

Uniaxial tensile tests are performed as described in chapter II (§III.3) at a strain rate $\dot{\epsilon} = 1.25 \cdot 10^{-4} \text{ s}^{-1}$ for $T = 0^\circ\text{C}$ and $\dot{\epsilon} = 5 \cdot 10^{-4} \text{ s}^{-1}$ for $T = 120^\circ\text{C}$. During tensile tests, a 2D SAXS pattern is taken every 0.25% of deformation at $T = 0^\circ\text{C}$ and every 1% of deformation at $T = 120^\circ\text{C}$, as shown in Figure V.6. 2D SAXS patterns are collected and treated as described in chapter II (§II.3). Each lamella stack scatters parallel to its normal and as every lamellae scatter and the material is isotropic, scattering occurs in every direction giving the pattern of a ring. The maximum of intensity corrected by Lorentz's factor as a function of the scattering vector q allows determining the long period as described in chapter II (§II.3).

The vertical direction on 2D SAXS patterns is parallel to the tensile direction (TD). Scattering in the vertical direction corresponds to the lamellae with the normal parallel to the tensile direction, which

according to the previous notation, belong to the family of “equatorial” lamellae. Scattering in horizontal direction corresponds to lamellae with \vec{n} horizontal.

I.2. Local strain of horizontal lamellae ($\psi = 0^\circ$)

During the deformation the scattering ring, initially perfectly circular, tends to become an ellipse with the long axis horizontal, larger than initial ring diameter, and the short axis shorter than initial ring diameter. This means that, during the tensile tests, the long period L_p contracts for lamellae with horizontal \vec{n} and it expands for lamellae with \vec{n} along TD, as depicted in Figure V.6. Also the intensity becomes modulated along the azimuthal angle ψ .

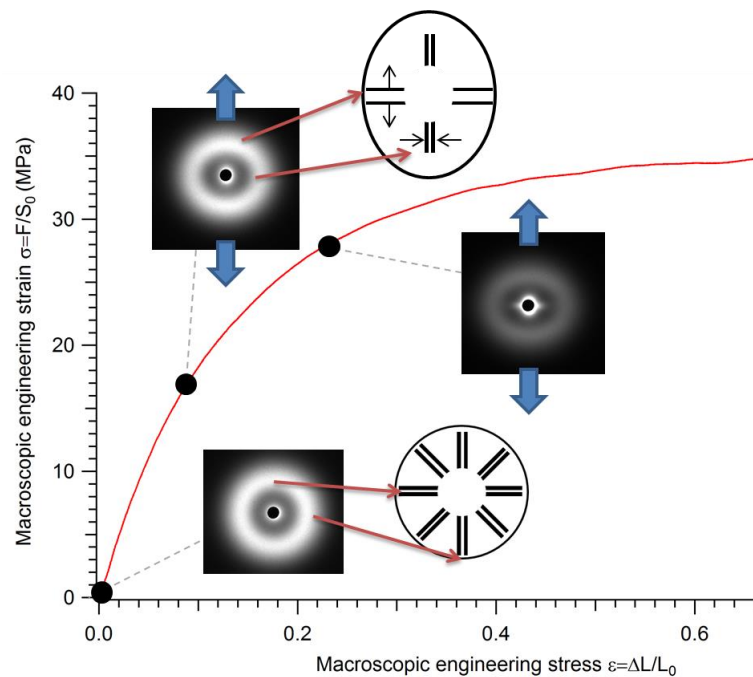


Figure V.6: Scheme of SAXS patterns during tensile test with the correspondence to lamellae position

For clarity, the local strain defined by the relative variation of long period $\Delta L_p/L_p$ will be first discussed specifically for horizontal lamellae, i.e. lamellae with $\psi = 0^\circ$, which have their normals along the tensile direction. Note that these lamellae belong to equatorial lamellae. The variation of the local strain with the azimuthal angle for various macroscopic strain will be lately discussed in §I.3. Finally, the modulation of intensity along the azimuthal angle ψ , related to the distribution of orientation of the lamellae will be discussed in § I.4.

I.2.1. Experimental data

By analyzing the SAXS patterns taken at different macroscopic strains, it is possible to determine the variation of the long period L_p as a function of the angle between \vec{n} and TD and the macroscopic strain. However, as mentioned earlier, we will first focus on horizontal lamellae (corresponding to vertical scattering direction) which are submitted to pure tensile stress along their normals. Thus, we will first measure the variation ΔL_p of the long period in vertical direction (corresponding to the direction of tensile axis). The local strain is defined as $\Delta L_p/L_p$. The local strain for equatorial lamellae as a function of engineering strain is plotted for the two temperatures of tensile tests in Figure V.7, for the various samples.

Let us first discuss the effect of macroscopic strain on the variation of long period. For both temperatures, at the beginning there is a linear regime of variation then a change of behavior happens. The change of behavior is defined by a limit, as depicted in Figure V.7. The extent of this linear domain is very roughly similar in all samples but depends quite strongly on temperature. This linear regime roughly corresponds to the elastic domain (see Figure V.4) for both temperatures. For $T < T_g$, the limit corresponds roughly to $\varepsilon = 0.06$ to 0.08 whereas for $T > T_g$, it corresponds to $\varepsilon = 0.2$. Below the glass transition, it is worth noticing that cavitation occurs but the central diffusion from the cavities is considered to be negligible below $\varepsilon \cong 0.06$ - 0.08 . The cavitation will be discussed in chapter VI. Anyway, the presence of voids does not impact the measurement of the long period. The slope of the curves in the linear regime gives the ratio of the local strain to the macroscopic strain, as defined below:

$$\frac{\varepsilon_{local}}{\varepsilon_{macro}} = \frac{\Delta L_p / L_p}{\varepsilon_{macro}} \quad (\text{E V.1})$$

Beyond the limit of the elastic domain defined above, the microscopic strain strongly deviates from the linear behavior. This deviation will be analyzed in chapter VI.

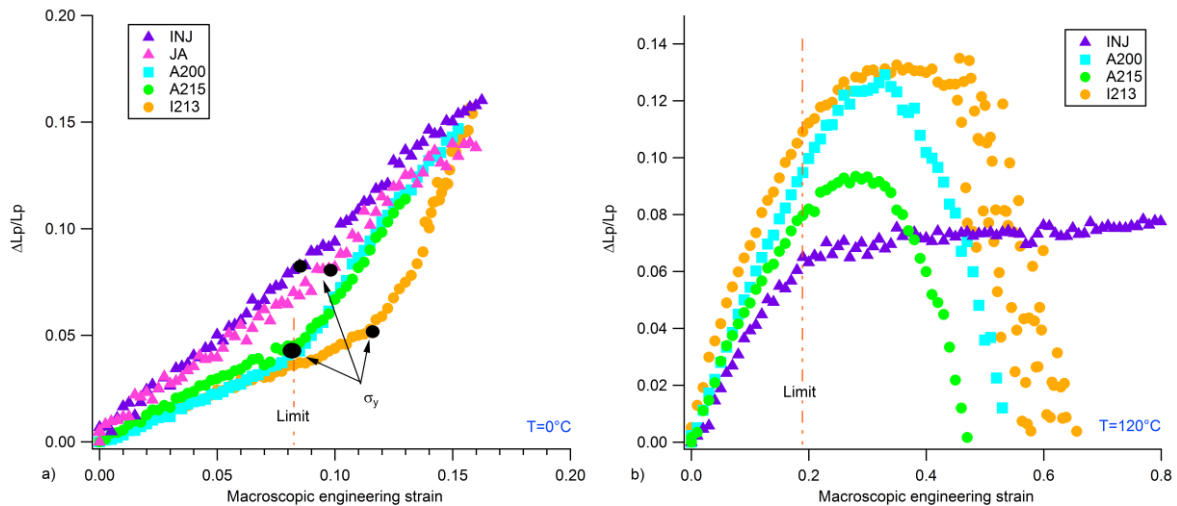


Figure V.7: Local strain as a function of macroscopic engineering strain at a) $T = 0^\circ\text{C}$ and b) $T = 120^\circ\text{C}$

Looking now in more details on the behavior of the various samples, a difference between the set of A200, A215 and I213 samples (containing predominantly α phase) and the set of INJ and JA samples (β phase) is observed in the elastic domain below glass transition, as shown in Figure V.7a. In the INJ and JA samples, the local strain is almost equal to the macroscopic strain (ratio close to one), while it is significantly lower (slope of the order 0.4) in the A200, A215 and I213 samples. This indicates that it is the predominant phase which plays the predominant role. Indeed, both A200 and INJ samples contain a minor fraction of γ phase in addition to α and β respectively, but behave in a way similar to samples with α phase and β phase respectively. In contrast, above T_g , there is no clear, systematic difference between the two sets of samples in the elastic domain, as shown in Figure V.7b. All samples have a local strain significantly smaller than one, with a ratio of the order 0.4 to 0.5.

Let us now discuss the effect of temperature. The way in which samples order according to their local strain values (the slopes of the curves in Figure V.7) changes and even inverts on going from below ($T = 0^\circ\text{C}$) to above glass transition. Indeed, the following order is found below T_g , from smaller to larger variation of long period: I213, A215, A200, JA and INJ. Above T_g , the reverse order, from INJ to I213 sample, is found. The non-linear deviations beyond the limit of the elastic regime are also very different at 0°C and at 120°C . At $T = 0^\circ\text{C}$, INJ and JA samples do not seem to feel the transition of the

yield stress, corresponding to the limit. This domain of strain will be further analyzed in chapter VI .Above T_g , there are also differences in behavior beyond the elastic limit. They will also be studied in chapter VI.

The above observations on the effect of temperature on the mechanical behavior of the various samples are summarized in Figure V.8. The ratio $\epsilon_{local}/\epsilon_{macro}$ defined by Eq. V.1 is plotted as a function of the crystallinity index X_c in Figure V.8 for the different PA6 samples at both temperatures.

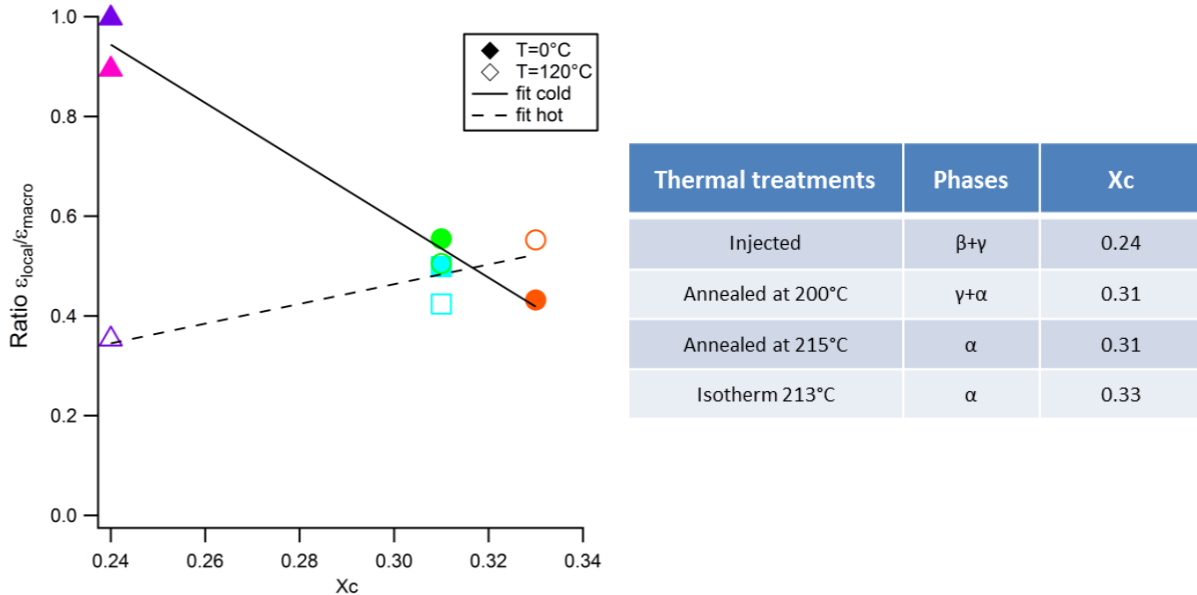


Figure V.8: Ratio $\epsilon_{local}/\epsilon_{macro}$ as a function of the crystallinity index X_c for PA6 samples at $T=0^\circ\text{C}$ (full symbols) and $T=120^\circ\text{C}$ (empty symbols)

As already noticed; at 120°C , all samples have a ratio smaller than one (between 0.35 and 0.55). However at 0°C , A200, A215 and I213 (containing α phase) still have a ratio strictly smaller than one whereas for INJ and JA samples (containing β phase) the ratios are close to one.

1.2.2. Discussion

Differences in the measured local strain suggest that samples with different crystalline phases have different mechanisms of deformation. Moreover, temperature has a different effect according to the crystalline phase. Indeed, samples with α phase (A200, A215 and I213) do not seem sensitive to the change of temperature, the ratio always being around 0.5, whereas there is a strong effect for the samples containing β phase (JA and INJ), as the ratio is close to one at low temperature (below T_g) and decreases by a factor nearly two at high temperature (above T_g).

These results are coherent with results observed on other polyamides, with some difference however. In the work by Hussein [1] on injected PA66 ($X_c \approx 0.33$), a ratio $\epsilon_{local}/\epsilon_{macro}$ of about 0.5 was found at $T = 150^\circ\text{C}$ (i.e. above T_g) and about 2 at $T = 23^\circ\text{C}$ (below T_g) for lamellae perpendicular to the tensile direction (with their normals along the tensile direction). This is somehow comparable to our injected sample, which shows a significant drop of the ratio $\epsilon_{local}/\epsilon_{macro}$ as well on going from below T_g to above T_g . On the other hand, tests done on injected PA11 have evidenced a ratio around 0.5 at $T = 120^\circ\text{C}$ and a ratio around 1.2 at $T = 0^\circ\text{C}$. This difference between PA6 and PA11 could be due to the strength of relaxation: there is a higher drop of elastic modulus after the glass transition for PA6 than PA11. In any case, the study on ratios $\epsilon_{local}/\epsilon_{macro}$ shows that polyamides behave in the same way

above T_g but below T_g , crystalline phases seem to have an impact. However, this is not our goal to study crystalline phases in other polyamides and furthermore we lack of data on the materials tested.

Measuring a ratio smaller than one means that the local strain is smaller than the macroscopic strain, or, in other words, that horizontal (equatorial) lamellar stacks are less deformed than the macroscopic sample. This is an important result in this work. Several hypotheses may explain this behavior:

- The local modulus (in the equator of spherulites) is larger than the average sample modulus
- The stress is smaller than the average stress: a load transfer could have happened for example
- The state of stress is different: for example instead of having only tensile state, shear could be present.

These various hypotheses may be rationalized in the following way. Let us model a horizontal lamellar stack by stacking of thin disks alternatively of crystalline and amorphous phases. Above T_g , the modulus of the amorphous phase is much smaller than that of the crystalline phase (2 to 3 orders of magnitude lower). A disk of amorphous phase behaves as an elastomer disk glued on two rigid substrates (the adjacent crystalline lamellae), submitted to tensile stress (see Figure V.9). As this elastomer disk cannot fully contract in the horizontal plane because it is attached to the crystalline lamellae, the tensile normal force is amplified by a mechanical mechanism similar to lubrication effect [2] [3]. This results in an amplified effective Young's modulus. Various regimes are described by various expressions, depending on the aspect ratio R/L_a of the stretched amorphous layer (where L_a is the thickness of the amorphous layer and R the lateral dimension of lamellae), for instance [2] [3] [4]:

$$E_{eff} \cong E \left[1 + \frac{1}{2} \left(\frac{R}{L_a} \right)^2 \right] \tag{E V.2}$$

where E is the Young's modulus of the elastomer disk (i.e. of the amorphous phase). If R/L_a becomes even larger, the effective modulus becomes $E_{eff} \sim E/(1 - 2\nu)$, which is comparable to the bulk modulus. The same effect (amplification of the effective Young's modulus) is present for vertical lamellae, which are submitted to compression.

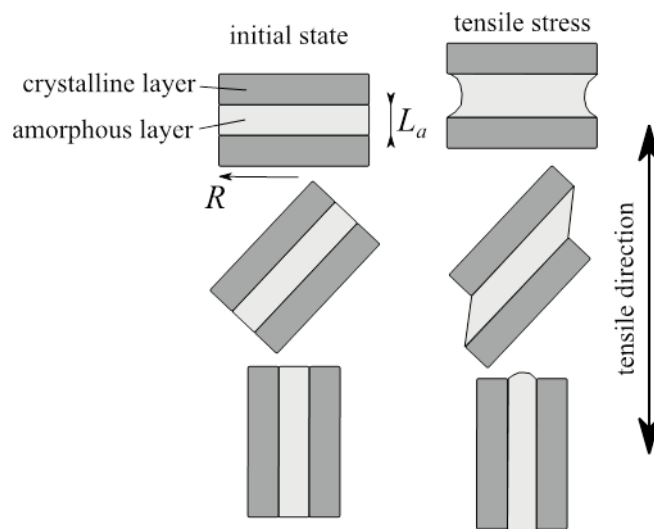


Figure V.9: Schematics of a lamellar stack: stacking of thin disks alternatively of crystalline and amorphous phases submitted to tensile stress

Above T_g , the shear modulus of the amorphous phase is much lower than the average modulus of the material. Lamellar stacks which are at an angle with respect to the tensile direction can be sheared easily (see Figure V.9). This picture explains the main observations:

- Above T_g , the effective modulus for horizontal (and vertical) lamellae is amplified, and therefore the strain in horizontal and vertical lamellae is decreased, while this lower strain is compensated by large shear strain in inclined lamellar stacks. This shear strain, however, is not detected in SAXS experiments.
- This effect is less pronounced or not present when the contrast of moduli between amorphous and crystalline phases becomes close to one, which may be the case for the sample with β phase below T_g .

I.3. Local strain as a function of orientation

In the previous section, the local strain $\Delta L_p/L_p$ was analyzed for lamellae at $\psi = 0^\circ$ corresponding to the tensile direction TD, i.e. horizontal lamellae. In order to see if the deformation inside the spherulite is heterogeneous or homogeneous, let us now generalize the previous investigation for the entire sample, i.e. for the full distribution of lamella orientation as a function of azimuthal angle ψ . The long period L_p has been measured for all azimuthal angles in the 2D SAXS patterns, that is for all lamellae orientation, for various macroscopic strains.

In the previous study, INJ and I213 samples represent the limiting behaviors of our polyamide samples. Thus, the generalization has been done for these two samples only, above and below glass transition. First, we start by presenting the method and the results on the behavior of the local strain observed in SAXS.

I.3.1. Experimental data

Corrections on 2D SAXS patterns were done in order to obtain the long period as explained before (see chapter II). However, extra corrections need eventually to be done concerning azimuthal data. In some cases, when treating the data, an azimuthal modulation with a period 360° appears. It is already present in the initial state and superposes to the additional modulation induced upon stretching. Note that the modulation induced upon stretching must have a period of 180° , due to the center symmetry of the pattern. We believe that this initial modulation is mostly due to a slightly imperfect determination of the center beam (since the incident beam at the synchrotron tends to drift along time). This artefactual modulation is shown in Figure V.10. To correct this artifact, we simply subtract the modulation in the initial state for each experiment. As a result, all successive patterns exhibit a nice 180° periodicity, as it should be.

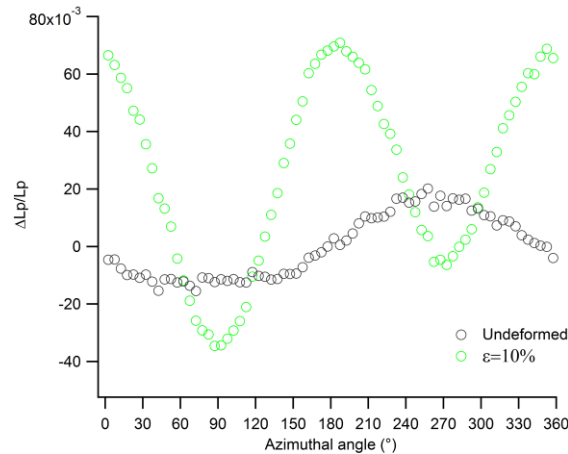


Figure V.10: $\Delta L_p/L_p$ as a function of azimuthal angle ψ for undeformed and $\varepsilon=10\%$ samples, obtained from treating raw data. The additional modulation with period 360° is mostly likely due to biased determination of center beam and is subtracted in the following.

The relative variation $\Delta L_p/L_p$ obtained after correction is plotted as a function of the azimuthal angle ψ in Figure V.11 for tensile test at $T = 0^\circ\text{C}$ (below T_g) for different macroscopic engineering strains. Vertical direction (parallel to tensile direction) corresponds to $\psi = 0^\circ$.

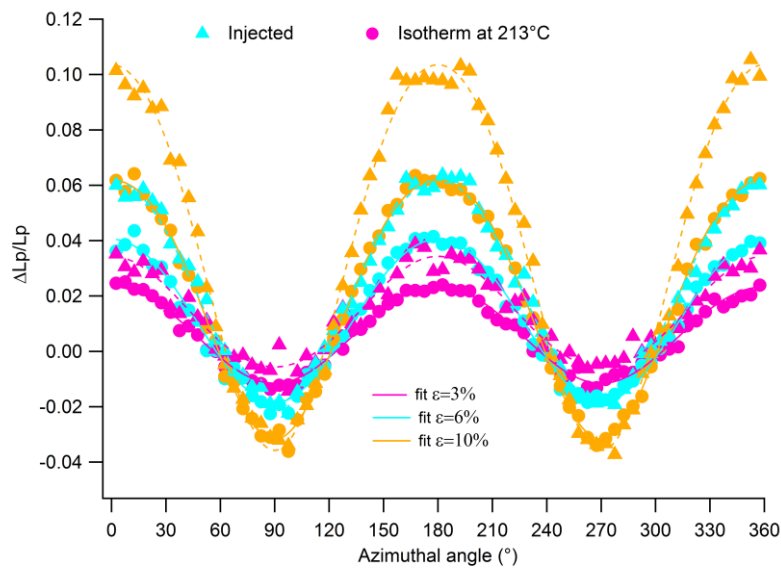


Figure V.11: $\Delta L_p/L_p$ as a function of the azimuthal angle ψ at $T = 0^\circ\text{C}$ for three different values of the macroscopic engineering strain and for two different samples: INJ and I213. Symbols are experimental points and curves are fit with Eq. V.14

One can notice in Figure V.11 that for the same macroscopic strain, the amplitude of local deformation is about twice larger for the injected material (INJ sample) than for the one with an isotherm at 213°C (I213 sample) for tensile tests performed at $T = 0^\circ\text{C}$. This means that for tensile tests below the glass transition ($T = 0^\circ\text{C}$), the INJ sample deforms more than I213 sample. This is of course coherent with Figure V.7a. However, for tensile tests above glass transition ($T = 120^\circ\text{C}$), as already noticed in Figure V.7b, the trend is inverted: for a same macroscopic strain, the amplitude of local deformation is larger for I213 sample than INJ sample, as shown in Figure V.12. This inversion could indicate a change of mechanism according to the temperature or/and the crystalline phase.

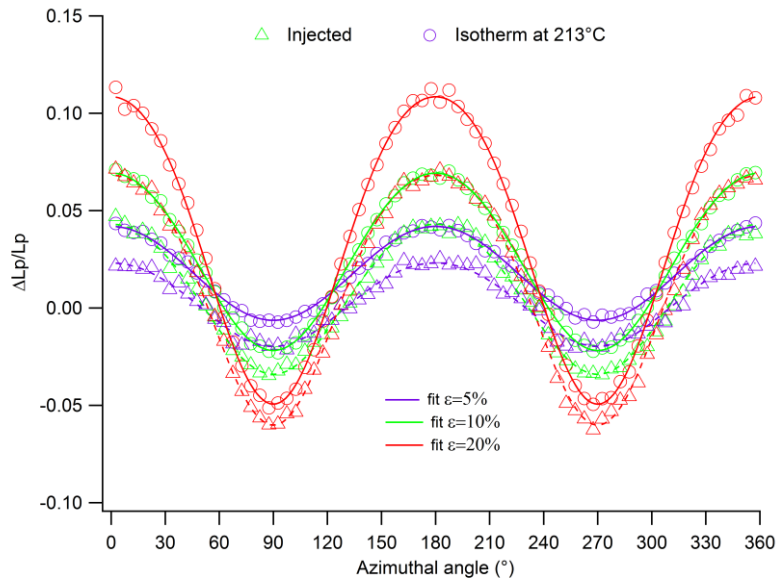


Figure V.12: $\Delta L_p/L_p$ as a function of azimuthal angle ψ for different values of the macroscopic engineering strain at $T = 120^\circ\text{C}$ and for two different samples: INJ and I213. Symbols are experimental points and curves are fit with Eq. V.14

To illustrate that I213 and INJ samples are affected differently by temperature, the variation of $\Delta L_p/L_p$ as a function of the azimuthal angle at both temperatures for different macroscopic engineering strains is shown in Figure V.13 and Figure V.14. For a given value of the macroscopic strain, the local strain in sample I213 (with α phase) does not change much with temperature. This does not mean, however, that the deformation mechanisms of the samples with α phase are not influenced by temperature (see §I.4 below).

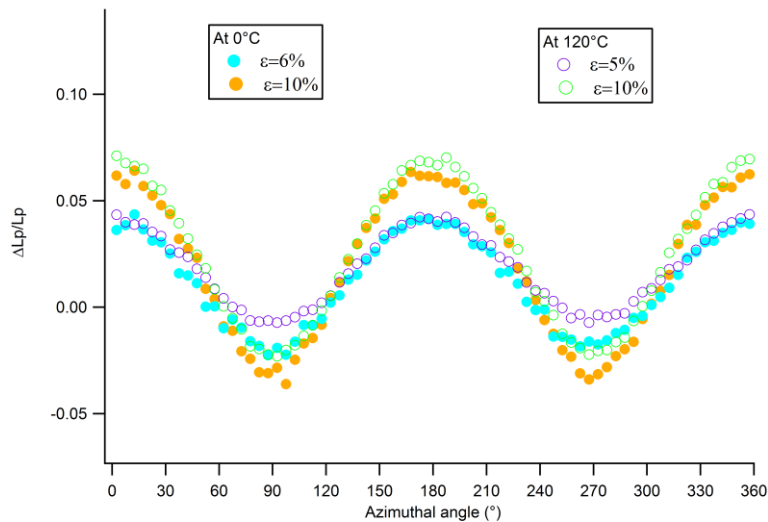


Figure V.13: Same data as in Figure V.11 and Figure V.12 for I213 sample but plotted differently. $\Delta L_p/L_p$ as a function of the azimuthal angle ψ for different macroscopic engineering strains for tensile tests at $T = 0^\circ\text{C}$ and $T = 120^\circ\text{C}$ for the I213 samples

In contrast, the local strain in sample INJ (with β phase) is affected by temperature. Indeed, the variation of long period is larger below the glass transition, as shown in Figure V.14, even for lower value of strain ϵ . This shows a major difference between samples with α and β phases. This may possibly allow an explanation on the macroscopic mechanical behavior as already reported.

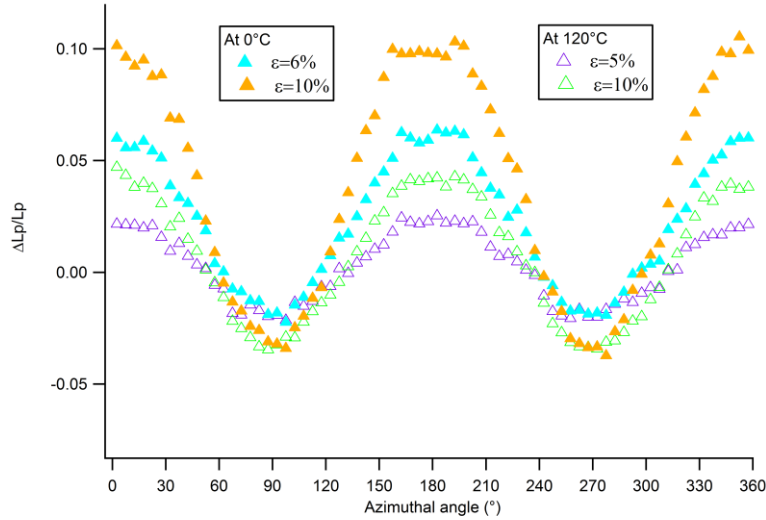


Figure V.14: Same data as in Figure V.11 and Figure V.12 for INJ sample but plotted differently. $\Delta L_p/L_p$ as a function of the azimuthal angle ψ for different macroscopic engineering strains for tensile tests at $T = 0^\circ\text{C}$ and $T = 120^\circ\text{C}$ for the INJ samples

I.3.2. Analysis of local strain

We now analyze in more details the variation of the long period $\Delta L_p/L_p$ as a function of the azimuthal angle ψ .

In a homogeneous material stretched with the tensile direction in the direction of axis Oz, the deviatoric stress tensor is:

$$\bar{\sigma} = \begin{bmatrix} 0 & 0 & 0 \\ 0 & 0 & 0 \\ 0 & 0 & \sigma_{zz} \end{bmatrix} \quad (\text{E V.3})$$

If the material is uniformly deformed, the deformation tensor u_{ij} ($i, j = x, y, z$) is related to the stress tensor σ_{ij} by the general constitutive law of elasticity [5]:

$$u_{ij} = \frac{1}{E} [(1 + \nu)\sigma_{ij} - \nu\sigma_{kk}\delta_{ij}] \quad (\text{E V.4})$$

where E is the Young's modulus and ν the Poisson's modulus. Implicit summation over repeated indices (Einstein's convention) has been used in Eq. V.4. This gives here:

$$\begin{cases} u_{xx} = u_{yy} = -\frac{\nu}{E}\sigma_{zz} \\ u_{zz} = \frac{\sigma_{zz}}{E} \end{cases} \quad (\text{E V.5})$$

Considering a small vector \vec{dr} in the material of length dl with an azimuthal angle ψ with respect to the tensile direction (axis Oz), its components are [5]:

$$\begin{cases} dx = dl \sin \psi \cos \varphi \\ dy = dl \sin \psi \sin \varphi \\ dz = dl \cos \varphi \end{cases} \quad (\text{E V.6})$$

\vec{dr} will be distorted into \vec{dr}' of components dx'_i and length dl' (see Figure V.15). dl' is given by the general relation:

$$dl'^2 = dl^2 + 2u_{ij}dx_i dx_j \quad (\text{E V.7})$$

Substituting Eqs. V.5 and V.6 into Eq. V.7, it gives:

$$dl'^2 = dl^2 \left[1 - \nu \frac{2\sigma_{zz}}{E} \sin^2\psi + \frac{2\sigma_{zz}}{E} \cos^2\psi \right] \quad (\text{E V.8})$$

Which may be rewritten (writing $\sigma = \sigma_{zz}$):

$$dl'^2 = dl^2 \left[1 + \frac{2\sigma}{3E} (1 - 2\nu) + \frac{4\sigma}{3E} (1 + \nu) \left(\frac{3\cos^2\psi - 1}{2} \right) \right] \quad (\text{E V.9})$$

And for small distortions:

$$dl' = dl \left[1 + \frac{1\sigma}{3E} (1 - 2\nu) + \frac{2\sigma}{3E} (1 + \nu) P_2(\cos\psi) \right] \quad (\text{E V.10})$$

where $P_2(\cos\psi)$ is the second order Legendre polynomial:

$$P_2(\cos\psi) = \frac{3\cos^2\psi - 1}{2} \quad (\text{E V.11})$$

Thus, identifying the relative variation $\Delta L_p/L_p$ (the local strain) to the relative length variation $(dl' - dl)/dl$ would give for a homogeneous deformation, as a function of the azimuthal angle ψ :

$$\frac{\Delta L_p}{L_p} = \frac{\varepsilon}{3} [(1 - 2\nu) + 2(1 + \nu) P_2(\cos\psi)] \quad (\text{E V.12})$$

where $\varepsilon = \sigma/E$ is the macroscopic strain. Note that for an incompressible material ($\nu = 1/2$), the following relation is recovered as expected:

$$\frac{\Delta L_p}{L_p} = \varepsilon P_2(\cos\psi) \quad (\text{E V.13})$$

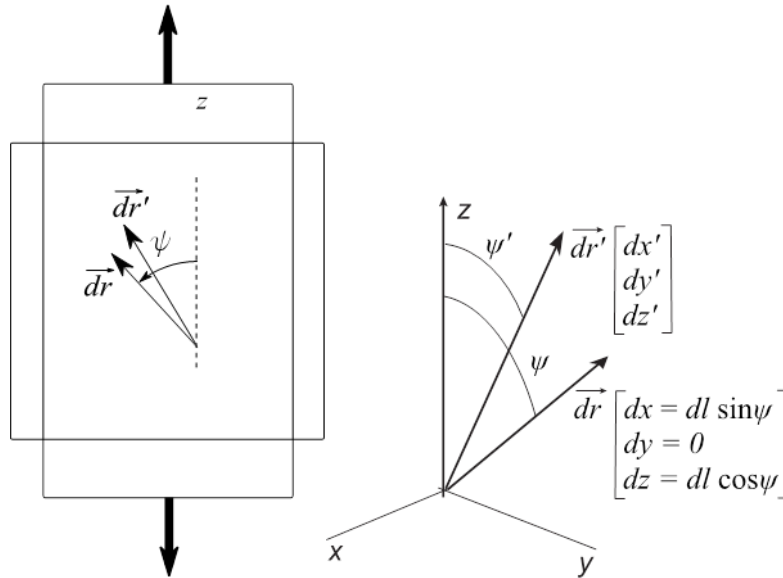


Figure V.15: A vector (the normal to a lamellae stack) before and after affine uniaxial deformation

Experimental results may now be compared to Eq V.12. Fitting the measured curve $\Delta L_p/L_p$ with Eq. V.14 and comparing with Eq. V.12 thus gives a comparison between the measured local strain and the expected value in a homogeneous (uniform) deformation. Therefore, it shows how much the local deformation deviates from uniform deformation. Figure V.16 shows the variation of local strain as a function of azimuthal angle for samples I213 (α phase) and INJ (β phase), at a macroscopic strain $\varepsilon = 5\%$. Full curves correspond to Eq. V.12. The Poisson's coefficients are $\nu = 0.395$ (I213) and $\nu = 0.457$ (INJ), determined as explained in Chapter IV. Figure V.16 shows the difference between the

macroscopic strain and the local strain defined by $\Delta L_p/L_p$. It shows that, for the INJ sample, lamellae which have their surfaces parallel to the tensile direction ($\psi = 90^\circ \text{ mod } 180^\circ$) are compressed to the same amount as predicted by the homogeneous deformation model, whereas lamella perpendicular to the tensile direction ($\psi = 0^\circ \text{ mod } 180^\circ$) are less stretched than predicted (by a factor of about 2, in concordance with Figure V.8). Concerning I213 sample, it shows that lamellae parallel (respectively normal) to TD are less compressed (respectively less stretched) than predicted. As already discussed before, this must be compensated by shearing of inclined lamellae (see Figure V.9).

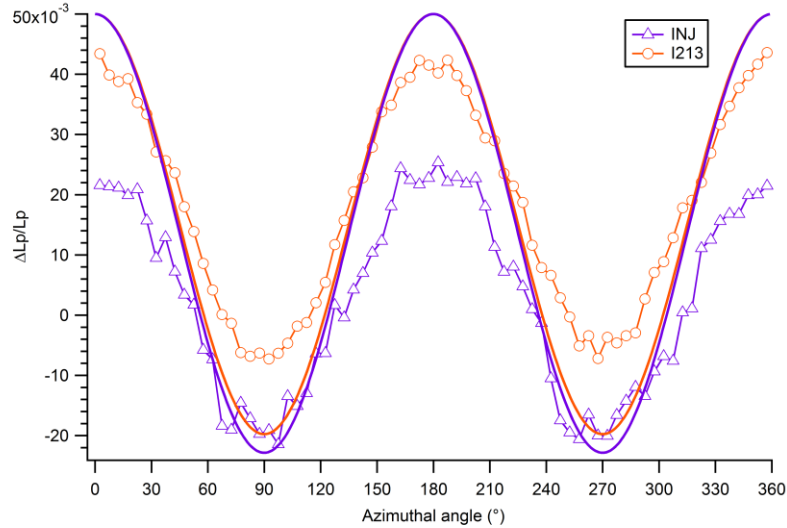


Figure V.16 : Variation of local strain as a function of azimuthal angle for samples I213 (α phase) and INJ (β phase) at temperature 120°C . Macroscopic strain $\epsilon = 5\%$. Full curves correspond to Eq. V.12 with Poisson's coefficients $\nu = 0.395$ (I213, orange curve) and $\nu = 0.457$ (INJ, purple curve).

The experimental curves $\Delta L_p/L_p$, vs azimuthal angle ψ are periodic with a period π and may be expressed as a series expansion of even Legendre polynomials of the azimuthal angle ψ as follows:

$$f(\psi) = p_0 + p_2 P_2(\cos \psi) + p_4 P_4(\cos \psi) + \dots \quad (\text{E V.14})$$

where $P_\alpha(\cos \psi)$ (α even integer) are Legendre polynomials. Expressions of Legendre polynomials are:

$$\begin{aligned} P_2(\psi) &= \frac{3 \cos^2 \psi - 1}{2} \\ P_4(\psi) &= \frac{1}{8} (35 \cos^4 \psi - 30 \cos^2 \psi + 3) \\ P_6(\psi) &= \frac{1}{16} (231 \cos^6 \psi - 315 \cos^4 \psi + 105 \cos^2 \psi + 5) \end{aligned} \quad (\text{E V.15})$$

According to Eq. V.12, in a homogeneously deformed material, only the terms up to second order (i.e. the coefficients p_0 and p_2 only) should be non zero.

In addition, by comparing Eqs. V.12 and V.14, the Poisson's ratio (the ratio between the transverse strain ϵ_\perp ($\psi = 90^\circ$) and the axial strain ϵ_\parallel ($\psi = 0^\circ$)) is given by

$$\nu = -\frac{\epsilon_\perp}{\epsilon_\parallel} = -\frac{(2p_0 - p_2 + \frac{3p_4}{4})}{2(p_0 + p_2 + p_4)} \quad (\text{E V.16})$$

As p_4 is much smaller than p_2 , it may be neglected, and finally, the following expression is obtained:

$$\nu = -\frac{\epsilon_\perp}{\epsilon_\parallel} = -\frac{(2p_0 - p_2)}{2(p_0 + p_2)} = \frac{(1 - 2p_0/p_2)}{2(p_0/p_2 + 1)} \quad (\text{E V.17})$$

When the Poisson's ratio ν is equal to 0.5 (incompressible, rubbery behavior), p_0 should be zero.

Note that the apparent Poisson's ratio, defined in Eq. V.17 corresponds to a comparison between the strains ε_{\perp} and ε_{\parallel} measured in different lamella stacks (or crystals in the context of WAXS, see §II.3). This is different from the actual Poisson's ratio of one lamella stack (or crystal). In such condition, it may be possible to observe values of the apparent Poisson's coefficient which are theoretically forbidden in elasticity ($\nu > 0.5$ or $\nu < -1$).

Thus, the knowledge of the coefficients p_0 , p_2 and p_4 provides some understanding of the mechanisms of deformation [6]. Experimental data were adjusted with series expansion Eq. V.14 up to fourth order, as shown in Figure V.17. Indeed, p_4 has a significant impact on the fit and it is clearly better to fit with Legendre polynomials of fourth degrees (see Figure V.17). The same applies for tensile tests at $T = 0^{\circ}\text{C}$ and both INJ and I213 samples.

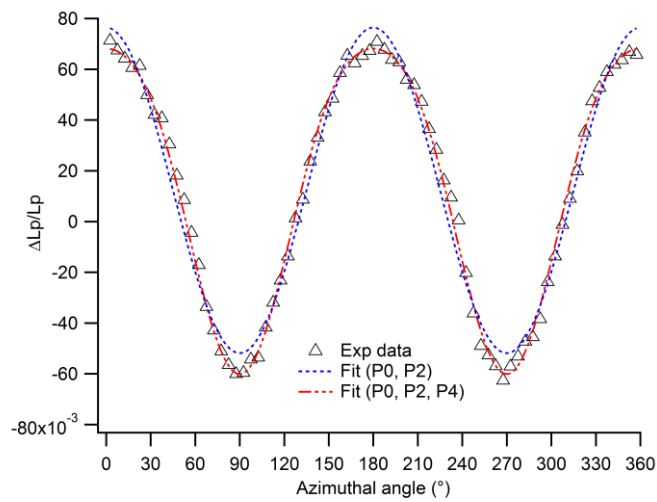


Figure V.17: Choice of even Legendre polynomials to fit experimental data at $\varepsilon = 30\%$ and $T = 120^{\circ}\text{C}$ for the INJ sample

Fits are shown in Figure V.11 and Figure V.12 on top of experimental distribution curves. p_2 and p_4 are plotted as a function of the macroscopic engineering strain in Figure V.18. Error bars of p_2 values are tiny but are larger for p_4 , as p_4 values are already small. p_2 increases linearly with the macroscopic strain both below and above T_g . Concerning the p_4 values, they are relatively low and negative. Finally, the presence of a non-zero p_4 coefficient is related to a deviation with respect to homogeneous deformation, which would contain only p_0 and p_2 , as discussed above. However, as p_4 remains relatively small, it indicates that the deformation of the lamellae systems is relatively homogeneous through the material. This is particular true, in the case of INJ sample at $T = 0^{\circ}\text{C}$, as p_2 corresponds to the macroscopic strain.

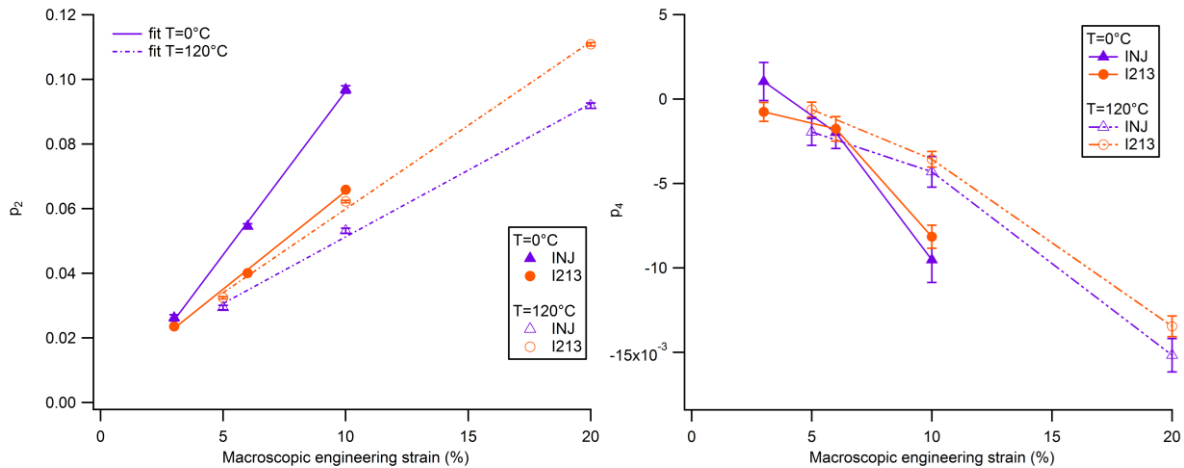


Figure V.18: p_2 and p_4 coefficients obtained by fitting experimental data with Eq. V.14 for INJ and I213 samples at $T = 0^\circ\text{C}$ and $T = 120^\circ\text{C}$.

p_0 as a function of macroscopic strain is plotted in Figure V.19a. If we exclude the case of the INJ sample above T_g , p_0 is increasing nearly linearly. In Figure V.19b, the apparent Poisson's ratio ν is plotted thanks to Eq. V.17 for the different samples at both temperatures. By comparing Figure V.19b and Figure V.16, it shows the concordance between the expected macroscopic behavior and the experimental local one. Indeed, above T_g , having a local Poisson coefficient close to 0.7 for INJ sample is in good agreement with Figure V.16 as it means that lamellae parallel and perpendicular to TD contract and stretch nearly in the same way. On the contrary, for I213 sample, having ν close to 0.3 means that the lamellae parallel to TD contract less than the lamellae perpendicular to TD stretch. This is still in agreement with Figure V.16. Below T_g , lamellae of both INJ and I213 samples behave nearly in the same way as ν is smaller than 0.5.

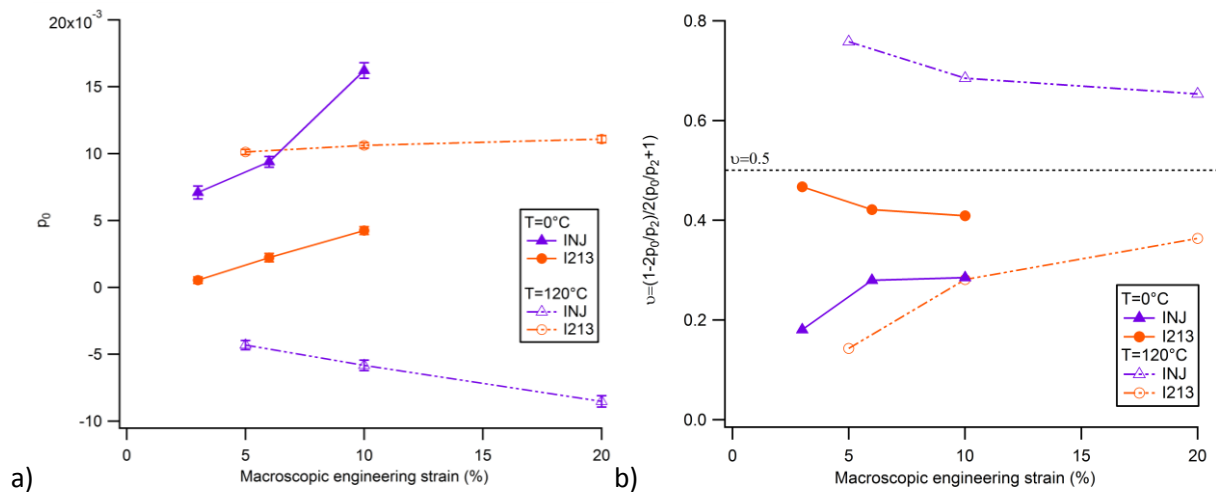


Figure V.19: a) p_0 coefficient Legendre polynomials obtained by fitting experimental data with Eq. V.14; b) Poisson's ratio ν plotted thanks to Eq. V.17 for INJ and I213 samples at $T=0^\circ\text{C}$ and $T=120^\circ\text{C}$

I.4. Orientational distribution of lamellae (SAXS investigation)

In the previous section, we have characterized the variation of the long period during tensile tests. In addition, as a result of sample deformation, the distribution of orientation of lamellae (supposed to be isotropic in the initial, overall isotropic state) becomes anisotropic. Experimentally, this is evidenced by the fact that the intensity becomes anisotropic. The anisotropy of the distribution of

orientation of lamellae can be studied quantitatively to fully characterize the local deformation in the stretched samples.

In SAXS experiments, scattering occurs in the direction of the normal to lamella surfaces. An enhancement of the ring intensity is generally observed in the vertical directions (parallel to the tensile direction). This means that, in the stretched state, there is an excess of lamellae with their normals oriented in the vertical region, that is, parallel to the stretching direction (i.e. lamellae with their larger surface perpendicular to the stretching direction, or horizontal lamellae), and conversely a relative deficit of lamellae with their normals perpendicular to the stretching direction, meaning vertical lamellae.

1.4.1. Experimental data

To characterize the distribution of orientation of the lamellae as a function of the macroscopic strains, we must analyze the distribution of intensity of the lamellar peak (corresponding to the long period), corrected by Lorentz's factor, as a function of the azimuthal angle ψ .

In order to obtain the amplitude quantitatively, we have used the log-normal intensity profile used for determining the long period, as described in chapter II (§II.3), as defined below:

$$f(q) = I_0 + \frac{A}{qw\sqrt{\pi}} \exp\left(-\left(\frac{\ln(q/q_{max})}{w}\right)^2\right) \quad (\text{E V.18})$$

The amplitude corresponds to the A parameter, with I_0 set to zero.

Finally, as we want to see the effect of orientation, the amplitude A obtained by the fit is corrected from the influence of the initial state and the drift of the center beam, as already explained in §1.3.1, thanks to the following equation:

$$A_f = A - A_{ini} + A_{ini}^{av} \quad (\text{E V.19})$$

With A_f the final amplitude

A the amplitude obtained by the fit

A_{ini} the amplitude of the initial state

A_{ini}^{av} the average amplitude of the initial state

The results for I213 and INJ samples at both temperatures (below and above T_g) are shown in Figure V.20.

Below T_g , intensity reinforcements at $\psi = k\pi$ ($k \in \{0,1,2\}$) are observed for each sample and strain below the glass transition as shown in Figure V.20a. It means that normals to lamellae orient preferentially vertically ($\psi = 0^\circ$). As this orientation is stronger as the strain increases, it means that more and more normals of lamella orient parallel to the tensile direction.

Above T_g , the effect of orientation is more complex and less pronounced (see Figure V.20b). For I213 sample (α phase), the normal orientation is found to be favored for $\psi = 90^\circ$ at $\epsilon = 20\%$, just below the yield point. This observation corresponds to a change of behavior for the I213 sample above T_g , as compared to the behavior below T_g . For the INJ sample at 120°C , the amplitude is nearly independent of the azimuthal angle, which is different from what has been observed at $T = 0^\circ\text{C}$. Note that the very small, relatively narrow peaks observed in the INJ sample at 120°C around $\psi = 70$ and 250° are due to imperfect subtraction of the curve in the initial state, which itself shows significant anisotropy in that case.

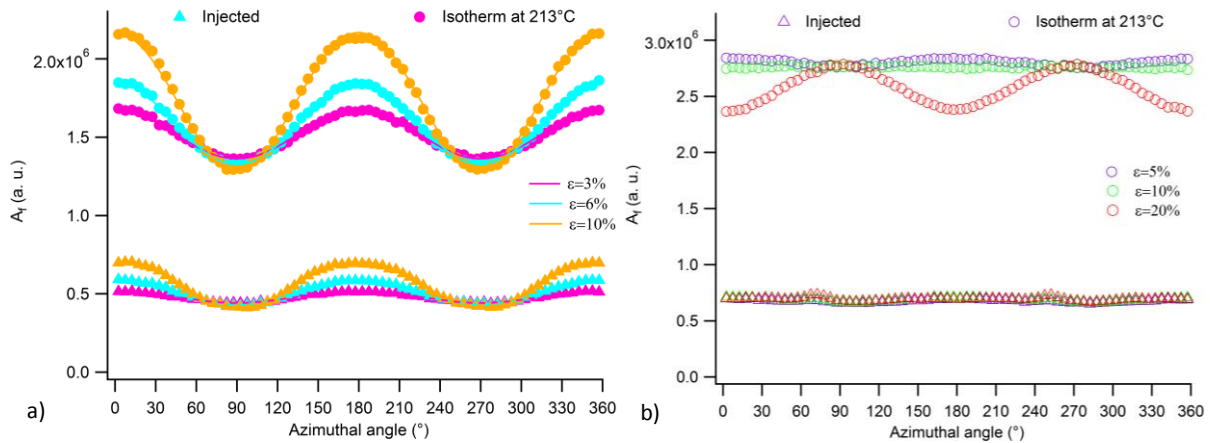


Figure V.20: Amplitude of intensity A_f as a function of azimuthal angle for different macroscopic engineering strains for tensile tests a) at $T = 0^\circ\text{C}$ and b) $T = 120^\circ\text{C}$ for I213 and INJ samples

The A200 ($\alpha + \gamma$ phase) and A215 (α phase) samples have also been studied. The amplitude A_f for samples A200 and A215 are plotted as a function of azimuthal angle in Figure V.21. It shows that the A215 sample behaves in the same way as the I213 sample whatever the temperature. Concerning the A200 sample, the behavior is closer to the one of the INJ sample, showing relative broad maxima peak for $\psi = 90$ and 270° at 0°C and almost no orientation at 120°C . The sudden shifts of peak around $\psi \approx 70^\circ$ and $\psi \approx 250^\circ$ above T_g are artifact due to imperfect subtraction of the curve in the initial state.

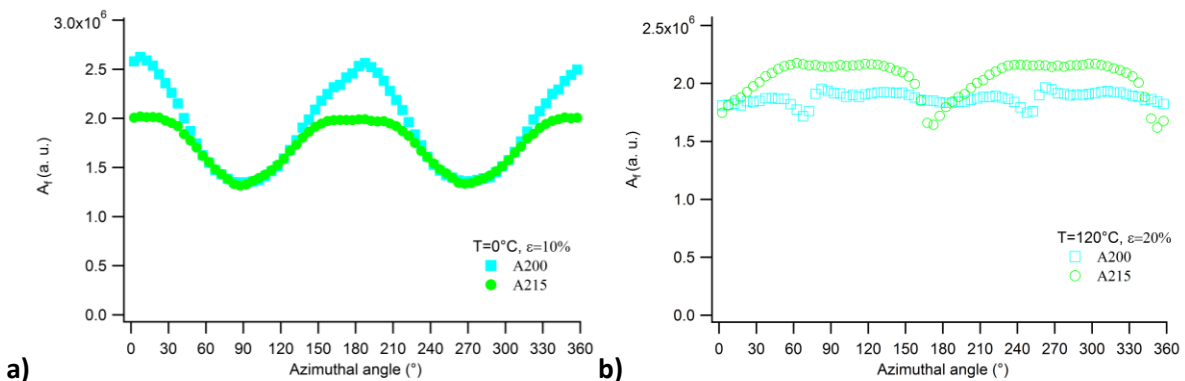


Figure V.21: Amplitude of intensity A_f as a function of azimuthal angle for A200 and A215 samples a) at $\epsilon = 10\%$ and $T = 0^\circ\text{C}$ and b) at $\epsilon = 20\%$ and $T = 120^\circ\text{C}$

I.4.2. Analysis of orientational distributions of lamellae

We now analyze in more details the distribution of orientation of lamellae, which is reflected in the variation of the scattered intensity as a function of the azimuthal angle ψ . At 0°C (below T_g), it has been observed that the lamellae tend to orient under tensile strain with their normal along the stretching direction, that is, the surface of the lamellae have a tendency to become perpendicular to the stretching direction. The most straightforward way to analyze this observation with a homogeneous deformation is to consider affine deformation of the lamella normals, as schematized in Figure V.22. Possible mechanisms leading to such type of deformation will be discussed later in §III.

Let us consider now that the vector \vec{dr} is along the chain within a crystalline lamella, that is along the normal to a lamella \vec{n} . So, the local deformation of a lamella can be schematized as in Figure V.22.

The Cartesian coordinates (x, y, z) of \vec{dr} in a frame with z axis along the tensile direction. After affine deformation, the coordinates are changed to $(x' = \lambda^{-1/2}x, y' = \lambda^{-1/2}y, z' = \lambda z)$, where $\lambda = L/L_0 = 1 + \varepsilon$ is the stretching ratio, as depicted in Figure V.22. The angle ψ between \vec{dr} and the tensile direction is given by $\tan \psi = (x^2 + y^2)^{1/2}/z$. It is changed into ψ' given by $\tan \psi' = \frac{(x'^2 + y'^2)^{1/2}}{z'} = \lambda^{-3/2} \tan \psi$.

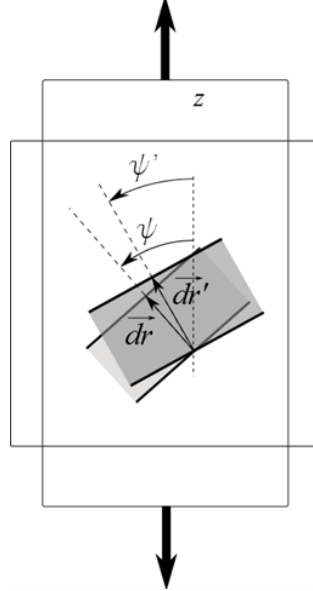


Figure V.22: A lamella (with the vector \vec{dr} along the normal) before and after affine uniaxial deformation. In this model for the deformation of the material, the lamellae tend to orient along the tensile direction.

In the initial, supposedly isotropic state, the density Φ_0 of lamella (i.e. of lamella normals) on the unit sphere is uniform. It is related to the total number N of lamellae within the scattering volume: $\Phi_0 = N/(4\pi)$. The number of lamella normals in the interval of angle $[\psi, \psi + d\psi]$ is $n(\psi)d\psi = 2\pi\Phi_0 \sin \psi d\psi$.

In the deformed state, the number of lamella within the interval $[\psi', \psi' + d\psi']$ is given by $n'(\psi')d\psi' = n(\psi)d\psi$. Calculation gives:

$$n_\lambda(\psi') = 2\pi\Phi_0 \frac{\lambda^3 \sin \psi'}{(\cos^2 \psi' + \lambda^3 \sin^2 \psi')^{3/2}} \quad (\text{E V.20})$$

The subscript λ indicates that the deformed distribution depends of course on the value of λ .

It follows that the density of lamellae on the unit sphere in the deformed state (which depends only on the angle ψ') is given by:

$$\Phi_\lambda(\psi') = \Phi_0 \frac{\lambda^3}{(\cos^2 \psi' + \lambda^3 \sin^2 \psi')^{3/2}} \quad (\text{E V.21})$$

Conservation of the scattering volume under stretching has been assumed. The effectively measured intensity comes from lamellae which are in position of reflection. It corresponds to the intersection of the sphere with the Ewald sphere (of thickness δ), which in the small angle limit, is identical to the plane of the detector (see Figure II.6 of chapter II). The intensity measured in the initial isotropic state is $I = F\Phi_0\delta$, independent of the azimuthal angle ψ (where F is an arbitrary normalization factor). In the stretched state, it is $I(\psi) = F\Phi_\lambda(\psi)\delta$ in which $\Phi_\lambda(\psi)$ is given by Eq. V.21.

Intensities calculated from Eq. V20 are plotted in Figure V.23 as a function of the azimuthal angle ψ , for different values of the strain ε (normalized to $F\delta = 1$).

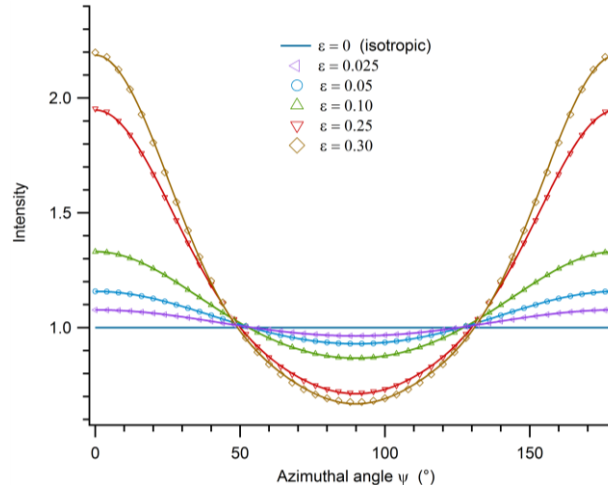


Figure V.23: Normalized intensities as a function of the azimuthal angle ψ , for different values of the strain ε , calculated using Eq. V.20, curves are fits using Eq. V.22 up to sixth order.

Intensity curves calculated with Eq. V.20 may be expressed as series expansions of even Legendre polynomials:

$$\Phi_{\lambda}(\psi) = p_0 + p_2(\lambda)P_2(\psi) + p_4(\lambda)P_4(\psi) + p_6(\lambda)P_6(\psi) + \dots \quad (\text{E V.22})$$

Expansion is limited to 6th order. Expressions of Legendre polynomials are:

$$P_2(\psi) = \frac{3 \cos^2 \psi - 1}{2}$$

$$P_4(\psi) = \frac{1}{8}(35 \cos^4 \psi - 30 \cos^2 \psi + 3)$$

$$P_6(\psi) = \frac{1}{16}(231 \cos^6 \psi - 315 \cos^4 \psi + 105 \cos^2 \psi + 5) \quad (\text{E V.23})$$

Fits are shown in Figure V.23 on top of calculated distribution curves for different values of the macroscopic strain ε (or equivalently stretching ratio $\lambda = 1 + \varepsilon$). The coefficients p_2 , p_4 and p_6 are plotted in Figure V.24 as a function of the strain ε .

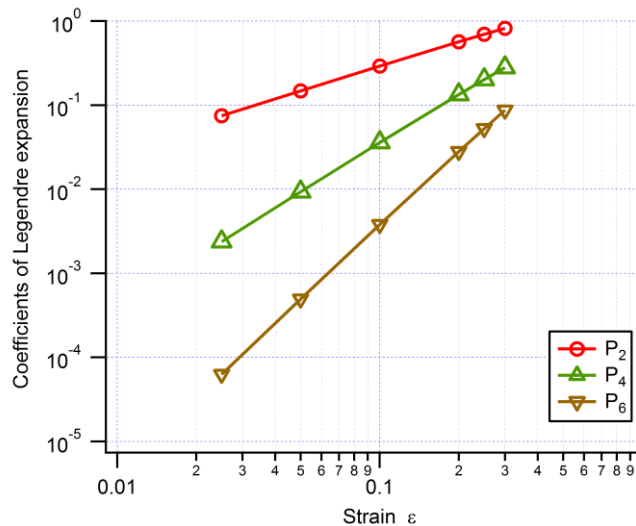


Figure V.24: Coefficients p_2 , p_4 and p_6 of the Legendre expansion Eq. V.6 as a function of the strain ε

Figure V.24 shows that the coefficients p_2 , p_4 and p_6 vary as power laws of the strain ε : $p_2 \approx \varepsilon$, $p_4 \approx \varepsilon^2$ and $p_6 \approx \varepsilon^3$.

Conservation of the scattering volume has been assumed. In fact, the sample thickness varies a little bit under stretching. This has two consequences which modify the measured intensity:

- Decrease of sample thickness e results in a decrease of the scattering volume $e\Phi_X$ (where Φ_X is the cross section area of the X ray beam), which shall decrease the scattered intensity accordingly.
- Decrease of sample thickness results in a decreased absorption, which shall lead to an increase of the measured intensity.

Let us now discuss the fitting of experimental data. We focus on the fit and the Legendre's coefficients. The fit has only been performed on the INJ and I213 samples below T_g and only for the INJ sample above T_g as the normals of I213 prefer to orient at $\psi=90$. p_2 and p_4 coefficients as a function of strain are plotted in Figure V.25. Finding that normals orient preferentially vertically as proposed by the affine model, means that the model qualitatively describes the orientation process in that case. In addition, p_2 coefficients vary linearly compare to the strain (Figure V.25a) as predicted by the model (see Figure V.24) for tensile tests below the glass transition. Above T_g , for the INJ sample, p_2 coefficients are really low, meaning that there is nearly no orientation. Concerning p_4 coefficients, it is found that most of p_4 coefficients are negative, meaning there is a variance compare to the affine model. Indeed, having negative coefficients has not been taken into account in the model. However, if p_4 values are negative, it is because in the case of experimental data the top peaks are flatter than the bottom peaks, in contrast to the affine model. As p_4 values are also very low, it means that in contrast to the model, they are negligible. Nonetheless, at the moment, we do not have clear physical significance for negative p_4 . Finally, concerning the I213 sample above T_g , the affine model does not apply. The corresponding mechanisms are discussed in §III, in parallel with WAXS results.

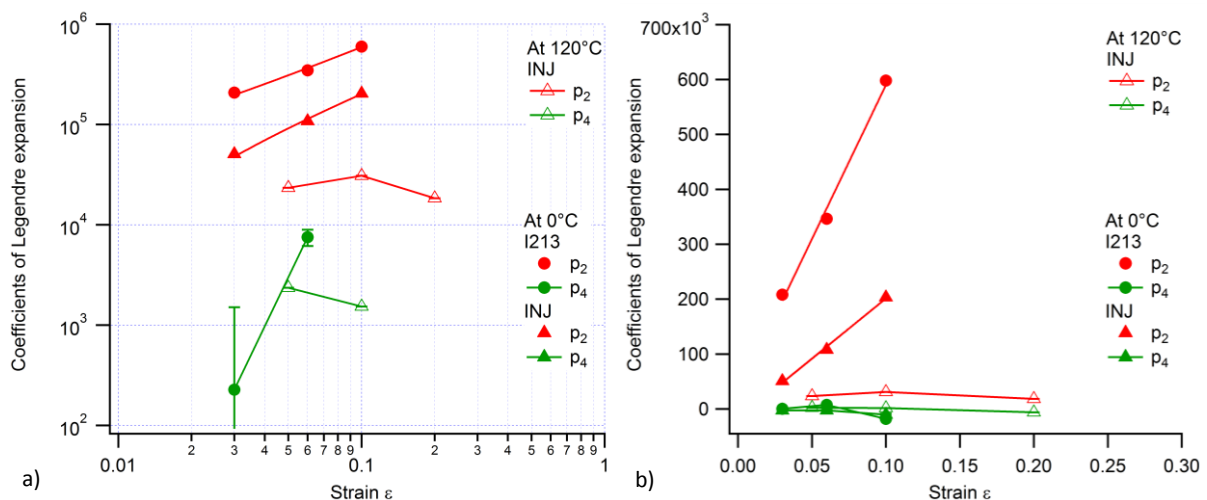


Figure V.25: Coefficient of Legendre expansion as a function of strain ϵ plotted on a) log and b) linear scales.

II. Elastic strain domain at the scale of crystalline unit cell, studied by WAXS

To investigate deformation mechanisms at the scale of the crystalline unit cell (i.e. as seen from inside crystalline lamellae), in-situ WAXS measurements were combined with SAXS measurements presented above.

II.1. WAXS protocol

As explained before, a slightly different temperature was chosen ($T = -10^\circ\text{C}$ instead of 0°C) for the tests at low temperature (below T_g). The macroscopic stress-strain curves are similar to those depicted in Figure V.4. Indeed, as said previously, there is no significant change on the strain-stress curves between $T = 0^\circ\text{C}$ and -10°C , as this interval corresponds to a broad minimum of G'' , which means that no mechanical relaxation process occurs within this temperature interval.

Examples of 2D WAXS patterns corresponding to in-situ stress-strain curves are shown in Figure V.26 for I213 and INJ samples at both temperatures. The intensity rings in the WAXS patterns are related to diffraction by families of lattice planes within the crystalline structure. During tensile tests, there is an evolution of the rings. It is this evolution that we are going to characterize and it will give us information about:

- The change of distance d between lattice planes (i.e. the deformation of the crystalline unit cell) versus the macroscopic strain (see §II.2)
- The change of distance d as a function of azimuthal angle for different values of the macroscopic strain (see §II.3)
- The change of orientational distribution of families of lattice planes, i.e. of crystallites (see §II.4)

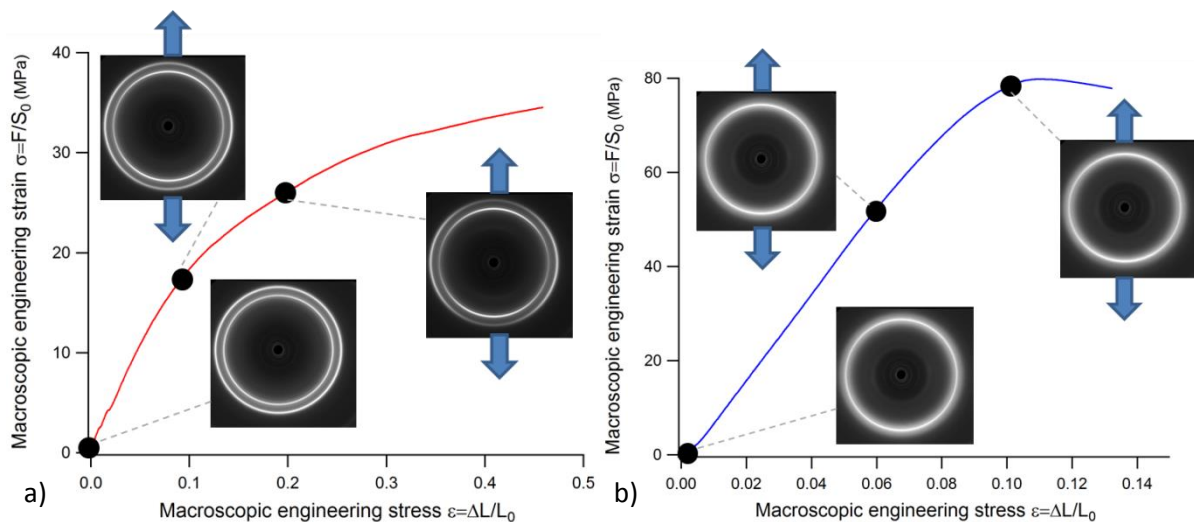


Figure V.26: Scheme of WAXS patterns during tensile test a) at $T = 120^\circ\text{C}$ for I213 sample (α phase) and b) at $T = -10^\circ\text{C}$ for INJ sample (β phase).

For samples with α phase, two main diffraction rings are present, the inner ring at scattering angle about 21° corresponds to the family of (200) planes, the outer ring at about 24° corresponds to (002) and (20 $\bar{2}$) planes (see chapter II and also Figure V.24a). For injected materials (β phase), there is only one relatively broad main peak around 22° corresponding to (002), (200) and (20 $\bar{2}$) planes, which are all equivalent in the case of the β phase.

All these planes are parallel to the chain axis, as shown in Figure V.27a and b. The diffraction by a family of planes is in the direction of the normal to the planes. Thus, vertical scattering (along the tensile direction TD) corresponds to crystal planes which are almost perpendicular to TD, that, with chains perpendicular to TD (strictly speaking, the corresponding planes are in Bragg's conditions, that is at an angle about 10° with respect to TD, see Figure II.15 of chapter II).

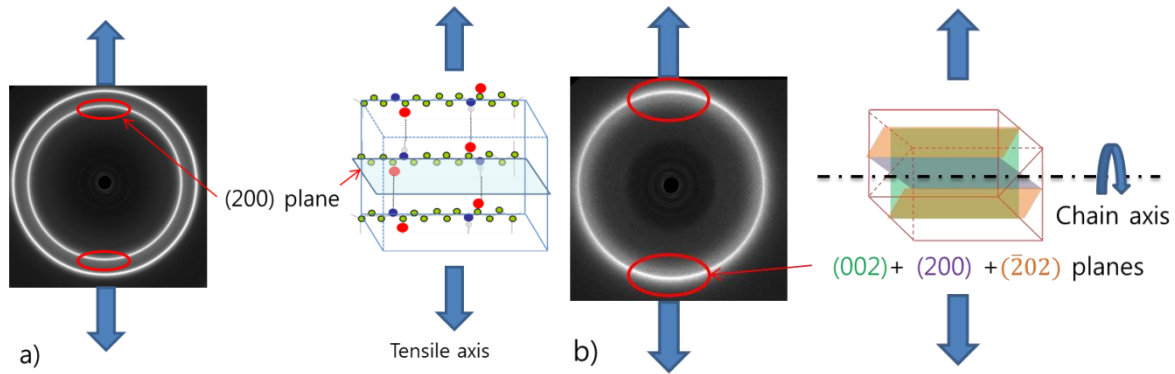


Figure V.27: Atomic planes deformation for a) α phase and b) $\beta+\gamma$ phases during tensile tests. Tensile direction is vertical.

Vertical scattering (along TD) thus always corresponds to families of planes which are almost in pure tensile mode. By following the displacement of the position of the peak, we can have access to the variation of the interplanar distance d . The change of distance d during tensile tests gives us information on the rigidity of the various crystalline phases.

II.2. Crystal strain in vertical scattering direction ($\psi = 0^\circ$)

Let us first focus on the change of distance for vertical scattering, along the tensile direction (TD). As mentioned just above, this corresponds to families of planes which are almost in pure tensile strain.

The variation of the distance d has been measured for various macroscopic strains within the elastic strain domain and for the different materials. The deformation of the scattering ring in WAXS (corresponding to a variation of d) is illustrated in Figure V.28 for the I213 sample. In vertical scattering direction along TD, d increases (as 2θ decreases) whereas in horizontal scattering region, d decreases (as 2θ increases). The variation of interplanar distance d corresponds to a crystal strain defined by:

$$\varepsilon_{crystal} = \frac{\Delta d}{d} \quad (\text{E V.24})$$

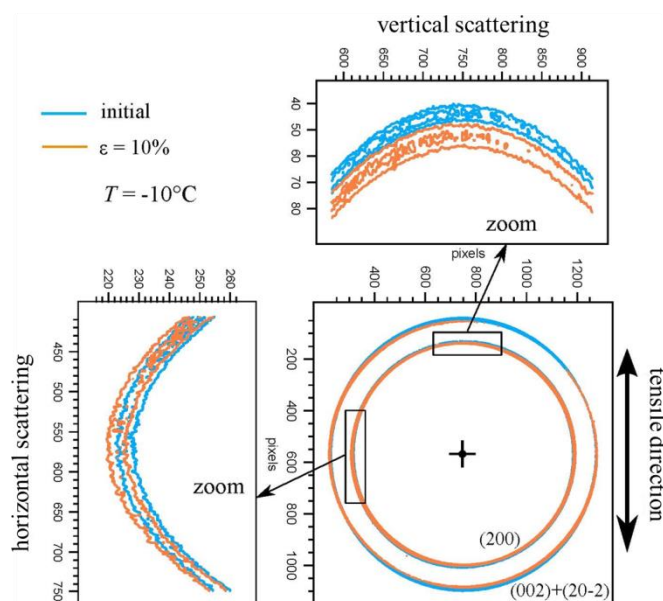


Figure V.28: Variation of 2θ angles, enhanced in vertical and horizontal scattering regions for I213 samples at undeformed and stretched ($\varepsilon_{macro}=10\%$) states, for $T=-10^\circ\text{C}$

The effects of temperature as well as the effect of crystalline phase on the variation of d as a function of the macroscopic strain ε in the vertical scattering direction are shown in Figure V.29. For both crystalline phases, the temperature plays a major role. Above T_g , the modulus of the amorphous phase drops down to a value much lower than crystalline phase. Thus, it is the amorphous phase which deforms more and that is why the crystal strain $\varepsilon_{crystal}$ is lower above T_g than below T_g . Below T_g , the difference of modulus between amorphous and crystalline phase is lower: this means that below T_g , the crystalline phase deforms more than above T_g , i.e. the crystal strain below T_g is higher than above T_g for a same macroscopic strain. For the I213 sample, with α phase, the effect of temperature is stronger than for the INJ sample (β phase). Now if we compare the impact of the crystalline phase at a same temperature, the crystal strain is always higher for β phase than α phase: this means that α crystals are more rigid than β crystals. Thus, this result gives a direct evidence that the β crystalline phase is more ductile than the α phase.

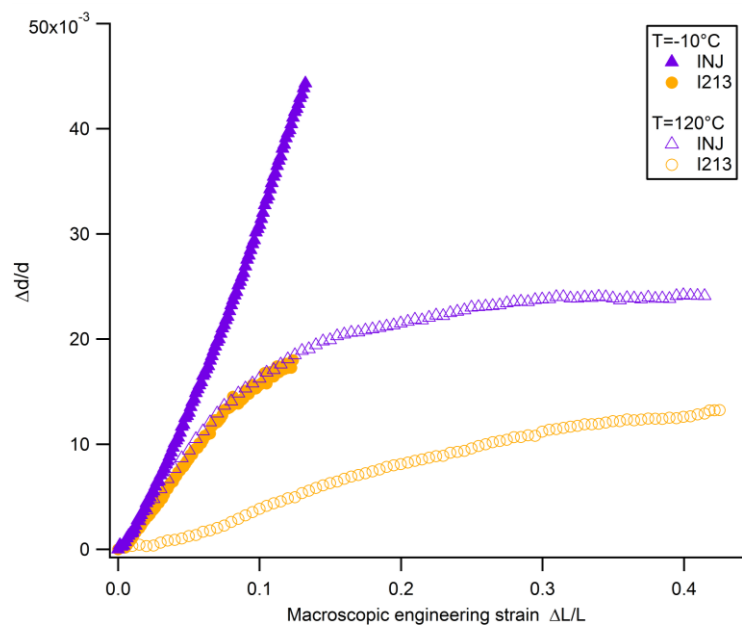


Figure V.29: Crystal strains in tensile direction for INJ (β phase) and I213 (α phase) samples at $T = -10^\circ\text{C}$ and $T = 120^\circ\text{C}$. Curves are drawn up to the yield point.

A comparison of the responses of α phase has been made for A215 and I213 samples, as shown in Figure V.30. For tensile tests below the glass transition, almost the same curves are observed in the linear regime. This result shows that at -10°C , the α phase is submitted to the same local stress in both samples. However there is a slight difference for tensile tests above the glass transition. Indeed, even though the general trend is the same, the crystal strain is a little bit smaller in the I213 sample than in A215. This difference could be due to:

- The rigidity of the crystal. Indeed in I213 sample, the crystalline perfection is higher and it could give a more rigid crystal, with local deformations of smaller amplitude for a given macroscopic strain/stress, meaning a smaller variation of d .
- The effect of the morphology and/or crystal/amorphous coupling. In this case the crystal would have the same rigidity, but would be placed in a different surrounding, which would result in a different local stress. Indeed, doing an isotherm or an annealing can affect the microstructure like for example the number of tie molecules, as reflected in the differences in long period L_p (see Chapters III and IV).

However, testing these hypotheses would require additional experiments.

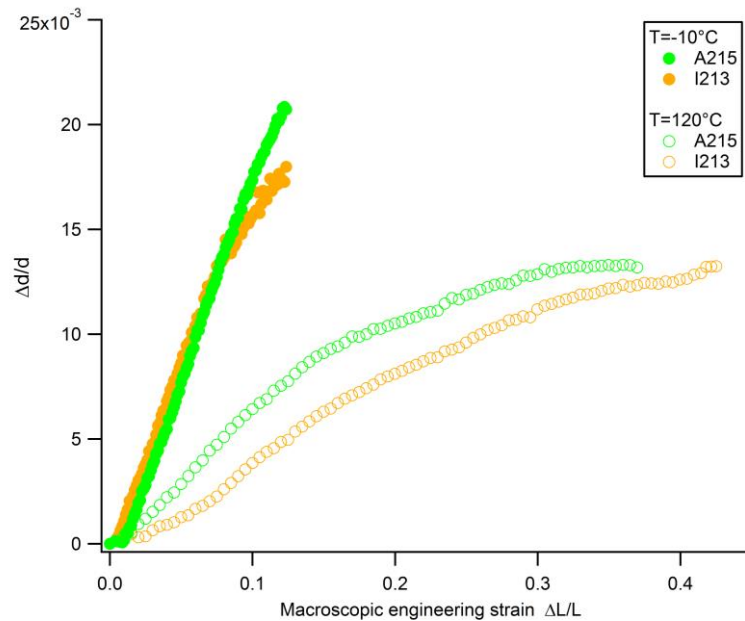


Figure V.30: Comparison of local crystal strains for samples with α phase I213 and A215 at $T = -10^\circ\text{C}$ and $T = 120^\circ\text{C}$.

II.3. Azimuthal distribution of crystal strain (WAXS investigation)

II.3.1. Experimental results

As in the case of the local strain measured by SAXS, we now investigate the azimuthal distribution of crystal strain.

As already mentioned above, for samples with α phase, the crystal strain $\Delta d/d$ has been measured for the inner scattering ring, corresponding to (200) lattice planes. For the sample with β phase, there is only one broad ring and it corresponds to all (002), (200) and ($\bar{2}$ 02) planes, which are all equivalent.

The crystal strain $\Delta d/d$ is plotted as a function of azimuthal angle ψ for both the INJ and I213 samples in Figure V.31. For both cases (Figure V.31a and Figure V.31b), the crystal strain is maximum at $\psi = [k\pi \mid k \in \{0,1,2\}]$, equivalent to 0, 180 and 360°. As $\psi = [k\pi \mid k \in \{0,1,2\}]$ corresponds to the tensile direction, it proves that (200) crystalline planes (for α phase) and (002)+(200)+($\bar{2}$ 02) planes (for β phase) are under maximum tensile load at these positions. Furthermore, it shows that the amplitude of the crystal strain is higher for INJ than I213 samples whatever the temperature, which is still in good agreement with the β phase being more ductile than the α phase.

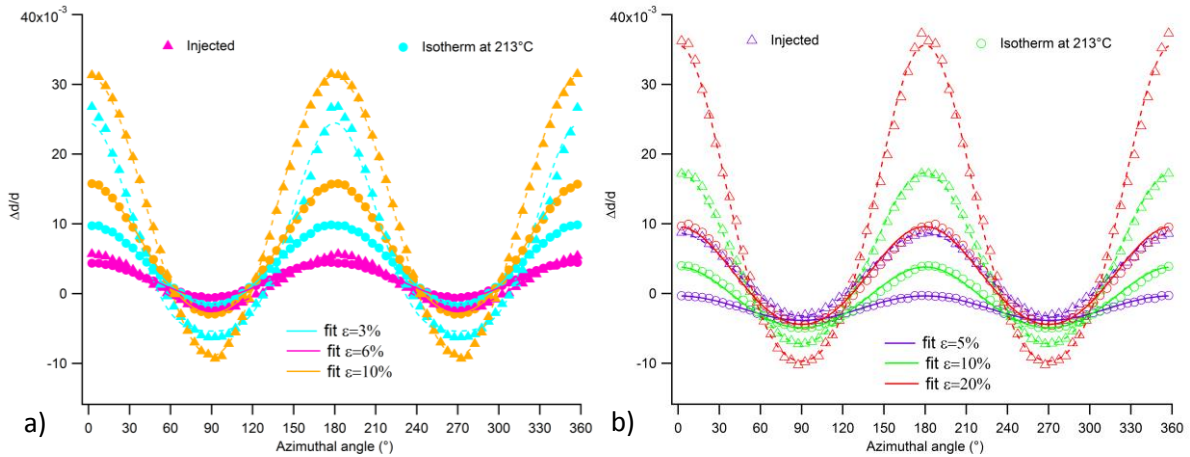


Figure V.31 : $\Delta d/d$ as a function of azimuthal angle ψ for different macroscopic engineering strains for INJ and I213 samples a) at $T = -10^\circ\text{C}$ and b) at $T = 120^\circ\text{C}$. Points are experimental data and curves are fits with a Legendre polynomial expansion (Eq. V.14).

The effect of the temperature is now further analyzed for both samples as shown in Figure V.32. In each case, the amplitude of the crystal strain is higher for tensile tests below T_g , at $T = -10^\circ\text{C}$. This means that the rigidity of the crystal is either directly affected by the temperature or either the surrounding of the crystal is affected by temperature and modifies the local stress. As said previously, it is impossible to know which effect is predominant at this stage.

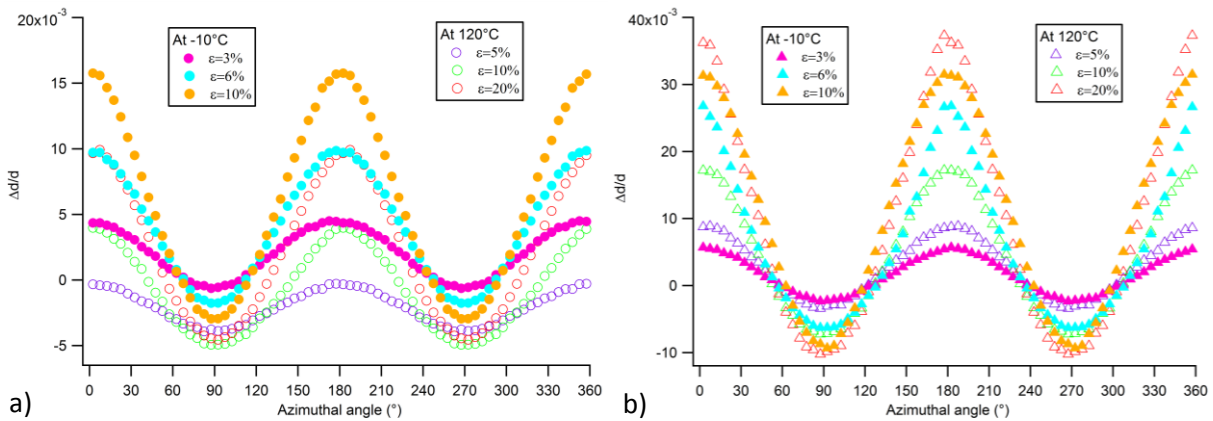


Figure V.32: Same data as in Figure V.31 but plotted differently. $\Delta d/d$ as a function of azimuthal angle for different macroscopic engineering strains for tensile tests at $T = -10^\circ\text{C}$ and $T = 120^\circ\text{C}$ for a) I213 samples and b) INJ samples

II.3.2. Analysis of the results

Curves showing the crystal strain as a function of the azimuthal angle have been fitted with a Legendre polynomials expansion limited to 4th degree (see Eq. V.14). The fits are shown in Figure V.31. p_2 and p_4 coefficients as a function of macroscopic strain are shown in Figure V.33. p_2 is always positive and increases linearly as a function of the strain. As said before, it shows that p_2 is higher for $T < T_g$ for both samples. For both temperatures, the p_2 coefficient is lower for I213 (containing α phase) than for INJ sample (containing predominantly β phase). β phase is more ductile than α phase

Concerning p_4 , values are either positive or negative depending on the strain but for they are still much lower than p_2 values. The presence of non zero p_4 values is related to the inhomogeneity of the strain in crystallites with different orientations. The fact that p_2 varies linearly with the strain and that

p_4 remains small compared to p_2 indicates that, in the linear regime of deformation, crystallites behave as if they were submitted to a nearly homogeneous strain.

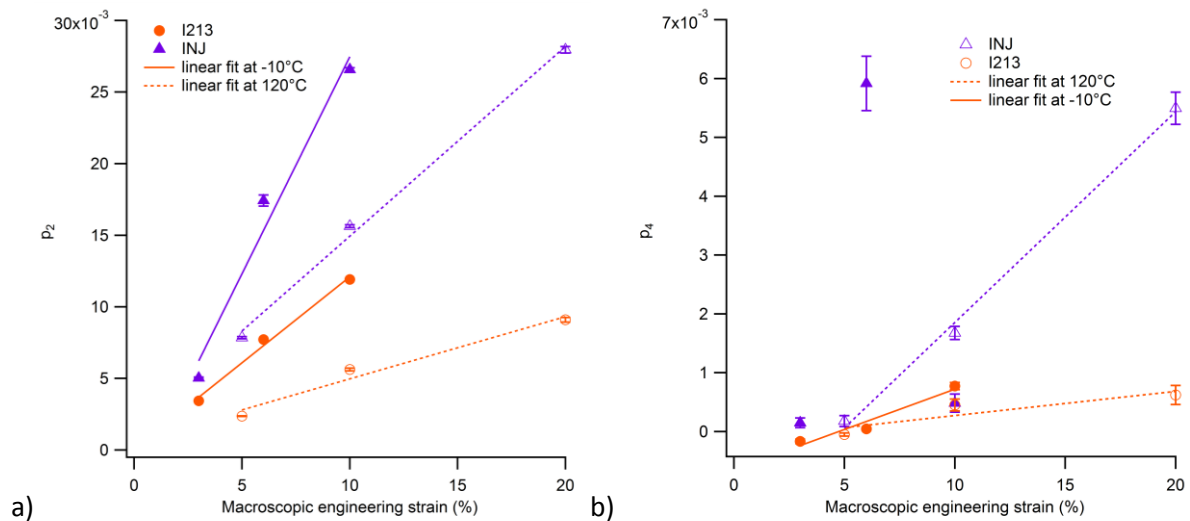


Figure V.33: a) p_2 and b) p_4 coefficients for INJ (purple Δ) and I213 (orange \circ) samples at various strains, full lines and points for $T = -10^\circ\text{C}$ and dotted lines and points for $T = 120^\circ\text{C}$

Concerning p_0 , values increase as a function of strain, as shown in Figure V.34a. p_0 is almost always positive except for I213 sample at $T = 120^\circ\text{C}$. The local Poisson coefficient of the crystals ν , calculated with Eq. V.17, is plotted as a function of macroscopic strain in Figure V.34b. It only concerns the behavior of the crystal. Concerning INJ sample and so β crystal, apparent ν value is around 0.4 whatever the temperature, i.e. close to the macroscopic ν value. It indicates that the stress/strain state is fairly homogeneous in the material.

On the contrary, I213 sample and so α crystal behaves differently according to the temperature. Below T_g , ν value is close to 0.1 meaning that crystals giving vertical scattering (crystals with horizontal (200) planes) are submitted to larger stress than crystals giving horizontal scattering (vertical (200) planes). It indicates in this case that the stress/strain state is not homogenous in the material. Above T_g , ν value decreases from 1 to 0.5, meaning that at first the vertical crystals are as stretched as the horizontal crystals are contracted. Observing values of the apparent Poisson's coefficient for the crystals very different from the macroscopic value, indicates that for I213 sample the stress/strain state is far from homogenous in the material.

Once again, the difference of behavior between α and β crystals is enhanced in Figure V.34b.

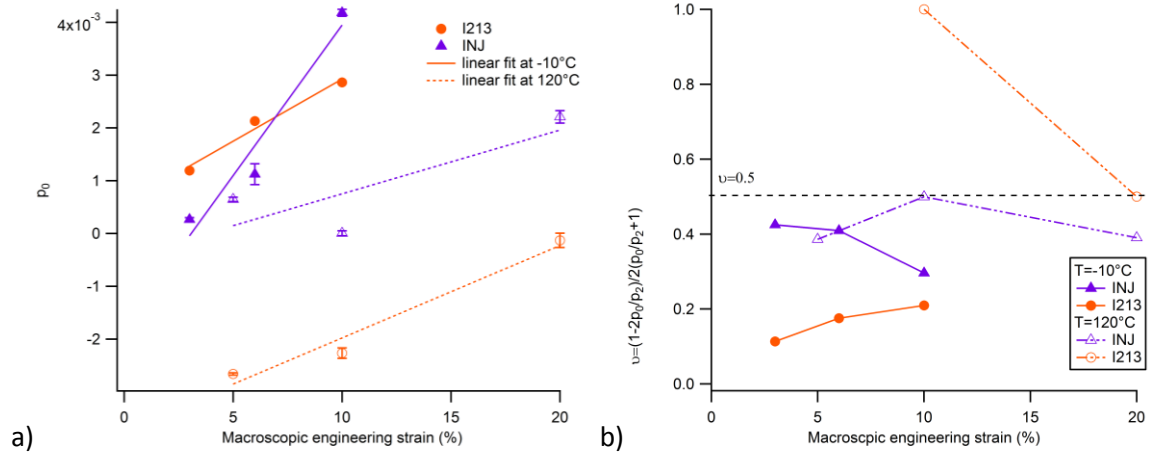


Figure V.34: a) ρ_0 coefficients and b) Poisson's ratio of the crystals ν plotted thanks to Eq. V.17 for INJ (purple Δ) and I213 (orange \circ) samples at various strains, full lines and points for $T=-10^\circ\text{C}$ and dotted lines and points for $T=120^\circ\text{C}$

II.4. Orientational distribution of crystalline planes, studied by WAXS

We now analyze the orientation of the crystalline planes at various macroscopic strains, still in the elastic domain. For that, the intensity is plotted as a function of azimuthal angle. However the intensity is plotted for each define crystalline peak. To illustrate the cases of samples with β or α crystalline phase, we will show results for the INJ (β phase) and I213 (α phase) samples. The effect of temperature has also been investigated in both cases. The case of sample with β phase will first be discussed.

The corrected intensity $I_{\psi f}$ which is plotted corresponds to one ring and was corrected as follow (see chapter VI §1.1 and §1.2 for further information concerning the definition of the scattering domain):

$$I_{\psi f} = I_{\psi} - I_{\psi ini} + I_{\psi ini}^{av} \quad (\text{E V.25})$$

with I_{ψ} the raw (uncorrected) intensity of a stretched sample

$I_{\psi ini}$ the intensity of the sample at initial state

$I_{\psi ini}^{av}$ the average intensity of the sample at initial state

This correction allows avoiding problems of possible initial orientation of the sample: it takes into account only the stretching. It is reminded that $\psi=0^\circ$ corresponds to vertical scattering, meaning along TD.

II.4.1. Case of INJ sample, with β crystalline phase

The β phase has a pseudo-hexagonal, relatively weakly ordered crystalline structure, with only one relatively broad peak corresponding to lattice planes of Miller indices $(h0l)$ ($h \pm 2, l \pm 2$). This indicates that all directions perpendicular to chain axis (axis \vec{b} of the crystalline unit cell) are roughly equivalent. The observed 2D patterns at initial state and just beyond the yield stress are shown in Figure V.35, as well as the correspondence between the planes and the crystalline lattice.

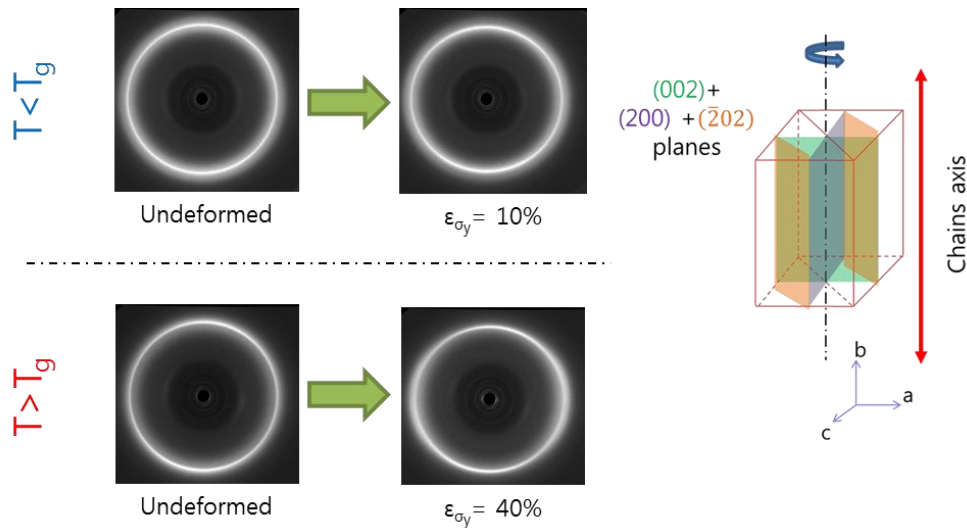


Figure V.35: WAXS patterns for sample INJ (β phase) in the initial (undeformed) state and at the yield stress point. TD is vertical

The intensity corresponding to the broad peak is plotted as a function of azimuthal angle in Figure V.36, at various macroscopic strains, for tensile tests below and above the glass transition. Whatever the temperature, peaks centered at $\psi = k\frac{\pi}{2}$ ($k \in \{1,3\}$) (horizontal scattering) are observed. This preferential orientation indicates that $(h0l)$ ($h \pm 2, l \pm 2$) crystalline planes have a tendency to orient parallel to TD. As the chain axis is parallel to these planes, it also means that chains within crystallites have a tendency to orient parallel to TD. It is worth noticing that the effect of orientation seems more affected by the drawing ratio than by the temperature: for a given strain value, the amplitude of the intensity modulation is nearly the same at both temperatures, i.e. below and above T_g . The deformation mechanisms which correspond to these situations will be discussed in §III.2.1.

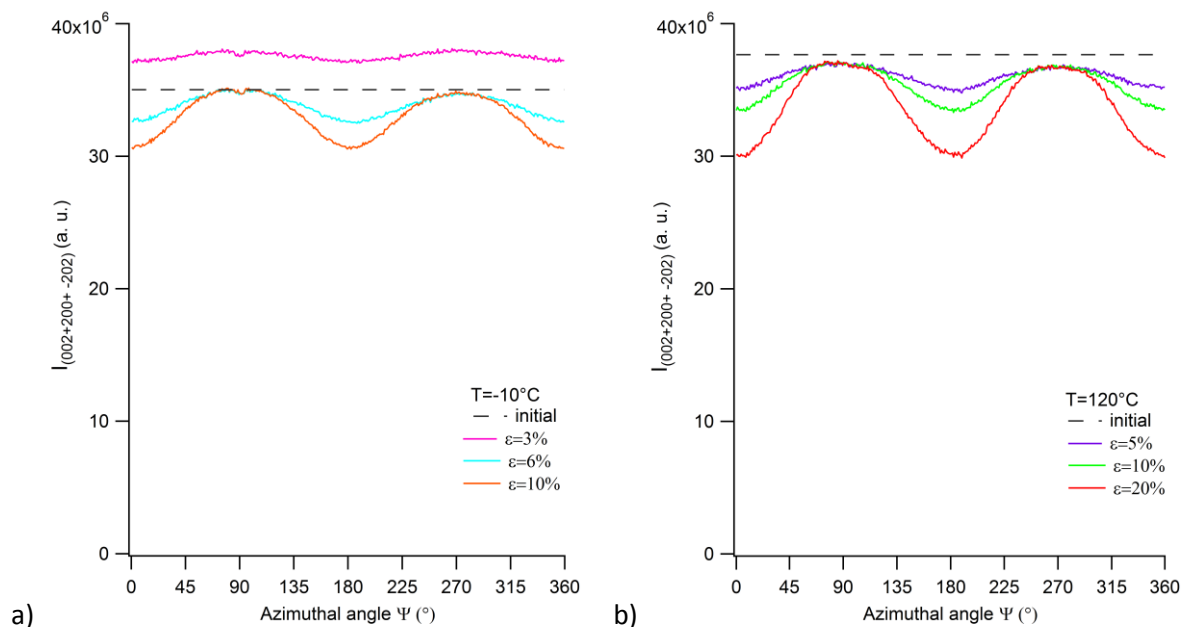


Figure V.36: Intensity in the ring corresponding to $(002+200+\bar{2}02)$ planes, from WAXS patterns, as a function of azimuthal angle for INJ samples at various strains; at a) $T = -10^\circ\text{C}$ and b) $T = 120^\circ\text{C}$ ($\psi = 0^\circ$ correspond to the TD)

II.4.2. Case of sample I213, with α crystalline phase

For the sample with α phase, 2D WAXS patterns consist of two narrow scattering rings at $2\theta \approx 20^\circ$ and $2\theta \approx 24^\circ$. These circular rings corresponds for the inner one to (200) planes and for the outer one to (002) + (20 $\bar{2}$) planes. These two families of planes are not equivalent. Their correspondences to the crystalline lattice and chains are reminded in Figure V.37, as well as the observed 2D WAXS patterns.

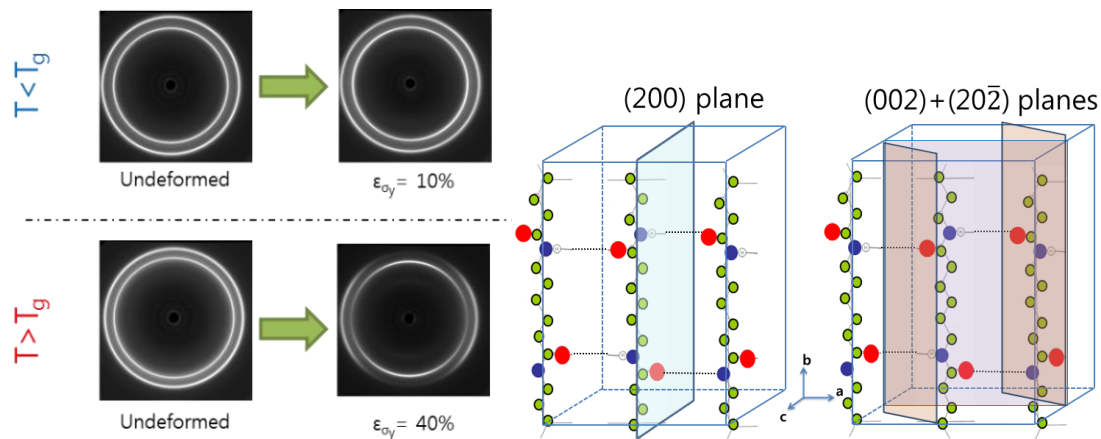


Figure V.37 : WAXS patterns for I213 (pure α phase) at undeformed state and at the yield stress state, TD is vertical

Intensity profiles as a function of azimuthal angle are plotted in Figure V.38 for the two scattering rings, for different values of the macroscopic strain ε . Concerning (200) planes (Figure V.38a), the intensity profile is modulated and shows maxima at $\psi = k\pi$ ($k \in \{0,1,2\}$), i.e. $\psi = 0^\circ \pm \pi$ rad. For (002) + (20 $\bar{2}$) planes (Figure V.38b), maxima are located at $\psi = -90$ (mod. 180°). The amplitude of the modulation increases as the macroscopic strain increases, reflecting increasing orientational anisotropy of the ensemble of crystallites. Looking in more details at the effect of temperature, one can notice that the orientational anisotropy of (200) planes is more affected than that of (002) + (20 $\bar{2}$) planes when temperature changes. Indeed, for (200) planes, the amplitude of the intensity modulation is much smaller below the glass transition than above. In contrast, for (002) + (20 $\bar{2}$) planes, the temperature does not impact significantly the amplitude of the intensity modulation.

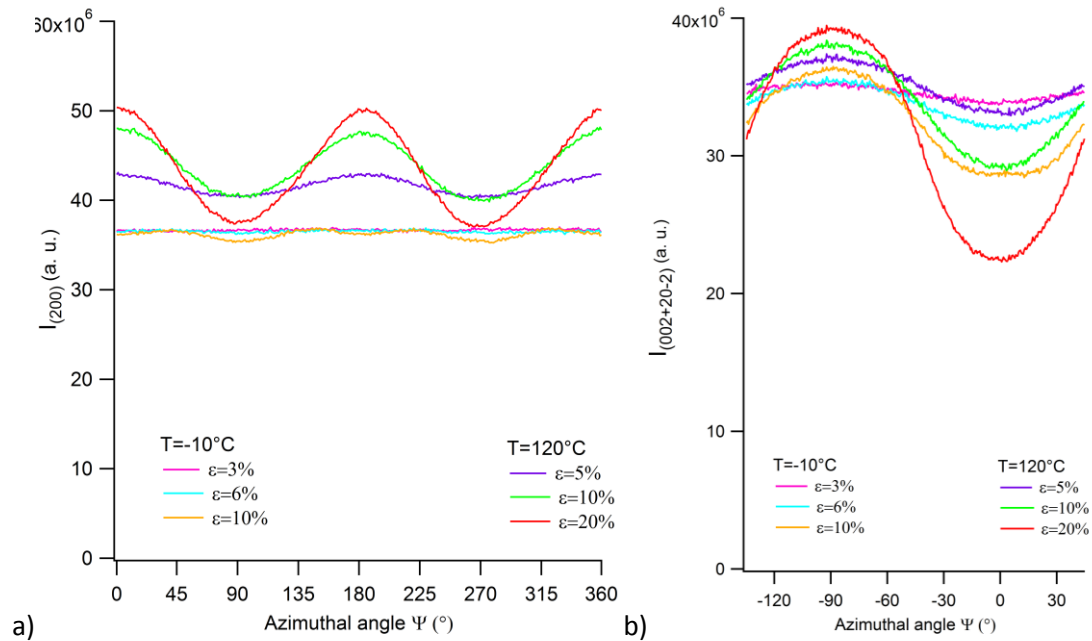


Figure V.38: Intensity from WAXS patterns as a function of azimuthal angle for I213 samples at both temperatures and various strains for a) (200) planes and b) (002) + (20 $\bar{2}$) planes, $\psi = 0^\circ$ corresponds to vertical scattering.

Let us now take a closer look at the correspondence between the observed orientation and the planes and chains orientations. Observing scattering of (200) planes at $\psi = 0^\circ$ (vertically) means that the corresponding (200) planes are horizontal, as depicted in Figure V.39 (left). Therefore, the chains, which are contained in the (200) planes, are perpendicular to TD. It means also that the lamellae have their normals perpendicular to tensile direction, since the lattice is monoclinic with chains perpendicular to the surfaces of lamellae. Then, in this configuration, (002) + (20 $\bar{2}$) planes scatter in directions of about 20° around the horizontal direction, as depicted in Figure V.39 (middle). Indeed, this is in agreement with what is effectively observed in Figure V.38b.

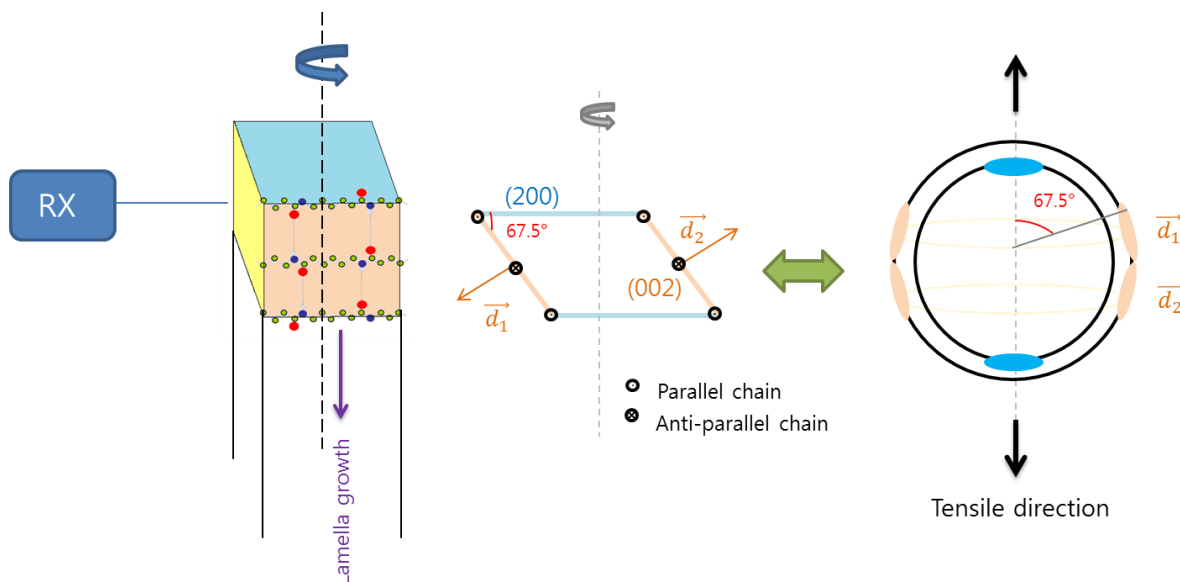


Figure V.39: Correspondence between polar lamellae and WAXS pattern in the case of crystalline lattice α

The deformation mechanisms which correspond to these situation will be discussed in §III.2.2 in parallel with SAXS observations.

III. Discussion: deformation mechanisms under stretching in the elastic regime

The discussion in this part allows reuniting the SAXS and WAXS observations described above and proposing mechanical models. Furthermore, both in SAXS and WAXS, changes in lamellar spacing and orientation or changes in crystalline lattice planes are detected as a function of lamella or crystal orientation. Here we discuss the connection to the spherulitic morphology.

First, one has to remind that observations made in SAXS or WAXS do not represent the entire populations of lamellae or crystalline planes but only those which are in Bragg's conditions for scattering. However, since the tensile experiment has uniaxial symmetry, it is relatively easy to infer the global distributions from scattering patterns.

In samples with predominantly β phase, the deformation is qualitatively described by affine deformation of the lamella normals. Lamellae tend to orient perpendicular to TD. The tensile strain in lamellar stacks perpendicular to TD is lower than the macroscopic tensile strain, which must be compensated by increased shear in inclined stacks. In samples with predominantly α phase, morphology changes are more complex. In a first step, some lattice planes orient perpendicular to TD, which implies that chains are perpendicular to TD. Beyond yield, lamellae reorient with their normal perpendicular to TD, thus chains themselves become parallel to TD, leading to a highly oriented fibrillar morphology.

III.1. Models

III.1.1. "Chain network" model (CN)

In polyamides, the crystallinity index is generally relatively low. In our PA6 samples, it is roughly between 25 and 35%. At low crystallinity index, a semicrystalline material may be described as a dispersion of crystalline entities or inclusions (lamellar stacks) embedded within a matrix of amorphous phase.

In the "chain network" model, the subchains between lamellae, acting as tie molecules, play the predominant role and transmit the stress. When submitted to a tensile load, chains are stretched. Crystalline parts of the chains (which are perpendicular to lamella surfaces) tend to orient along the tensile direction and thus exert a torque on crystalline lamellae, which tend to orient the normal to lamella surfaces parallel to tensile direction. This deformation process is schematized in Figure V.40. In this process, lamellae follow the motion of chains and tend to orient towards the equator. In the initial (undeformed) state, the material is supposed to be isotropic, both in terms of lamellar spacing and orientational distribution of crystalline lamellae.

Horizontal lamellar stacks (located in the equator of spherulites) are submitted to pure tensile stress, which results in an increase of the long period L_p . Vertical lamellar stacks (which may be located either in the equator or in the polar regions of spherulites, see Figure V.1) are submitted to compressive stress, which results in a decrease of L_p .

In order to orient towards horizontal orientation, initially inclined lamellae stacks undergo both rotation and shear (shear cannot be detected in our scattering experiments, however).

This process is schematized in Figure V.40: during tensile load, a chains stretching happens and this leads to the tilting of lamellae stacks as well as a slight shear (step 1 to step 2 of Figure V.40). This is shown in Figure V.42: dotted line represents the form of a spherulite but the model can either work for a non-spherulitic structure. Indeed, as mentioned before, spherulitic morphology is not a prerequisite for this model.

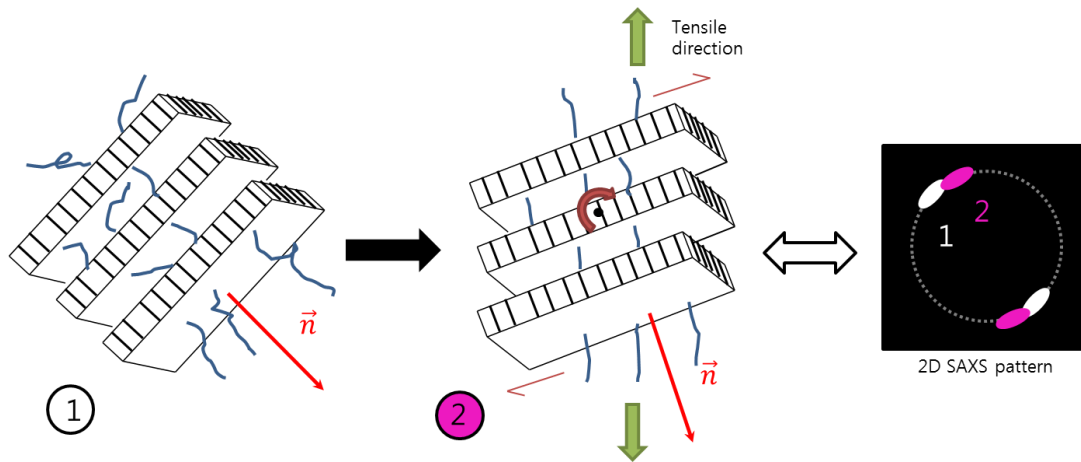


Figure V.40: Focus on the mechanisms of rotation and shear linked to the “CN” model. Effect on the distribution of intensity observed in 2D SAXS pattern is shown on the right

The consequences of the “Chain network” (CN) model on SAXS and WAXS patterns are schematized in Figure V.42 :

- In SAXS, as the lamellae rotate to the equator, this means that more normals to lamella surfaces scatter in vertical direction, resulting in an enhancement of intensity in vertical direction. This effect is illustrated in Figure V.40.
- In WAXS, main diffraction peaks come from lattice planes which are perpendicular to lamella surfaces and contain chain axis. Since lamella surfaces tend to orient perpendicular to the tensile direction, diffracting planes tend to orient parallel to the tensile direction, that is, they tend to scatter horizontally. In the sample with α crystalline phase, this is true for both (200) , $(20\bar{2})$ and (002) planes. Concerning the sample with β crystalline phase, all $(h0l)$ planes (which are all equivalent) scatter horizontally.

III.1.2. “Rigid Lamella” model (RL)

A quite different deformation mechanism may possibly occur. Consider a lamella or a crystallite made of a lamellar stack with large aspect ratio, embedded within a homogeneously deformed material. Under tensile strain, the crystallite will have a tendency to orient with the larger dimension parallel to the tensile direction, as depicted in Figure V.41 from step 1 to 2. In this situation, the stress is not transmitted to crystallites by stretched individual chains, but by the amorphous phase as a whole, acting as a homogeneous elastic (or viscoelastic) matrix. This mode of deformation is denoted here “Rigid lamella” model (RL).

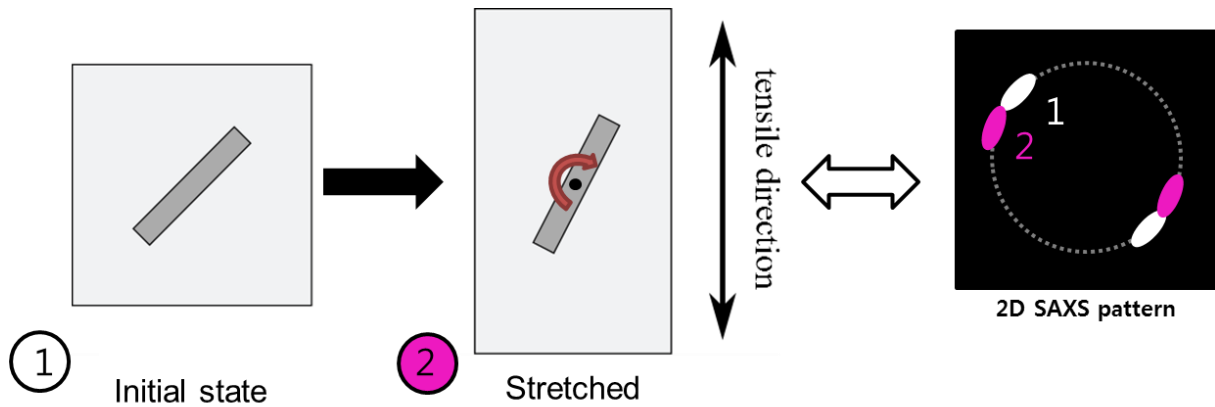


Figure V.41: Schematics of the induced orientation of a crystallite within the “Rigid lamella” model of deformation.

In the case of a crystalline network, the crystallinity index is supposed to be high. In our case, the higher crystallinity index concerns I213 samples. Microscopic observations under polarized lights have revealed the presence of spherulites. That is why we have already adapted the model for the case of spherulite. So at underformed state, lamellae are homogeneously and randomly distributed. When the stretching starts, as lamellae are thick and numerous, their motion is stronger than the ones of amorphous chains. That is why lamellae follow a fluid motion: lamellae tend to orient parallel to the tensile direction. This means that more lamellae orient in polar way. As the tensile is uniaxial but homogeneous, equatorial lamellae are considered to remain oriented at equator but their long period L_p increases as lamellae stacks are getting away from each other. This is represented in Figure V.42.

The consequences of the “Rigid lamella” model (RL) on SAXS and WAXS patterns are schematized in Figure V.42 :

- In SAXS, as the crystallites (lamellar stacks) tend to rotate parallel to the tensile direction, this means that more normals to lamella surfaces scatter in horizontal direction, resulting in an enhancement of intensity in horizontal direction. This effect is illustrated in Figure V.41.
- In WAXS, since crystallites (lamellae) tend to orient vertically (Figure V.41), chain axis tend to orient horizontally. Then, different lattice planes may orient differently around the chain axis direction.
 - Concerning the sample with α phase, the situation depends on which lattice direction corresponds to the main growth direction.
 - Concerning the sample with β phase, all $(h0l)$ lattice planes (which contain the chain axis) are equivalent. Since crystallites (lamellae) tend to orient vertically (Figure V.41), chain axis tends to orient horizontally. However, $(h0l)$ lattice planes are distributed around the chain axis direction and not preferred orientation should be detected in the WAXS pattern.

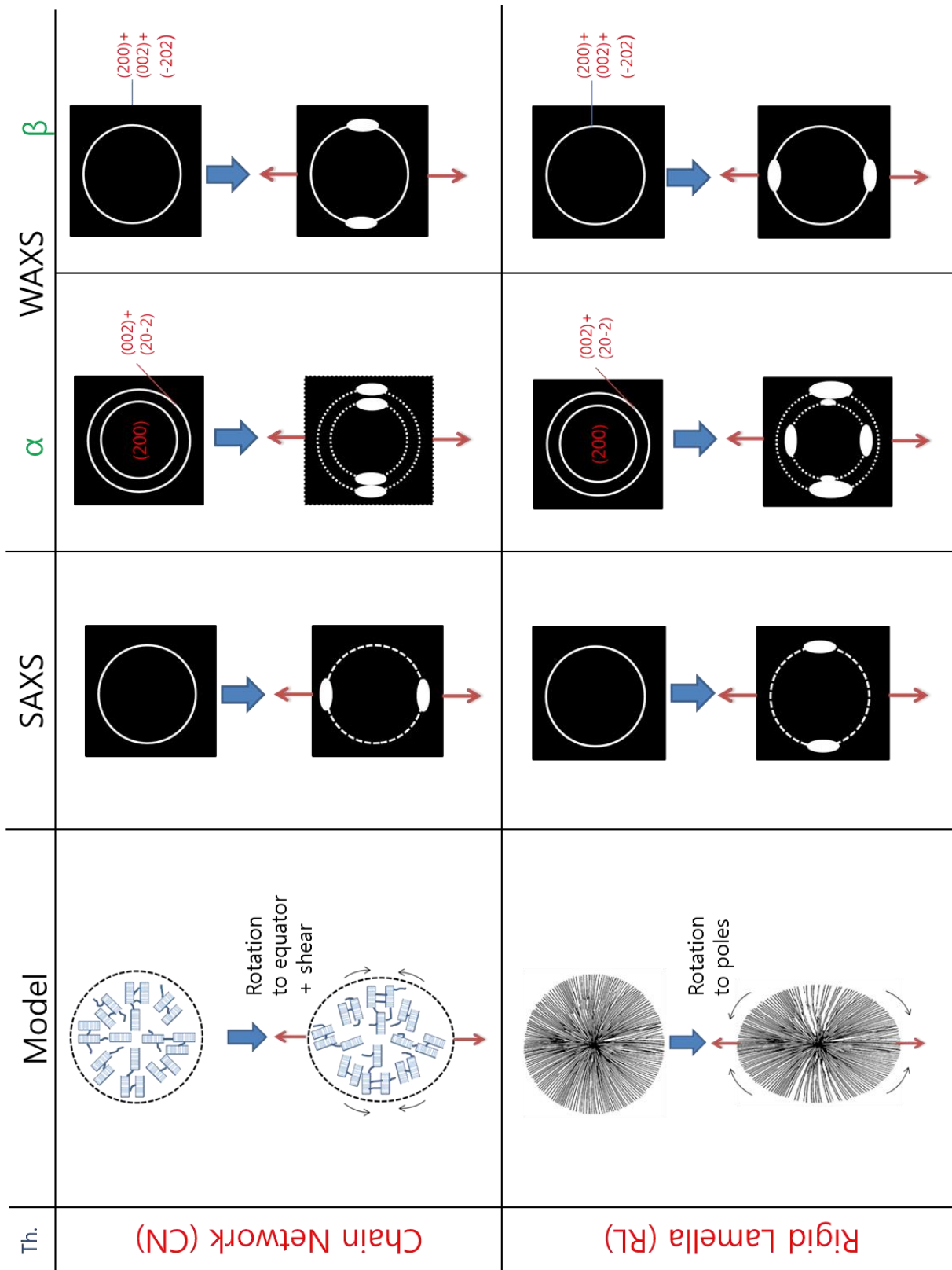


Figure V.42: Presentation of models and their concordances on SAXS/WAXS patterns, symbolizes the reinforcement of intensity, not spot

III.2. Comparison to experimental data

The models and their consequence/correspondence on SAXS/WAXS patterns were described in Figure V.42. Let us now focus on experimental data and confront SAXS and WAXS data. Intensities as a function of azimuthal angle for each sample, temperature and techniques are reminded in Figure V.43. This is these data that will help us to determine which model is the best fit in each case.

III.2.1. Case of β phase

In SAXS, the orientation is the same for both temperatures even if the effect is stronger below the glass transition. It has been observed that the lamellae normals orient preferentially in the tensile direction. This means that more lamellae are in equatorial position and so that the chain network model applies. Furthermore, concerning scattering at $\psi=90^\circ$, the intensity seems to be constant. This could be explained by the fact that polar lamellae can undergo interlamellar slips. Indeed this relative motion can justify the presence of deformation but it does not affect SAXS or WAXS. Moreover, polar lamellae can tilt around \vec{g}_1 or \vec{g}_2 without affecting SAXS or WAXS due to the rotational symmetry.

Back to WAXS data, it has been observed a favored orientation at $\psi=90^\circ$, normal to TD. This is also in agreement with a CN model. Concerning the effect of temperature, the distribution depends more on the macroscopic strain than the amorphous state: the horizontal reinforcements increase as a function of drawing ratio.

Finally, this means that concerning INJ samples (containing major β phase), WAXS and SAXS patterns are coherent with a Chain Network model. The case of Rigid Lamella model is never encountered.

III.2.2. Case of α phase

The case of α phase concerns both I213 and A215 samples. The following discussion is made for I213 samples but the same applies for A215 samples.

In the case of I213 samples, the effect of temperature seems to influence the mechanisms, according to the amorphous state. Indeed, for SAXS experiments, lamellae normals orient preferentially at $\psi=0^\circ$ or at $\psi=90^\circ$. That is why the coherence between WAXS and SAXS experiments are discussed according to the temperature.

In the case of tensile tests below T_g , lamellae normals prefer to orient at $\psi=0^\circ$. This is in adequacy with a CN model. The same discussions on polar lamellae apply like the ones made for INJ sample. Concerning WAXS data, nearly no orientation has been observed for (200) planes. (002)+(20 $\bar{2}$) planes orient at $\psi=90^\circ$. Thus, this is still in agreement with a Chain Network model.

Concerning tensile tests above T_g , SAXS data corrected by Lorentz's factor show that lamellae normal prefer to orient at $\psi=90^\circ$. Back to WAXS data, it is found that experimentally (200) planes scatter vertically whereas (002)+(20 $\bar{2}$) planes scatter horizontally. This is in agreement with a Rigid Lamella (RL) model. The motion of polar lamellae is schematized in Figure V.44. Indeed, equatorial lamellae are supposed to be only submitted to lamellar separation.

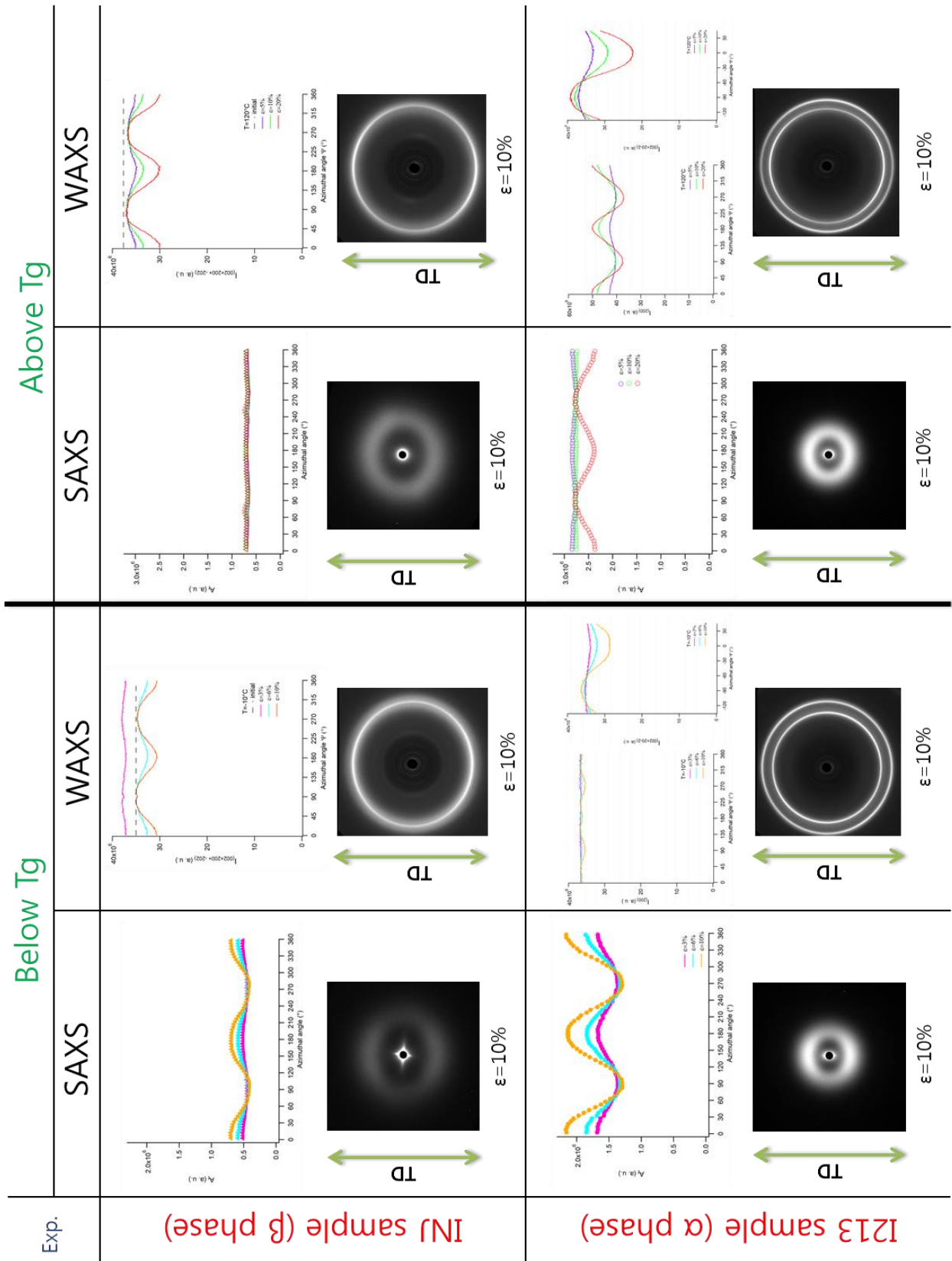


Figure V.43: Reminder of SAXS/WAXS results for INJ and I213 samples below and above T_g

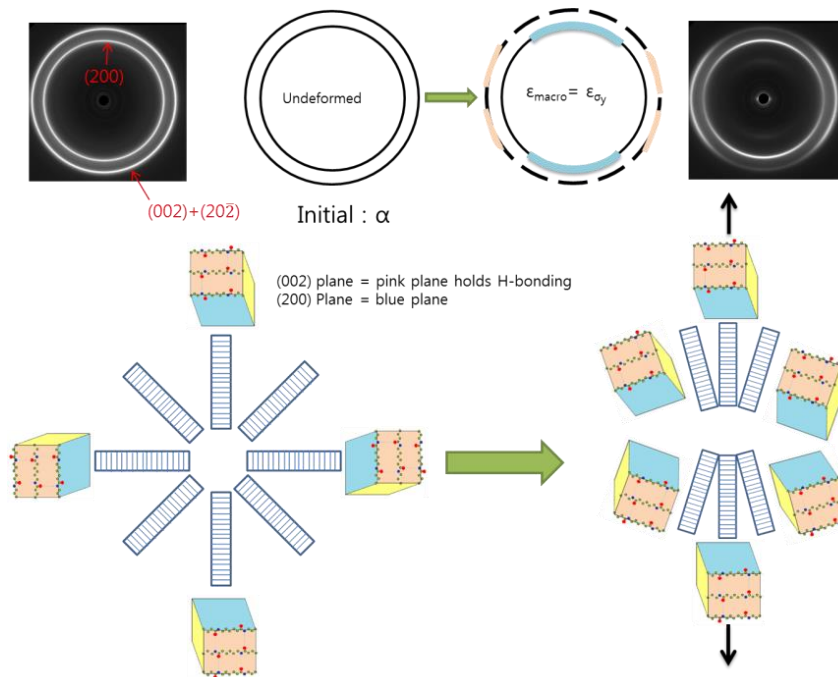


Figure V.44: Mechanisms of elastic deformation up to the yield stress for α phase, tensile axis is vertical

Finally, according to the state of the amorphous state (below or above T_g), the mechanisms are not the same. This could be explained by the morphology of the lamellae. Indeed, the shape factor has to be taken into account for α phase. As reported in literature [7], for PA6, the favor growth direction is the one for H-bonds, meaning \vec{g}_1 for α phase. In the case of β phase, there is no impact of shape factor because there is no favored growth directions as H-bonds are randomly distributed in planes perpendicular to \vec{n} . This means that lamellae are ribbon-like for α phase and that lamellae rotations are not equivalent as shown in Figure V.45. Indeed, because the lamellae are like stick, they can easily rotate along y and z axis but it is nearly impossible for them to rotate along x axis. Thus, according to the amorphous state, it is easier:

- for the lamellae to tilt to the poles above the glass transition
- for the tie chains to stretch and lead the lamellae to tilt to the equator below T_g

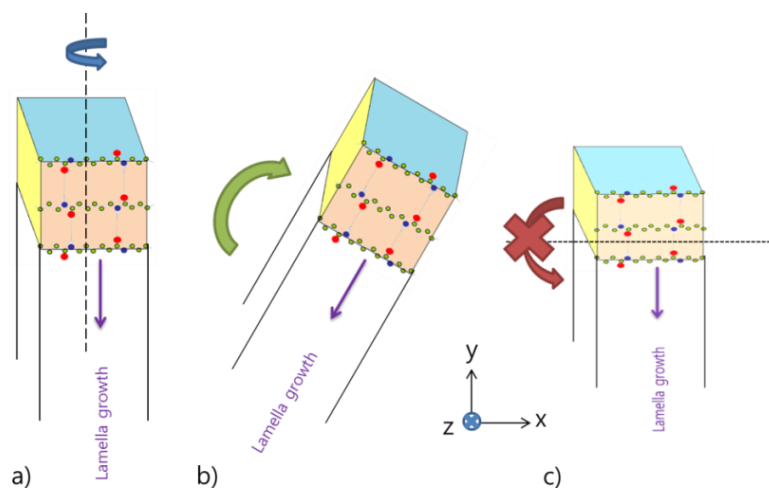


Figure V.45: Lamella rotation along a) y axis corresponding to tensile axis, b) z axis and c) x axis

III.2.3. Case of $\alpha+\gamma$ phases

This mixture concerns the A200 samples. As mentioned above, SAXS data give the following observations:

- Below T_g , the normals prefer to orient at $\psi=0^\circ$
- Above T_g , the normals show no clear preferential orientation

Concerning WAXS data, the following observations were made:

- Below T_g , the (020) and (200) rings of γ and α phases seem unaffected. The scattering of (002)+(20 $\bar{2}$) planes reinforce horizontal to TD.
- Above T_g , the scattering of (200) and (020) planes of α and γ phases are really close, however vertical reinforcements of (200) planes are visible. Concerning the (020) ring, it seems unaffected. (002)+(20 $\bar{2}$) planes orient at $\psi=90^\circ$.

Shortly, this allows us concluding that below the glass transition A200 samples follow the chain network model whereas above T_g , the material tends to follow the rigid lamella model. This case will be further detailed in the next chapter concerning the plastic deformation.

III.2.4. Additional information

In SAXS, an increase of intensity during stretching has been observed. This is depicted in Figure V.46a. As it concerns the orientational distribution of the normals of the lamellae fitted by an affine model (see §1.4), the sample I213 above the glass transition is not represented as this sample does not follow this model. In any case, we do not have a clear significance of the increase of intensity in SAXS. However, one of the possible hypotheses would be an increased coherence of lamellae stackings under stretching, as illustrated in Figure V.46b and c. This model could apply to all samples without interfering with the previously mentioned CN and RL models. It concerns lamellae stacks whose stacking axis is parallel to TD and which therefore are stretched (Figure V.46b). During deformation, tie chains would tend to align lamellae or so increase the stacking coherence (Figure V.46c).

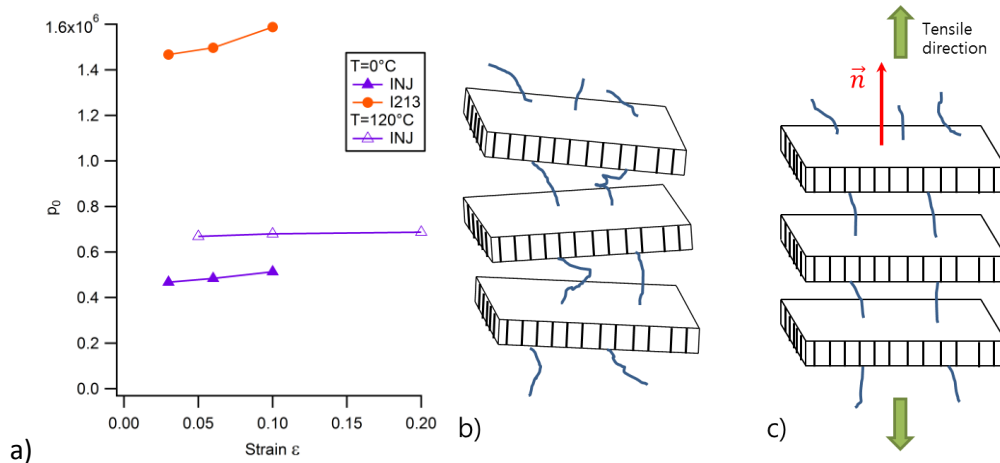


Figure V.46: a) Coefficients p_0 of the Legendre in the case of the orientational distribution of lamella (see §1.4); Schematic of the rope-ladder model in a) the initial state and b) the deformed state

This “rope-ladder” model is also supported by the literature: the presence of tilted and untilted lamellae has already been reported by Murthy [8] [9] in the case of PA6 fibers. He also adds that the lamellae either have no tilt or have a tilt angle that is determined by the conditions during crystallization. However, at the moment, additional SAXS data are still necessary to conclude on this increase of intensity.

III.3. Conclusion

Firstly, the study on the local strain by SAXS has shown that polar lamellae contract and equatorial lamellae stretch. Furthermore, the ratio between the local and the macroscopic strains is always measured smaller than one. In addition, by analyzing the azimuthal distribution of the local strain, it was also found that the deformation of the lamellae system was relatively homogeneous through the material for all samples. However, since the local variation of the period of the lamella stacking is smaller than expected, this must be compensated by shear deformation in inclined lamella stacks (see Figure V.9). As a matter of fact, interlamellar shear is easier than either compression or stretching normal to lamellae surface. Indeed, compression or stretching involves an effective modulus which may be significantly higher than the Young's modulus of the amorphous phase.

Concerning the crystal strain, the WAXS study has revealed that α crystal is more rigid than β crystal. The degree of homogeneity of the local strain/stress state was deduced from the azimuthal distribution of the crystal strain. It was found that for INJ sample with β phase, the strain or stress is relatively homogeneous, whereas for I213 sample with α phase, the strain/stress state is far from homogeneous.

If we now focus on the deformation mechanisms, thanks to the orientational distribution of both lamellae and crystalline planes, we found that they are different depending on the crystalline phase and the temperature. Two models have been developed: the Crystalline Network (CN) and the Rigid Lamella (RL) models. In the CN model, the orientation mechanisms are ruled by the amorphous chains which transmit the stress between adjacent lamellae. In the RL model, the lamellae govern their own mechanisms of orientation, possibly due to their high aspect ratio.

In the case of INJ sample (β phase), the CN model applies whatever the temperature. However in the case of I213 sample (α phase), the temperature influences the mechanisms: below the glass transition, the CN model applies whereas above T_g , it is the RL model. In the case of $\alpha+\gamma$ mixture, below T_g , the deformation mechanisms still follow the CN model, however above T_g , the deformation mechanisms are more complex and tend to follow the RL model.

In other words, the deformation mechanisms differ depending on temperature. Below T_g , it is always the CN model which applies whereas above T_g , depending on the crystalline phase it is not the same deformation mechanism which occur. This change of mechanisms was indirectly observed through the difference of behaviors observed in Figure V.11 and Figure V.12 (§I.3).

References

- [1] N. Hussein, "Enhancement of the mechanical performance of semi-crystalline polyamides by tailoring the intermolecular interaction in the amorphous phase," Ecole doctorale Matériaux, INSA, Lyon, 2013.
- [2] O. Reynolds, "On the theory of lubrication and its application to Mr. Beauchamp tower's experiments, including an experimental determination of the viscosity of olive oil," *The Philosophical Transactions of the Royal Society of London*, vol. 177, pp. 157-234, 1886.
- [3] A. Gent, "Compression of rubber blocks," *Rubber Chemistry and Technology*, vol. 67, pp. 549-558, 1994.
- [4] K. L. Johnson, *Contact Mechanics*, Cambridge University Press, 1985.
- [5] L. Landau and Lifchitz, *Théorie de l'Elasticité*, Moscou: Editions Mir, 1967.
- [6] M. Ward, "The measurement of molecular orientation in polymers by spectroscopic techniques," *Journal of Polymer Science: Polymer Symposium*, vol. 58, pp. 1-21, 1977.
- [7] R. Huisman and H. Heuvel, "Quantitative information from X-Ray diffraction of Nylon-6 yarns. II. Physical aspects of some quantitative parameters," *Journal of Polymer Science: Polymer Physics Edition*, vol. 14, pp. 941-954, 1976.
- [8] N. Murthy and D. Grubb, "Deformation of lamellar structures: simultaneous Small and Wide-Angle X-ray Scattering studies of polyamide-6," *Journal of Polymer Science: Part B: Polymer Physics*, vol. 40, pp. 691-705, 2002.
- [9] N. S. Murthy, "Hydrogen bonding, mobility and structural transitions in aliphatic polyamides," *Journal of Polymer Science: Polymer Physics*, vol. 44, pp. 1763-1782, 2006.

Chapter VI: Microscopic study – Plastic strain domain

Introduction.....	154
I. Deformation mechanisms at the scale of the crystalline lattice, investigated by WAXS.....	155
I.1. Injected (INJ) sample: predominant β phase	155
I.1.1. Evolution in the plastic domain above T_g	155
I.1.2. Evolution in the plastic domain below T_g	160
I.1.3. Discussion: temperature and deformation mechanisms of the sample with β phase in the plastic strain domain.....	161
I.1.3.1. Orientation of lattice planes in the β phase and effect of the temperature	162
I.1.3.2. Fibrillation and $\beta \rightarrow \alpha$ transformation	163
I.1.3.3. Proposed mechanism	165
I.2. Annealed (A215) and isotherm-treated (I213) samples: pure α phase	166
I.2.1. Evolution in the plastic strain domain above T_g	167
I.2.2. Evolution in the plastic strain domain below T_g	170
I.2.3. Discussion: temperatures and deformation mechanisms of the plastic strain domain for α phase	171
I.2.3.1. Effect of temperature.....	171
I.2.3.2. Proposed mechanisms	173
I.3. Discussion on A200 sample: mixture of α and γ phases	175
I.4. Conclusion on ductility	176
II. Deformation mechanisms at the scale of lamellae, investigated by SAXS	177
II.1. Fibrillar transformation	177
II.2. Cavitation	178
III. Conclusion	180
References.....	181

Introduction

In the previous chapter, the impact of uniaxial stretching on the crystalline morphology was studied in the linear regime of deformation, at both the scale of crystalline lamellae and the scale of the crystalline unit cell, by combining small and wide angle X scattering (SAXS and WAXS). It was seen that the chain length does not impact the mechanical behavior significantly, at least in the linear regime. Thus, the study in the linear regime was performed on samples with $M_n = 31\,000$ g/mol (31K samples) only. In this chapter, we extend the same approach with the same combination of SAXS and WAXS to higher deformation, in the plastic strain domain up to final failure of the materials. We still focus on the same 31K samples as before. The list of samples is reminded in Table VI.1. The various thermal treatments which have been applied in order to give different predominant crystalline phases have been described in chapter III.

Table VI.1: The 31K samples with various thermal treatments chosen for microscopic in-situ studies.

Sample name	Thermal treatment	Predominant crystalline phase	Color and symbol
INJ	Injected	$\beta+\gamma$	▲
A200	Annealed at 200°C	$\alpha+\gamma$	■
A215	Annealed at 215°C	α	●
I213	Isotherm at 213°C	α	●

The same convention for the orientation of lamellae as adopted in chapter V is kept. In all figures and schematics, the tensile direction (TD) is vertical. The azimuthal angle ψ in 2D WAXS and SAXS patterns is referred to the tensile direction (TD): vertical scattering corresponds to $\psi = 0^\circ$, horizontal scattering to $\psi = 90^\circ$.

To describe the deformation of crystalline structure under uniaxial stretching in the elastic strain domain, two different models were proposed (see chapter V). They have been denoted Chain Network (CN) model and Rigid Lamella (RL) model. They are schematized in Figure VI.1.

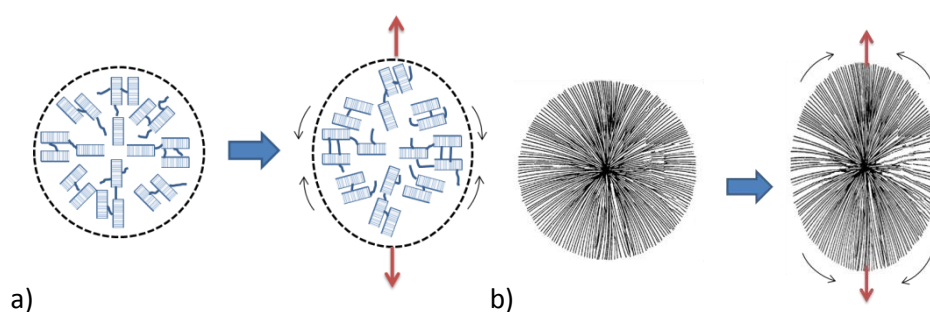


Figure VI.1 : a) Chain network model; b) Rigid lamella model

From the previous chapter, it was concluded that:

- INJ samples follow the CN model at both tensile test temperatures
- I213 samples (as A215 samples) follow the CN model below the glass transition but follow the RL model above the glass transition.
- A200 samples follow the CN model below the glass transition but above the glass transition, it is an intermediate state between chain network and rigid lamella models.

Let us now focus on the plastic strain domain below and above the glass transition. As mentioned in chapter I, the plastic deformation is a complex process during which a transition from a lamellar

(spherulitic) morphology into a fibrillar structure may eventually happen. The first part is focused on the impact of deformation on the orientation of crystalline lattice planes in the various samples, investigated by WAXS. The second part II is focused on the impact of deformation at larger scales, investigated by SAXS: fibrillation and cavitation phenomena are discussed.

I. Deformation mechanisms at the scale of the crystalline lattice, investigated by WAXS

The plastic strain domain has been studied above and below the glass transition ($T = -10^\circ\text{C}$ and 120°C). In situ tensile tests have been performed at a strain rate of 3.10^{-3} s^{-1} . As a reminder, the strain-stress curves measured in-situ are shown in Figure VI.2. Above glass transition ($T = 120^\circ\text{C}$), the yield strain corresponds to about $\epsilon \cong 0.5$ for all samples. Below T_g , the yield strain corresponds to $\epsilon \cong 0.15$ for the INJ sample and to $\epsilon \cong 0.25$ for the other samples. The cases of samples with predominant β (sample INJ) and α phase (samples A200, A215 and I213) will be discussed separately.

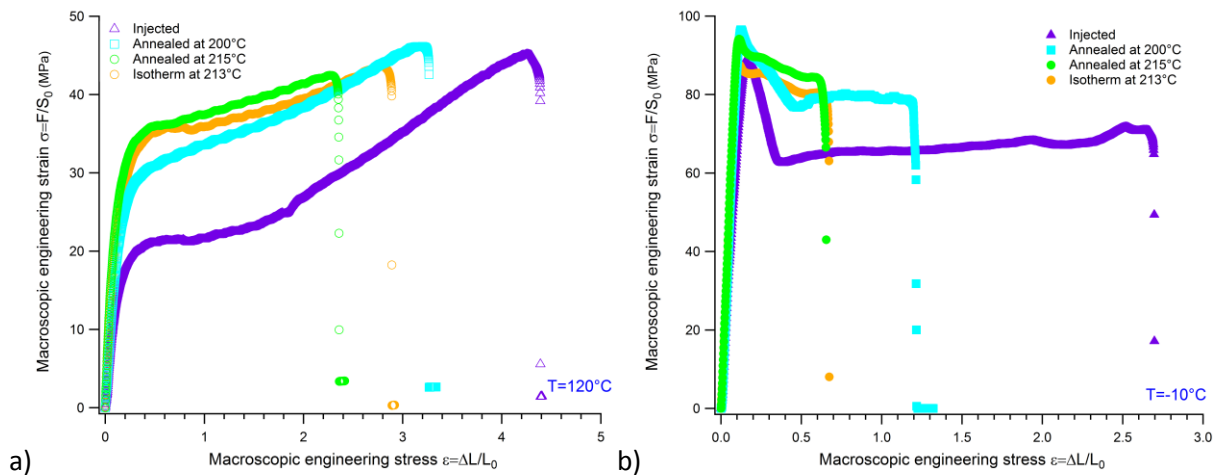


Figure VI.2: In situ strain-stress curves in tensile stretching at strain rate = 3.10^{-3} s^{-1} for 31K samples obtained after various thermal treatments, at two different temperatures: a) $T = 120^\circ\text{C}$ (above T_g) and b) $T = -10^\circ\text{C}$ (below T_g). All samples have been stretched up to failure.

The issues addressed in chapter IV were mainly focused on the difference between INJ sample and the other ones. Indeed, it was observed that the INJ sample has a higher stretching ratio before failure than the other samples, both at high and low temperature (see also Figure VI.2). Above T_g , the yield stress in INJ is also twice lower than in the other samples, but below T_g , it is nearly the same, questioning the fact that considering the crystallinity ratio alone could not fully explain the difference and suggesting that other parameters should be taken into account (see chapter IV). As mentioned above, in chapter V, two models describing the deformation modes under stretching were discussed for the elastic strain domain. We now extend the study to the plastic strain domain.

I.1. Injected (INJ) sample: predominant β phase

I.1.1. Evolution in the plastic domain above T_g

Stress-strain curves of the INJ sample at two different strain rates at $T = 120^\circ\text{C}$ (above T_g) are shown in Figure VI.3, together with representative WAXS patterns acquired in-situ. Figure VI.3 illustrates the

general behavior of the INJ sample as a function of the strain. It shows and confirms that, at this temperature, the strain rate does not influence the mechanical behavior of the material.

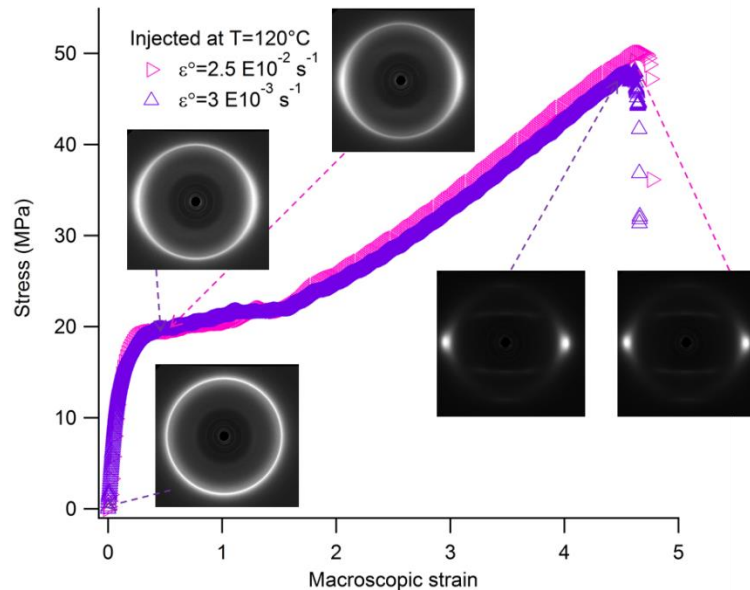


Figure VI.3 : In-situ tensile stress-strain curves above T_g for INJ sample at various tensile rates, $\dot{\epsilon}=2.5 \cdot 10^{-2} \text{ s}^{-1}$ and $\dot{\epsilon}=3 \cdot 10^{-3} \text{ s}^{-1}$. Corresponding WAXS patterns are shown.

The evolution of 2D WAXS patterns along in-situ tensile tests is shown in Figure VI.4, for the injected sample (INJ), which contains predominantly β phase. The elastic strain domain runs from the initial, undeformed state (step 1 in Figure VI.4) to the yield state (step 2 in Figure VI.4): it was studied previously in chapter V. The plastic strain domain studied here runs from step 2 to step 3 in Figure VI.4. Step 4 corresponds to a sample which has been stretched up to $\epsilon = 450\%$ and then unloaded.

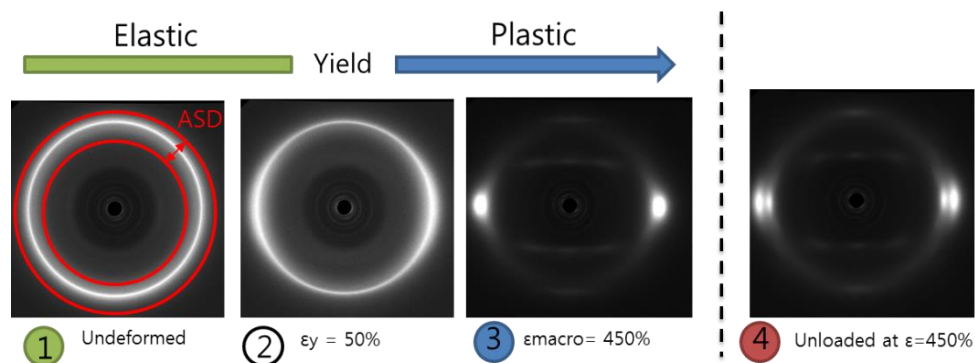


Figure VI.4: 2D WAXS patterns obtained at different strain values in the of INJ sample above T_g ($T=120^\circ\text{C}$). TD is vertical. In step 4, the sample has been unloaded after stretching up to $\epsilon = 450\%$. The various steps 1 to 4 are analyzed in the text.

Let us first describe the observed patterns of Figure VI.4. In the initial, isotropic state (step 1), an apparently isotropic, relatively broad ring is observed with a maximum of intensity at $2\theta \approx 21^\circ$. This ring corresponds to the diffraction by (002), (200) and $(\bar{2}02)$ planes, which are all equivalent in the pseudo-hexagonal β phase [1]. These planes contain the chain axis. At the yield point (step 2), the diffraction ring of the β phase has become anisotropic, with more intensity in the horizontal plane. This modulation of the azimuthal intensity is related to the distribution of orientations of lattice planes. It indicates that all diffracting families of planes tend to orient with their normals in the horizontal plane, that is, perpendicular to the stretching direction. Since chains axis are along the intersection of all these planes, it follows that chains tend to orient along the tensile direction, as

already mentioned in chapter V. The pattern at step 3 exhibits a major change with respect to step 2. It corresponds to a highly oriented morphology, with Bragg spots which are known to be characteristic of fibrillar morphology. This indicates that fibrillation has occurred within the plastic regime, between step 2 and 3. In addition, step 4 indicates that the metastable β phase has transformed into α phase. This is evidenced by the fact that the broad ring at about $2\theta \approx 21^\circ$, in which the intensity is now concentrated mostly in the horizontal plane, splits into two spots with different scattering angles ($2\theta \approx 20^\circ$ and $2\theta \approx 24^\circ$), which indicates the presence of α phase (step 4 in Figure VI.4). The fibrillation and the $\beta \rightarrow \alpha$ transformation, as well as the indexing of the spots at $2\theta \approx 10.2^\circ$ and $2\theta \approx 13^\circ$ (indicating the presence of a highly ordered phase, or in any case more ordered than the initial β phase), will be further analyzed in §I.1.3.2.

2D intensity patterns shown in Figure VI.4 are now analyzed more quantitatively. To illustrate the anisotropy which appears in the patterns, diffraction curves (intensity as a function of scattering angle 2θ) measured in horizontal and vertical directions (integrated over a azimuthal sector of width 5°) are shown in Figure VI.5b. The initial state is isotropic (identical pattern in all directions). At 50% strain, there is more intensity in the horizontal direction. Also, the maximum of the peak is slightly shifted towards smaller (resp. larger) 2θ values in the vertical (resp. horizontal) direction. This indicates that the distance between lattice planes slightly increases when planes are perpendicular to the tensile direction, and decreases when planes are parallel to the tensile direction. This small distortion of the lattice unit cell has been analyzed in the linear regime in Chapter V to estimate the local strain in crystalline lamellae. At 450% strain, the intensity is almost completely concentrated in the horizontal direction.

In order to analyze quantitatively the intensity patterns shown in Figure VI.4 (reproduced again in Figure VI.5a for clarity), an Azimuthal Scattering Domain (ASD as schematized in pattern 1 in Figure VI.4) covering entirely the scattering ring $2\theta \approx 21^\circ$ of the β phase has been defined. For each azimuthal angle ψ , the scattering intensity is integrated in the range of scattering vector Q values in between the inner and outer rings drawn in red in Figure VI.4 (pattern 1). The obtained integrated intensity is then studied as a function of the azimuth angle ψ , to see in which direction reinforcements or spots of intensity are encountered. As in chapter V, the scattering intensities are corrected by subtracting the (small) modulation observed in the initial state and adding the average intensity of the sample in the initial state (see Eq. V.25).

Intensities integrated in the ASD for different macroscopic strains are shown in Figure VI.5c. In the elastic strain domain (i.e. from the undeformed state (step 1) up to $\epsilon = 50\%$ (step 2)), an intensity reinforcement centered on the horizontal plane ($\psi = 90^\circ$) appears. At the beginning (small strain values), the modulation of intensity is small and broad: indeed, for $\epsilon = 20\%$, the width at half-height of the modulation covers an azimuthal range of $\approx 100^\circ$. Then, at the yield strain ($\epsilon = 50\%$), the width has decreased down to an azimuthal range of $\approx 71^\circ$. This indicates an increasing anisotropy of the orientation distribution of the normals to the planes. As the strain increases further, the amplitude of the intensity modulation continues to grow and the width continues to decrease. At $\epsilon = 450\%$, the intensity shows two sharp maxima in the horizontal plane ($\psi = 90^\circ$), with a width at half-height of ca. 16° (see Figure VI.6a, $T = 120^\circ\text{C}$).

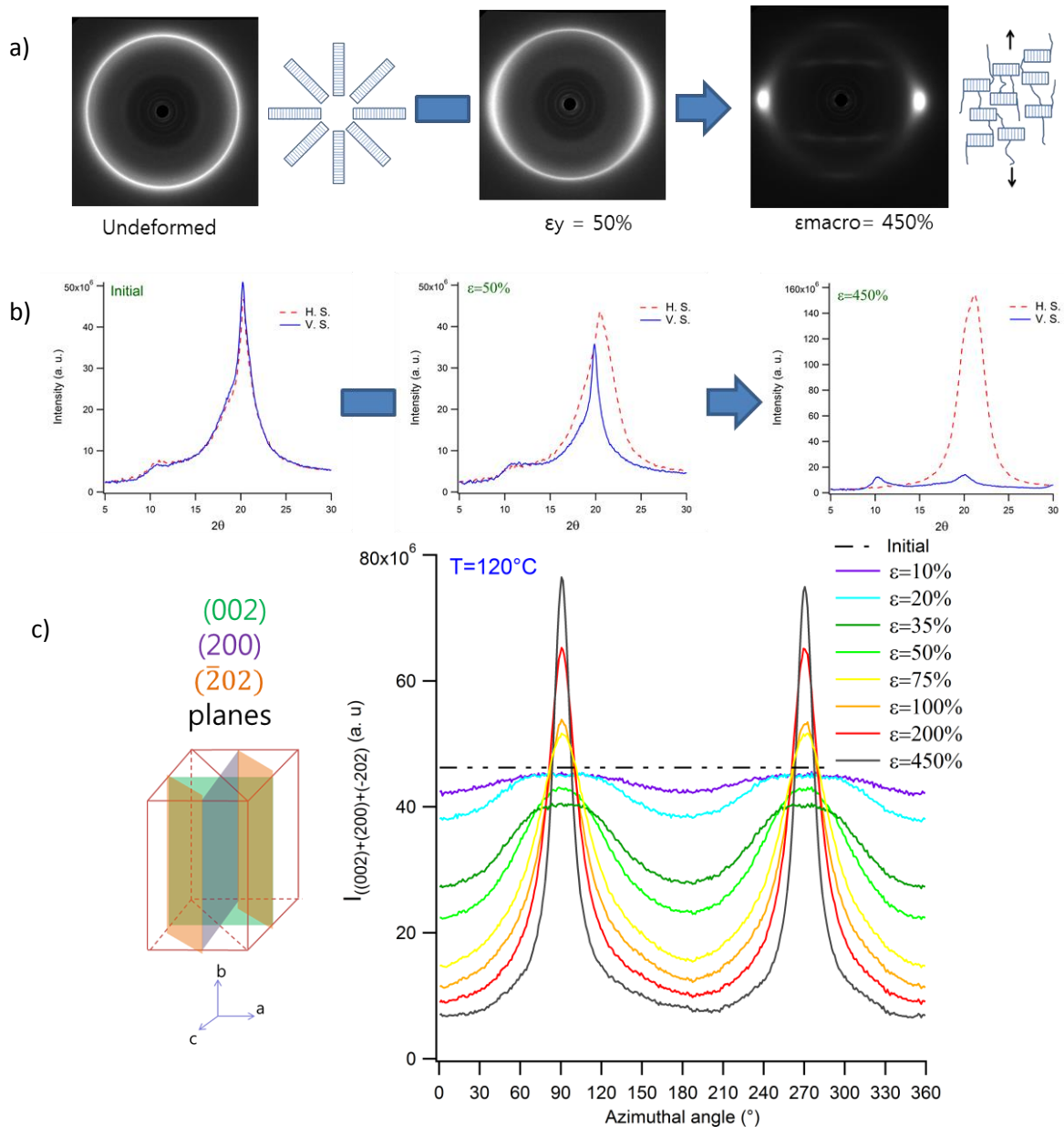
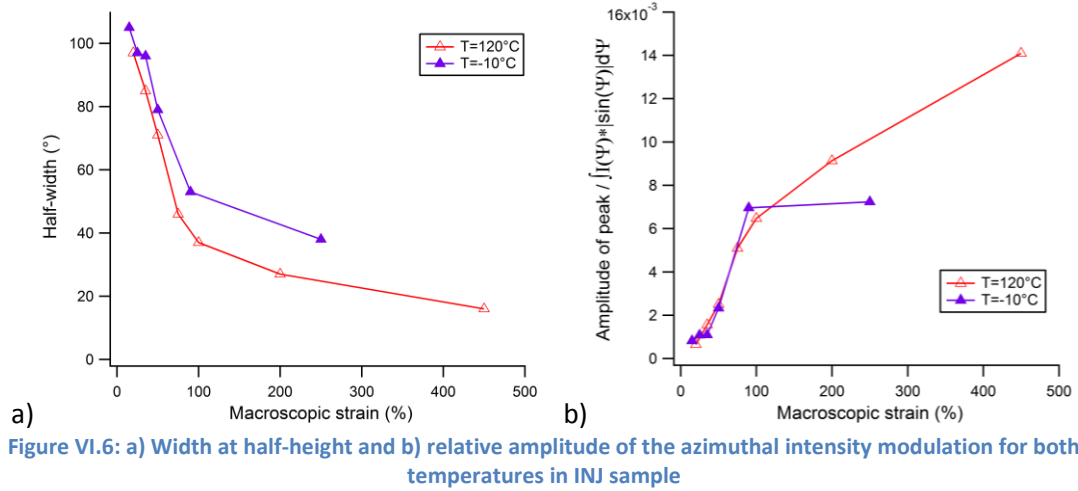


Figure VI.5: a) 2D intensity patterns for INJ sample at various strain values at $T = 120^\circ\text{C}$ (above T_g) (same as in Figure VI.4), shown again for clarity; b): intensity as a function of scattering angle in horizontal (H. S.: horizontal scattering, normal to TD) and vertical directions (V. S.: vertical scattering, parallel to TD); c): Azimuthal intensity profiles. The tensile direction is vertical (azimuthal angle $\psi = 0^\circ$). Preferred plane orientation, corresponding to intensity reinforcements, with normals in the horizontal plane and chain axis along the tensile direction, is schematized

The width at half-height and the relative amplitude of the modulation are shown as a function of the strain in Figure VI.6a and b (see curves in red corresponding to $T = 120^\circ\text{C}$). The variations of both quantities do not show discontinuities. They are continuous but not linear as a function of the strain. There seems to be an inflexion of the rate of change for both the width and amplitude of the intensity reinforcements at $\psi = 90^\circ$ around 100% strain (or more precisely, between 100 and 200% strain). This inflexion is concomitant with the appearance of diffraction spots at $2\theta \approx 13^\circ$ and $\psi = 45^\circ$ and at $2\theta \approx 10.2^\circ$ and $\psi = 45^\circ$ at ca. $\epsilon = 200\%$ (these spots are visible in pattern 3 and 4 of Figure VI.4). Thus, the inflexion points could also be related to the $\beta \rightarrow \alpha$ phase transformation. As already mentioned above, this transformation will be further discussed in §1.1.3.2.



As regards the amplitude of the azimuthal modulation, related to the degree of anisotropy of the crystalline morphology, the quantity which has physical significance is the *relative amplitude*, defined as the amplitude (measured e.g. on the graph in Figure VI.5c as the difference between maxima and minima), divided by the average (integrated) intensity. Taking into account uniaxiality of the overall sample, the average (integrated) intensity is defined as:

$$I_{av} = \frac{\int_0^\pi I(\psi) \sin \psi d\psi}{\int_0^\pi \sin \psi d\psi} \quad (\text{E. VI.1})$$

The total integrated intensity is plotted as a function of the macroscopic strain in Figure VI.7. For each value of the macroscopic strain ϵ , the measured intensity has been divided by the thickness $e(\epsilon) = e_0(1 + \epsilon)^{-1/2}$, assuming incompressibility of the sample. For a collection of N scattering objects (coherent lamellar stacks) each of volume V, with a volume fraction $\Phi = NV$, immersed within an amorphous background, not correlated with each other, the total intensity (normalized by the sample thickness and transmission, by the intensity of the incident beam and by the Thompson factor) may be expressed as :

$$I(2\theta) = (\Delta\rho)^2 V^2 N F(2\theta) = (\Delta\rho)^2 V \Phi F(2\theta) \quad (\text{E. VI.2})$$

where $(\Delta\rho)^2$ is the electron density contrasts between objects (crystallites) and surrounding medium (amorphous phase), and $F(2\theta)$ is the normalized structure factor of the diffracting objects.

For a constant number of objects, unaffected in their size and shape during tensile tests, the normalized integrated intensity should stay constant. The decrease in intensity as the strain increases may be related either to a decrease of the volume fraction Φ (decrease of crystallinity index under the effect of the tensile strain), or to a decrease of the volume V of the objects (crystallites). It has been reported in the literature [2] [3] that in polyamide 6 spun fibers with an initial isotropic state, the crystallinity increases with the strain. Thus, the observed decrease of scattered intensity, as depicted in Figure VI.7, may be more probably related to a decrease of the volume or size of coherently scattering crystallites, that is, to a fragmentation of crystallite.

Another qualitative indication of crystallite fragmentation is observed in WAXS patterns, see e.g the pattern obtained at 50% strain during tensile test at 120°C shown in Figure VI.5a. There is significant broadening of the diffraction ring, as compared to the ring observed in the initial state, particularly in

the direction of horizontal scattering. According to Scherrer's formula, this may be related to fragmentation of crystallite in the direction perpendicular to the tensile direction, as roughly schematized in Figure VI.14.

Finally, at larger strain values (roughly beyond 100% strain), the slight increase of scattered intensity, as shown in Figure VI.7, may be related to an increase of crystallinity due to chain elongation at high strain, or to the development of α phase (see §1.1.3.2). The global mechanisms will be discussed in §1.1.3.3.

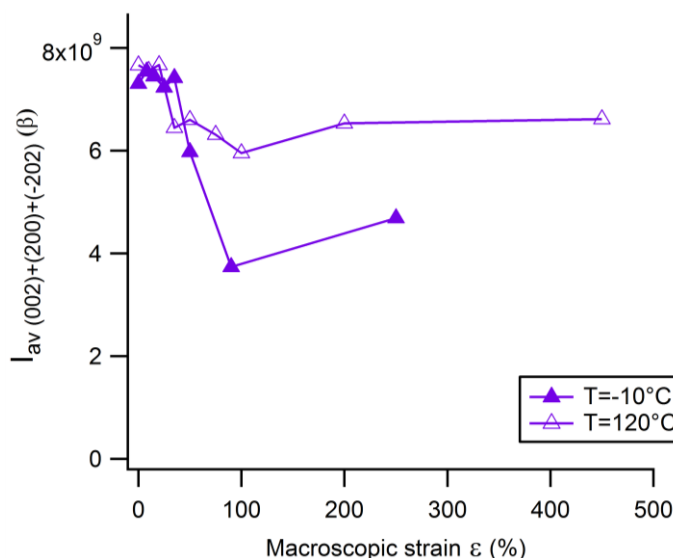


Figure VI.7: Evolution of the integrated intensity as a function of macroscopic strain in INJ sample for both tensile test temperatures

1.1.2. Evolution in the plastic domain below T_g

The same analysis has been done for in-situ tensile stretching experiments performed below T_g ($T = -10^\circ\text{C}$). Azimuthal intensity profiles for different macroscopic strains are shown in Figure VI.8c. Corresponding 2D patterns in the initial, undeformed state, at the yield strain ($\epsilon = 15\%$), and at maximum strain (at failure) are also shown in Figure VI.8a. The diffraction curves ($I(2\theta)$) are depicted in Figure VI.8b: they show the same trend as in Figure VI.5b. The most striking difference concerns the final stage where only two spots located at $2\theta \approx 10.2^\circ$ are visible. They probably belong to α phase and thus their appearance could correspond to the $\beta \rightarrow \alpha$ transformation. Thus, overall, the behavior seems to be qualitatively similar to that at 120°C (above T_g), with horizontal reinforcements of the intensity of increasing amplitude as the strain increases. As before, these reinforcements indicate that all equivalent $(002)+(200)+(\bar{2}02)$ lattice planes tend to orient with their normals in the horizontal plane, that is, chains tend to orient along the tensile direction.

It is worth noticing that at $\epsilon = 35\%$ in Figure VI.8b, horizontal reinforcements in fact consist in a plateau made of two peaks located symmetrically on each side of the horizontal plane, meaning two preferential orientations of the planes separated by ca. 40° . Thus, these orientations are located at azimuthal angles $\approx \pm 20^\circ$ with respect to the horizontal plane ($\psi = 90^\circ$). As the strain increases further, the two maxima merge and the width at half-height decreases as shown in Figure VI.6a. The relative amplitude of the intensity modulation increases as the strain increases. It is shown as a function of the strain in Figure VI.6b. There seems to be a quite abrupt variation of both width and amplitude of the orientation distribution between 35 and 150% strain. It is worth noticing that the point of inflexion is quite sharp in Figure VI.6b.

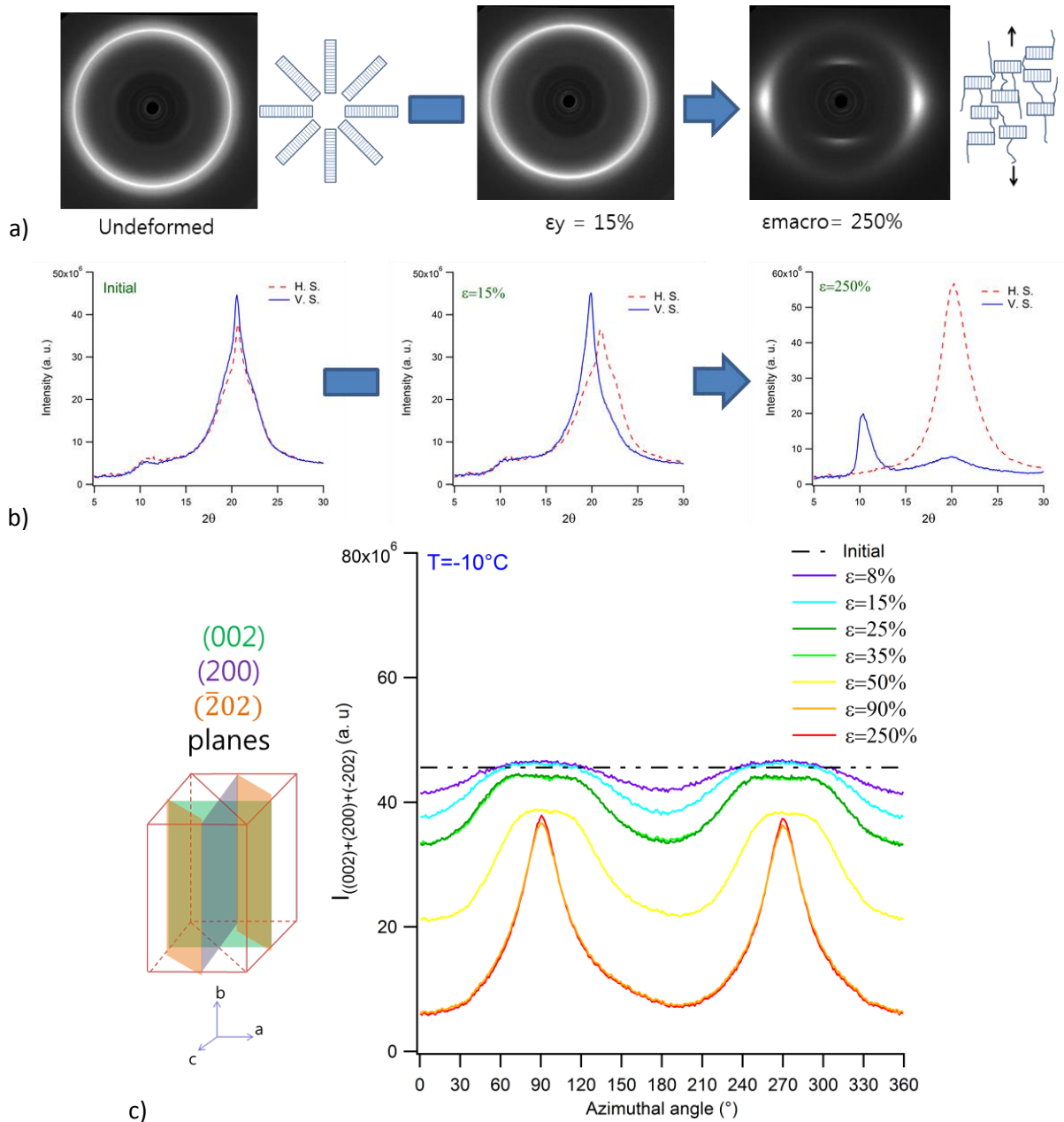


Figure VI.8: a) 2D intensity patterns for INJ sample at various strain values at $T = -10^\circ\text{C}$ (below T_g); b) intensity as a function of scattering angle in horizontal (H. S.: horizontal scattering, normal to TD) and vertical directions (V. S.: vertical scattering, parallel to TD); c) Azimuthal intensity profiles. The tensile direction is vertical (azimuthal angle $\psi = 0^\circ$). Preferred plane orientation, corresponding to intensity reinforcements, with normals in the horizontal plane and chain axis along the tensile direction, is schematized.

I.1.3. Discussion: temperature and deformation mechanisms of the sample with β phase in the plastic strain domain

The results presented above show that two distinct processes occur during uniaxial stretching for the INJ samples, investigated below and above the glass transition.

1.1.3.1. Orientation of lattice planes in the β phase and effect of the temperature

In a first step, the anisotropy which develops in the WAXS patterns relate to the distribution of orientation of (002), (200) and $(\bar{2}02)$ lattice planes, which are all equivalent because the β phase is pseudo-hexagonal. At both temperatures, the behavior is qualitatively the same. These planes tend to orient with their normals in the horizontal plane, that is, chains tend to orient along the tensile direction.

In order to better compare the influence of the temperature, the intensities as a function of the azimuthal angle ψ are plotted again in Figure VI.9, for the two different temperatures studied. The first difference concerns the intensity: for a same strain, the intensity of the horizontal reinforcement is higher above T_g than below.

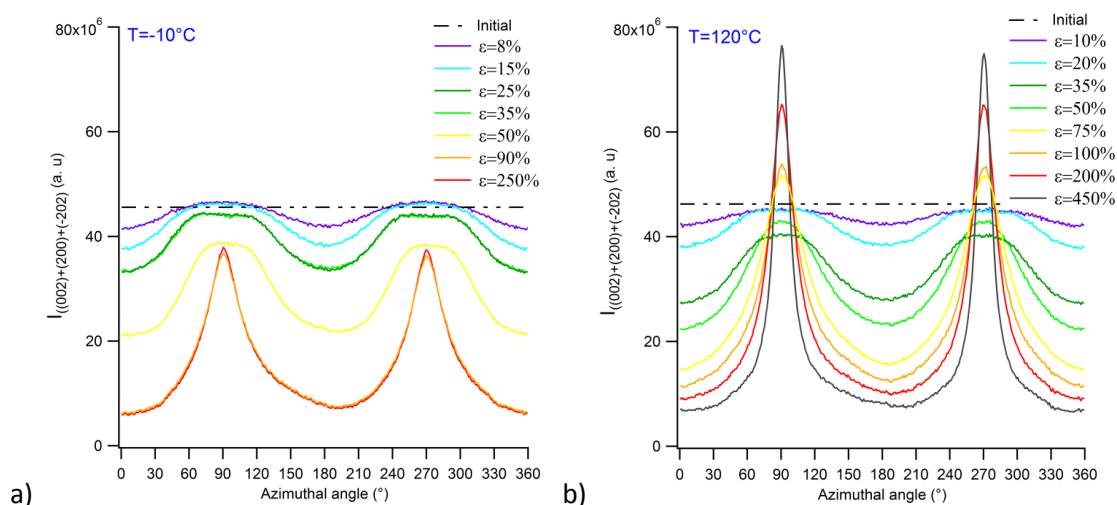


Figure VI.9: Influence of the strain on the scattering intensity of (002)+(200)+(202) planes of β phases, at a) -10°C and b) 120°C . Same curves as in Figure VI.5c and Figure VI.8c, shown again to emphasize the effect of the temperature of the tensile test.

If we now focus on the width at half-height of the main reinforced peak (see Figure VI.6a), the point of inflexion is sharper below T_g but it seems that this inflexion occurs nearly at the same strain whatever the temperature. The same observations apply for the amplitude of the peak (Figure VI.6b).

However, when looking in more details, the temperature has an influence on the orientation process. Indeed, it was observed below T_g that for $\epsilon = 35\%$ the horizontal reinforcements (around $\psi = 90^\circ$) consist of two plateau whereas above T_g only one broad horizontal reinforcement was found (see Figure VI.9). The two plateaus could be explained by a phenomenon of “chevron”, as depicted in Figure VI.10.

The chevron-like structure is a kind of texture that occurs at the transition between elastic and plastic strain domains in soft-hard alternating lamellar systems when lamella stacks are submitted to a transverse compressive stress, i.e. stress operating parallel to the lamella surface [4] [5] [6] [7] [8]. This phenomenon results from the elastic buckling of the lamellae. Its occurrence has been indirectly observed via 4-spot patterns in SAXS of semi-crystalline polymers such as polyethylene and lamellar block copolymers of the kind of thermoplastic elastomers [6] [7]. In single-crystal-like structures with lamella oriented in a single direction over the whole material, the process occurs at a macroscopic scale [6]. In the case of grain-like lamellar structures, the process occurs only in those lamella stacks being under transverse compressive stress [9]. The occurrence of 4-spot pattern in SAXS is an

indication of the periodicity of the phenomenon that has been confirmed by direct TEM observations [9] [8]. A theoretical approach of this surprising periodicity has been performed via Molecular Simulations [5]. In the present instance of semi-crystalline polymer, the occurrence of this phenomenon is likely to result in quadrant crystalline reflections. The overlapping of the broad reflections in Figure VI.9 is relevant to a rather poor periodicity of the phenomenon. This WAXS feature gives additional information that the onset of plastic deformation should involve buckling and yielding of the crystalline lamellae in the situation of transverse compressive stress (see Figure VI.10).

However in order to check out this hypothesis, SAXS patterns are needed: if chevron-like pattern with two preferred orientations of the lamellae are observed then it would confirm the hypothesis. Nonetheless, at the moment, we do not have these data as only the elastic strain domain (up to $\epsilon \approx 17\%$) has been investigated by SAXS.

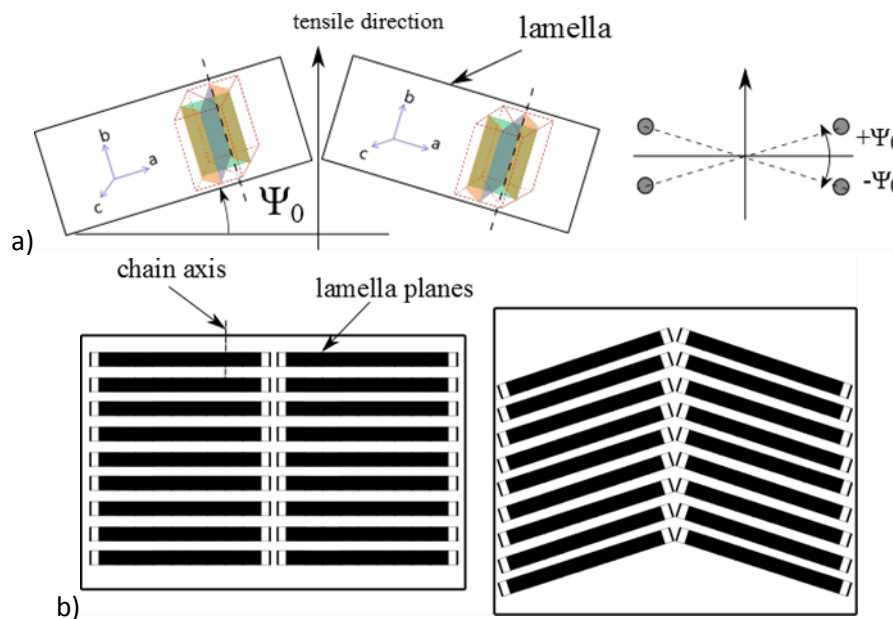


Figure VI.10: a) Schematics of chevron-like morphology, with corresponding scattering peaks (or intensity reinforcements) from oriented lattice planes. Lamellae are inclined at an angle ψ_0 . b) Schematics of the buckling instability of lamellae under transverse compression, which results in a chevron-like texture. Tensile direction is vertical.

1.1.3.2. Fibrillation and $\beta \rightarrow \alpha$ transformation

It is reported in the literature that the β phase is metastable and may transform into α phase upon heating or stretching [10]. In chapter III, we have indeed observed the occurrence of the transformation upon annealing. Concerning stretching, as noticed above, it is confirmed that the transformation occurs as well, both at low and high temperature. It is concomitant with fibrillar transformation.

Indeed, in a second step, at higher deformations, the WAXS patterns change qualitatively, indicating a transformation towards a fibrillar α phase. Indeed, two vertical inner spots at scattering angle $2\theta \approx 10^\circ$ appear at both temperatures, below and above T_g . In addition, four spots at $2\theta \approx 13^\circ$ at an azimuth $\psi = 45^\circ$ are also observed above the glass transition. This shows that the fibrillation is more pronounced above T_g , or more precisely, that fibrillation leads to a more perfect α phase above T_g . The indexation of these α spots is explained just below.

Indeed, thanks to Figure VI.11 and Eq. II.21 (see chapter II, §II.4), the indexation corresponds to α phases and the reflections (020) for $2\theta = 10.2^\circ$ and (120) for $2\theta \approx 13^\circ$. The same indexation was also found in literature [11] for (120) planes. These spots constitute evidence that β transforms or starts to transform into α phase during stretching. In addition, in §I.1.1 and Figure VI.6, points of inflexion in the evolution of the azimuthal modulation of the intensity between $\varepsilon = 100\%$ and $\varepsilon = 200\%$ were discussed. These points could be also related to the onset of phase transformation. Indeed, the phase transformation should be mainly controlled by the drawing ratio, the strain rate having no significant influence as depicted in Figure VI.3. Concerning the influence of temperature, it was observed that the points of inflexion were found at the same strain whatever the temperature (see Figure VI.6). However, below T_g , in the final step ($\varepsilon = 250\%$), only the two spots at $2\theta \approx 10^\circ$ were observed and they were broad. This could be explained by the fact that the phase transformation is indeed progressive and need a higher drawing ratio, as well as a certain accommodation time or some degree of molecular relaxation in order to be achieved.

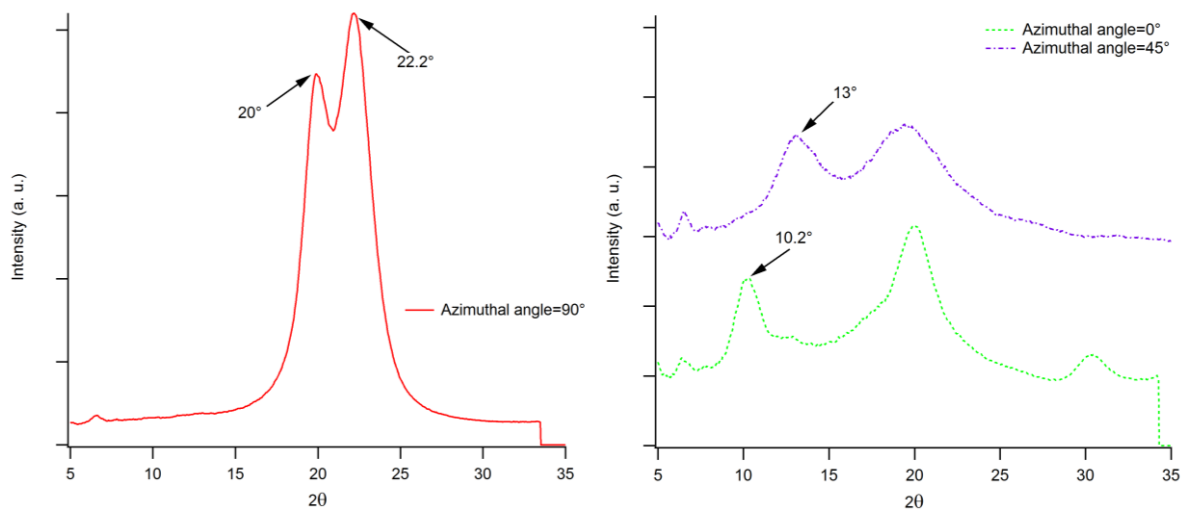


Figure VI.11: Indexation of 2θ angles corresponding to the various spots

The hypothesis of having a $\beta \rightarrow \alpha$ transformation with slow kinetics is also supported by the fact that the broad ring at about $2\theta \approx 21$ splits into two spots with different scattering angles ($2\theta \approx 20^\circ$ and $2\theta \approx 24^\circ$), proving the presence of α phase, only after unloading the sample (see Figure VI.12). The presence of these two spots splits was also found by Penel-Pierron [12] [11] upon $\varepsilon = 200\%$ at 120°C . Nonetheless, as their WAXS patterns were taken ex-situ, it also means that the sample had time to relax upon unloading.

This kind of behavior has been observed for PET [13]: it concerned the strain-induced crystallization in bulk amorphous PET but the conclusion of the authors was that a certain accommodation time or a minimum level of molecular relaxation was necessary for the crystallization to be effective. The same process could apply for the $\beta \rightarrow \alpha$ transformation.

tend to orient preferentially in the TD. As said in the chapter V, INJ samples follow a chain network model in the elastic strain domain.

As the strain increases, there is an increasing relative fraction of planes which orient parallel to the TD. After the yield, the lamellae rotate further and the chains continue to orient in the TD. This is the beginning of fibrillation and thus one can suppose that lamellae also start to fragment, as it can be reported in literature [15]. The hypothesis of fragmentation is also supported by the decrease of integrated intensity as discussed in Figure VI.7. It is worth noticing that at $\epsilon = 450\%$, the WAXS pattern corresponds to the same one as observed in fibers [14], meaning at this strain value, the morphology is entirely fibrillar, whereas the material was initially an isotropic bulk.

Concerning the possibility of the $\beta \rightarrow \alpha$ transformation mentioned above, it does not seem that this transformation affects the mechanisms however it could have an influence on the drawing ratio and could be explained why INJ samples stretch more than the others.

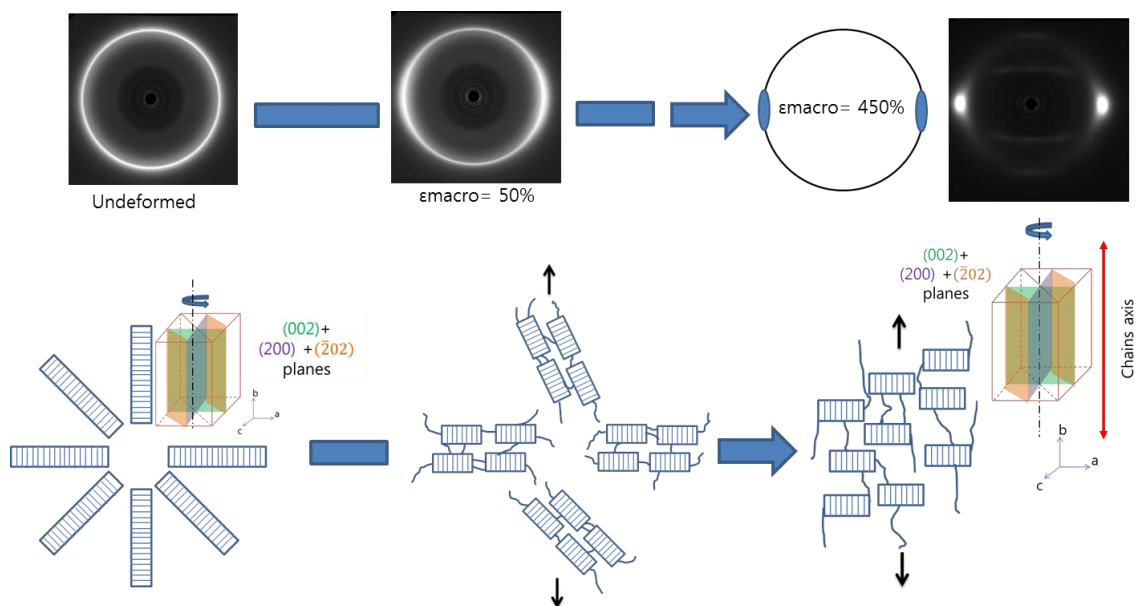


Figure VI.14 : Mechanisms of deformation for PA6 containing predominantly β phase, tensile axis is vertical. WAXS patterns are taken during tests at $T = 120^\circ\text{C}$.

I.2. Annealed (A215) and isotherm-treated (I213) samples: pure α phase

The same characterization method as for the INJ sample has been applied to the A215 (annealed at 215°C) and I213 (isothermally treated at 213°C) samples, which contain only α phase.

In WAXS data (shown here for I213 sample) the α -crystal form is evidenced by the two distinct (200) and (002)+(20 $\bar{2}$) reflections located at scattering angles $2\theta \approx 20^\circ$ and $2\theta \approx 24^\circ$ respectively. These two families of planes are not equivalent and may possibly orient differently under stretching. It is thus *a priori* necessary to analyze their evolutions separately. Thus, distinct Azimuthal Scattering Domains (ASD) have been defined to measure the intensity corresponding to each family of planes, as depicted in Figure VI.15a in the first two 2D WAXS patterns: red dotted circles represent the domain of scattering vectors investigated for (200) planes (ring at $2\theta \approx 20^\circ$) whereas green plain half-circles represent the domain investigated for (002)+(20 $\bar{2}$) planes (ring at $2\theta \approx 24^\circ$). The same ASD method was applied below and above the glass transition. Both samples A215 and I213 behave in very similar ways. We show here only the results for the I213 sample.

I.2.1. Evolution in the plastic strain domain above T_g

The evolution of 2D WAXS patterns along in-situ tensile tests performed at $T = 120^\circ\text{C}$ (above T_g) is shown in Figure VI.15a. As described previously, in the initial state, the two rings correspond to two distinct families of planes. In order to illustrate the anisotropy which appears in the 2D WAXS patterns, diffraction curves (intensity as a function of scattering angle 2θ) measured in horizontal and vertical directions (integrated over a azimuthal sector of width 5°) are depicted in Figure VI.15b. At the yield state, only vertical reinforcements are present for (200) planes, i.e. the unique presence of a peak at $2\theta \approx 20^\circ$. Concerning the horizontal scattering, both families of planes scatter but the presence of the $((002)+(20\bar{2}))$ planes is predominant as the peak at $2\theta \approx 24^\circ$ has a higher maximum. The elastic domain corresponding to the initial state until the yield point has already been investigated in chapter V. Finally, in the last stage, there is a broad horizontal scattering for both family planes and a weak vertical scattering for (200) planes still remains.

Thus, in sample I213 (as well as in sample A215, not shown) the intensity profiles evolve in a complex way as the strain progressively increases, with different successive steps. These different steps are described in what follows. The azimuthal intensity profiles for different macroscopic strains are shown in Figure VI.15c and d: the two graphs correspond to the two distinct scattering rings, corresponding to distinct families of planes.

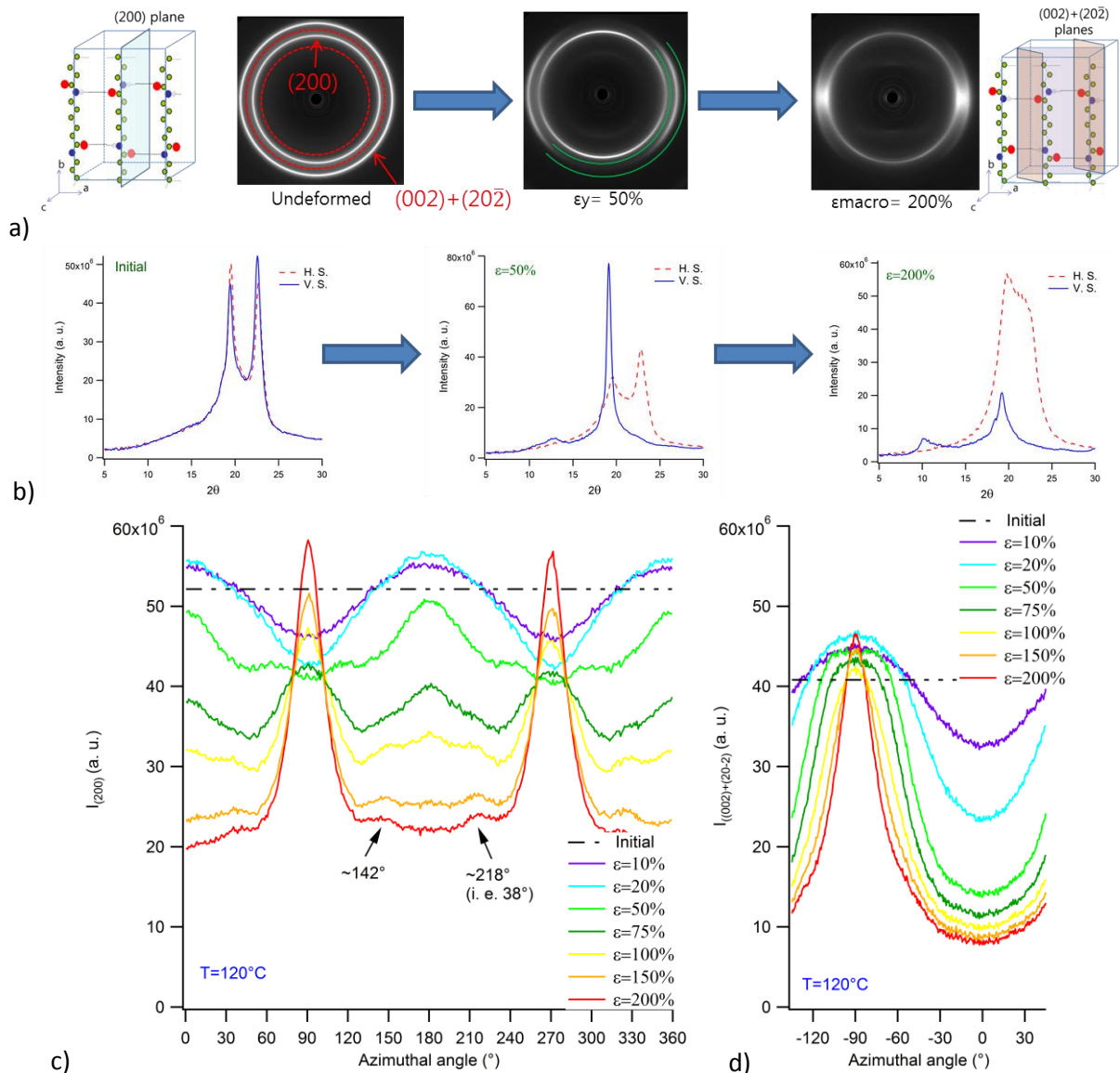


Figure VI.15: I213 sample under tensile test at $T = 120^\circ\text{C}$. a) 2D WAXS patterns with red dotted circles representing the ASD for (200) plane and green plain half-circles representing the ASD for (002)+(20 $\bar{2}$) planes.

b) Intensity as a function of 2θ scattering angle in horizontal (H. S.: horizontal scattering, normal to TD) and vertical directions (V. S.: vertical scattering, parallel to TD).

Azimuthal intensity profiles as a function of the azimuthal angle for c) the inner peak (corresponding to (200) planes) and d) the outer peak (corresponding to (002)+(20 $\bar{2}$) planes). Tensile axis is vertical corresponding to $\psi = 0^\circ$.

Let us first investigate the orientation of (200) planes (ring at $2\theta \approx 20^\circ$) (see Figure VI.15c). The orientation of these planes shows a complex evolution. From $\epsilon = 10\%$ to $\epsilon = 20\%$, i.e. in the elastic strain domain, vertical reinforcements ($\psi = 0^\circ \text{ [mod } 180^\circ]$) start to appear for (200) planes. This means that (200) planes tend to orient first with their normals parallel to the tensile direction (TD), in this strain regime. At yield, i.e. $\epsilon = 50\%$, two weak secondary reinforcements appear at ca. $\psi \approx 70^\circ$ and $\psi \approx 110^\circ$: they correspond to a fraction of (200) planes oriented with their normals at an angle ca. $\approx \pm 20^\circ$ with respect to the horizontal plane. Then, as the strain further increases, the two maxima merge and the width at half-height decreases. This behavior is similar to what has been observed in INJ sample below T_g (see in Figure VI.8c). Concerning the vertical reinforcements, they are still present but their intensity and angular width have decreased. From ca. $\epsilon = 75\%$ and beyond, horizontal reinforcements appear and their amplitude increases progressively as the amplitude of vertical reinforcements decreases. In the last stage of deformation, at $\epsilon = 200\%$, horizontal reinforcements are predominant. Vertical reinforcements have completely vanished. Minor

reinforcements with maxima at $\psi \approx 38^\circ$, $\psi \approx 142^\circ$, $\psi \approx 218^\circ$ and $\psi \approx 322^\circ$ appear. These minor reinforcements correspond to a fraction of (200) planes which have their normals oriented at an azimuth of ca. $\approx 38^\circ$ with respect to the tensile direction, or equivalently at ca. $\approx \pm 52^\circ$ with respect to the horizontal plane.

Let us now describe the orientation of (002) and $(20\bar{2})$ families of planes (ring at $2\theta \approx 24^\circ$) (Figure VI.15d). As the strain increases right from the beginning of the experiment, only horizontal reinforcements ($\psi = -90^\circ$) are observed, whose amplitude increases progressively while their width at half-height decreases accordingly. This corresponds to a tendency for the (002) and $(20\bar{2})$ planes to orient with their normals in the horizontal plane, that is perpendicular to the tensile direction.

Thus, in the elastic strain domain, the ring corresponding to (200) planes is reinforced in the vertical (meridian) direction (see also chapter V), meaning a tendency for these planes to orient normal to TD, or equivalently, with their normals parallel to TD. This situation is schematized in Figure VI.16. Then, accordingly, (002) planes should scatter in directions inclined at an azimuth angle $\pm 22.5^\circ$ with respect to the equator (assuming an angle $\beta = 67.5^\circ$ in the crystalline unit cell) and $(20\bar{2})$ planes should scatter in directions inclined at an azimuth angle $\pm 34^\circ$ from the equator (that is $\psi \approx 56^\circ$ and $\psi = 124^\circ$) (see Figure VI.16). It is difficult to clearly distinguish these contributions in the azimuthal modulation of the intensity of the corresponding ring (see Figure VI.15d). However, these scattering contributions of both (002) and $(20\bar{2})$ planes qualitatively agree with the modulation observed in Figure VI.18d.

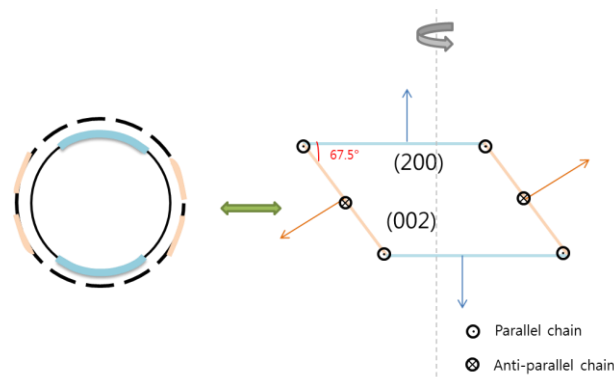


Figure VI.16: Scheme of WAXS pattern and its equivalent to oriented crystalline lattice at the yield state, tensile axis is vertical (the drawing of the crystalline unit cell is not to the scale)

At the yield point (between 20 and 50% strain), the modulation of the intensity as a function of the azimuth angle for the (200) planes changes qualitatively. Maxima at 0° disappear progressively and new maxima at 90° appear progressively.

As the situation evolves at the yield, it means that a different orientation of the planes occurs. Indeed, for (200) planes two vertical reinforcements appear at $\psi \approx 70^\circ$ and $\psi \approx 110^\circ$, before becoming only one vertical reinforcement centered on $\psi = 90^\circ$ from $\epsilon = 75\%$. A part of the final orientation of the planes at $\epsilon = 200\%$ can be depicted as in Figure VI.17. Indeed the horizontal reinforcements of (200) planes are not shown in Figure VI.17. The only possibility to explain the different orientations observed for (200) planes is to take into account two different populations of (200) planes. The Figure VI.17 shows a great accordance between the two minor reinforcements at $\psi = 142^\circ$ and $\psi = 218^\circ$ observed for (200) planes and the horizontal reinforcements observed for (002) and $(20\bar{2})$ planes.

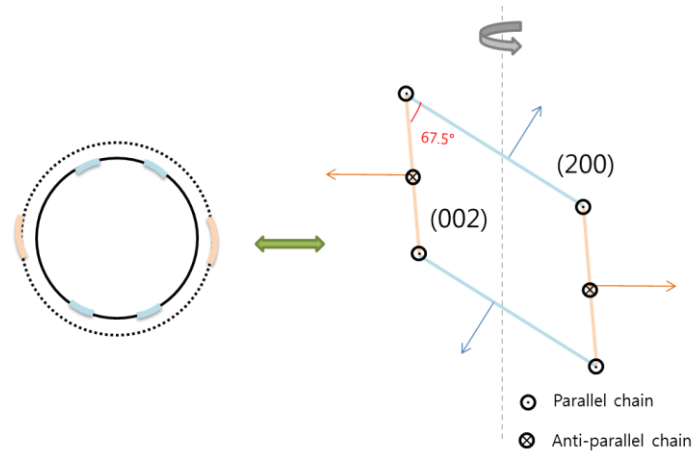


Figure VI.17 : Scheme of WAXS pattern and its equivalent to oriented crystalline lattice for a part of the chains/lamellae at $\epsilon=200\%$, tensile axis is vertical (the drawing of the crystalline unit cell is not to the scale)

Finally, at the last stage of deformation, a part of the planes is oriented in the way depicted by Figure VI.17 meaning that some chains are oriented normal to TD. The other part is oriented with (200) planes normal to TD, meaning that chains orient parallel to TD as depicted in Figure VI.16.

I.2.2. Evolution in the plastic strain domain below T_g

For tensile tests performed at $T = -10^\circ\text{C}$ (below the glass transition) and beyond the yield, the same trend applies with slight differences. 2D WAXS patterns and their corresponding 2θ profiles are depicted in Figure VI.18a and b. Overall, the same observations made above T_g apply for Figure VI.18a and b. The azimuthal intensity profiles for different macroscopic strains are shown in Figure VI.18c and d for both families of planes.

For (200) planes (see Figure VI.18c), there is at first two vertical reinforcements for $\epsilon = 10\%$ which become one for $\epsilon = 25\%$, i.e. at the yield strain. In the plastic strain domain, horizontal reinforcements appear and increase whereas vertical reinforcements decrease and nearly vanished at $\epsilon=60\%$ just before the failure of I213 sample. The horizontal reinforcements first start as a broad plateau of $\approx 90^\circ$ (two minima located at 45° and 135° , as depicted in Figure VI.18c for $\epsilon = 37\%$). One can also notice that the vertical reinforcements first continue to increase as the horizontal reinforcements start to appear before finally decrease.

Concerning (002) and $(20\bar{2})$ planes (see Figure VI.18d), there is at first a broad horizontal reinforcement at $\epsilon=10\%$ in the elastic strain domain. At the yield, two plateaus are visible at 19° of the horizontal azimuth angle ($\psi=90^\circ$). The width covered by these two plateaus decreases as the strain increases. At $\epsilon=60\%$ there is no more plateaus but only one horizontal reinforcement.

Finally the yield state corresponds entirely to the orientation of the lattice depicted in Figure VI.16, meaning that chains are oriented normal to TD. However in the last stage of deformation, most of (200) planes are oriented normal to TD, meaning that most of the chains are oriented parallel to TD.

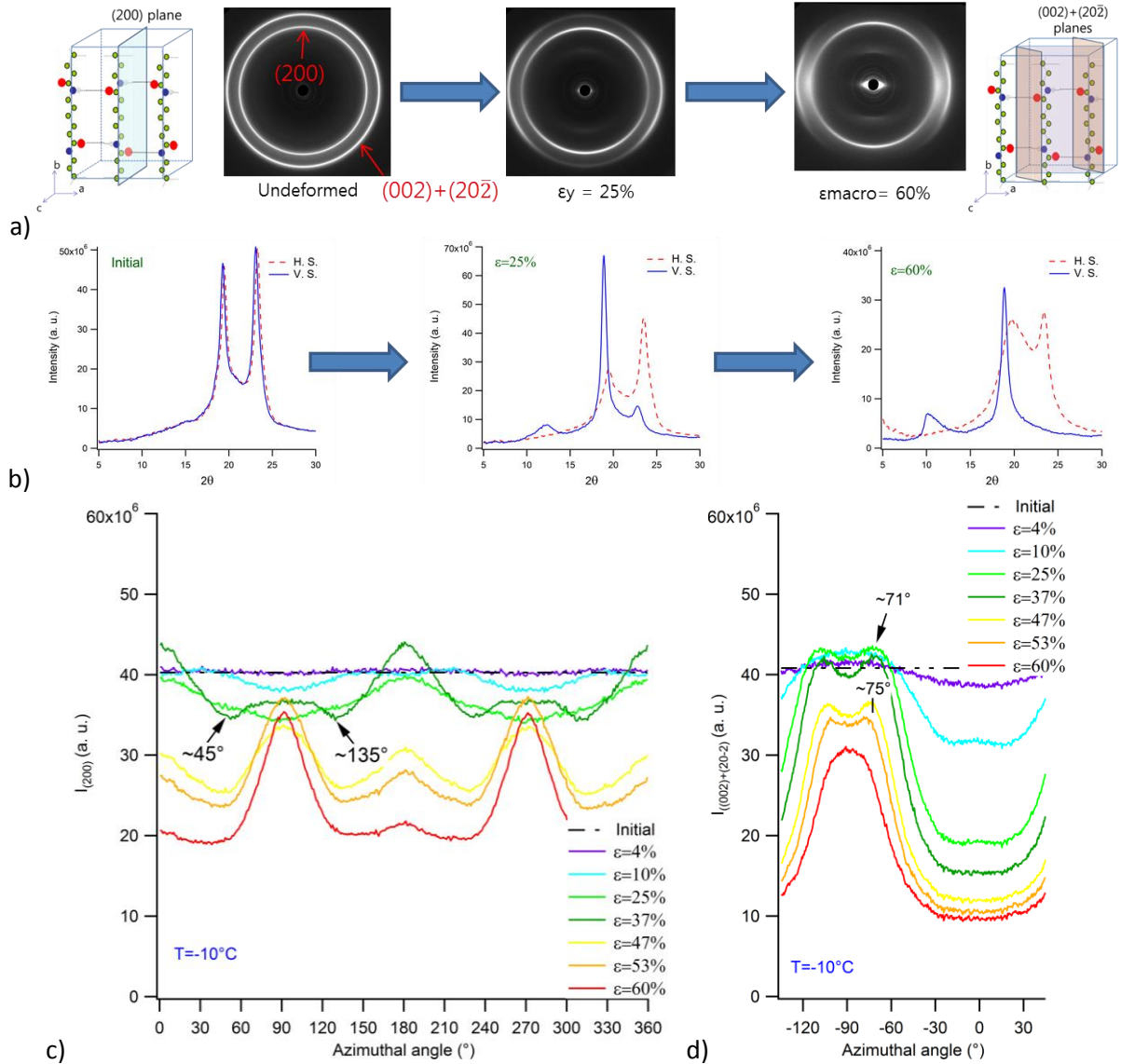


Figure VI.18: i213 sample under tensile test at $T = -10^\circ\text{C}$. a) 2D WAXS patterns. b) Intensity as a function of 2θ scattering angle in horizontal (H. S.: horizontal scattering, normal to TD) and vertical directions (V. S.: vertical scattering, parallel to TD). c) Azimuthal intensity profiles as a function of the azimuthal angle for c) the inner peak (corresponding to (200) planes) and d) the outer peak (corresponding to (002)+(202) planes). Tensile axis is vertical corresponding to $\psi=0^\circ$.

I.2.3. Discussion: temperatures and deformation mechanisms of the plastic strain domain for α phase

I.2.3.1. Effect of temperature

Let us first discuss the effect of temperature on the orientation of planes. By using Eq. V.25, the absolute azimuthal scattering intensity for (200) planes is plotted in Figure VI.19 for various strains below and above the glass transition. At first glance, the reinforcements have the same trend but are magnified above T_g . In addition beyond the ϵ yield, the peak of intensity centered at $\psi=90^\circ$ has a smaller half-width above T_g than below, meaning a smaller distribution of orientation of the (200) planes. Another difference has to be point out concerning the orientation of (200) planes around $\psi=0^\circ$: below T_g , the vertical reinforcement is unique whereas above T_g two minor reinforcements are observed.

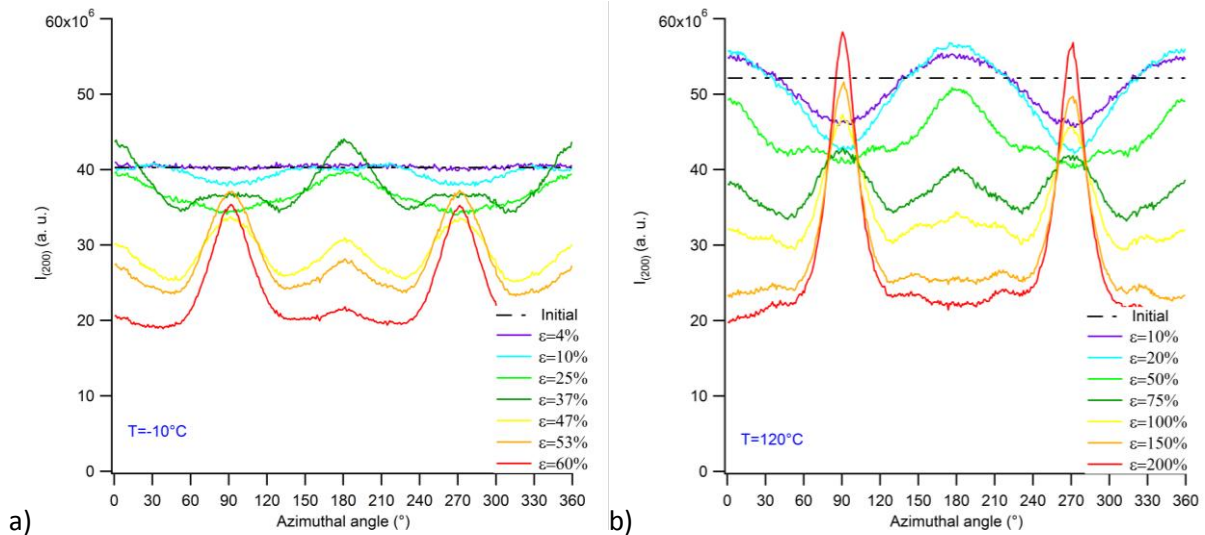


Figure VI.19: Absolute azimuthal scattering intensity of (200) planes at a) -10°C and b) 120°C for I213 samples

With Eq. V.25, the absolute azimuthal scattering intensity for (002)+(20 $\bar{2}$) planes is also plotted in Figure VI.20 for various strains below and above the glass transition. The difference of orientation according to temperature is striking for (002)+(20 $\bar{2}$) planes: beyond the yield two plateaus around $\psi = -90^\circ$ are visible from $\epsilon = 25\%$ to $\epsilon = 53\%$ before becoming only one at $\epsilon = 60\%$ below the glass transition whereas above T_g , there is no plateau only one horizontal reinforcement. Below T_g , a small orientation at $\psi = 0^\circ$ appears from $\epsilon = 15\%$ to $\epsilon = 25\%$, just after the yield which is not the case above T_g . The amplitude of intensity seems to be relative to the macroscopic strain whatever the temperature.

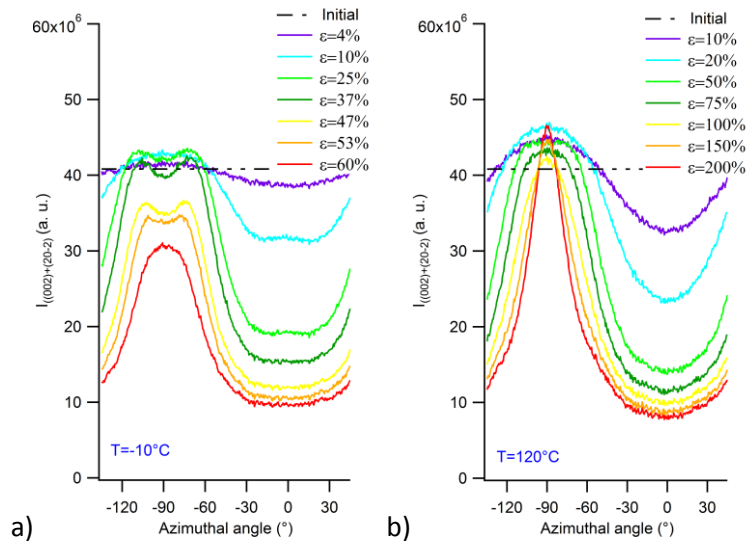


Figure VI.20: Azimuthal scattering intensity of ((002)+(20 $\bar{2}$)) planes at a) -10°C and b) 120°C for I213 samples

As for the INJ sample, let us now focus on the intensity of the scattering lamellae. The two families of planes have been investigated separately. The evolution of the integrated intensity, as described by Eq. VI.1, is plotted as a function of macroscopic strain for (200) planes in Figure VI.21a and for ((002)+(20 $\bar{2}$) planes in Figure VI.21b. For both temperatures, the intensity decreases but the decrease is sharper below the glass transition. If this decrease is related to the fragmentation of lamellae, as explained in §1.1.1 for INJ sample, it seems logical that, as both crystalline and amorphous phases become more rigid below T_g , the fragmentation occurs more abruptly, i.e. a sharper slope.

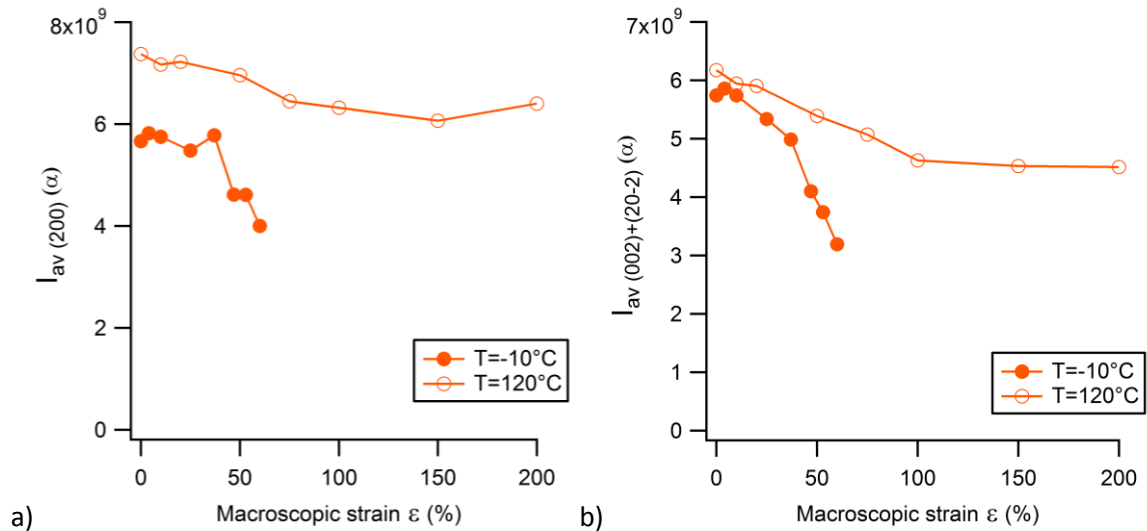


Figure VI.21: Evolution of the integrated intensity as a function of macroscopic strain in I213 sample for both tensile test temperatures concerning a) (200) planes and b) ((002)+(20 $\bar{2}$)) planes

1.2.3.2. Proposed mechanisms

Let us now detail the deformation mechanisms. In chapter V, it was earlier found that the initial mechanism in the elastic strain domain was not the same according to temperature. Below T_g , a Chain Network (CN) model applies and above T_g , a Rigid Lamella (RL) model applies. If we now focus on the steps after the yield, it can be found that the mechanisms explaining the plastic strain domain are nearly the same, only the stage 1, as well as part of stage 3 of Figure VI.23, change depending on the temperature, as it is explained below.

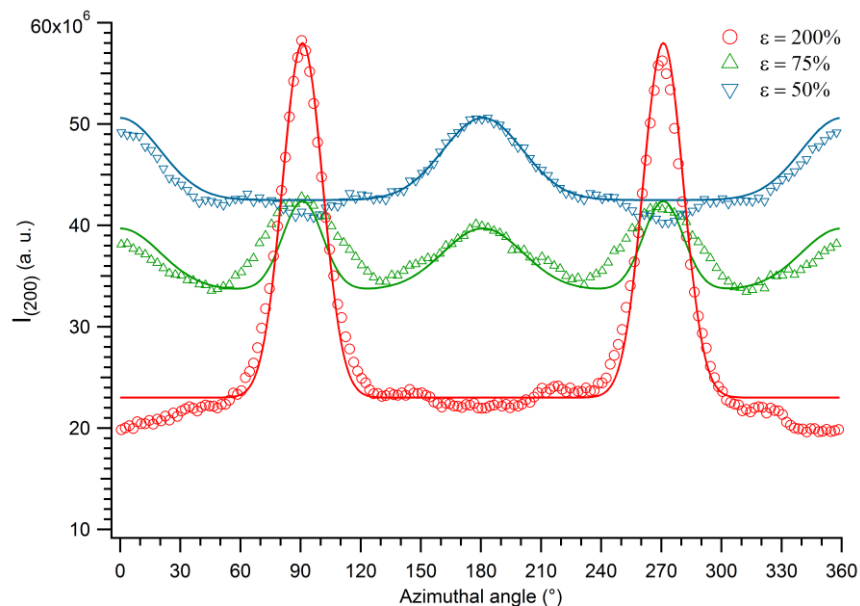


Figure VI.22: Intensity for the peak from (200) planes as a function of the azimuthal angle ψ , for three different strain values. Points are experimental data (same data as in Figure VI.19b), curves are heuristic adjustments with Gaussian peaks centered either on $\psi = 0^\circ$ (mod 180°) or on $\psi = 90^\circ$ (mod. 180°). The fitting curve at 75% strain is a linear combination of those at 50% and 200%.

In Figure VI.22, the curve at 75% strain has been fitted with a linear combination of the fitting curves at 50 and 200% strain, in the form:

$$I_{75\%}(\psi) = 0.75I_{50\%}(\psi) + 0.25I_{200\%}(\psi) \quad (\text{E. VI.3})$$

Figure VI.22 illustrates the fact that the material at 75% strain contains two distinct populations of lamellae, one still with the same orientation distribution as observed at 50% strain (relative fraction 75%) and one with a new distribution of orientation (relative fraction 25%), in which the preferred orientation is now with chains axis along the tensile direction.

Above the glass transition, the mechanisms of deformation are schematized in Figure VI.23. After the yield point (corresponding to step 1 in Figure VI.23), two types of behavior seem to be in competition: part of the polar lamellae keep following the RL model whereas the rest of the lamellae seems to follow the CN model in order to achieve the fibrillar transformation. Indeed, the vertical reinforcements corresponding to polar lamellae still remind, proving that a part of the lamellae keep this orientation. However, horizontal reinforcements of (200) planes also appears. It was previously concluded in §1.2.1 that two populations of (200) planes coexist. It could be explained by the fact that:

- A part of the lamellae stays in polar orientation,
- Another part rotates in order to orientate chains parallel to tensile direction and supposedly starts to fragment, as represented on the step 2 in Figure VI.23.

In step 3, few polar lamellae have remained unchanged whereas the rest of the lamella have rotated and supposedly fragmented: fibrillation has occurred and chains are oriented parallel to the tensile direction.

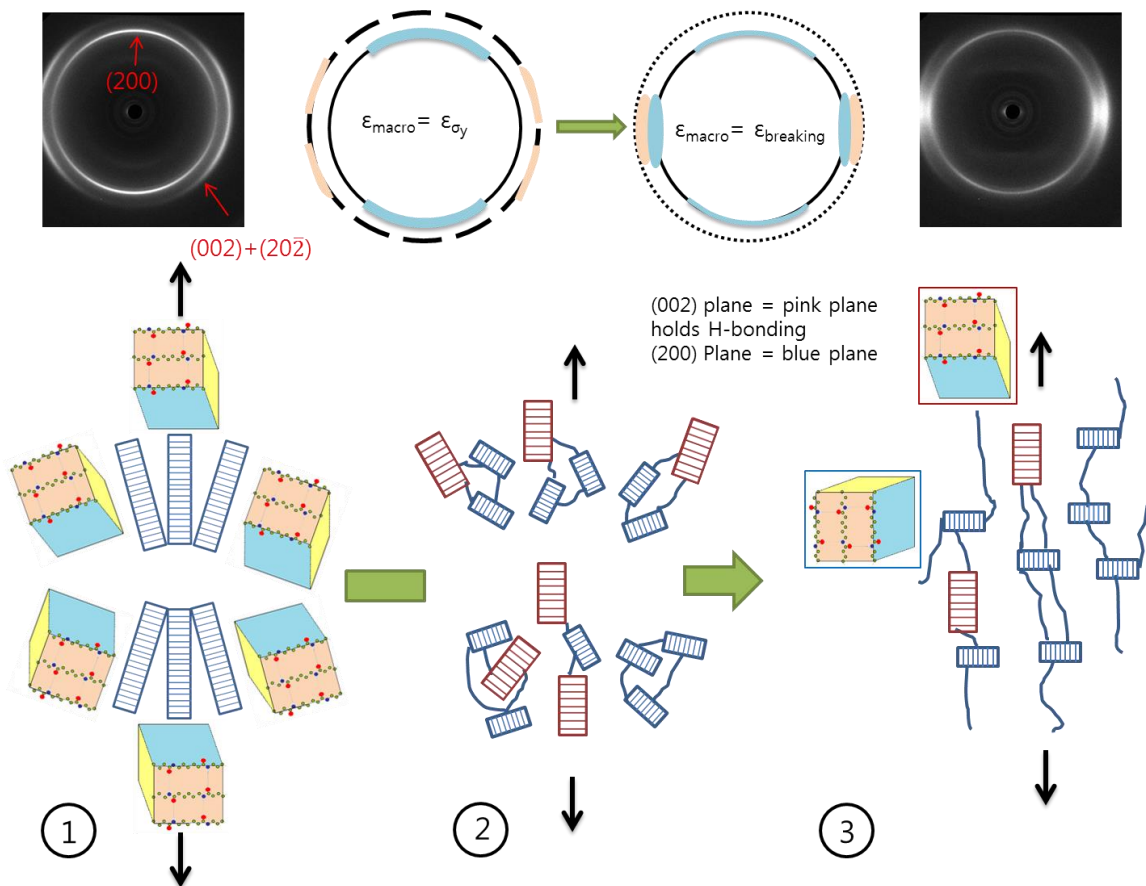


Figure VI.23 : Mechanisms of plastic deformation for PA6 with pure α phase from yield stress, tensile axis is vertical

As mentioned earlier, the competition between the two models is enhanced by temperature. Indeed, below or above the glass transition, the mechanisms in the elastic strain domain are not the same, which explains why according to temperature the final orientation of untouched lamellae is not exactly the same. Indeed, above T_g , remained lamellae are oriented with H-bonds parallel to the tensile direction whereas below T_g , (200) planes are normal to tensile direction. In addition, below T_g , cavitation is visible as it will further described in §II.2.

I.3. Discussion on A200 sample: mixture of α and γ phases

As A200 samples contain a mixture of α and γ phases, it is interesting to study them in order to see if the γ phase may have an impact on the deformation mechanisms, even in cases when it is the minority crystalline phase. The different steps of deformation are easier to follow below the glass transition as the various rings are then better resolved, as shown in Figure VI.24a. Scattering from the α phase is evidenced by the (200) and (002)+(202 $\bar{1}$) reflections located at $2\theta \approx 20^\circ$ and $2\theta \approx 24^\circ$ respectively. Scattering from the γ phase is evidenced by the (001)+(200)+(002) and (020) reflections located at $2\theta \approx 21^\circ$ and $2\theta \approx 10.5^\circ$ respectively.

As mentioned in chapter V, in the elastic strain domain, A200 follows a chain network model below the glass transition but has a more complex behavior above the glass transition.

Let us now focus on the plastic strain domain. At the yield point, the scattering from (200) planes for α crystals and the scattering from (001)+(200)+(002) planes for γ crystals are reinforced in the vertical direction (see pattern at $\epsilon = 10\%$ in Figure VI.24a). However, beyond the yield and up to near the breaking point, there is no more vertical reinforcement of these rings but only horizontal spots in WAXS patterns. This means that contrary to A215 and I213 samples (pure α phase), no polar lamellae (with chains normal to TD) remain and all chains are parallel to the tensile direction, leading to the same final fibrillation state as INJ samples. One can also observe that in the last stage of deformation, the fibrillation is more pronounced above T_g (presence of 6 inner spots) than below T_g (only two spots), as discussed previously.

Even though the precise location of α and γ phases in spherulites is not known, if we make the hypothesis that they are both present inside the same spherulite, it would seem that γ phase promotes the fragmentation of lamellae. As γ phase is more ductile, a lamella made of γ phase would break sooner and so promote the fragmentation as well as the rotation of all lamellae (including lamellae made of α phase), allowing the orientation of all chains along TD. This process may be possible since the γ phase has a significant fraction (see Table III.7 of chapter III), even though it is the minority phase. At this step, we do not have direct information on the distribution of both phases neither on the distribution of long periods.

direction (TD) than α phase. Indeed, as α phase keeps some intact lamellae, these lamellae consist of hard nodes in the chain network, which is not the case for β phase where all the lamellae are rotated in the same way. However, for A200 sample the presence of γ phase seems to change the deal: in the last stage of deformation only horizontal reinforcements are present, meaning only one population of lamellae with chains oriented parallel to TD.

II. Deformation mechanisms at the scale of lamellae, investigated by SAXS

Complex mechanisms of deformation have been described thanks to WAXS data, in terms of the evolution of the orientation distribution of crystalline lattice planes as a function of the strain, in the plastic domain (beyond the yield point). However, deformation processes involve mechanisms which occur at larger scales. It concerns fibrillation and cavitation. These may be analyzed by looking at SAXS data.

II.1. Fibrillar transformation

Whatever the PA6 samples, we have observed that all of them undergo fibrillation. However, this fibril transformation does not begin at the same strain for everyone and does not behave in the same way for all. The influence of the temperature is also investigated. Thus, the long period as a function of macroscopic strain is plotted in Figure VI.25 for both temperatures.

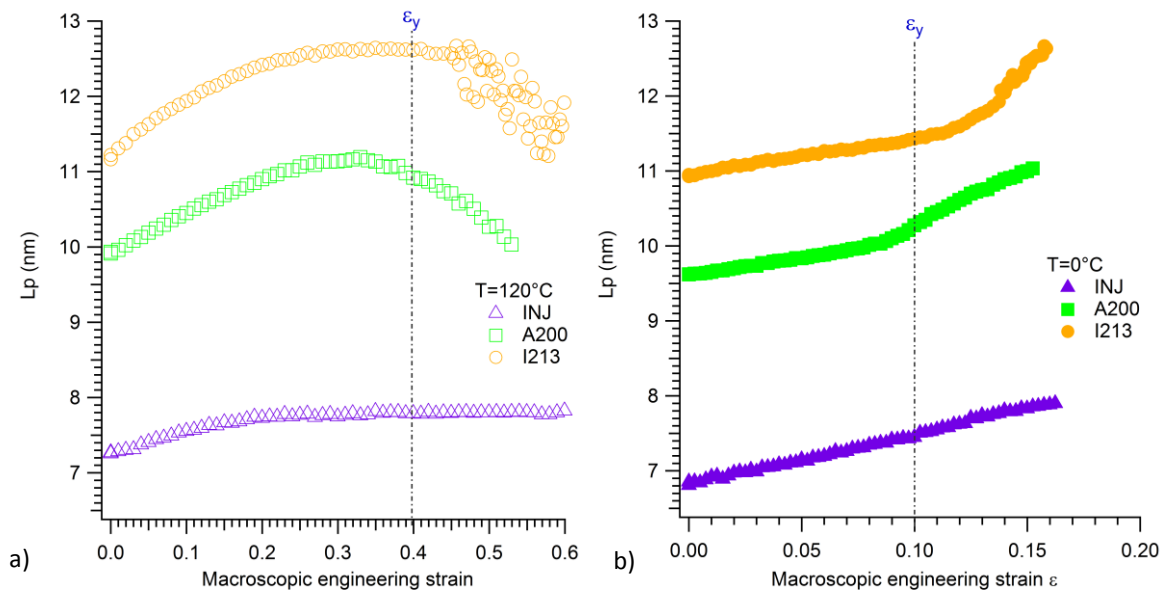


Figure VI.25: Long period L_p as a function of macroscopic strain at a) $T=120^\circ\text{C}$ and b) $T=0^\circ\text{C}$

For $T > T_g$ (Figure VI.25a), the long period for samples containing only α phase (A215 and I213) increases until the yield strain is reached then L_p collapses until reaching the value of the initial L_p or less, corresponding to the period of fibrils. In contrast, the long period of INJ samples increases until reaching a plateau corresponding to the period of fibrils. This difference could be due to the difference of mechanisms, as INJ sample follows the chain network model and I213 sample follows the rigid lamella model. Anyway, the initial L_p for β phase is shorter and this also maybe why it is easier for lamella of β phase to rotate and orientate chains in tensile direction. Furthermore, because

the period of fibrils is reached at $\epsilon=0.2$ (meaning below the yield strain ϵ_y), it could also indicate that during elastic domain, lamellae of β phase start to fragment. Thus, for α phase, with the same approach, it should indicate that the fragmentation starts after the yield point except for some polar lamellae which remained untouched as explained below.

For $T < T_g$ (Figure VI.25b), the long period increases as well as the strain but after the yield, it undergoes a sharp increase for samples with α phase. On the contrary, for β phase, the long period is strictly linear and does not seem to be affected by the yield. This could be due to the fact that the samples undergo cavitation. Anyway, these behaviors are completely different from those of tensile tests above T_g .

In any case, these results are really interesting because it is known in literature that fibril structure of polyethylene and polypropylene depends only on the temperature at which the drawing is performed [17]. However, this conclusion does not seem to apply to polyamide 6. At the moment, no clear physical significance has been evidenced.

II.2. Cavitation

Cavitation initiates for every samples at $T < T_g$. The strain of initiation as a function of crystallinity index is plotted in Figure VI.26. The strain of initiation was detected by SAXS and corresponds in fact to the onset detected for our SAXS set-up, meaning a q range of $0.1\text{-}1.51\text{ nm}^{-1}$, i.e. objects size of minimum 4 nm.

Back to Figure VI.26, it shows that the lower the crystallinity index, the sooner the cavitation starts. However, as for the Young's modulus, one can wonder it is really due to crystallinity or to the crystalline phase. Indeed, for lower crystallinity index, the samples contain β phase whereas for higher X_c , the samples contain α phase. Below the glass transition, the yield strain is near 10%, meaning that the cavitation starts before reaching the yield for INJ samples.

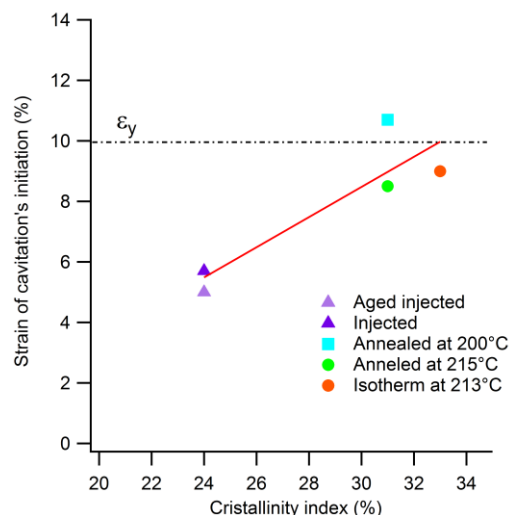


Figure VI.26: Strain of initiation's cavitation as a function of crystallinity index for PA6 samples at $T=0^\circ\text{C}$

If we take a closer look at the SAXS patterns, shown in Figure VI.27, it appears that the cavitation is not the same according to the crystalline phase. Indeed, for β samples (1 and 2), voids scatter parallel and normal to the tensile direction whereas for α samples (3, 4 and 5), they scatter parallel to the tensile direction. These observations seem to confirm that there is more than just an effect of crystallinity index.

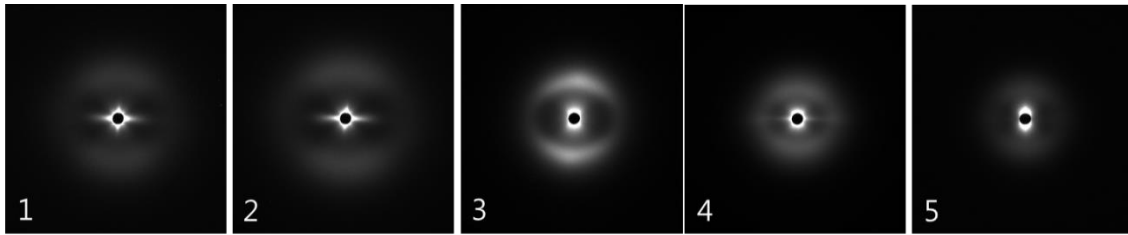


Figure VI.27: SAXS patterns of cavitation at $\epsilon=15\%$ for $T < T_g$ ($T=0^\circ\text{C}$) for PA6 samples : 1) aged injected, 2) injected, 3) annealed at 200°C , 4) annealed at 215°C and 5) isotherm at 213°C ; tensile direction is vertical

Let us now focus on INJ sample. The different steps of cavitation of INJ sample are shown in Figure VI.28. It starts with cavities normal to tensile direction but soon cavities parallel to tensile direction appear. This means that for INJ samples at first the cavities have a shape of oblate ellipsoids with their major axis oriented normal to the tensile direction. Rapidly, normal scattering of the voids to TD adds to the parallel scattering. This means the cavity shape are prolate ellipsoids elongated in TD. As the strain increases, there is also shear banding associated to crazes. That is why the SAXS pattern at $\epsilon \approx 15,2\%$ also scatters at 45° (see Figure VI.28b).

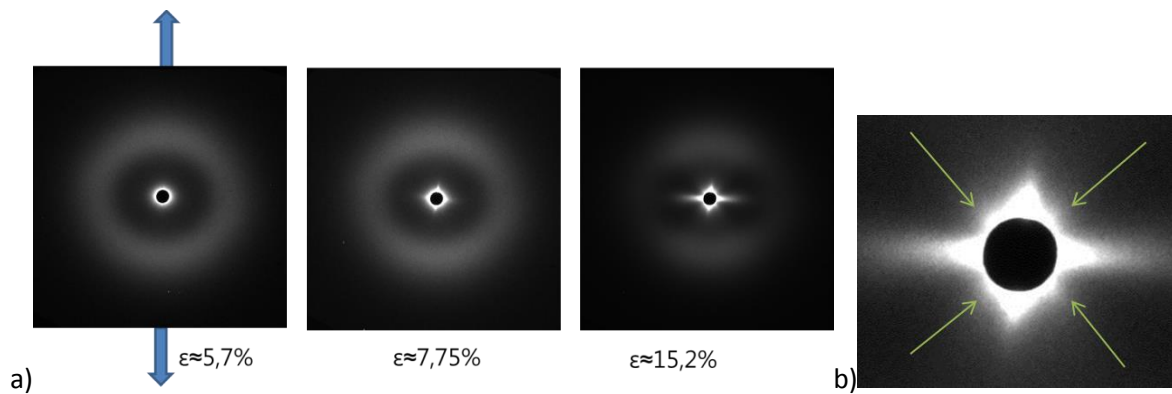


Figure VI.28: a) Steps of cavitation for INJ sample (predominant β phase) at $T=0^\circ\text{C}$; b) Zoom for $\epsilon \approx 15,2\%$

In contrast, the steps of cavitation for I213 sample are depicted in Figure VI.29. In this case, cavities appear only normal to tensile direction, meaning that the cavities have a shape of oblate ellipsoids with their major axis oriented normal to TD.

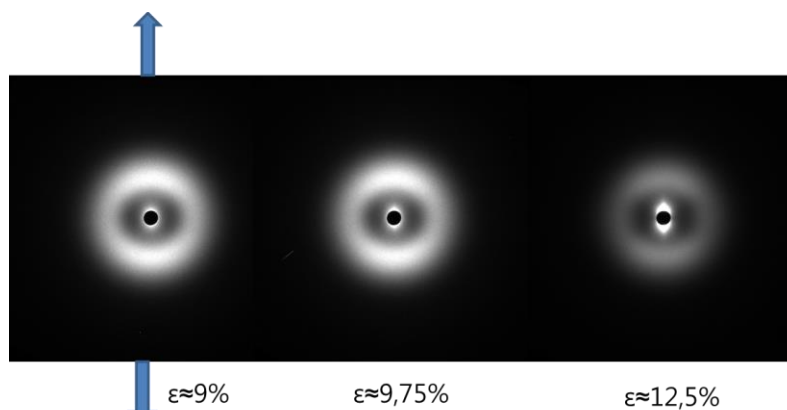


Figure VI.29 : Steps of cavitation for I213 sample (α phase) at $T=0^\circ\text{C}$

The effect of temperature on cavitation for the various crystalline phases is presented in Figure VI.30. Above the glass transition, β and α phases behave in the same way, the observed pattern is not due to cavitation but it corresponds to fibrillation. Indeed, there is no cavitation at high temperature.

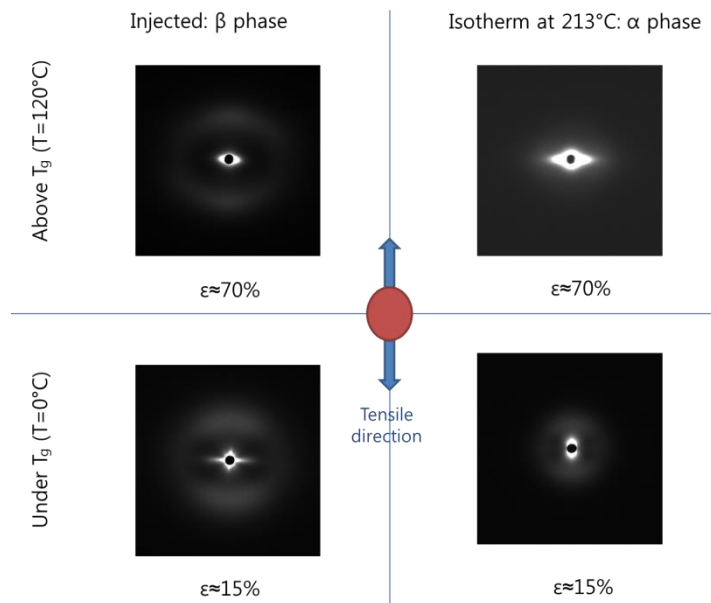


Figure VI.30: 2D SAXS patterns for β and α phases, above and below T_g

III. Conclusion

Finally, the analysis of WAXS measurements has shown that samples with β or α phase behave in quite different ways in the plastic domain.

In samples with β phase, chains tend to orient along TD during all the deformation process (i.e. including the viscoelastic regime, denoted as the CN model). This tendency is magnified in the plastic strain regime until a high degree of orientation is reached. This kind of behavior is commonly observed for semi-crystalline polymers. Concomitantly the β phase transforms into α phase. However this transformation seems to require some relaxation time. In the final fibrillar stage, all the crystals are oriented with their normal along TD, or equivalently all chains are oriented along TD.

In samples with α phase, a different two-step process occurs. In the first step, as described in the previous chapter, lamellae orient preferentially along TD, i.e. the chains being normal to TD (this the RL model mentioned in chapter V). In the second step, in the plastic regime, a major fraction of crystallites reorients normal to TD, i.e. with chains parallel to TD while a minor fraction remains oriented along TD.

Considering the ultimate stage of deformation that we have investigated in this work, the final fibrillar state seems to strongly depend on the initial microstructure of the sample. Concerning the effect of temperature, it has been observed that for all samples, the final stage is better oriented above the glass transition.

References

- [1] F. Auriemma, V. Petraccone, L. Parravicini and P. Corradini, "Mesomorphic form (β) of Nylon 6," *Macromolecules*, vol. 30, pp. 7554-7559, 1997.
- [2] J. Gianchandani, J. Spruiell and E. Clark, "Polymorphism and orientation development in melt spinning, drawing, and annealing of nylon-6 filaments," *Journal of Applied Polymer Science*, vol. 27, pp. 3527-3551, 1982.
- [3] C. Ibanes, L. David, M. De Boissieu, R. Seguela, T. Epicier and G. Robert, "Structure and mechanical behavior of nylon-6 fibers filled with organic and mineral nanoparticles. I. Microstructure of spun and drawn fibers," *Journal of Polymer Science: Part B: Polymer Physics*, vol. 42, pp. 3876-3892, 2004.
- [4] D. Read, R. Duckett, J. Sweeny and T. McLeish, "The chevron folding instability in thermoplastic elastomers and other layered material," *Journal of Physics D: Applied Physics*, vol. 32, pp. 2087-2099, 1999.
- [5] A. Makke, M. Perez, O. Lame and J.-L. Barrat, "Nanoscale buckling deformation in layered copolymer materials," *Proceedings of the National Academy of Sciences*, vol. 109, pp. 680-685, 2012.
- [6] Y. Cohen, R. Albalak, B. Dair, M. Capel and E. Thomas, "Deformation of oriented lamellar block copolymer films," *Macromolecules*, vol. 33, pp. 6502-6516, 2000.
- [7] V. I. Gerasimov, Y. V. Genin and D. Y. Tsvankin, "Small-angle x-ray study of deformed bulk polyethylene," *Journal of Polymer Science: Polymer Physics Edition*, vol. 12, pp. 2035-2046, 1974.
- [8] M. Krumova, S. Henning and G. Michler, "Chevron morphology in deformed semicrystalline polymers," *Philosophical Magazine*, vol. 86, pp. 1689-1712, 2006.
- [9] T. Hashimoto, M. Fujimura, K. Saijo, H. Kawai, J. Diamant and M. Shen, "Strain-induced plastic-to-rubber transition of a SBS block copolymer and its blend with PS," *Advances in Chemistry Series*, vol. 176, pp. 257-275, 1979.
- [10] L. Penel-Pierron, C. Depecker, R. Seguela and J.-M. Lefebvre, "Structural and mechanical behavior of nylon 6 films. Part I: Identification and stability of the crystalline phases," *Journal of Polymer Science: Part B: Polymer Physics*, vol. 39, pp. 484-495, 2001.
- [11] L. Penel-Pierron, "Transition de phase induite par déformation dans les polymères à liaisons hydrogène : cas des polymères éthylène/alcool vinylique et du polyamide 6," USTL, Lille, 1998.
- [12] L. Penel-Pierron, R. Seguela, J.-M. Lefebvre, V. Miri, C. Depecker, M. Jutigny and J. Pabiot, "Structural and mechanical behavior of nylon-6 films. Part II: Uniaxial and biaxial drawing," *Journal of Polymer Science: Part B: Polymer Physics*, vol. 39, pp. 1224-1236, 2001.

- [13] E. Gorlier, J. Haudin and N. Billon, "Strain-induced crystallization in bulk amorphous PET under uni-axial loading," *Polymer*, vol. 42, pp. 9541-9549, 2001.
- [14] M. Kohan, *Nylon Plastics handbook*, Wilmington: Hanser, 1995.
- [15] A. Peterlin, "Molecular model of drawing polyethylene and polypropylene," *Journal of Materials Science*, vol. 6, pp. 490-508, 1971.
- [16] M. Ito, K. Mizuochi and T. Kanamoto, "Effects of crystalline forms on the deformation behaviour of nylon-6," *Polymer*, vol. 39, pp. 4593-4598, 1998.
- [17] R. Seguela, "Plasticity of semi-crystalline polymers: crystal slip versus melting-recrystallization," *e-Polymers*, vol. 032, pp. 1-20, 2007.

Conclusion

Our aim was to understand the mechanisms of deformation of bulk polyamide 6. In order to have a global view of the mechanisms, a multi-scale investigation was performed below and above the glass transition to modify the state of the amorphous phase (i.e. glassy or rubbery). The crystalline microstructure was modified thanks to thermal treatments in order to see the influence of various parameters (X_c , crystalline phase, L_p , M_n).

PA6 is a polymorphic polymer and exhibits several crystalline lattices, defined as α , γ and β phases. γ and α phases are ordered phases whereas β is a disordered and metastable phase. Indeed, thanks to annealing treatment, we have evidenced by WAXS that β phase transforms into α phase. Furthermore, the fraction of β phase transforming into α depends upon the time and the annealing temperature. Anyway, upon 195°C, the transformation was complete, as evidenced by WAXS. We also observed that the annealing treatment had consequences on the increase of the crystallinity index X_c as well as of the long period L_p . It also seemed that this transformation could be evidenced indirectly by SAXS, since a change of slope of the long period versus temperature curve was found around 180°C, which is the same temperature at which the $\beta \rightarrow \alpha$ transformation starts (for the studied range of annealing times) as observed by WAXS. The $\gamma \rightarrow \alpha$ transformation was also evidenced with an annealing temperature of 215°C. It would be interesting to study in more details the transformation process.

We can make the following hypotheses: the $\beta \rightarrow \alpha$ transformation could proceed by fusion/recrystallization or by cannibalism; concerning the $\gamma \rightarrow \alpha$ transformation the fusion/recrystallization process seems to be the more likely one in our opinion, due to the fact that the melting point of γ phase is close to 215°C. Back to other thermal treatments, we have learned that isotherms above 200°C lead to have only pure α phase. The long period increases with the isotherm temperature but the crystallinity index levels off. Even though quenching was not thoroughly efficient for bulk samples, we have observed that PA6 exhibits cold-crystallization leading to β phase. In case of cold-crystallization, one must keep in mind that for the assessment of crystallinity index, the temperature dependence of the melting enthalpy should be taken into account.

Finally, with all the experiment and literature data, a scheme of a time-temperature-crystallization (TTC) diagram was established for PA6. Concerning the choice of materials, eight samples were selected for the mechanical investigation (a set of two different molecular masses and four types of samples with different crystalline structures). In addition to the initial injected samples (INJ), three thermal treatments were employed: they consist in annealings at 200°C and 215°C (A200 and A215) and an isotherm at 213°C (I213). This panel of samples shows a wide range of microstructures: various crystalline phases ($\beta+\gamma$, $\alpha+\gamma$ and pure α), a variation of X_c from 24 to 35% and a variation of L_p from 7 to 12 nm. Concerning the effect of molecular mass on the microstructure, it was concluded that, for a given process or heat treatment, the same crystalline structure was obtained. However the crystallinity index was always higher for the lower molecular mass (i.e. 15K samples) than for the higher molecular mass (i.e. 31K samples).

Thanks to dynamical mechanical analysis, the choice of temperatures for carrying out tensile tests below and above the glass transition was the following: $T = -10^\circ\text{C} = T_g - 65^\circ\text{C}$ and $T = 120^\circ\text{C} = T_g + 65^\circ\text{C}$, i.e. at the location of the minima of the $\tan \varphi$ curve on both sides of the main relaxation of the amorphous phase. Macroscopic uniaxial tensile tests were carried out on the whole set of samples. Above T_g , a difference of behavior was pointed out between INJ and the others samples, whatever the molecular mass: it was found that the yield stress was nearly twice lower for INJ samples compared to I213 samples. At first sight, this could be explained by a difference of crystallinity index

but one may wonder about the role of the crystalline phase. Indeed, it is reported in the literature that β phase is more ductile than α phase. Anyway, a linear relationship between the Young's modulus and the crystallinity index was found. Also, the fact that the yield stress is more sensitive to the crystallinity index than the Young's modulus could be explained via a dislocation approach of the plastic yielding of semi-crystalline polymers above T_g .

In contrast, below T_g , all the samples display nearly the same yield point meaning that the crystallinity index no longer plays a major role. Indeed, observing the same values of yield stress suggests that yielding at such low temperature, i.e. far below both the melting point and the glass transition temperature, is not only controlled by conventional plastic processes such as micro shear bands but also by damaging processes such as cavitation and crazing.

Finally, the effect of the crystalline phase and of the lamellar morphology as well (thickness and shape for example) could play a role in the mechanisms of deformation: investigations at smaller scale during tensile tests are needed. Last but not least, no clear influence of the molecular mass has been evidenced concerning the studied mechanical properties: it could be interesting to investigate mechanical properties in the case of a molecular mass close to or lower than the critical molecular mass defined as $M_c \approx 2M_e$. Therefore, it has been decided to focus the microscopic investigation only on the higher molecular mass.

The investigation at the microscopic scale was divided into two parts: the elastic and plastic strain domains. Let us remind the conclusion of the results obtained in the elastic strain domain. SAXS allows following the deformation at the scale of lamella stacks. Firstly, the study on the local strain by SAXS has shown that polar lamellae contract and equatorial lamellae stretch. Furthermore, the ratio between the local and the macroscopic strains is always measured smaller than one. In addition, by analyzing the azimuthal distribution of the local strain, it was also found that the deformation of the lamellae system was relatively homogeneous through the material for all samples. However, since the local variation of the period of the lamella stacking is smaller than expected, this must be compensated by shear deformation in inclined lamella stacks. As a matter of fact, interlamellar shear is easier than either compression or stretching normal to lamellae surface. Indeed, compression or stretching involves an effective modulus which may be significantly higher than the Young's modulus of the amorphous phase.

Secondly, in order to characterize the stiffness of the crystalline phase, the crystal strain was followed by WAXS for samples with α and β phases at both temperatures. Above T_g , it was confirmed that the modulus of the amorphous phase drops down to a value much lower than the crystalline phase, as the crystal strain is much lower than below T_g , meaning that the amorphous phase is much more compliant than the crystals. Concerning the effect of crystalline phase, indeed, the crystal strain is always higher for β phase than α phase whatever the temperature, explaining why β phase is less stiff than α phase. The degree of homogeneity of the local strain/stress state was deduced from the azimuthal distribution of the crystal strain. It was found that for INJ sample with β phase, the strain or stress is relatively homogeneous, whereas for I213 sample with α phase, the strain/stress state is far from homogeneous.

Finally, the azimuthal distribution of the lamellae (SAXS) and the azimuthal distribution of the various crystalline planes (WAXS) have led us to define two models concerning the mechanisms of deformation: the Chain Network (CN) model and the Rigid Lamella (RL) model. In the CN model, the chains of the amorphous phase orient parallel to the tensile direction (TD), i.e. the lamellae orient normal to TD. In the RL model, lamellae orient parallel to TD, i.e. the chains are normal to TD. In the CN model, the orientation mechanisms are ruled by the amorphous chains which transmit the stress between adjacent lamellae. In the RL model, the lamellae govern their own mechanisms of orientation, possibly due to their high aspect ratio.

The occurrence of the mechanisms corresponding to the two models depends on the type of crystalline phase and on the tensile temperature (below or above T_g). In the case of INJ samples with β phase, it was found that the CN model applies whatever the temperature. In contrast, I213 and A215 samples with α phase follow the CN model below T_g but follow the RL model above T_g .

Concerning A200 samples ($\alpha+\gamma$ mixture), below T_g , the deformation mechanisms still follow the CN model, however above T_g , the deformation mechanisms are more complex and tend to follow the RL model.

The mechanical investigation was then pursued for the plastic strain domain, i.e. beyond the yield, through the processes of fibrillation, cavitation and phase transformation. The analysis of WAXS measurements has shown that samples with β or α phase behave in quite different ways in the plastic domain.

In samples with β phase, chains tend to orient along TD during all the deformation process (i.e. including the viscoelastic regime, denoted as the CN model). This tendency is magnified in the plastic strain regime until a high degree of orientation is reached. This kind of behavior is commonly observed for semi-crystalline polymers. When looking into more details, it was found that below T_g a “chevron-like” structure develops. This specific structure would deserve further SAXS and/or WAXS or other structural investigations. Concomitantly the β phase transforms into α phase. However this transformation seems to require a certain accommodation time or a minimum level of molecular relaxation since the 2 meridian spots at $2\theta=10.2^\circ$ and 4 off-meridian spots at $2\theta\approx 13^\circ$, due to α phase, were visible in-situ starting from $\epsilon=200\%$ but the two equatorial spots corresponding to (200) and (002)+(20 $\bar{2}$) reflections of α phase were not. The latter ones were distinctly visible only after unloading. Further investigations would be of great interest on the understanding of the transformation process. Nonetheless, the $\beta \rightarrow \alpha$ transformation does not seem to affect the deformation mechanisms.

In samples with α phase, a different two-step process occurs. In the first step, as described in the previous chapter, lamellae orient preferentially along TD, i.e. the chains being normal to TD (this the RL model mentioned in chapter V). In the second step, in the plastic regime, a major fraction of crystallites reorients normal to TD, i.e. with chains parallel to TD while a minor fraction remains oriented along TD. The position of the “intact” polar lamellae depends on the tensile test temperature: below T_g (200) planes are normal to TD whereas above T_g H-bonds are parallel to TD. It could be interesting to further investigate the reasons of this difference.

Concerning A200 samples with $\alpha+\gamma$ phases, the precise location of α and γ phases in spherulites is still an open question. Indeed, assuming that they are both present inside the same spherulite, it would seem that γ phase promotes the fragmentation of lamellae. As γ phase is more ductile, a lamella made of γ phase would break sooner and so promote the fragmentation as well as the rotation of all lamellae (including lamellae made of α phase), allowing the orientation of all chains along TD. This process may be possible since the γ phase has a significant fraction even though it is the minority phase.

Considering the ultimate stage of deformation that we have investigated in this work, the final fibrillar state seems to strongly depend on the initial microstructure of the sample. Concerning the effect of temperature, it has been observed that for all samples, the final stage is better oriented above the glass transition. Regarding the phenomenon of cavitation, it was found that, below T_g , cavitation occurs for all samples but not in the same way depending on the crystalline phases. It would be interesting to study more in details this phenomenon in order to understand why the process of cavitation is different for the various samples.

Finally, back to our multi-scale approach, we can now better understand the difference of behavior observed at the macroscopic scale. Finding that β phase is more ductile than α phase is one of the key parameters which can explain the difference of ductility between the INJ and I213 samples. Furthermore, we found that it was easier for β phase to extend its chains and orient them in tensile direction (TD) than α phase. Concerning the difference of behavior above T_g between INJ and other samples, it could also be explained by the fact that only INJ samples follow the CN model at this temperature whereas the others follow the RL model. In contrast, all the samples follow the CN model below T_g and this could be the reason why the same macroscopic behavior was observed for all.

Appendix

Article: *“Assessment of polyamide-6 crystallinity by DSC: the temperature dependence of the melting enthalpy”*

Coraline Millot, Louise-Anne Fillot, Olivier Lame, Paul Sotta, Roland Seguela
Journal of Thermal Analysis and Calorimetry

DOI : 10.1007/s10973-015-4670-5

FOLIO ADMINISTRATIF

THESE SOUTENUE DEVANT L'INSTITUT NATIONAL DES SCIENCES APPLIQUEES DE LYON

NOM : MILLOT

DATE de SOUTENANCE : 7 Avril 2015

Prénom : Coraline

TITRE : Caractérisation multi-échelle des mécanismes de déformation du polyamide 6 massif en traction au-dessus et au-dessous de la transition vitreuse

NATURE : Doctorat

Numéro d'ordre : 2015 ISAL 0028

Ecole doctorale : Matériaux de Lyon

Spécialité : Génie des matériaux : microstructure, comportement mécanique

RESUME :

Notre étude a porté sur la compréhension microscopique des mécanismes de déformation du polyamide 6 (PA6) à l'état massif. Par des traitements thermiques appropriés, on a obtenu un jeu d'échantillons présentant des microstructures semi-cristallines variées, avec différentes formes cristallographiques (allotropes : α , γ ou β), différents taux de cristallinité (de 24 à 35%), différentes périodes de l'empilement des lamelles cristallines (de 7 à 12nm), ceci pour deux masses moléculaires différentes. Les propriétés mécaniques en traction ont été caractérisées au-dessus et au-dessous de la transition vitreuse de la phase amorphe (T_g). Les différents matériaux présentent des différences notables de comportements. Le taux de cristallinité semble être le facteur prédominant au-dessus de T_g , mais d'autres facteurs sont à prendre en compte en dessous de T_g , comme la forme cristalline et la morphologie lamellaire (épaisseur et facteur de forme). Grâce à un dispositif expérimental fabriqué sur mesure, des essais de traction ont été suivis par diffusion des rayons X aux petits (SAXS) et grands angles (WAXS) sur la ligne D2AM, ESRF, pour caractériser les déformations à l'échelle des empilements lamellaires et à l'échelle de la maille cristalline. Dans les échantillons présentant principalement de la phase cristalline β , les lamelles tendent à s'orienter perpendiculairement à la direction de traction (TD). Ce mécanisme d'orientation local (que nous appelons « modèle de réseau de chaînes ») est induit par la transmission des contraintes par les chaînes amorphes reliant les lamelles cristallines adjacentes. L'allongement local est plus faible que l'allongement macroscopique dans les lamelles perpendiculaire à TD, ce qui implique que les lamelles inclinées doivent être cisailées. De plus, la phase β se transforme en phase α aux fortes extensions. Dans les échantillons présentant principalement de la phase α (la plus rigide), au-dessus de T_g , dans le régime élastique, les chaînes tendent d'abord à s'orienter perpendiculairement à TD, ce qui implique que les lamelles s'orientent parallèlement à TD (« modèle de lamelles rigides »). Ensuite, dans le régime plastique, une majeure partie des lamelles se réoriente perpendiculairement à TD, comme dans le « modèle de réseau de chaînes », tandis qu'une fraction mineure reste orientée parallèlement à TD. Une morphologie fibrillaire fortement orientée est finalement obtenue pour tous les échantillons quelle que soit la température.

MOTS-CLES : polyamide 6, WAXS, SAXS, traction in-situ, domaine élastique, domaine plastique, transformation de phases

Laboratoire (s) de recherche :

MATEIS – INSA de LYON / CNRS (UMR 5510)

LPMA – SOLVAY / CNRS (UMR 5268)

Directeurs de thèse: LAME Olivier (MATEIS), SOTTA Paul (LPMA)

Président de jury : BILLON Noëlle

Composition du jury : AURIEMMA Finizia, BILLON Noëlle, FILLOT Louise-Anne, LAME Olivier, MIRI Valérie, SEGUELA Roland, SOTTA Paul, ROCHAS Cyrille